

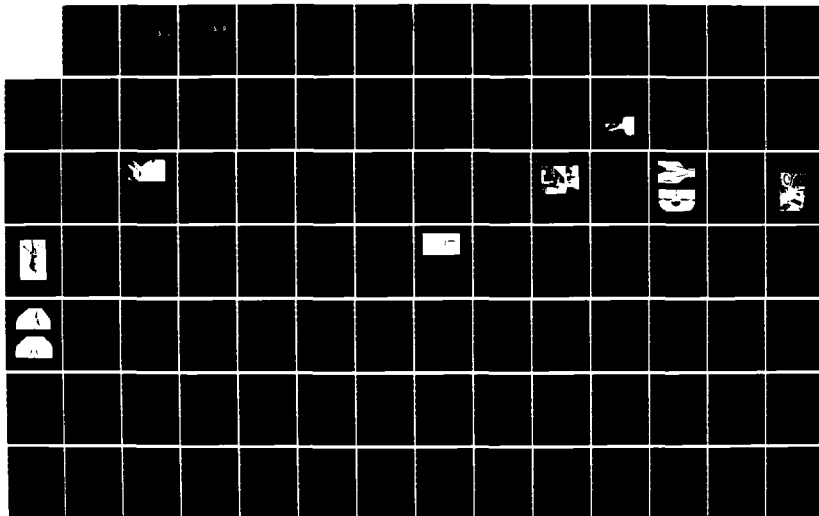
AD-A164 104

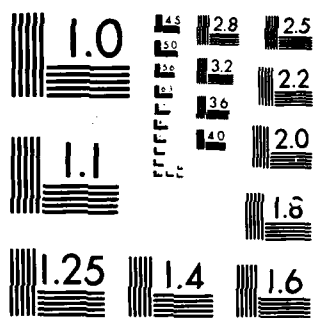
EXPERIMENTAL ASSESSMENT OF VORTEX RETAINING CAVITY
FLAPS FOR MANEUVERABIL... (U) AIR FORCE INST OF TECH
WRIGHT-PATTERSON AFB OH SCHOOL OF ENGI... H C SMITH
DEC 85 AFIT/GAE/AA/85D-13 F/G 1/3

1/3

UNCLASSIFIED

NL

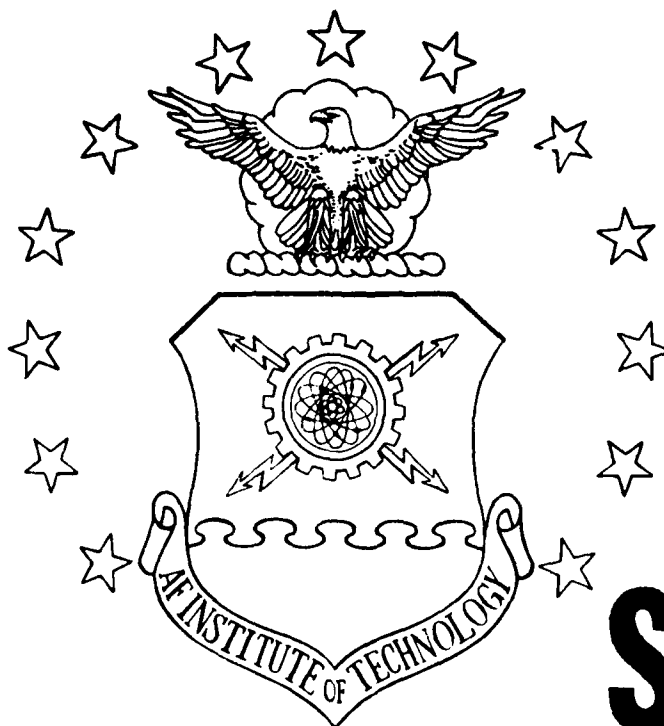




MICROCOPY RESOLUTION TEST CHART
NATIONAL BUREAU OF STANDARDS 1963-A

AD-A164 104

FILE COPY



DTIC
ELECTE
FEB 14 1986
S D

EXPERIMENTAL ASSESSMENT OF VORTEX
RETAINING CAVITY FLAPS FOR
MANEUVERABILITY IMPROVEMENT ON
DELTA WING FIGHTER AIRCRAFT

THESIS

Huland Christopher Smith
Captain, United States Air Force

AFIT/GAE/AA/85D-13

DISTRIBUTION STATEMENT A

Approved for public release;
Distribution Unlimited

DEPARTMENT OF THE AIR FORCE

AIR UNIVERSITY

AIR FORCE INSTITUTE OF TECHNOLOGY

Wright-Patterson Air Force Base, Ohio

86 0 1 1 005

AFIT/GAE/AA/85D-13

DTIC
ELECTE
FEB 14 1986
S D D

EXPERIMENTAL ASSESSMENT OF VORTEX
RETAINING CAVITY FLAPS FOR
MANEUVERABILITY IMPROVEMENT ON
DELTA WING FIGHTER AIRCRAFT

THESIS

Huland Christopher Smith
Captain, United States Air Force

AFIT/GAE/AA/85D-13

Approved for public release; distribution unlimited.

AFIT/GAE/AA/85D-13

EXPERIMENTAL ASSESSMENT OF VORTEX RETAINING CAVITY FLAPS FOR
MANEUVERABILITY IMPROVEMENT ON DELTA WING FIGHTER AIRCRAFT

THESIS

Presented to the Faculty of the School of Engineering
of the Air Force Institute of Technology

Air University

In Partial Fulfillment of the

Requirements for the Degree of

Master of Science in Aeronautical Engineering

Huland Christopher Smith, B.S.E.

Captain, United States Air Force

December 1985

Accession For	
NTIS CRA&I	<input checked="checked" type="checkbox"/>
DTIC TAB	<input type="checkbox"/>
Unannounced	<input type="checkbox"/>
Justification	
By	
Distribution /	
Availability Codes	
Dist	Avail and/or Special
A-1	

Approved for public release; distribution unlimited.

Acknowledgements

This study is not the sole effort of one lone graduate student toiling for months on end. It is the collective effort of various individuals to whom I am deeply indebted. First, and foremost, I express my sincere appreciation to Mr. Andy Rimenschnider, AFIT's wind tunnel technician. Andy made my baptism into wind tunnel testing less painful and a lot more productive. His vast experience with the operational side of wind tunnel testing and his willingness to go that "extra mile" in helping me was a valuable asset to my thesis project.

Of course, no testing can be done if a model does not exist. Therefore, I take pleasure in thanking the AFIT fabrication shop personnel, especially Mr. John Brohaus and Mr. Jack Tiffany. John did the bulk of the model building while Jack made numerous cavity flap shapes I designed. The precision of the model and flaps, and the dedication these two men have shown my thesis project deserves more credit and praise than I can give them here.

Wind tunnel testing involves the acquisition of aerodynamic data. I received a great deal of help in this department from Mr. Jim Grove of the Flight Dynamics Laboratory. Jim helped set up the data acquisition system and software, helped with the instrumentation calibration,

and freely answered a seemingly endless number of questions that I put before him about it all. Thank you, Jim.

Every project needs someone that can tie all the pieces together, to act as a sponsor. Here, I relied heavily on First Lieutenant Mark Frassinelli of the Flight Dynamics Laboratory. Mark was instrumental in coordinating outside organizations needed to get my thesis project going and to keep it going. This left me free to concern myself with other tasks at hand.

Likewise, every project needs someone that can solve those unexpected problems that plague even the best projects. A hearty thanks goes to Mr. Nicholas Yardich, AFIT's laboratory supervisor. Nick handled several problems throughout my thesis project which again left me free to attend to my testing.

Last, but certainly not least, I express my appreciation to my thesis advisor, Captain Wesley Cox. He was the source of a lot of answers to questions that arose during my thesis project. I am also thankful to Captain Cox for his friendly encouragement, comments and suggestions on the writing of this thesis.

Huland Christopher Smith

Table of Contents

	Page
Acknowledgements	ii
List of Figures	vi
List of Tables	xiii
Notation	xiv
Abstract	xvii
I. Introduction	1
Purpose	1
Background	1
Approach	3
II. Theory	6
Longitudinal Control	10
Lateral Control	11
Directional Control	12
III. Test Equipment	14
Wind Tunnel	14
Instrumentation	15
Model	16
Support Apparatus	19
Data Acquisition	22
IV. Calibration	23
Internal Balance	23
Sting Deflection	24
Flow Angularity	24
Angle of Attack	25
Sideslip Angle	26
V. Procedure and Analysis	27
Procedure	27
Data Analysis	28

VI. Results	32
Longitudinal Control	37
Lateral Control	38
Directional Control	40
Lift and Drag Considerations	41
Oil Flow Visualization	42
VII. Conclusions and Recommendations	94
Conclusions	94
Recommendations	96
Appendix A: Test Data Plots	A-1
Appendix B: Oil Flow Visualizations	B-1
Bibliography	BIB-1
Vita	VIT-1

List of Figures

	Page
1. 60° Swept Delta Wing Model.....	3
2. Aircraft Body Reference Frame.....	5
3. Leading Edge Vortex Structure.....	7
4. Cavity Flaps Deployed on Delta Wing Model.....	9
5. Tunnel Acquisition and Computer Support Equipment...	16
6. Dimensions of Delta Wing Model Used in Study.....	17
7. Bottom View of Model Showing Nose Strake.....	18
8. Frontal View of Model Showing Nose Strake.....	18
9. Tunnel Operator's Station.....	20
10. Modified Sting Showing 20° Offset.....	21
11. Nose Oil Flow Visualization Showing Rubber Band, Strake, and Flow Detachment.....	28
12. Internal Strain Gage Balance Positive Components....	29
13. Cavity Flap Locations Relative to the Wing.....	34
14. Model with Asymmetrically Deployed Cavity Flap.....	35
15. Model with Symmetrically Deployed Cavity Flaps.....	35
16. C1 Flap ΔC_L and ΔC_D for Various Deflection Angles (asymmetric).....	43
17. C1 Flap ΔC_m and ΔC_i for Various Deflection Angles (asymmetric).....	44
18. C1 Flap ΔC_v and ΔC_n for Various Deflection Angles (asymmetric).....	45
19. C1 Flap ΔC_L and ΔC_D for Various Deflection Angles (symmetric).....	46
20. C1 Flap ΔC_m and ΔC_i for Various Deflection Angles (symmetric).....	47
21. C1 Flap ΔC_v and ΔC_n for Various Deflection Angles (symmetric).....	48
22. C2 Flap ΔC_L and ΔC_D for Various Deflection Angles (asymmetric).....	49
23. C2 Flap ΔC_m and ΔC_i for Various Deflection Angles (asymmetric).....	50

24.	C2 Flap ΔC_v and ΔC_m for Various Deflection Angles (asymmetric).....	51
25.	C2 Flap ΔC_L and ΔC_D for Various Deflection Angles (symmetric).....	52
26.	C2 Flap ΔC_m and ΔC_i for Various Deflection Angles (symmetric).....	53
27.	C2 Flap ΔC_v and ΔC_m for Various Deflection Angles (symmetric).....	54
28.	C3 Flap ΔC_L and ΔC_D for Various Deflection Angles (asymmetric).....	55
29.	C3 Flap ΔC_m and ΔC_i for Various Deflection Angles (asymmetric).....	56
30.	C3 Flap ΔC_v and ΔC_m for Various Deflection Angles (asymmetric).....	57
31.	C3 Flap ΔC_L and ΔC_D for Various Deflection Angles (symmetric).....	58
32.	C3 Flap ΔC_m and ΔC_i for Various Deflection Angles (symmetric).....	59
33.	C3 Flap ΔC_v and ΔC_m for Various Deflection Angles (symmetric).....	60
34.	C4 Flap ΔC_L and ΔC_D for Various Deflection Angles (asymmetric).....	61
35.	C4 Flap ΔC_m and ΔC_i for Various Deflection Angles (asymmetric).....	62
36.	C4 Flap ΔC_v and ΔC_m for Various Deflection Angles (asymmetric).....	63
37.	C4 Flap ΔC_L and ΔC_D for Various Deflection Angles (symmetric).....	64
38.	C4 Flap ΔC_m and ΔC_i for Various Deflection Angles (symmetric).....	65
39.	C4 Flap ΔC_v and ΔC_m for Various Deflection Angles (symmetric).....	66
40.	ΔC_L and ΔC_D for Various Sweep Angles at 45° Deflection (asymmetric).....	67
41.	ΔC_m and ΔC_i for Various Sweep Angles at 45° Deflection (asymmetric).....	68
42.	ΔC_v and ΔC_m for Various Sweep Angles at 45° Deflection (asymmetric).....	69
43.	ΔC_L and ΔC_D for Various Sweep Angles at 60° Deflection (asymmetric).....	70
44.	ΔC_m and ΔC_i for Various Sweep Angles at 60° Deflection (asymmetric).....	71
45.	ΔC_v and ΔC_m for Various Sweep Angles at 60° Deflection (asymmetric).....	72
46.	ΔC_L and ΔC_D for Various Sweep Angles at 45° Deflection (symmetric).....	73
47.	ΔC_m and ΔC_i for Various Sweep Angles at 45° Deflection (symmetric).....	74
48.	ΔC_v and ΔC_m for Various Sweep Angles at 45° Deflection (symmetric).....	75
49.	ΔC_L and ΔC_D for Various Sweep Angles at 60° Deflection (symmetric).....	76

50.	ΔC_m and ΔC_l for Various Sweep Angles at 60° Deflection (symmetric).....	77
51.	ΔC_v and ΔC_n for Various Sweep Angles at 60° Deflection (symmetric).....	78
52.	ΔC_L and ΔC_D for Various Flap Areas at 45° Deflection (asymmetric).....	79
53.	ΔC_m and ΔC_l for Various Flap Areas at 45° Deflection (asymmetric).....	80
54.	ΔC_v and ΔC_n for Various Flap Areas at 45° Deflection (asymmetric).....	81
55.	ΔC_L and ΔC_D for Various Flap Areas at 60° Deflection (asymmetric).....	82
56.	ΔC_m and ΔC_l for Various Flap Areas at 60° Deflection (asymmetric).....	83
57.	ΔC_v and ΔC_n for Various Flap Areas at 60° Deflection (asymmetric).....	84
58.	ΔC_L and ΔC_D for Various Flap Areas at 60° Deflection (symmetric).....	85
59.	ΔC_m and ΔC_l for Various Flap Areas at 60° Deflection (symmetric).....	86
60.	ΔC_v and ΔC_n for Various Flap Areas at 60° Deflection (symmetric).....	87
61.	ΔC_L and ΔC_D for Various Yaw Angles at 60° Deflection (asymmetric).....	88
62.	ΔC_m and ΔC_l for Various Yaw Angles at 60° Deflection (asymmetric).....	89
63.	ΔC_v and ΔC_n for Various Yaw Angles at 60° Deflection (asymmetric).....	90
64.	ΔC_L and ΔC_D for Various Yaw Angles at 60° Deflection (symmetric).....	91
65.	ΔC_m and ΔC_l for Various Yaw Angles at 60° Deflection (symmetric).....	92
66.	ΔC_v and ΔC_n for Various Yaw Angles at 60° Deflection (symmetric).....	93

Appendix A

A1.	Model Baseline Lift and Drag Data (no cavity flaps).....	A-3
A2.	Model Baseline Side Force and Moments Data (no cavity flaps).....	A-4
A3.	Model Baseline Lift and Drag Data (+6 deg yaw).....	A-5
A4.	Model Baseline Side Force and Moments Data (+6 deg yaw).....	A-6
A5.	Model Baseline Lift and Drag Data (-6 deg yaw).....	A-7
A6.	Model Baseline Side Force and Moments Data (-6 deg yaw).....	A-8
A7.	C1 Flap Lift and Drag Data (deployed 30 deg asymmetric).....	A-9

A8.	C1 Flap Side Force and Moments Data (deployed 30 deg asymmetric).....	A-10
A9.	C1 Flap Force and Moment Changes (deployed 30 deg asymmetric).....	A-11
A10.	C1 Flap Lift and Drag Data (deployed 30 deg symmetric).....	A-12
A11.	C1 Flap Side Force and Moments Data (deployed 30 deg symmetric).....	A-13
A12.	C1 Flap Force and Moment Changes (deployed 30 deg symmetric).....	A-14
A13.	C1 Flap Lift and Drag Data (deployed 45 deg asymmetric).....	A-15
A14.	C1 Flap Side Force and Moments Data (deployed 45 deg asymmetric).....	A-16
A15.	C1 Flap Force and Moment Changes (deployed 45 deg asymmetric).....	A-17
A16.	C1 Flap Lift and Drag Data (deployed 45 deg symmetric).....	A-18
A17.	C1 Flap Side Force and Moments Data (deployed 45 deg symmetric).....	A-19
A18.	C1 Flap Force and Moment Changes (deployed 45 deg symmetric).....	A-20
A19.	C1 Flap Lift and Drag Data (deployed 60 deg asymmetric).....	A-21
A20.	C1 Flap Side Force and Moments Data (deployed 60 deg asymmetric).....	A-22
A21.	C1 Flap Force and Moment Changes (deployed 60 deg asymmetric).....	A-23
A22.	C1 Flap Lift and Drag Data (deployed 60 deg symmetric).....	A-24
A23.	C1 Flap Side Force and Moments Data (deployed 60 deg symmetric).....	A-25
A24.	C1 Flap Force and Moment Changes (deployed 60 deg symmetric).....	A-26
A25.	C1 Flap Lift and Drag Data (deployed 75 deg asymmetric).....	A-27
A26.	C1 Flap Side Force and Moments Data (deployed 75 deg asymmetric).....	A-28
A27.	C1 Flap Force and Moment Changes (deployed 75 deg asymmetric).....	A-29
A28.	C2 Flap Lift and Drag Data (deployed 30 deg asymmetric).....	A-30
A29.	C2 Flap Side Force and Moments Data (deployed 30 deg asymmetric).....	A-31
A30.	C2 Flap Force and Moment Changes (deployed 30 deg asymmetric).....	A-32
A31.	C2 Flap Lift and Drag Data (deployed 30 deg symmetric).....	A-33
A32.	C2 Flap Side Force and Moments Data (deployed 30 deg symmetric).....	A-34
A33.	C2 Flap Force and Moment Changes (deployed 30 deg symmetric).....	A-35

A34.	C2 Flap Lift and Drag Data (deployed 45 deg asymmetric).....	A-36
A35.	C2 Flap Side Force and Moments Data (deployed 45 deg asymmetric).....	A-37
A36.	C2 Flap Force and Moment Changes (deployed 45 deg asymmetric).....	A-38
A37.	C2 Flap Lift and Drag Data (deployed 60 deg asymmetric).....	A-39
A38.	C2 Flap Side Force and Moments Data (deployed 60 deg asymmetric).....	A-40
A39.	C2 Flap Force and Moment Changes (deployed 60 deg asymmetric).....	A-41
A40.	C2 Flap Lift and Drag Data (deployed 60 deg symmetric).....	A-42
A41.	C2 Flap Side Force and Moments Data (deployed 60 deg symmetric).....	A-43
A42.	C2 Flap Force and Moment Changes (deployed 60 deg symmetric).....	A-44
A43.	C2 Flap Lift and Drag Data (deployed 75 deg asymmetric).....	A-45
A44.	C2 Flap Side Force and Moments Data (deployed 75 deg asymmetric).....	A-46
A45.	C2 Flap Force and Moment Changes (deployed 75 deg asymmetric).....	A-47
A46.	C3 Flap Lift and Drag Data (deployed 45 deg asymmetric).....	A-48
A47.	C3 Flap Side Force and Moments Data (deployed 45 deg asymmetric).....	A-49
A48.	C3 Flap Force and Moment Changes (deployed 45 deg asymmetric).....	A-50
A49.	C3 Flap Lift and Drag Data (deployed 45 deg symmetric).....	A-51
A50.	C3 Flap Side Force and Moments Data (deployed 45 deg symmetric).....	A-52
A51.	C3 Flap Force and Moment Changes (deployed 45 deg symmetric).....	A-53
A52.	C3 Flap Lift and Drag Data (deployed 60 deg asymmetric).....	A-54
A53.	C3 Flap Side Force and Moments Data (deployed 60 deg asymmetric).....	A-55
A54.	C3 Flap Force and Moment Changes (deployed 60 deg asymmetric).....	A-56
A55.	C3 Flap Lift and Drag Data (deployed 60 deg symmetric).....	A-57
A56.	C3 Flap Side Force and Moments Data (deployed 60 deg symmetric).....	A-58
A57.	C3 Flap Force and Moment Changes (deployed 60 deg symmetric).....	A-59
A58.	C4 Flap Lift and Drag Data (deployed 30 deg asymmetric).....	A-60
A59.	C4 Flap Side Force and Moments Data (deployed 30 deg asymmetric).....	A-61

A60.	C4 Flap Force and Moment Changes (deployed 30 deg asymmetric).....	A-62
A61.	C4 Flap Lift and Drag Data (deployed 30 deg symmetric).....	A-63
A62.	C4 Flap Side Force and Moments Data (deployed 30 deg symmetric).....	A-64
A63.	C4 Flap Force and Moment Changes (deployed 30 deg symmetric).....	A-65
A64.	C4 Flap Lift and Drag Data (deployed 60 deg asymmetric).....	A-66
A65.	C4 Flap Side Force and Moments Data (deployed 60 deg asymmetric).....	A-67
A66.	C4 Flap Force and Moment Changes (deployed 60 deg asymmetric).....	A-68
A67.	C4 Flap Lift and Drag Data (deployed 60 deg symmetric).....	A-69
A68.	C4 Flap Side Force and Moments Data (deployed 60 deg symmetric).....	A-70
A69.	C4 Flap Force and Moment Changes (deployed 60 deg symmetric).....	A-71
A70.	C4 Flap Lift and Drag Data (deployed 90 deg asymmetric).....	A-72
A71.	C4 Flap Side Force and Moments Data (deployed 90 deg asymmetric).....	A-73
A72.	C4 Flap Force and Moment Changes (deployed 90 deg asymmetric).....	A-74
A73.	C4 Flap Lift and Drag Data (deployed 90 deg symmetric).....	A-75
A74.	C4 Flap Side Force and Moments Data (deployed 90 deg symmetric).....	A-76
A75.	C4 Flap Force and Moment Changes (deployed 90 deg symmetric).....	A-77
A76.	C5 Flap Lift and Drag Data (deployed 60 deg asymmetric).....	A-78
A77.	C5 Flap Side Force and Moments Data (deployed 60 deg asymmetric).....	A-79
A78.	C5 Flap Force and Moment Changes (deployed 60 deg asymmetric).....	A-80
A79.	C5 Flap Lift and Drag Data (deployed 75 deg asymmetric).....	A-81
A80.	C5 Flap Side Force and Moments Data (deployed 75 deg asymmetric).....	A-82
A81.	C5 Flap Force and Moment Changes (deployed 75 deg asymmetric).....	A-83
A82.	C6 Flap Lift and Drag Data (deployed 90 deg asymmetric).....	A-84
A83.	C6 Flap Side Force and Moments Data (deployed 90 deg asymmetric).....	A-85
A84.	C6 Flap Force and Moment Changes (deployed 90 deg asymmetric).....	A-86
A85.	C7 Flap Lift and Drag Data (deployed 90 deg asymmetric).....	A-87

A86.	C7 Flap Side Force and Moments Data (deployed 90 deg asymmetric).....	A-88
A87.	C7 Flap Force and Moment Changes (deployed 90 deg asymmetric).....	A-89
A88.	C8 Flap Lift and Drag Data (deployed 90 deg asymmetric).....	A-90
A89.	C8 Flap Side Force and Moments Data (deployed 90 deg asymmetric).....	A-91
A90.	C8 Flap Force and Moment Changes (deployed 90 deg asymmetric).....	A-92
A91.	C9 Flap Lift and Drag Data (deployed 30 deg asymmetric).....	A-93
A92.	C9 Flap Side Force and Moments Data (deployed 30 deg asymmetric).....	A-94
A93.	C9 Flap Force and Moment Changes (deployed 30 deg asymmetric).....	A-95
A94.	C10 Flap Lift and Drag Data (deployed 60 deg asymmetric).....	A-96
A95.	C10 Flap Side Force and Moments Data (deployed 60 deg asymmetric).....	A-97
A96.	C10 Flap Force and Moment Changes (deployed 60 deg asymmetric).....	A-98
A97.	C1 Flap Lift and Drag Data (deployed 60 deg asymmetric)(+6 deg yaw).....	A-99
A98.	C1 Flap Side Force and Moments Data (deployed 60 deg asymmetric)(+6 deg yaw).....	A-100
A99.	C1 Flap Force and Moment Changes (deployed 60 deg asymmetric)(+6 deg yaw).....	A-101
A100.	C1 Flap Lift and Drag Data (deployed 60 deg symmetric)(+6 deg yaw).....	A-102
A101.	C1 Flap Side Force and Moments Data (deployed 60 deg symmetric)(+6 deg yaw).....	A-103
A102.	C1 Flap Force and Moment Changes (deployed 60 deg symmetric)(+6 deg yaw).....	A-104
A103.	C1 Flap Lift and Drag Data (deployed 60 deg asymmetric)(-6 deg yaw).....	A-105
A104.	C1 Flap Side Force and Moments Data (deployed 60 deg asymmetric)(-6 deg yaw).....	A-106
A105.	C1 Flap Force and Moment Changes (deployed 60 deg asymmetric)(-6 deg yaw).....	A-107
A106.	C1 Flap Lift and Drag Data (deployed 60 deg symmetric)(-6 deg yaw).....	A-108
A107.	C1 Flap Side Force and Moments Data (deployed 60 deg symmetric)(-6 deg yaw).....	A-109
A108.	C1 Flap Force and Moment Changes (deployed 60 deg symmetric)(-6 deg yaw).....	A-110

Appendix B

B1.	Upper Wing Surface of Model Baseline at 9.5° α	B-3
-----	--	-----

B2.	Lower Wing Surface of Model Baseline at 9.5° α	B-3
B3.	Upper Wing Surface of Model Baseline at 20° α	B-4
B4.	Lower Wing Surface of Model Baseline at 20° α	B-4
B5.	Upper Wing Surface of Model Baseline at 30° α	B-5
B6.	Lower Wing Surface of Model Baseline at 30° α	B-5
B7.	Lower Wing Surface with C1 Flap Deployed 60° at 9.5° α	B-6
B8.	Inside Surface of C1 Cavity Flap Deployed 60° at 9.5° α	B-6
B9.	Lower Wing Surface With C1 Flap Deployed 60° at 20° α	B-7
B10.	Inside Surface of C1 Cavity Flap Deployed 60° at 20° α	B-7
B11.	Lower Wing Surface with C1 Flap Deployed 60° at 30° α	B-8
B12.	Inside Surface of C1 Cavity Flap Deployed 60° at 30° α	B-8
B13.	Lower Wing Surface with C2 Flap Deployed 60° at 9.5° α	B-9
B14.	Lower Wing Surface with C2 Flap Deployed 60° at 20° α	B-9
B15.	Inside Surface of C2 Cavity Flap Deployed 60° at 20° α	B-10
B16.	Lower Wing Surface with C2 Flap Deployed 60° at 30° α	B-10
B17.	Inside Surface of C2 Cavity Flap Deployed 60° at 30° α	B-11
B18.	Upper Wing Surface wiht C3 Flap Deployed 60° at 30° α	B-11
B19.	Lower Wing Surface with C3 Flap Deployed 60° at 30° α	B-12
B20.	Inside Surface of C3 Cavity Flap Deployed 60° at 30° α	B-12
B21.	Lower Wing Surface with C4 Flap Deployed 60° at 20° α	B-13
B22.	Upper Wing Surface with C4 Flap Deployed 60° at 20° α	B-13

List of Tables

1.	Strain Gage Interaction Matrix.....	24
2.	Description of Cavity Flaps Tested.....	33

Notation

A	Axial Force (pounds)
AFB	Air Force Base
AFFDL	Air Force Flight Dynamics Laboratory
AFIT	Air Force Institute of Technology
A1	Axial Force Component Balance Output
C	Wind Tunnel Test Section Area (square feet)
C_D	Drag Coefficient (D/qS)
C_L	Lift Coefficient (L/qS)
C_Y	Side Force Coefficient (Y/qS)
C_l	Rolling Moment Coefficient (l/qSb)
C_m	Pitching Moment Coefficient ($m/qS\bar{c}$)
C_n	Yawing Moment Coefficient (n/qSb)
C1 - C10	Cavity Flap Configurations
D	Aerodynamic Drag (pounds)
D_u	Uncorrected Drag (pounds)
DACU	Data Acquisition and Control Unit
L	Aerodynamic Lift (pounds)
L_u	Uncorrected Lift (pounds)
M	Mach Number (u/a)
N	Normal Force (pounds)
N1	Fore Normal Force Component Balance Output
N2	Aft Normal Force Component Balance Output
R1	Rolling Moment Component Balance Output

Re	Reynolds Number
S	Model Wing Area (square feet)
S1	Fore Side Force Component Balance Output
S2	Aft Side Force Component Balance Output
V	Model Volume (cubic feet)
V _∞	Free Stream Velocity (feet per second)
ViRA	Vigyan Research Associates, Inc.
Y	Side Force (pounds)
Y _u	Uncorrected Side Force (pounds)
a	Speed of Sound (feet per second)
b	Model Wing Span (feet)
b.l.	Boundary Layer
\bar{c}	Mean Aerodynamic Chord (m.a.c.) (feet)
fps	feet per second
l	Aerodynamic Rolling moment (inch pounds)
l _u	Uncorrected Rolling Moment (inch pounds)
l.e.	Leading Edge
m	Aerodynamic Pitching Moment (inch pounds)
m _u	Uncorrected Pitching Moment (inch pounds)
n	Aerodynamic Yawing Moment (inch pounds)
n _u	Uncorrected Yawing Moment (inch pounds)
psf	Pounds per Square Foot
psi	Pounds per Square inch
q	Dynamic Pressure ($\frac{1}{2}\rho V^2$) (pounds per square foot)
q _c	Corrected Dynamic Pressure
q _u	Uncorrected Dynamic Pressure

t.e.	Trailing Edge
u	Flight Velocity (feet per second)
unit Re	Unit Reynolds Number (per foot) (qu/μ)
α	Aircraft Angle of Attack (degrees)
β	Aircraft Sideslip Angle (degrees)
δ	Cavity Flap Deflection Angle (degrees)
E	Test Section Total Blockage Factor
E_{sb}	Solid Blockage Factor
E_{wb}	Wake Blockage Factor
ρ	Atmospheric Density (slugs per cubic foot)
σ	Cavity Flap Hinge Line Sweep Angle (degrees)
μ	Flow Viscosity (slug per foot second)

Abstract

An experimental study was conducted to determine the effectiveness of cavity flaps on delta wing aircraft maneuverability. Cavity flaps are conformal control surfaces deployed in the apex region on the wing's lower surface. A 60° swept delta wing model was built and tested in the Air Force Institute of Technology five-foot diameter, subsonic wind tunnel. Ten different cavity flap configurations were tested at deflection angles ranging from 30° to 90° for both asymmetric and symmetric deployments. One configuration was tested at sideslip angles of -6° and 6° to determine the effect of yaw on the cavity flap. For all configurations the angle of attack was varied from -6° to 49°.

Coefficients of aerodynamic forces and moments versus angle of attack along with the lift to drag ratio versus lift coefficient and the drag polar were plotted for each flap configuration. The changes to the aerodynamic coefficients produced by adding the cavity flaps were also plotted. Oil flow visualization studies were performed on a limited number of cavity flap configurations at different angles of attack: 9.5, 20, and 30 degrees.

Results indicate that for longitudinal, lateral and directional maneuverability, the best cavity flap deflection angle will vary depending on the desired response. However,

the smaller deflection angles, 30° and 45° , gave the greatest moment changes. These results confirmed an earlier yaw control investigation by Rao at high angles of attack using a cavity flap deflected 45° along the fuselage. Data results also indicated it is best not to have the cavity flap hinge line located along or parallel to the fuselage for rolling and pitching moment considerations. Of the two hinge line sweep angles tested, 75° and 90° , the former produced greater moment changes. The cavity flap surface area had a large influence on the aerodynamic moments. The larger areas tested, 6% and 12% of the total wing area, showed the greatest changes. These larger areas were also responsible for significant drag reductions, up to 15%, in some configurations. But minimum lift losses as a result of cavity flap deployments came from the smaller cavity flap areas tested, 3% and 6% of the total wing area.

EXPERIMENTAL ASSESSMENT OF VORTEX RETAINING CAVITY FLAPS FOR MANEUVERABILITY IMPROVEMENT ON DELTA WING FIGHTER AIRCRAFT

I. Introduction

Purpose

The purpose of this study was to conduct basic aerodynamic research on the cavity flap concept. A cavity flap is a fully conformal lower wing surface flap that creates an external cavity between itself and the wing when it is deployed. Its hinge line location can vary from the wing's root chord to the wing's leading edge (l.e.). According to a vortex flow theory developed for analysis of their effect, these cavity flaps change the longitudinal, lateral, and directional maneuverability of delta wing aircraft. The objectives of this study were to evaluate the effects of the following parameters on cavity flap performance: cavity flap hinge line sweep angle (σ), cavity flap deflection angle (δ), asymmetric versus symmetric deployment, and cavity flap surface area.

Background

Based on current trends, future air combat will require tactical fighter aircraft with sustained cruise and maneuver capabilities in several flight regimes. The advantages of a

delta wing configuration have been emphasized in recent supersonic studies (9). Because of the wing's sharp leading edge, delta wing aircraft offer enhanced supersonic cruise ability but they are constrained by a vortex dominated flowfield in subsonic flight. For highly swept wings, flow detachment and vortex breakdown limit the effectiveness of conventional control surfaces at high angles of attack (α) and results in undesirable stability and control problems (12,5). Problems of this type would most likely occur shortly after takeoff during rapid ascent and in low speed, high α inflight maneuvers. The use of cavity flaps can control the formation and development of free vortices created at l.e. of the wings, and thus improve the maneuverability of the aircraft in these situations.

This research was conducted at the request of the Air Force Flight Dynamics Laboratory (AFFDL), Wright-Patterson Air Force Base (AFB), Ohio. It is the second phase in an ongoing study managed by AFFDL. The first phase was completed by Vigyan Research Associates, Inc. (ViRA) using North Carolina State University's low speed wind tunnel (10). ViRA used a half span model instrumentated for pressure measurements. The purpose of their research was to identify promising cavity flap shapes (10).

The Air Force Institute of Technology (AFIT) accepted the request from AFFDL to provide the research for the second phase. The research was divided into two parts, each

conducted as a separate thesis project. The research reported here dealt with the lower wing surface cavity flaps. The other thesis project concentrated on upper wing surface devices called apex fences. The data and results of that project are reported under another thesis title by Stuart (14).

Approach

The request from AFFD' called for an investigation of cavity flaps on a generic delta wing model, concentrating on high α 's. A model, based on the design used previously by ViRA (10), was scaled for use in the AFIT five-foot diameter subsonic wind tunnel and was built in the AFIT fabrication shop (Figure 1). A total of ten cavity flap configurations were built and tested.



Figure 1. 60° Swept Delta Wing Model

A six component, internal strain gage balance was used with a data acquisition and control unit for taking measurements of the forces and moments acting on the model. These body forces and moments were referenced to a conventional coordinate system and sign convention depicted in Figure 2 (2). A minicomputer was used to operate the acquisition system, and to collect the data, transform it to aerodynamic forces and moments, and store it for later use. Appendix A contains the plots of longitudinal, lateral, and directional data for each flap configuration tested, and plots of the changes the cavity flaps made to the data when compared to the model's baseline data. Longitudinal data plots consist of the lift coefficient (C_L), the drag coefficient (C_D), and the pitching moment coefficient (C_m) versus α , the lift to drag ratio (L/D) versus C_L , and the drag polar (C_D versus C_L). Lateral and directional data plots consist of the side force coefficient (C_Y), the rolling moment coefficient (C_l), and the yawing moment coefficient (C_n) versus α . The changes in C_L , C_D , C_Y , C_l , C_m , and C_n are plotted against α .

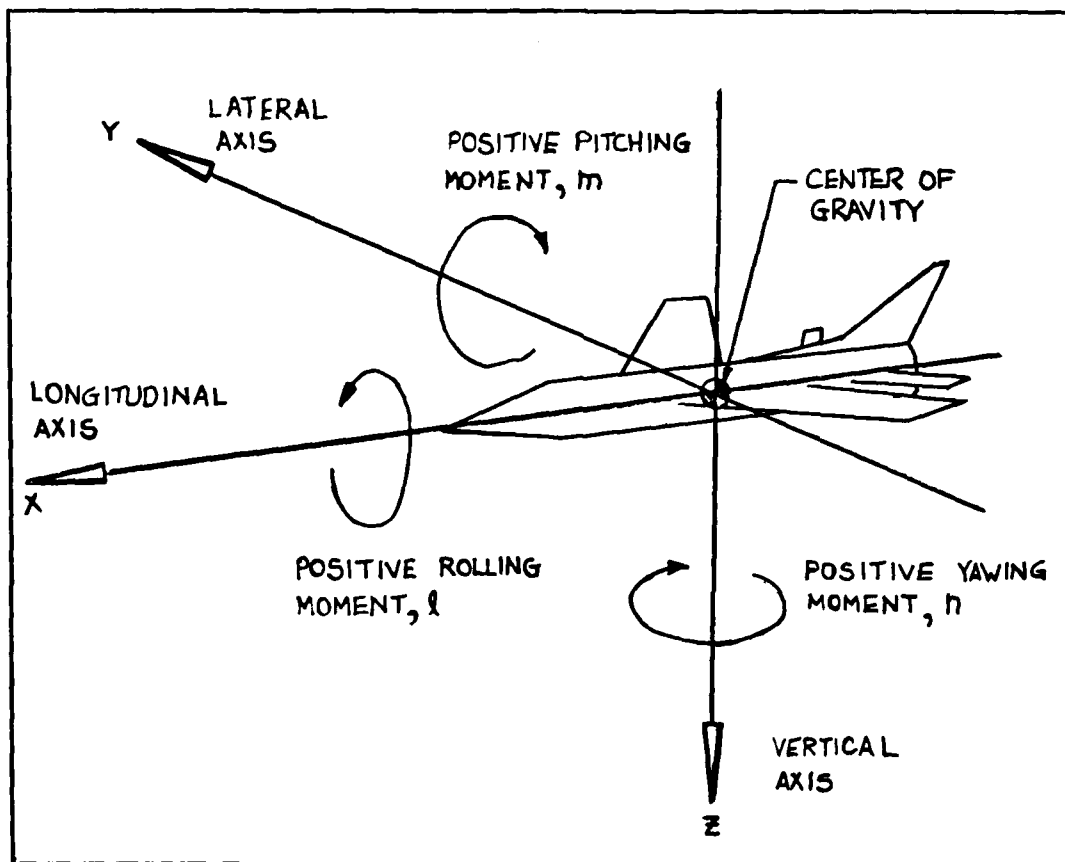


Figure 2. Aircraft Body Reference Frame

II. Theory

Vortex Lift Effect

Vortices are produced on delta wing aircraft by flow separation and detachment on the wing's upper surface. At all positive α 's, a stagnation line forms on the wing's lower surface. The flow ahead of the stagnation line travels forward around the wing's leading edge (l.e.) and then up and over the wing's upper surface. Due to the usually sharp l.e. radius (suited for supersonic flight) of a delta wing aircraft, the flow has trouble negotiating the sharp turning angles and detaches. This detached flow tends to roll up into a vortex and travels downstream at some angle to the wing's leading edge. Figure 3 shows the concept and some basic terms associated with a l.e. vortex.

The "vortex lift effect" is the production of lift from a l.e. vortex positioned over the wing's upper surface. Based on thin airfoil theory, the sectional lift of an airfoil is a function of the vorticity present in the flow (4). By integrating over the span of the wing, the total lift produced by the vortex can be obtained. The vortical flow will continue to travel downstream in a straight line until the core is perturbed and deviates from its path. At this point the vortex starts to disperse since the vorticity is distributed over a larger area. This phenomenon is known as

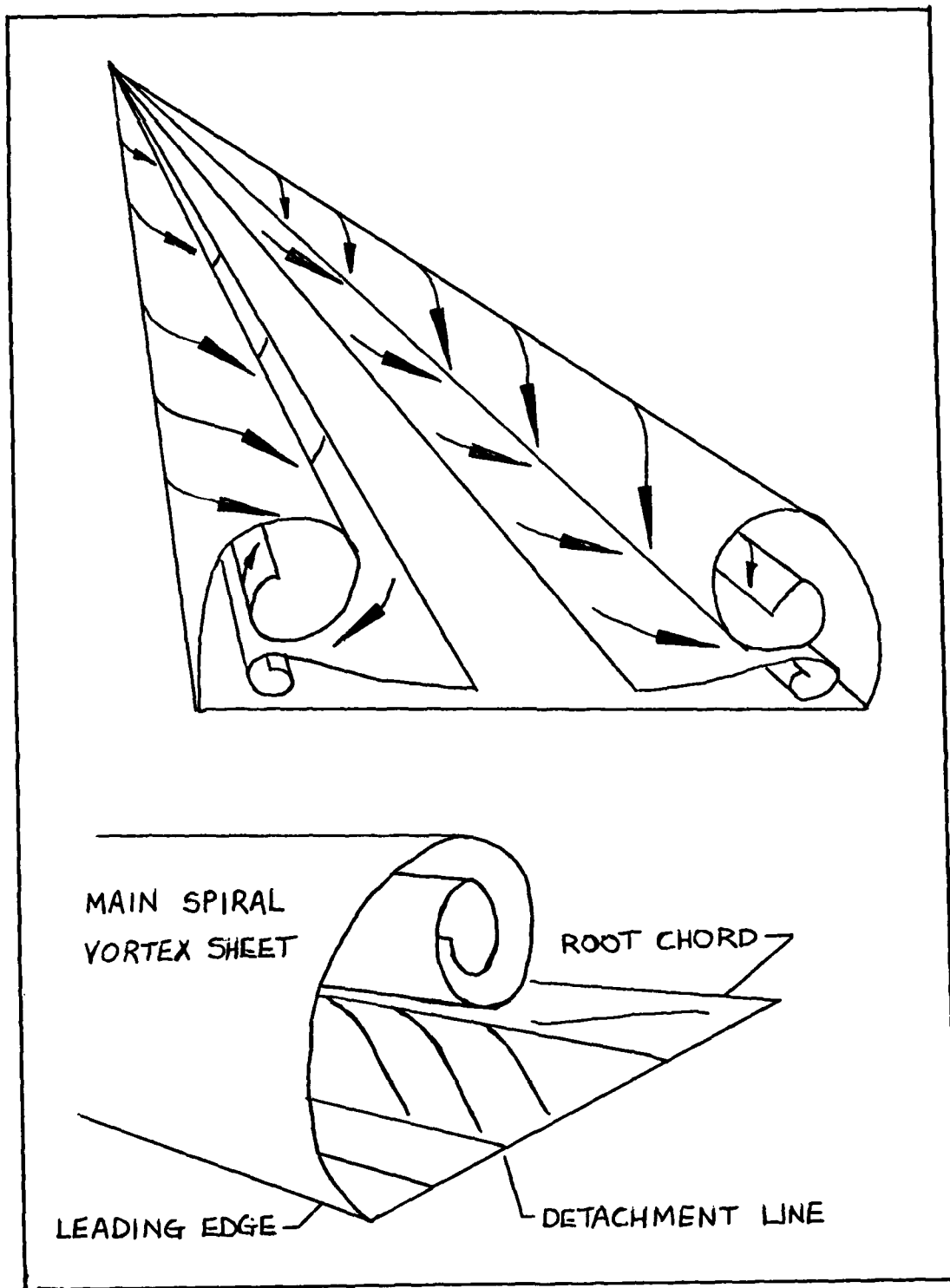


Figure 3. Leading Edge Vortex Structure

vortex breakdown and is characterized by high turbulence levels (7).

A major restriction to high α maneuvers in a delta wing aircraft is the degradation of longitudinal, lateral, and directional control needed due to the detached flow on the wing's upper surface. On these highly swept wing aircraft, asymmetric shedding of forebody and l.e. vortices create severe sidewash effects on the vertical tail which produces directional instability (11). Likewise, the wing's trailing edge (t.e.) flaps, used for both longitudinal and lateral control, have less effect in this detached, vortical flow on the wing's upper surface. These problems could possibly be eliminated or reduced significantly with the use of a vortex flow control device, the cavity flap (3). The cavity referred to here is the external region between the cavity flap and the wing's closest lower surface (Figure 4).

The cavity flap and its influence on aircraft maneuvers of delta wing aircraft was originally intended to correct directional instability but its use in longitudinal and lateral control are worth investigating. Dr. Dhanvada M. Rao of ViRA reported the cavity flap's effectiveness on changing the yawing moment in a report earlier this year (11). The cavity flap uses vortex generation and control, and the vortex lift effect to produce the desired responses for aircraft maneuvers.



Figure 4. Cavity Flaps Deployed on Delta Wing Model

The wing's lower surface is the logical place for cavity flaps since they would be exposed to the free stream velocity (V_∞) and not embedded in the detached flow above the wing. Here the cavity flaps could, with increasing α , take advantage of the vortex lift effect acting on its area to produce sizeable forces for maneuverability. These additional aerodynamic forces are dependent, to a large extent, on how the cavity flap is deployed. The production of these forces would be a function of symmetric or asymmetric deployment, the hinge line sweep angle (σ), the deflection angle (δ), and the cavity flap surface area.

Longitudinal Control

Longitudinal control needed is a function of the pitching moment of an aircraft in flight. The pitching moment on a delta wing aircraft is controlled with the t.e. flaps by deflecting them symmetrically. A positive t.e. flap deflection will produce a positive pitching moment, and vice versa. At high α 's the t.e. flaps are less capable of producing a pitching moment because of flow detachment on the wing's upper surface. By symmetrically deploying cavity flaps under the wing the existing pitching moment could be altered. With symmetrical deployment, both upper wing surface vortices are altered by the same amount primarily in the region of the cavity flaps. As a result, the vortex lift generated in these regions would be decreased, and the aerodynamic center would shift rearward. This would have the net effect of producing a nose down pitching moment. Any side forces produced from vortex lift by vortices forming in the cavities of the flaps would cancel because they would be equal in magnitude but opposite in direction. Therefore, there should be no net rolling moment or yawing moment generated. However, depending on the cavity flap hinge line sweep angle, a possible forward force representing a component of the normal force created by the vortex lift effect on the cavity flap's surface could be produced. This additional thrust term would reduce the drag the aircraft experiences.

Lateral Control

Lateral control needed is a function of the rolling moment of an aircraft in flight. The rolling moment is controlled by deflecting the t.e. flaps the same amount but in opposite directions. This has the effect of increasing the drag and decreasing the lift on the wing with a positive deflection (up) and increasing the lift on the other wing. However, at high α 's the wing has stalled and the flow has detached. The t.e. flaps are now less effective in producing the rolling moment needed to roll the aircraft. By asymmetrically deploying a cavity flap, the rolling moment could be modified. The deployed cavity flap would alter the wing's upper surface vortex on that wing. This would decrease the lift on that wing while the lift remains the same on the other wing, and a net rolling moment is produced. The sense of this additional rolling moment would be to lower the cavity flap deployed wing and raise the undeployed wing. Thus the existing rolling moment could be increased or decreased depending on which side of the aircraft the cavity flap was deployed.

With an asymmetrically deployed cavity flap the existing pitching moment would change due to the decreased lift on one wing. Also, a possible yawing moment could be produced depending on the side force generated on the cavity flap. The yawing moment is a function not only of the side

force but also the location of the applied side force to the moment reference center of the aircraft. The yawing moment concept is covered under directional control.

Directional Control

The directional control needed, like longitudinal and lateral control, is also a function of a moment, the yawing moment, of an aircraft in flight. The yawing moment is primarily produced by a vertical tail rudder deflection. A positive rudder deflection (right) will produce a positive yawing moment for an aft rudder location. This works well for α 's up to about 30° , but degrades steadily after 30° . The rudder is completely ineffective at an α of 50° and above because of detached flow and strong wakes (9,11). By asymmetrically deploying a cavity flap a side force could be generated. At all positive α 's, the cavity flap experiences a stagnation line on its surface exposed to V_∞ . Flow detachment occurs on the other side of the cavity flap and a vortex is formed in the external cavity region. The vortex, through the vortex lift effect, creates a force normal to the cavity flap's surface. Since the cavity flap is deflected at some δ and its hinge line is swept back at some σ , this normal force can be resolved into a side force, a forward force, and a lift force referenced to the aircraft's body axes. The greatest side force occurs when σ is 90° , the cavity flap deployed along the aircraft fuselage (5).

For changes to the yaw moment, the side force created by the asymmetrical deployment of the cavity flap must act over a distance to create a moment about the aircraft's moment reference center. The greater this distance, the greater the yawing moment produced. If the side force acted through the moment reference center then no yawing moment would be produced at all. Therefore, one would expect that the cavity flap should be deployed as far behind the reference center as possible. This would suggest possible deployment along the leading edge of the wing to produce the largest destabilizing effect.

Again, as with the idea of lateral control, an asymmetrically deployed cavity flap will most likely change the existing pitching moment and the rolling moment on the aircraft. These interactions are best determined by experimental investigation.

III. Test Equipment

Wind Tunnel

The AFIT wind tunnel was built at McCook Field in Dayton, Ohio in 1919. It was moved to its present location in Building 19 at Wright-Patterson AFB, Ohio in 1931 (1). Although the wooden tunnel is an open circuit continuous flow type, it is entirely contained within the large building. The building thus provides a return passage for the air on both sides. The tunnel has a circular five foot diameter, closed test section that is 18 feet long. Its inlet contraction ratio is 3.7 to 1. The tunnel airflow is induced by two 12-foot diameter counterrotating fans, each driven by two 400 horsepower direct current (d.c.) motors. The fans are rated to produce a maximum airflow of 300 feet per second (fps), corresponding to a unit Reynolds number (unit Re) of 1.9 million per foot under standard conditions (13). Total pressure is atmospheric (barometric). Static pressure is measured by a piezometer ring containing eight static pressure ports. These ports are evenly distributed around the perimeter of a constant area duct located 2.5 feet upstream of the test section. Dynamic pressure (q) is measured by a Validyne Model DP15 pressure transducer with a range of 0.1 pounds per square inch (psi) differential (6). A micromanometer is used as a backup and check for the

pressure transducer. The transducer was calibrated against the micromanometer before data collection starts. The dynamic pressure is controlled by the tunnel operator while observing the pressure transducer output. Fine adjustments to q are made with the micromanometer.

Instrumentation

A Task Mark 1 six component, internal strain gage balance, with a 0.75 inch outside diameter was used for this study. The balance was loaned to AFIT by AFFDL. The six force and moment components obtained from this balance were normal force (N), side force (Y), axial force (A), rolling moment (l), pitching moment (m) and yawing moment (n). The balance allowed direct measurements of all three forces and the rolling moment. The balance load limits were 80 pounds normal, 80 pounds axial, and 40 pounds side. The rolling moment limit was 60 inch pounds. The balance uses two strain gages fore and aft of the balance center for measuring both the normal and side forces. By knowing the distance between the fore and aft gages, it was possible to compute the pitching moments from the two normal loads and the yawing moment from the two side loads. The balance was mounted inside the model at its aerodynamic center with its output leads connected to a Hewlett-Packard 3497A Data Acquisition and Control Unit (DACU). A Hewlett-Packard 9826 minicomputer was used to control the DACU, collect the data,

and store it for later use. The control unit and computer used during the study are shown in Figure 5.

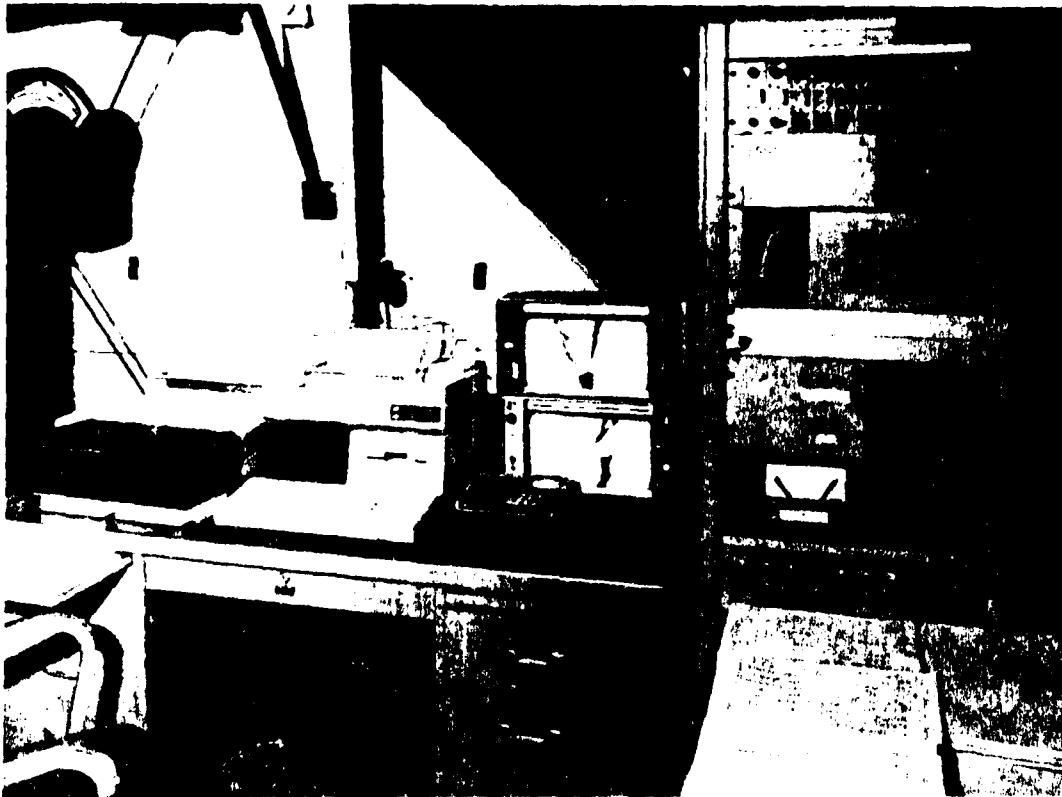


Figure 5. Tunnel Acquisition and Computer Support Equipment

Model

The model used was a generic, 60 degree swept delta wing aircraft with double wedge airfoils. It was based on a half span model used by Vigyan Research Associates, Incorporated (ViRA) in their research at the North Carolina State University wind tunnel (10). Their design was scaled for use in the AFIT five foot wind tunnel (Figure 1). The

model was constructed of aluminum, except for the nose forebody which was made of wood to reduce the model's weight. Dimensions of the model are shown in Figure 6. The nose strake (Figures 7 and 8) was added after the model was built when erratic data were encountered. This scattering was thought to be the result of dynamic excitation caused by asymmetric shedding of forebody and l.e. vortices (9).

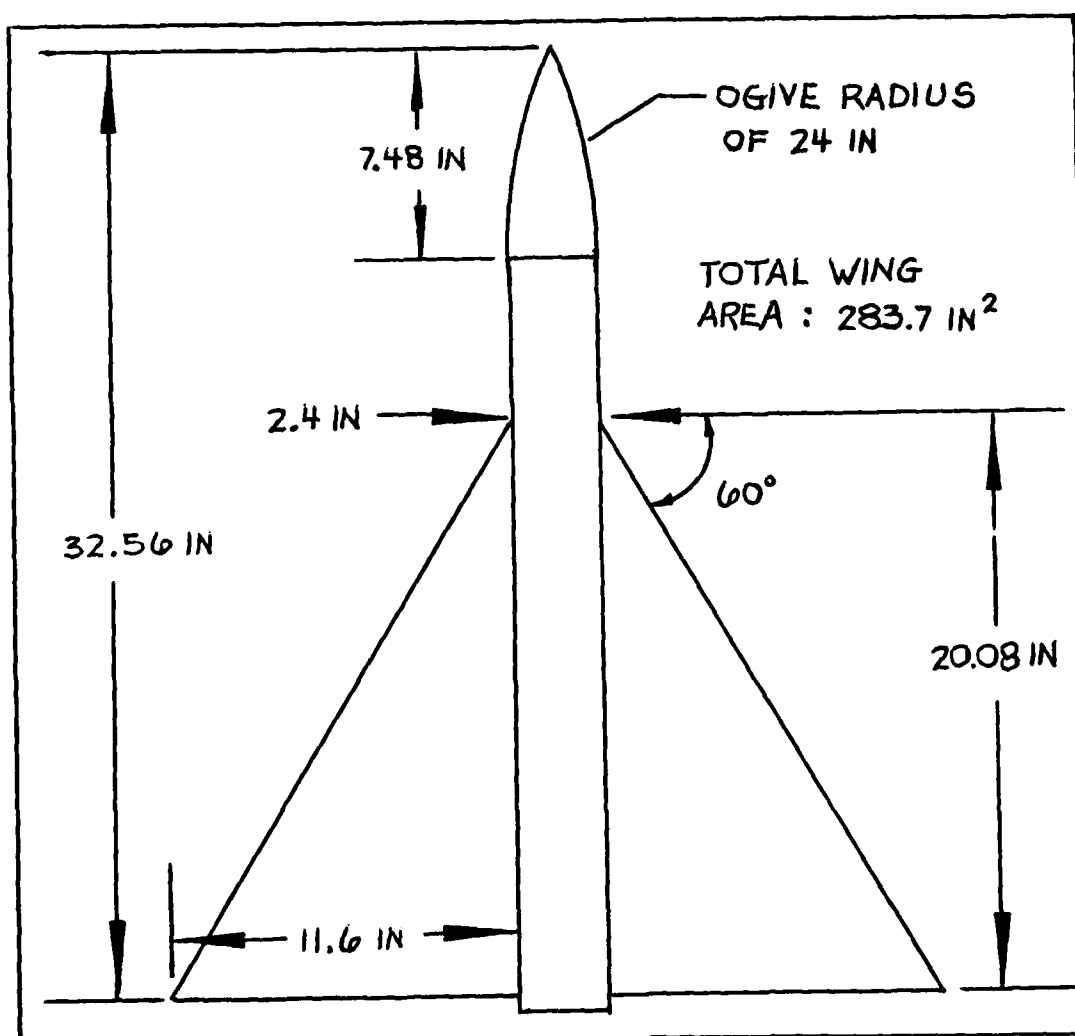


Figure 6. Dimensions of Delta Wing Model Used in Study

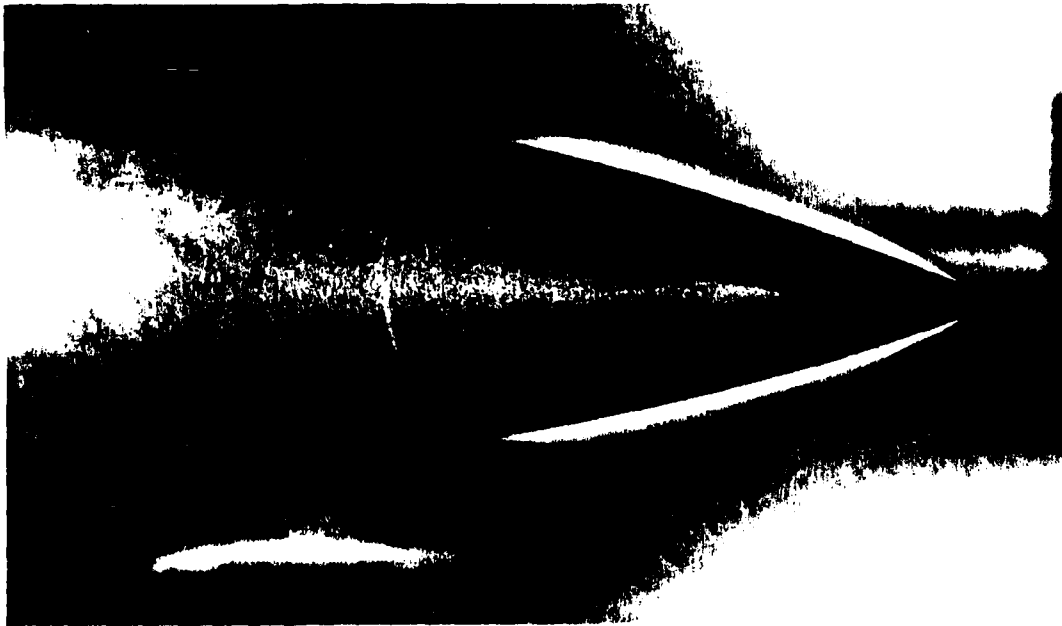


Figure 7. Bottom View of Model Showing Nose Strake

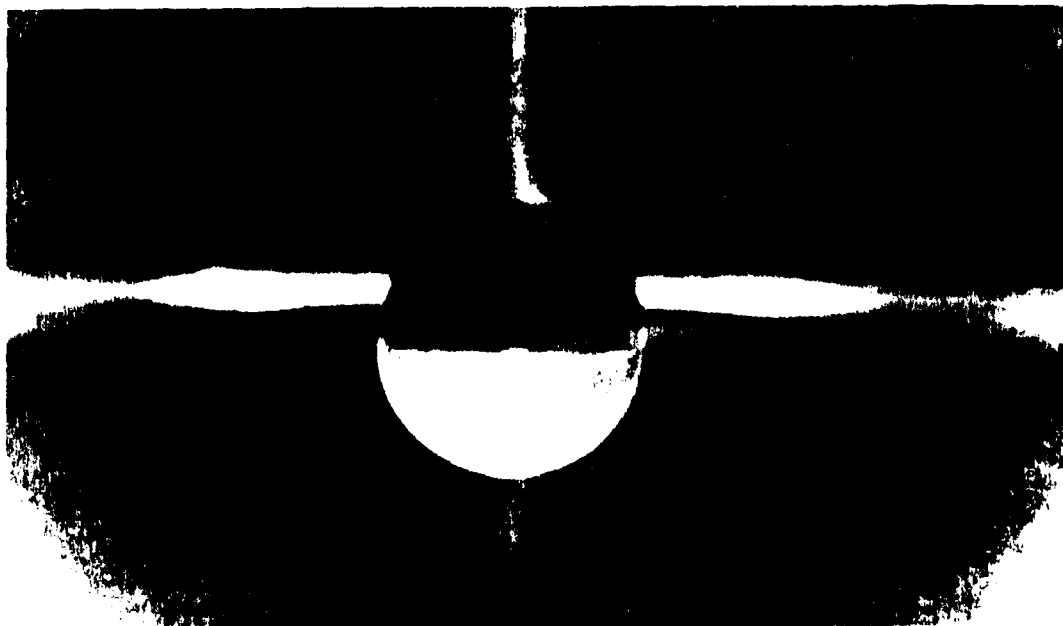


Figure 8. Frontal View of Model Showing Nose Strake

Support Apparatus

The internal balance was fitted to a stainless steel sting and yoke support structure. The model support system could achieve angles from -6° to 26° with the model in the center of the test section. The angles were controlled by the tunnel operator from the operator's station (Figure 9) using a d.c. motor driving a steel cable. An open loop, cable drive was used for pitch control with overhead weights providing the necessary vertical tension. A potentiometer attached to the cable drive produced direct readout of the sting's α .

The unique sting design (Figure 10) was designed in conjunction with AFFDL and has the ability to offset the angle of attack by a $+20^\circ$ increment. This prebending allowed operating at high angles of attack from 14° to 46° while again keeping the model virtually in the center of the test section. Centering the model was necessary to avoid boundary layer and wall interactions. With this sting, α 's up to 50° were obtained due to sting deflections. These deflections were a result of the aerodynamic loading at high angles of attack, and were accounted for in data reduction.

The two forward attachment points of the yoke are supported on each side of the tunnel test section by a roller in a circular arc track (Figure 1). This allows a maximum sideslip angle (β) of $\pm 6^\circ$. The sideslip angles are controlled by the tunnel operator using a cable driven by a

d.c. motor. A potentiometer attached to the closed loop cable drive produced direct readout of the sting's β .

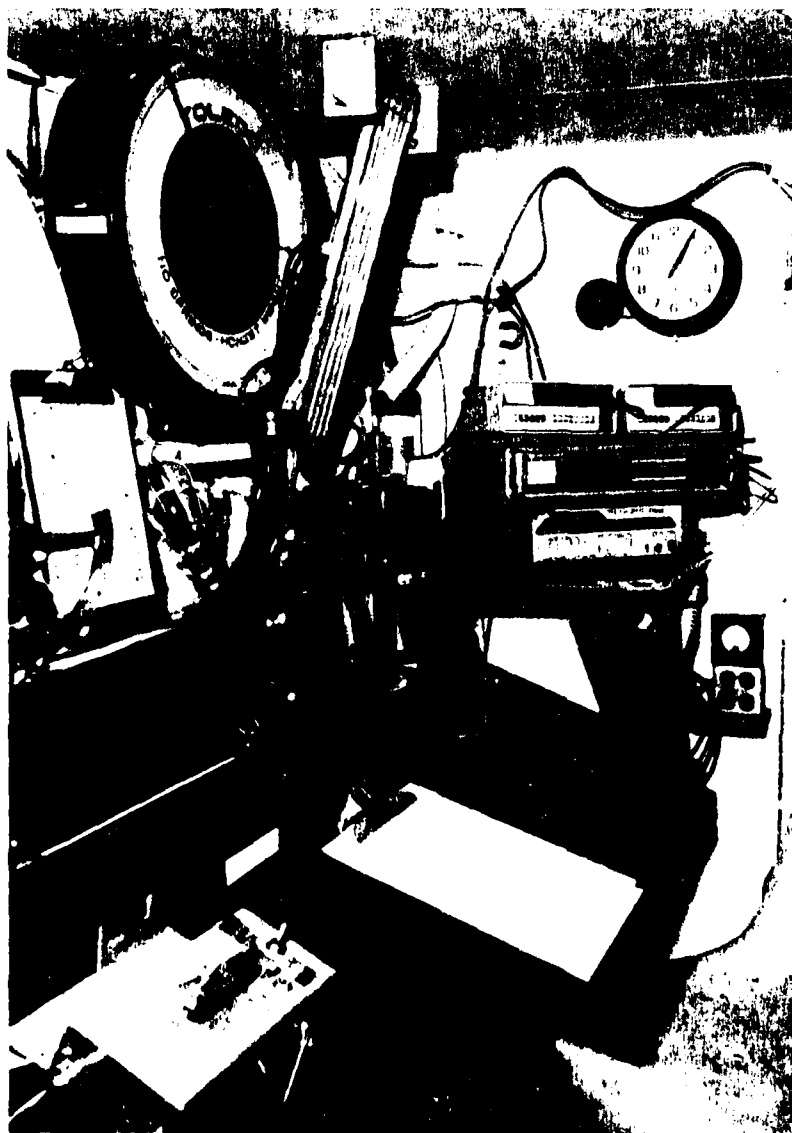


Figure 9. Tunnel Operator's Station

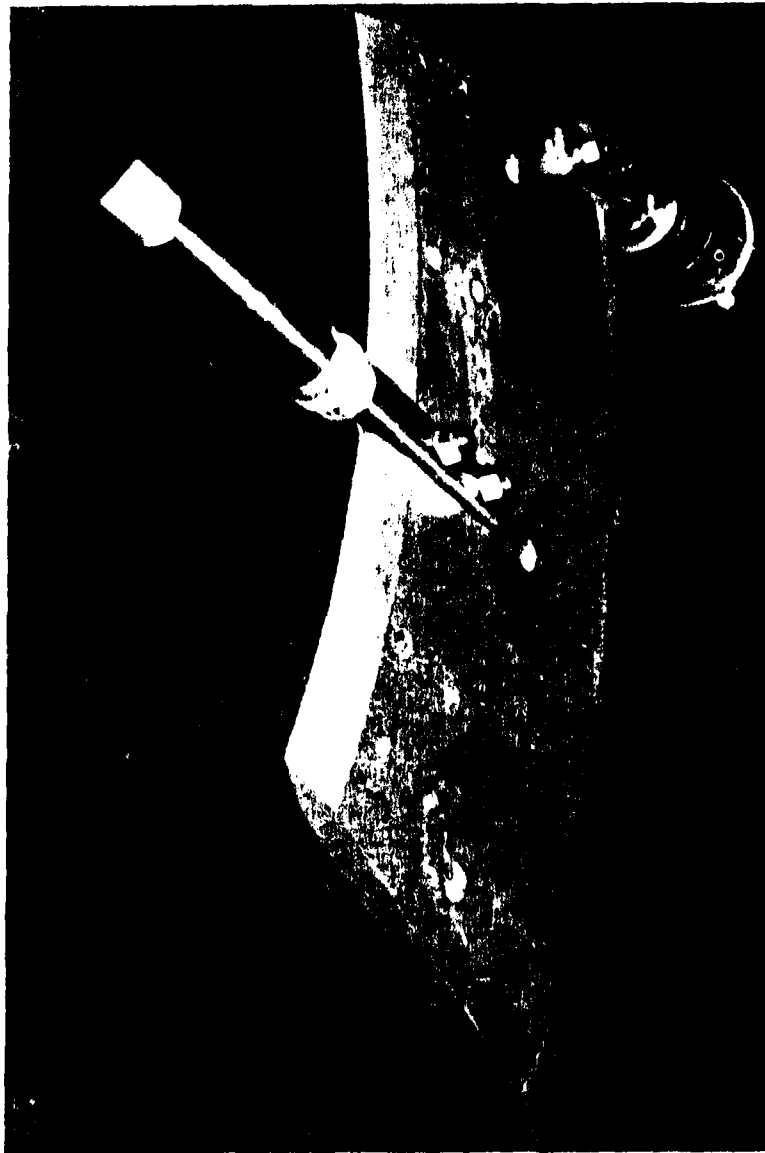


Figure 10. Modified Sting Showing 20° offset

Data Acquisition

As mentioned earlier, the internal balance output leads were connected to a Hewlett-Packard 3497A Data Acquisition and Control Unit (DACU). The unit was programed to scan 15 different channels for the data needed. On certain channels, the tunnel q , and the balance force and moment outputs, the unit was programed to sample each channel nine times before moving on to the next one. This procedure was repeated an additional four times, giving a total of 45 samples for each channel. These samples were then averaged to provide a single output value.

The DACU was connected to a Hewlett-Packard 9826 minicomputer. This computer ran the software written to control the DACU and to reduce the data obtained. The data was scaled based on calibration of the internal balance and the sting's attitude control system. It was also corrected for sting deflections and interactions, flow angularities, and tare (nonaerodynamic) loads. The normal loads were separated into lift (L) and drag (D) based on the corrected α . Finally, all the forces and moments were converted to nondimensionalized parameter coefficients. The data were transferred to floppy disks for storage and later use.

Software was written for the 9826 computer to control a Hewlett-Packard 9872C Pen Plotter. This allowed for plotting of the data immediately after it was collected, but before the next configuration change.

IV. Calibration

Internal Balance

Static calibration of the internal strain gage balance was done by manually loading the six strain gages to their maximum limits. The maximum loads for the axial force and two normal force gages were 40 pounds each and 20 pounds each for the two side force gages. Sixty inch pounds was the maximum moment applied to the rolling moment gage. Each strain gage was loaded separately and all strain gage outputs were recorded. Ideally, only the loaded strain gage would produce an output. However, interactions among the strain gages are unavoidable in balances of this type (8). From the data collected it was possible to create a 6 by 6 first order interaction matrix given in Table 1. The main diagonal terms are the strain gages' outputs resulting from being loaded themselves. The off diagonal terms are the interactions from the other strain gages. For the test data to be valid, it must account for these interactions. The reduction software calculated the actual test data by multiplying the inverse of the interaction matrix with the indicated data (8). This gave the actual strain gage outputs as a functions of all the strain gage outputs. The interaction matrix was applied to all test data collected before computing the actual aerodynamic loadings.

	N1 Gage	N2 Gage	S1 Gage	S2 Gage	A1 Gage	R1 Gage
N1 Gage	+6.0453	-4.0757	-0.0005	-0.0003	+0.0043	+0.0002
N2 Gage	-19.9411	+5.7453	-0.0012	+0.0049	+0.0016	+0.0066
S1 Gage	-0.0051	-0.0018	+3.1416	-2.7479	+0.0039	+0.0032
S2 Gage	-0.0032	+0.0002	-9.3456	+2.9003	-0.0060	-0.0057
A1 Gage	-0.0058	-0.0055	-0.0046	-0.0005	+7.3722	-0.0057
R1 Gage	-0.0002	+0.0014	-0.0019	-0.0012	+0.0027	+5.5636

Table 1. Strain Gage Interaction Matrix

Sting Deflection

While the strain gages were being loaded for static calibration of the internal balance, the sting deflections were measured with an inclinometer and recorded. By applying a first order, least squares fit routine to the data collected, a linear equation was obtained that gave sting deflections as a function of the applied forces and moments. This expression was used by the reduction software to account for sting deflections during testing.

Flow Angularity

The wind tunnel model used during this study was instrumental in determining the flow angularity of the test section. With the wind tunnel operating, data were col-

lected for the model as it was moved through an α sweep at 2° increments from -6° to 6° . The model was then inverted on the sting and the procedure was repeated. Lift was plotted against α for both cases on the same graph. Had there not been any flow angularity in the vertical plane, the two curves would have coincided. However, the curves did not. The flow angularity for α was taken as half the α difference between the two curves for the same amount of lift (8). This gave a flow angularity in the vertical plane of 0.29° upwash. This correction was applied to all the α measurements taken. The same procedure was done for flow angularity in the horizontal plane by rolling the model 90° , first clockwise and then counterclockwise, and moving it through a β sweep. Lift was plotted against the support apparatus sideslip angle (α for the model). Since the two curves only differed by a few minutes of arc no correction was made for flow angularity in the horizontal plane.

Angle of Attack

Calibration of α was done with an inclinometer. The model was pitched to a desired α using the inclinometer as a reference. The output from the pitch potentiometer was recorded. This procedure was repeated for several different α 's over the entire model support apparatus range. A first order, least squares fit routine was applied to the data collected. It yielded a linear equation for α as a function

of the pitch potentiometer output. This equation was used by the reduction software to calculate true α 's. The tunnel operator also used this curve fit to select α during the test runs. This calibration procedure was done separately at β 's of 0°, 6°, and -6°, since interactions between the pitch and yaw cable systems exist.

Sideslip Angle

Calibration of β was done with a plumb and a special ray board (1). The ray board was placed in the test section under the sting with its apex directly below the center of curvature of the model support apparatus. The rays extended forward to the end of the sting where the plumb was hanging. The sting was yawed to a reference angle on the ray board and the output of the yaw potentiometer was recorded. A first order, least squares fit routine was applied to the data which yielded a linear equation for β as a function of the yaw potentiometer output. This expression was used in the reduction software to calculate β . It was also used by the tunnel operator to assure accurate and repeatable sideslip angles.

V. Procedure and Analysis

Procedure

This study was conducted at a dynamic pressure of 20 pounds per square foot (psf). Since the wind tunnel is an open type, the test section total temperature and total pressure were dependent on atmospheric conditions. This produced small variations in the Mach number (M) and the unit Re . Average values for M and unit Re were 0.12 and 0.936 million per foot, respectively. Gritting the model's nose was considered for aiding earlier forebody boundary layer (b.l.) transitioning and thus simulating higher Re . Initially, a rubber band was placed on the model's nose to find the best possible location for applying the grit. However, when the grit was applied no noticeable change to the data was evident. Based on these results, the rubber band was used in tripping the b.l. and simulating higher Re . An oil flow visualization done to identify forebody free vortex shedding (Figure 11) shows how the nose strakes help align the flow for symmetric shedding. The detachment line for the vortex sheets can be seen clearly. The rubber band is in place as it was for testing.

The data for each cavity flap configuration presented in this study was actually collected in two separate data runs. They were merged after data collection to present a

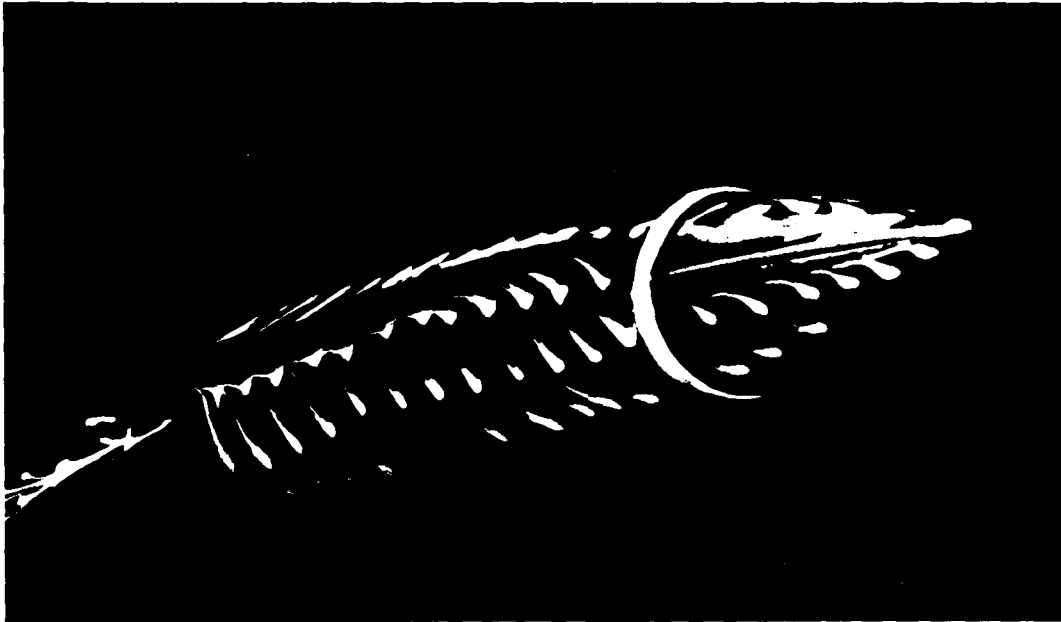


Figure 11. Nose Oil Flow Visualization Showing Rubber Band, Strake, and Flow Detachment

single test. One run was taken with no prebend in the sting. This gave an α sweep from -6° to 26° in 2° increments. The other data run was made with a $+20^\circ$ prebend in the model's sting. This gave an α sweep from 14° to 46° in 2° increments. Each data run was reduced separately and then merged to form a single test. Ten data points, α 's ranging from -6° to 14° , were taken from the low α sweep while 17 data points, α 's ranging from 16° to 46° , were taken from the high α sweep.

Data Analysis

The conditions under which a model is tested in a wind tunnel are not the same as those of free air. There is no

difference between having the model remain still and the air move past it and that of having the model fly through the air. However, the longitudinal static pressure gradient (horizontal buoyancy) and the jet boundaries present in the closed test section will produce extraneous forces and must be removed. A long list of correction which are required can be found in any text on wind tunnel testing (8). Fortunately, most tests only require a few of these corrections. Data collected and presented in this study were corrected for solid blockage, wake blockage, horizontal buoyancy and flow angularity.

Before the aerodynamic forces and moments were calculated, the data from the six component strain gage balance were corrected for first order balance interactions, sting deflections and flow angularity (Section IV). These balance components (Figure 12) were then combined to arrive

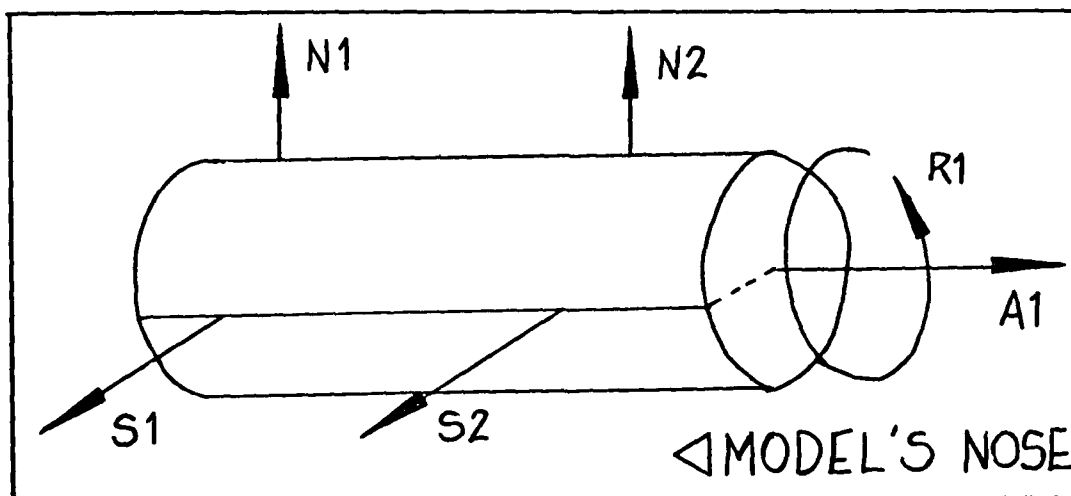


Figure 12. Internal Strain Gage Balance Positive Components

at the conventional body axis lift (L), drag (D), side force (Y), rolling moment (l), pitching moment (m), and yawing moment (n). A Hewlett-Packard 9826 minicomputer performed the following correction calculations during data reduction. The subscript "u" in the following equations denotes uncorrected data.

A blockage correction factor (ϵ) which combines the effects of solid blockage (ϵ_{sb}) and wake blockage (ϵ_{wb}) was computed and applied to the aerodynamic data (8).

$$\epsilon = \epsilon_{wb} + \epsilon_{sb}, \text{ where } \epsilon_{wb} = (S/4C)C_{Du} \text{ and } \epsilon_{sb} = KV/C^{3/2}$$

S is the model wing area, C is the tunnel test section area, V is the model volume and K is a model shape factor (8).

Since the test section velocity will vary with total blockage, a correction to the dynamic pressure must be applied. The linearized form of the correction for ϵ much less than unity is given below. This corrected q was then use in computing the aerodynamic coefficients.

$$q_b = q_u(1+2\epsilon)$$

Drag must be corrected for horizontal buoyancy because of the longitudinal variation of the static pressure (dp/dx) in the test section caused by a growing wall boundary layers. An adjustment to the drag can be calculated from

$$D_b = (-dp/dx)V$$

With these corrections for blockage and horizontal buoyancy, the aerodynamic forces and moments can be corrected and nondimensionalized in the following manner.

Lift:	$C_L = L_u/(q_b S)$
Drag:	$C_D = (D_u - D_b)/(q_b S) + C_L^2 S/(8C)$
Side Force:	$C_Y = Y_u/(q_b S)$
Rolling Moment:	$C_L = l_u/(q_b S b)$
Pitching Moment:	$C_m = m_u/(q_b S \bar{c})$
Yawing Moment:	$C_n = n_u/(q_b S b)$

For evaluation purposes, the longitudinal, lateral and directional coefficients were plotted versus α (Appendix A). The model baseline coefficients were subtracted from the ones obtained when a cavity flap configuration was installed on the model. These differences were also depicted graphically as a function of α in Appendix A.

To help identify how the cavity flaps actually affected the flow, an oil flow visualization study was completed with a limited number of cavity flaps at selected angles of attack. These photographs can be found in Appendix B.

VI. Results

Ten cavity flaps were tested in the AFIT wind tunnel to determine their performance on altering the longitudinal, lateral and directional maneuverability of a generic delta wing fighter aircraft. Table 2 gives a description of each cavity flap tested. Cavity flap hinge lines relative to the model's wing are shown in Figure 13. As stated in Section I, the ability of a cavity flap to modify the maneuverability of an aircraft from which they are deployed would be dependent on such parameters as the cavity flap deflection angle, δ , the cavity flap hinge line sweep angle, σ , the size of the cavity flap surface, and whether they are deployed symmetrically or asymmetrically.

A variety of cavity flap deflection angles for both asymmetric and symmetric deployments (Figures 14 and 15) were accomplished on cavity flaps C1 through C4. Data collected for cavity flaps C5 through C10 are a scattering of partial runs (either at high or low α 's). These partial data runs, done in conjunction with ViRA, were a digression from actual testing. They were primarily a "what if" type of testing as to the placement of cavity flaps in locations other than the apex region. Since the testing of cavity flaps C5 through C10 was not extensive, the data collected for them could not be included with the analysis of cavity

Flap	Length (in)	Area (in ²)	Flap Shape	Sweep Hinge	Angles Flap	Flap Apex Location
C1	7.33	15.5	Delta	90°	60°	at wing apex
C2	7.33	7.2	Delta	75°	75°	at wing apex
C3	7.33	15.5	Delta	75°	60°	at wing apex
C4	7.33	15.5	Delta	60°	60°	at wing apex
C5	13.75	13.7	Delta	60°	80°	at wing apex
C6	13.75	13.7	Gothic	60°	---	7.8" aft wing apex along l.e.
C7	7.33	15.5	Delta	60°	60°	3.0" aft wing apex along l.e.
C8	7.33	15.5	Delta	60°	60°	11.8" aft wing apex along body
C9	7.33	7.2	Delta	75°	60°	10.0" aft wing apex along body
C10	7.33	15.5	Delta	90°	60°	13.7" aft wing apex along body

Table 2. Description of Cavity Flaps Tested

flaps C1 through C4. However, the data collected for cavity flaps C5 through C10 and their changes to the model baseline aerodynamic coefficients are presented in Appendix A.

Not all possible combinations of cavity flaps and test parameters were tested but a large sampling was performed to determine trends that affect cavity flap effectiveness. Each cavity flap was tested at a number of different deflection angles. This allowed determination of effective deflection angles for individual flaps and for drawing general conclusions about the relation between deflection angle and cavity flap performance. The effect of hinge line

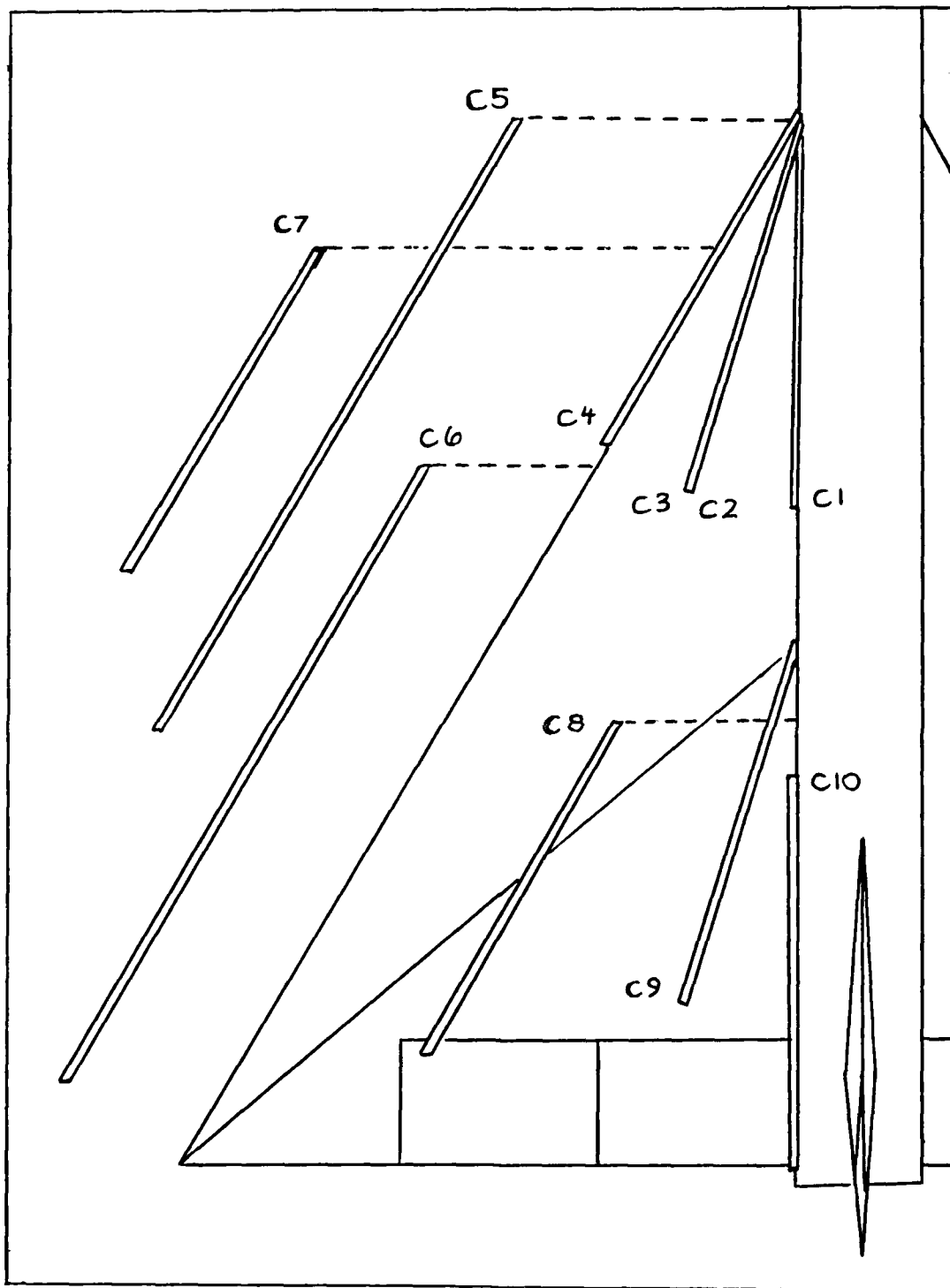


Figure 13. Cavity Flap Locations Relative to the Wing



Figure 14. Model with Asymmetrically Deployed Cavity Flap

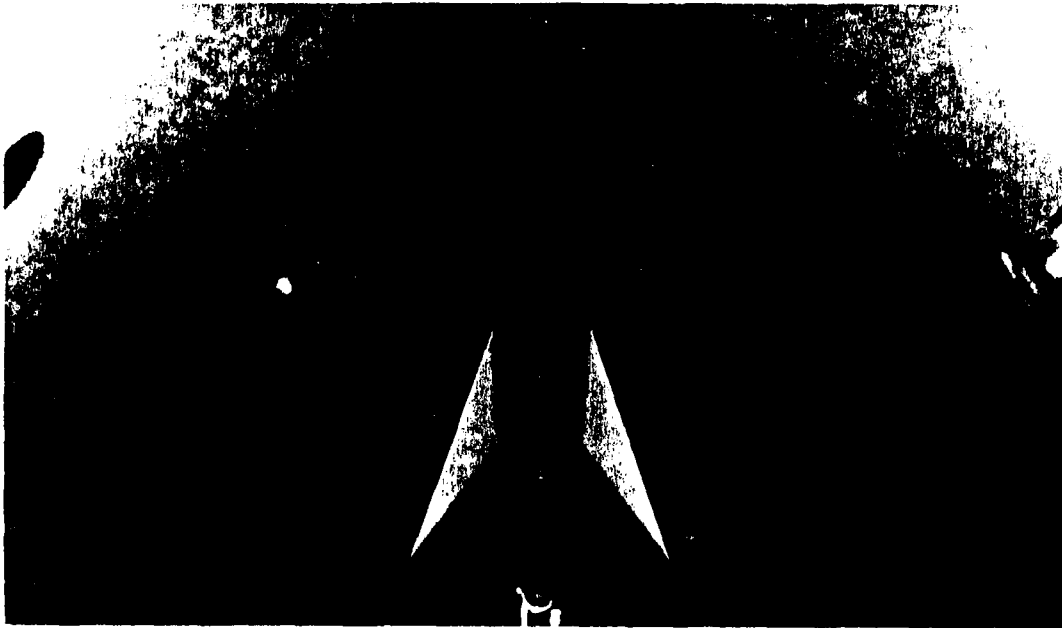


Figure 15. Model with Symmetrically Deployed Cavity Flaps

sweep angle was evaluated by comparing data from cavity flaps C1 and C3. They were the same flap design but deployed from different hinge line sweep angles. The role of surface area on cavity flap performance was determined by comparing data collected for cavity flaps C2 and C3. These two cavity flaps were deployed at the same hinge line sweep angle and differed only in the surface area, C3 being about twice the size of C2. The effects of yaw on cavity flaps were studied by testing cavity flap C1 deployed 60° , both asymmetrically and symmetrically, at 6° and -6° of yaw.

Since the model was generic in design, the results presented here are basic research results and must be considered a parametric or "trend" analysis. They cannot be related to specific aircraft, only to a class or type of aircraft. Due to the large volume of data collected and to the numerous ways it can be grouped for analysis, the most efficient way to present the results is through the use of data plots. Figures 16 through 39 are the results of varying the deflection angle for each cavity flap. Figures 40 through 51 deal with the hinge line sweep angle effects. Figures 52 through 60 show the effects of area variation on the cavity flaps. The area variations are related to a percentage of the total wing area. When two cavity flaps were deployed, the sum of their areas was used to determine the percentage. Figures 61 through 66 deal with the effect of yaw on cavity flap.

Longitudinal Control

The change in C_m was used to determine the effectiveness of the parameters studied in improving longitudinal maneuverability. As predicted by theory, the greatest changes came from symmetrically deploying the cavity flaps. For that reason, the analysis for longitudinal control enhancement considered only symmetric deployment of cavity flaps. Asymmetric deployment did produce changes in C_m (i.e., Figure 17) but not as much as did symmetric deployment. Figure 20 gives the effects of deflection angle on longitudinal maneuverability for cavity flap C1. A 30° deflection produced the greatest change in C_m . Figure 26 gives the effects of deflection angle for cavity flap C2. As with cavity flap C1, The greatest change produced by cavity flap C2 occurred at a 30° deflection. Figure 32 gives the effects of deflection angle for cavity flap C3. As can be seen from the figure, considerable changes to C_m occurred but there was not much variation in the effects between deflection angles of 45° and 60°. Figure 38 gives the effects of deflection angles for cavity C4. A cavity flap deflection angle of 90° proved to be the best deflection for this cavity flap.

The effect of cavity flap hinge line sweep angle on C_m can be seen in figures 47 and 50. These plots are symmetric deployments for cavity flap deflection angles of 45° and 60°. In both, a 75° sweep angle causes the greatest change in C_m .

Figure 59 shows the influence of cavity flap area on the longitudinal control enhancement for cavity flaps deflected 60° with a hinge line sweep angle of 75° . The larger area provided considerably more modification to C_m than the smaller area.

Figure 65 shows the effects of yaw on the cavity flaps. There is no appreciable change in C_m at either positive or negative yaw.

In summing up the effects of symmetrically deployed cavity flaps on the longitudinal control enhancement, the greatest changes can be expected from a cavity flap with a moderate deflection angle, at a hinge line sweep angle less than 90° and a sizeable surface area.

Lateral Control

The changes in C_l were used to determine cavity flap performance on the lateral maneuverability. Since the forces acting on a cavity flap that produce the rolling moment cancel in symmetric deployment (i.e., Figure 20), only the asymmetric deployments were considered in the analysis. Figure 17 shows the effects of different deflection angles for cavity flap C1. The greatest change occurred between 30° and 40° α and was attributed to a 30° deflection angle. Figure 23 shows the effects of deflection angles for cavity flap C2. Here again the largest change comes from the 30° cavity flap deflection at moderately high

α 's. Figure 29 shows the effects of deflection angles for cavity flap C3. There was much difference between a 45° and 60° deflection. Each provided about the same amount of change. Figure 35 shows the effects of deflection angles for cavity flap C4. Here a 90° deflection gives the greatest change in C_1 at higher α 's.

Figures 41 and 44 show the effects of hinge line sweep angle for cavity flap deflection angles of 45° and 60°. Both cases imply that a 75° sweep angle for the cavity flap hinge line would give the most enhancement to lateral control.

Figures 53 and 56 show the effects of cavity flap size on C_1 at cavity flap deflection angles of 45° and 60°. In each case the larger areas produced the most change, but the changes were about the same magnitude for both deflection angles.

Figure 62 shows the effect of yaw on the cavity flap's ability to change the rolling moment. As can be seen, a -6° of yaw has a small change on C_1 . This change could probably be attributed not to the cavity flap itself but to the yawing of the model.

In summing up the results for lateral control enhancement, the majority of the flaps tested provided better results with a small to moderate deflection angle, a hinge line sweep angle less than 90° and a larger area.

Directional Control

Again, with directional control enhancement, the primary emphasis was on the changes to C_n . The yawing moment can be considered a measure of the directional maneuverability of an aircraft. Similar to lateral control enhancement, only the asymmetric deployments need to be looked at since the side forces that would produce a yawing moment cancel in symmetric deployment (i.e., Figure 21).

Figure 18 shows the effects of cavity flap deflections on C_n for cavity flap C1. The greatest changes occurs with a 60° deflection up to 30° α . After 30°, the data shows a significant departure in the normal trend of C_n changes, a type of yaw departure. Figure 24 shows the effects of deflection angles for cavity flap C2. As can be seen from the figure, no one deflection angle could be considered the most effective. Again the yaw departure is present about 30° α . Figure 30 shows the effects of deflection angles for cavity flap C3. There was considerable change to C_n in the lower α range for both the 45° and the 60° deflection angles. Note that the spike in C_n data for C3 is not present at high α 's as it was with C1 and C2. Figure 36 shows the effects of deflection angles for cavity flap C4. The data suggest that a 90° deflection produces the greatest change in C_n .

Figures 42 and 45 show the influence of cavity flap hinge line sweep angle on the cavity flap's ability to change C_n . For both the 45° and 60° deflection angles, the 90°

sweep angle gives the greatest change to the coefficient at α 's above 10° . The magnitude of these changes agree closely with an earlier yaw control investigation by Rao (11). He used an asymmetrically deployed cavity flap deflected 45° with a hinge line sweep of 90° . Figures 54 and 57 show the effects of cavity flap surface area on C_n for deflection angles of 45° and 60° . In both cases, the larger area produced the greater changes and damped out the yaw departure.

Figure 63 suggests that a negative yaw of the aircraft would produce greater changes in C_n up to about $20^\circ \alpha$. Notice also that the yaw departure evident at $0^\circ \beta$ for an asymmetrically deployed cavity flap has been significantly reduced by the aircraft yaw.

In summing up the effects on directional control enhancement, a cavity flap deflected 60° asymmetrically with a cavity flap hinge line sweep angle of 90° will provide the greater change in C_n . The larger the cavity flap surface area, the greater this change.

Lift and Drag Considerations

In reviewing the figures that present the changes in the lift and drag coefficient data for the configurations considered during this study, a general conclusion can be made. For minimum lift loss and minimum drag increase a smaller deflection angle is better suited for smaller α 's.

As α increases the deflection angle should also increase to keep losses to a minimum. The greatest reduction in drag comes from a cavity flap with a 75° hinge line sweep angle and a larger cavity flap area. The smallest reduction in lift also comes from a 75° hinge line sweep angle. The lift losses were directly proportional to the cavity flap surface area. As for yaw effects, there was no noticeable difference in the cavity flap induced changes for the lift and drag coefficients.

Oil Flow Visualization

A limited amount of flow visualization was done during this study. Even with the few cavity flaps tested, the results were very supportive of the cavity flap theory. Appendix B contains all the photographs taken during the visualization study. It is clearly evident in some of the pictures that a vortex has been generated in the cavity. Up until the time of the flow visualization, all testing had been based on the assumption that a vortex was indeed forming in the cavity.

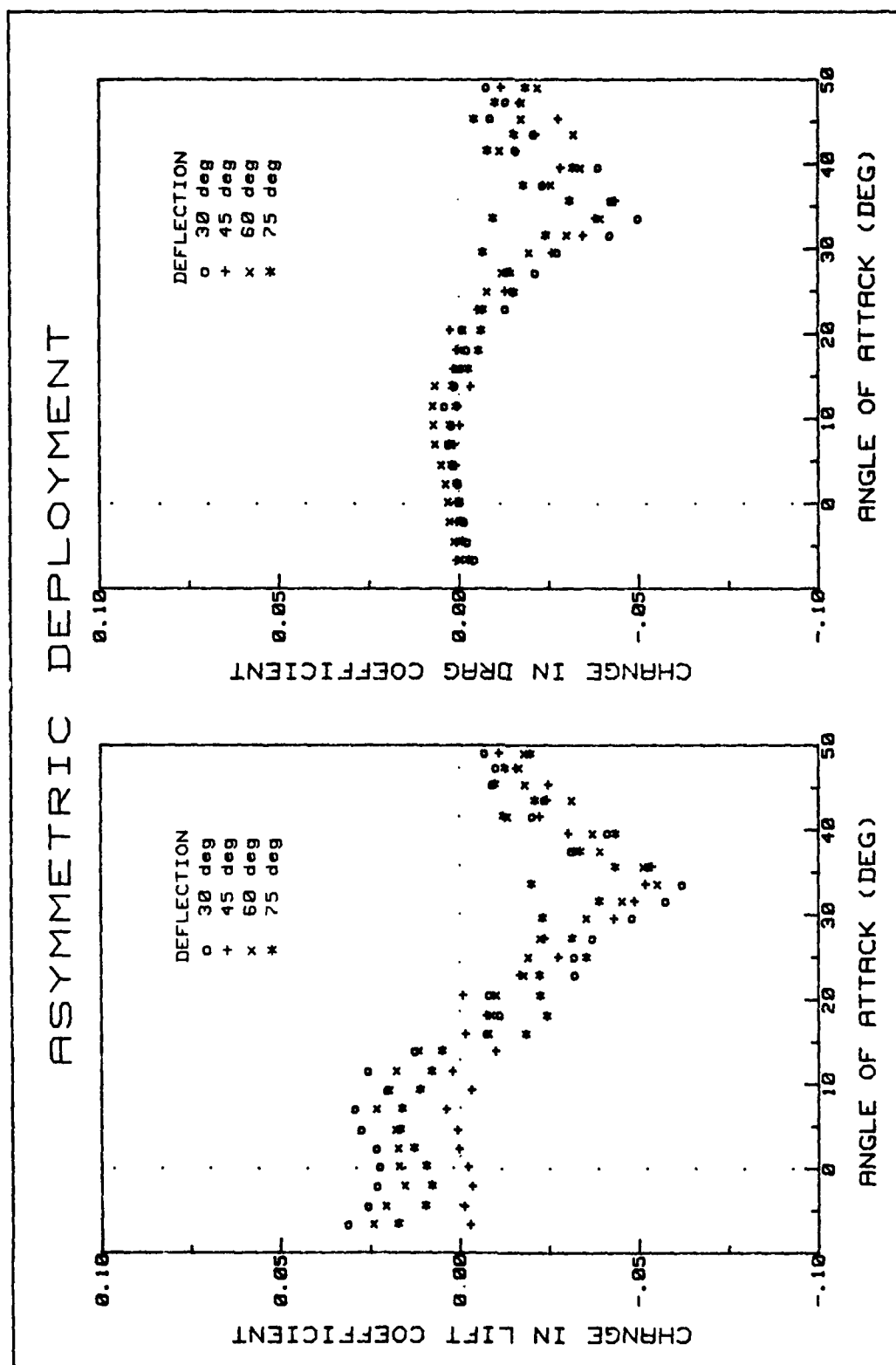


Figure 16. C_l Flap ΔC_L and ΔC_D for Various Deflection Angles (asymmetric)

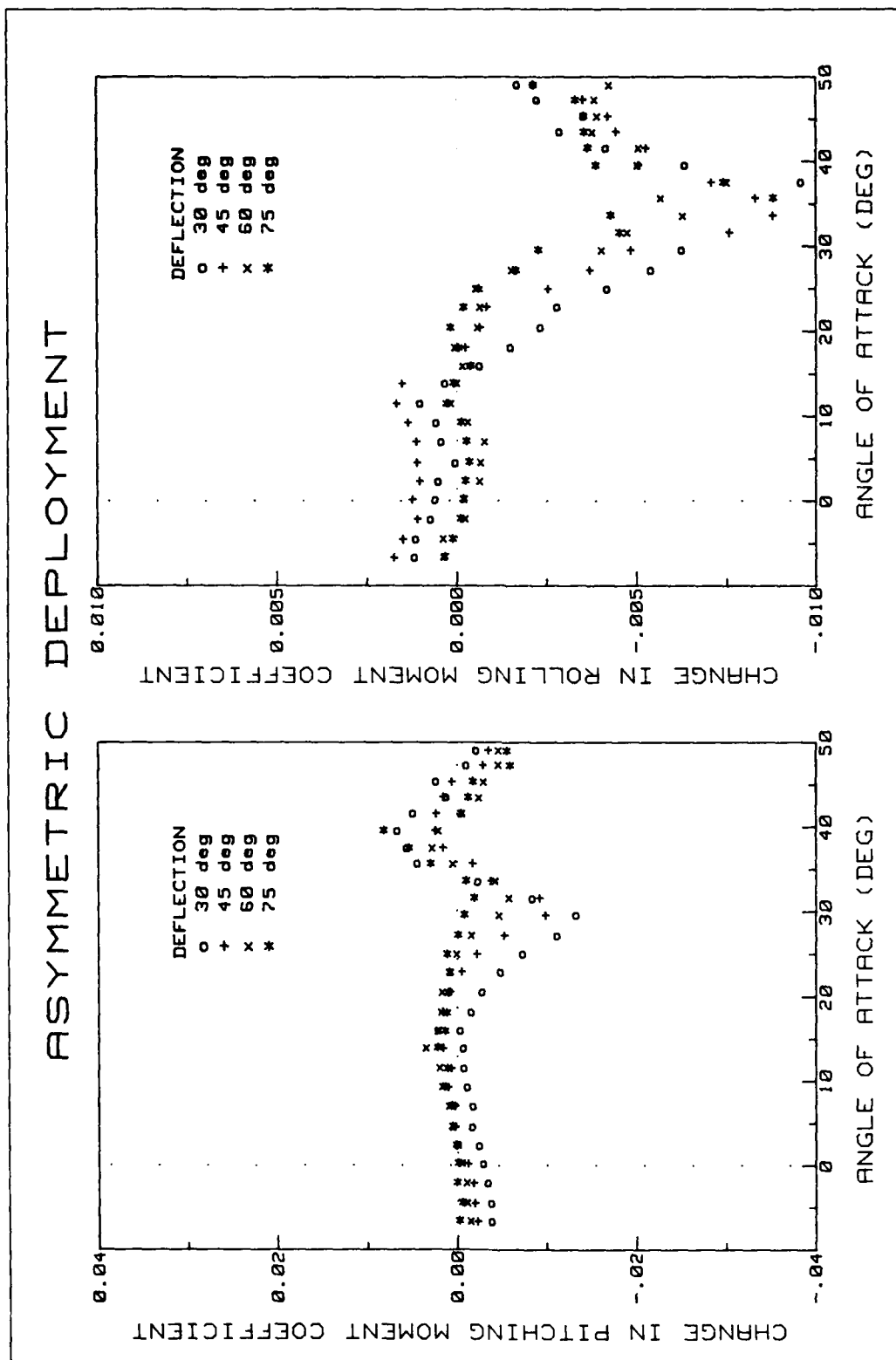


Figure 17. C1 Flap ΔC_m and ΔC_l for Various Deflection Angles (asymmetric)

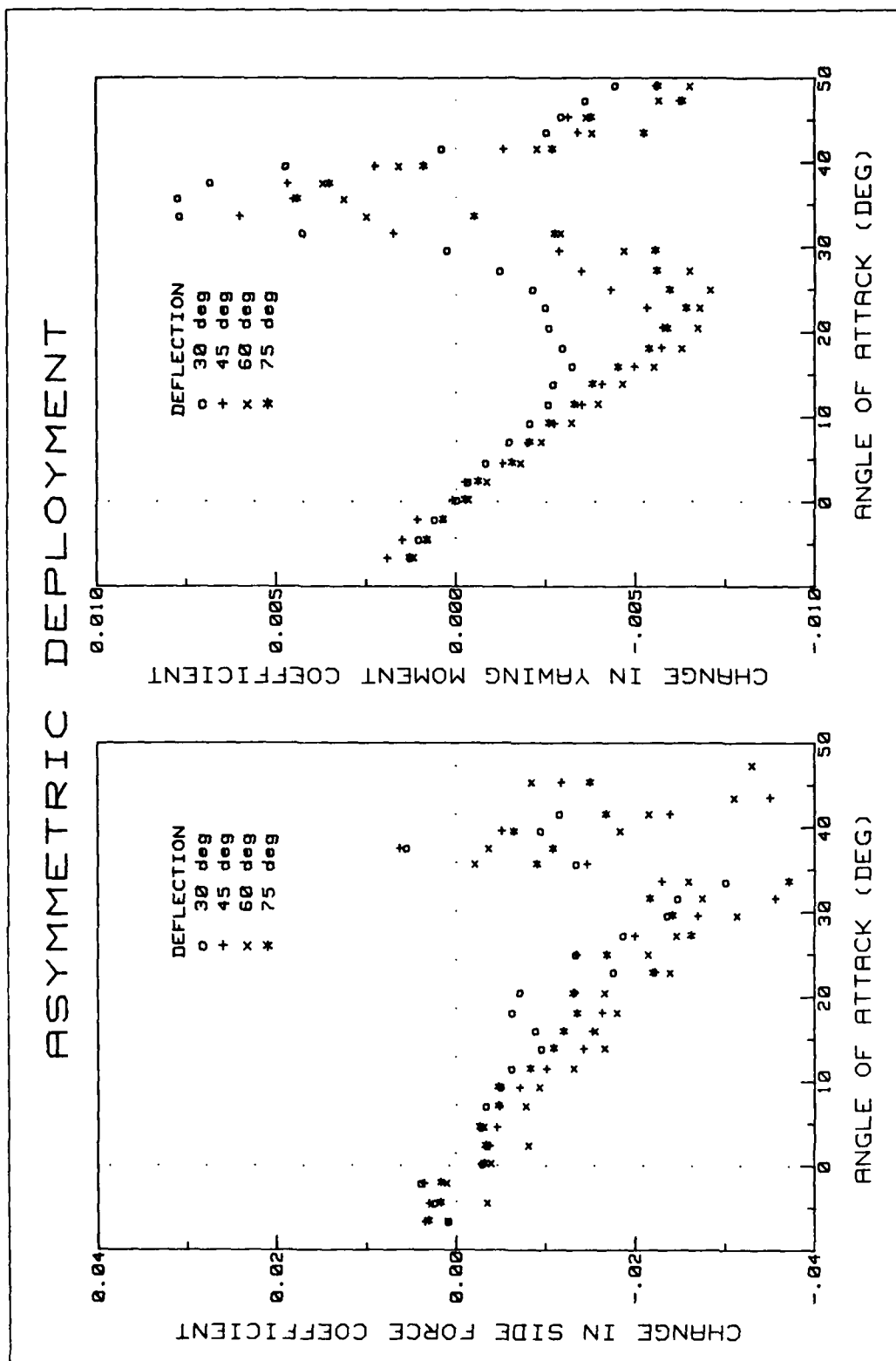


Figure 18. C1 Flap ΔC_Y and ΔC_n for Various Deflection Angles (asymmetric)

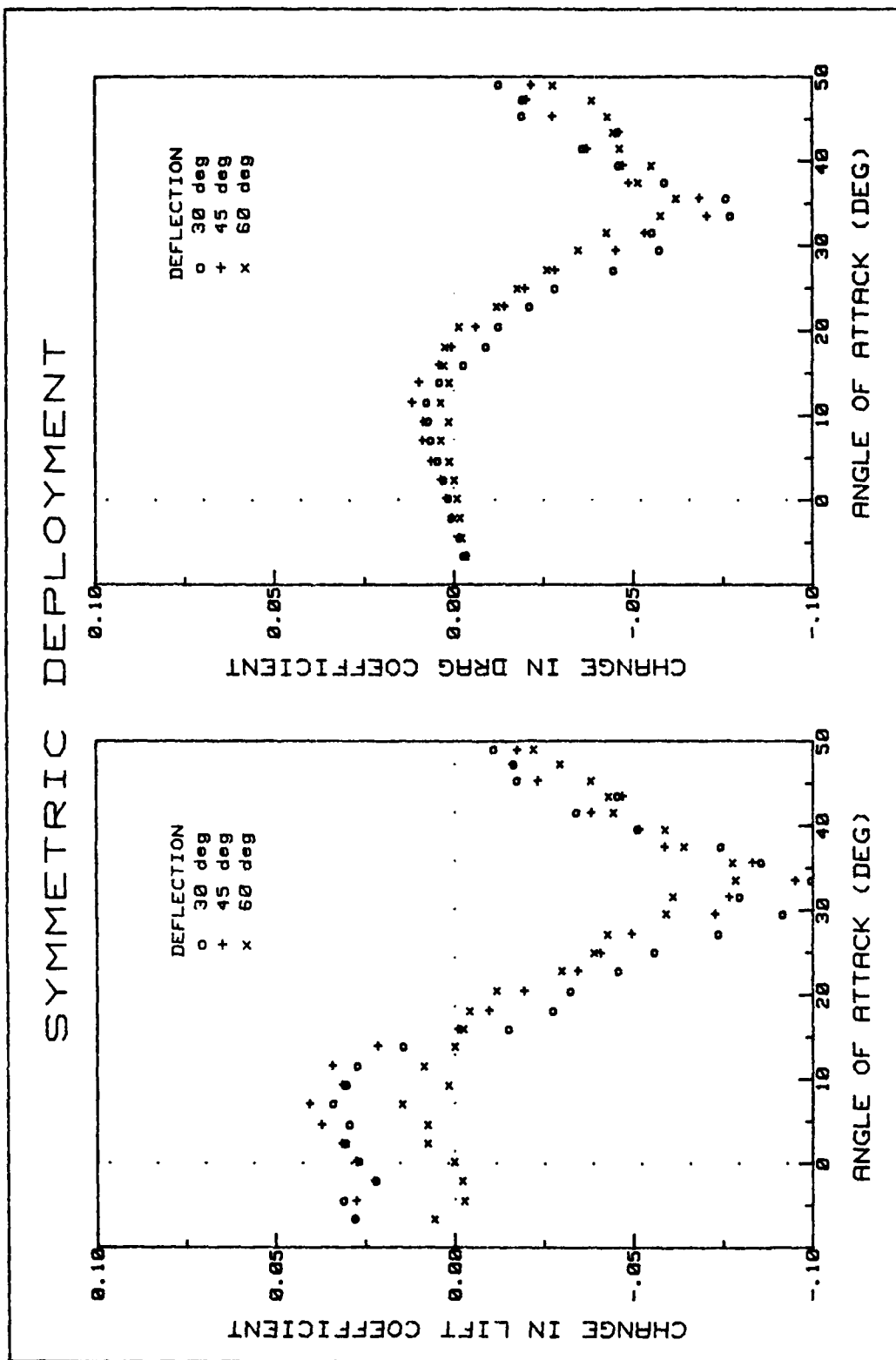


Figure 19. C1 Flap ΔC_L and ΔC_D for Various Deflection Angles (symmetric)

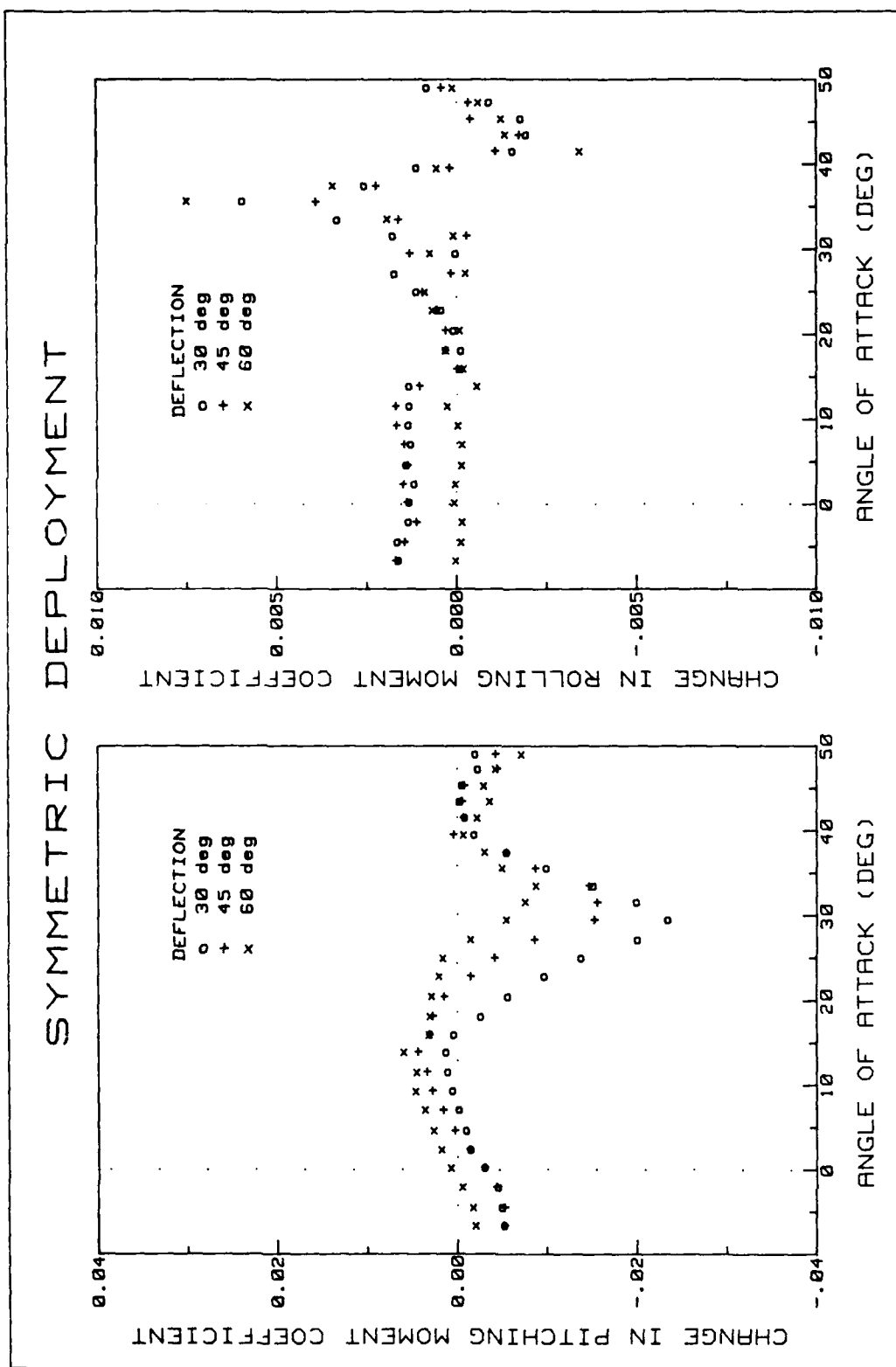


Figure 20. C1 Flap ΔC_m and ΔC_l for Various Deflection Angles (symmetric)

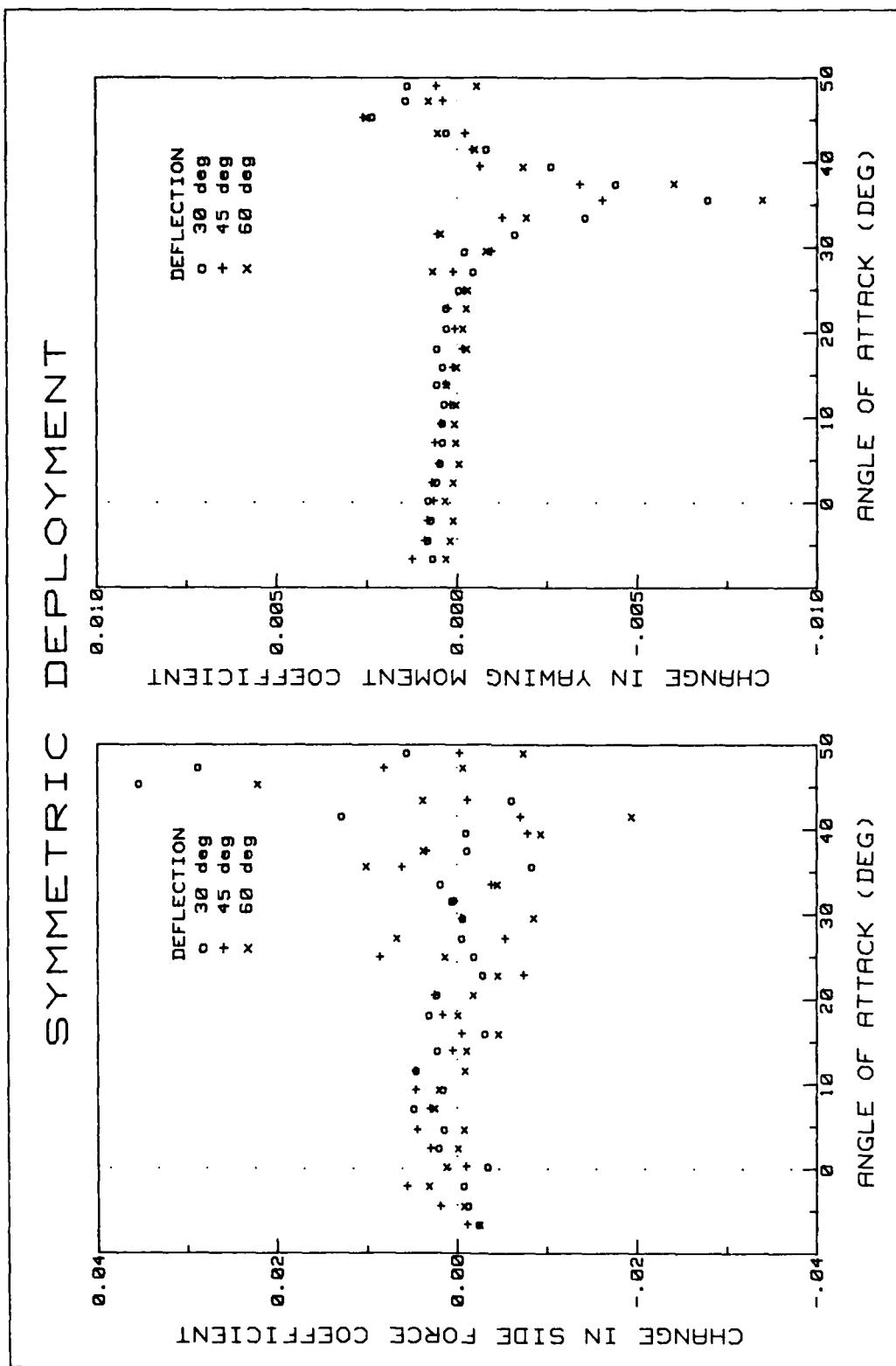


Figure 21. C1 Flap ΔC_Y and ΔC_n for Various Deflection Angles (symmetric)

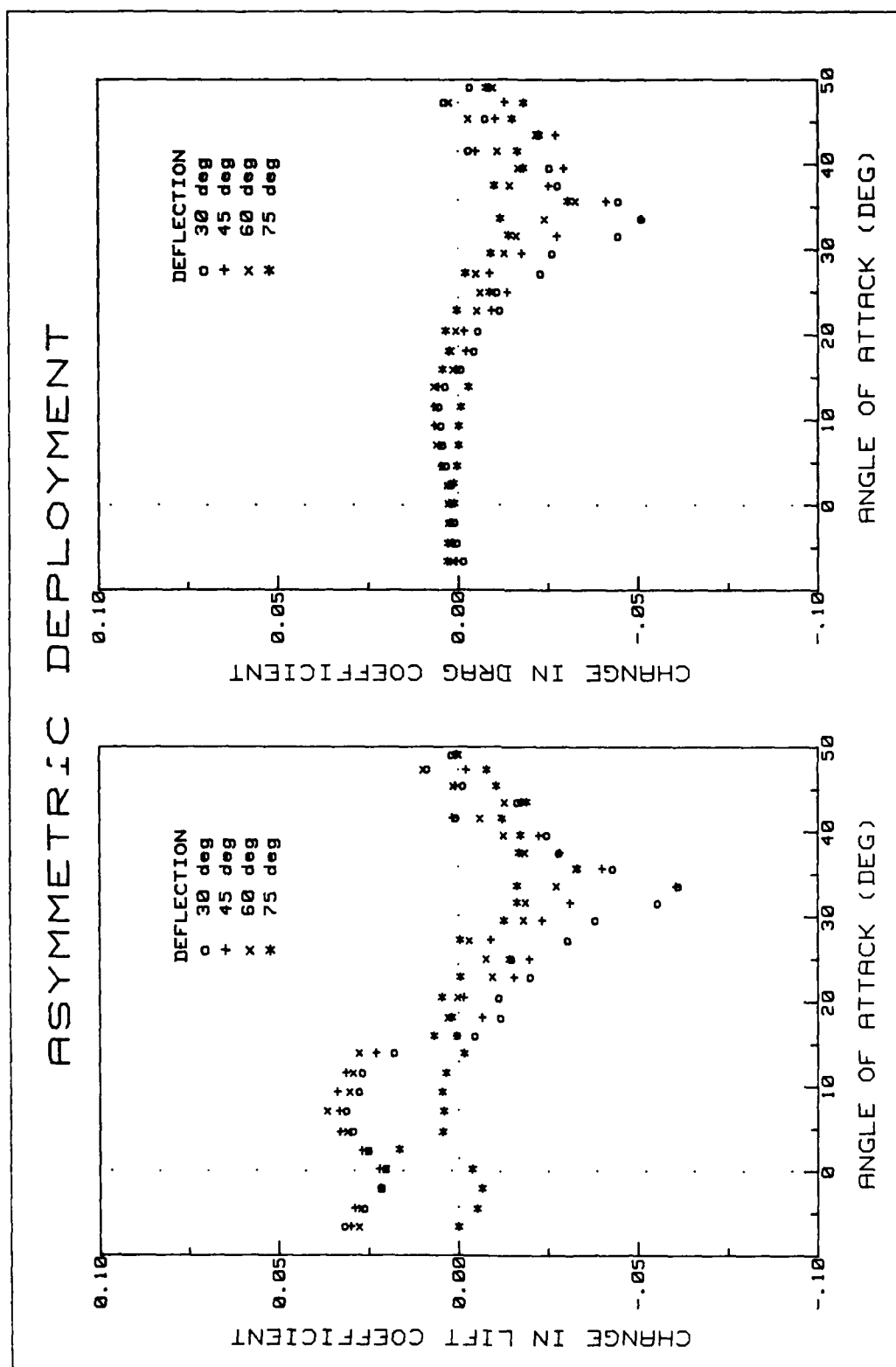


Figure 22. C2 Flap ΔC_L and ΔC_D for Various Deflection Angles (asymmetric)

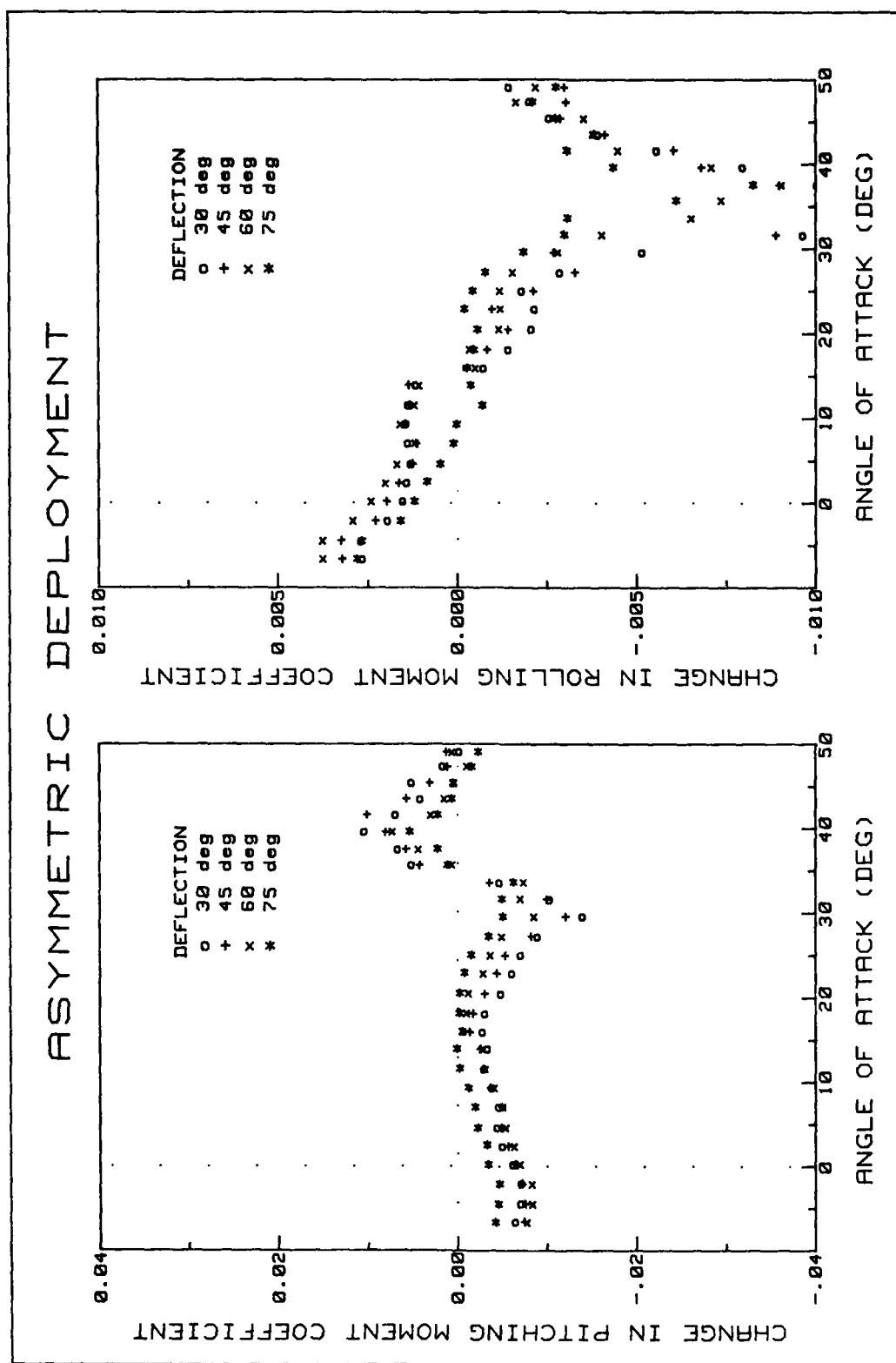


Figure 23. C2 Flap ΔC_m and ΔC_l for Various Deflection Angles (asymmetric)

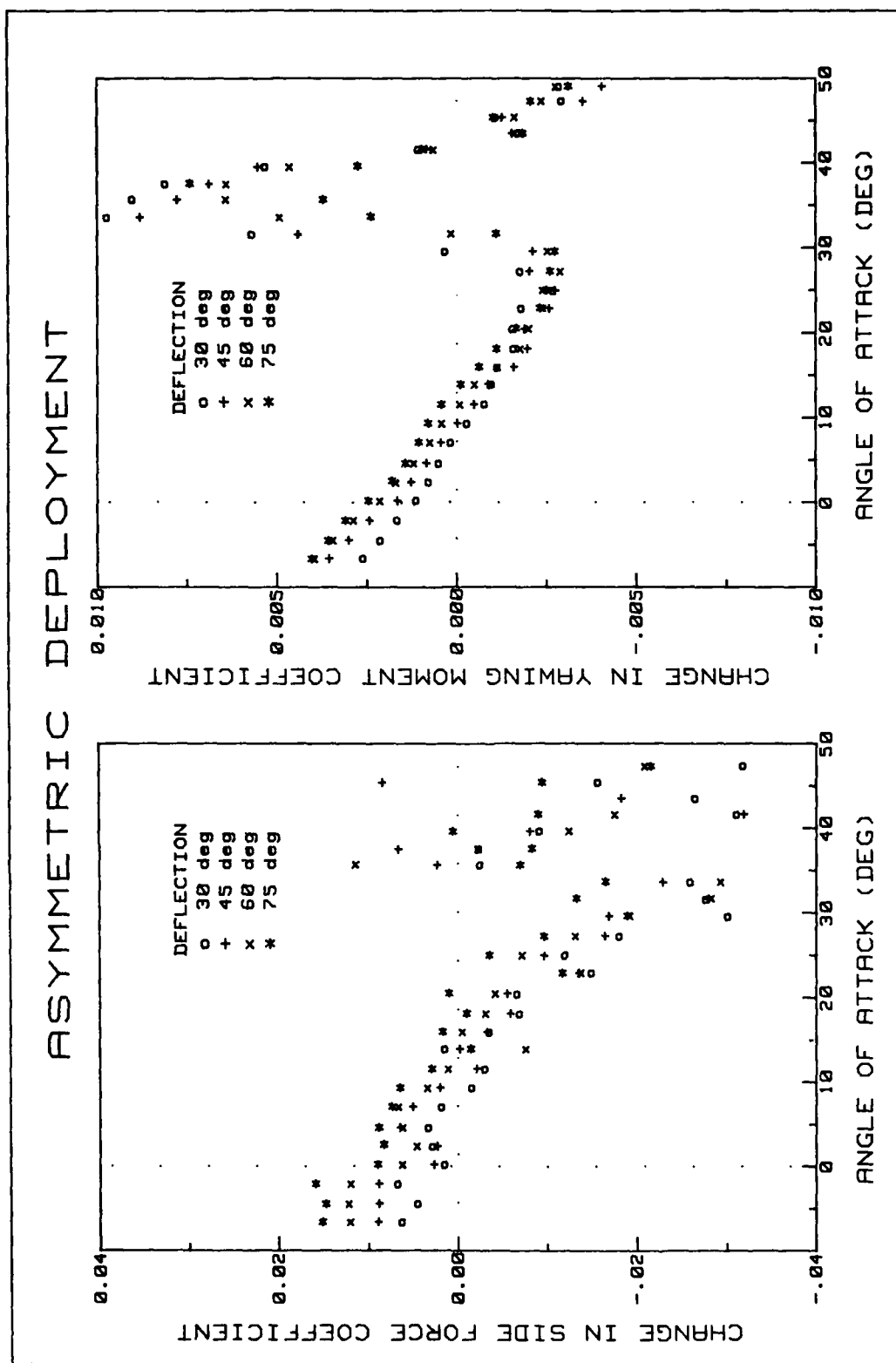


Figure 24. C2 Flap ΔC_y and ΔC_n for Various Deflection Angles (asymmetric)

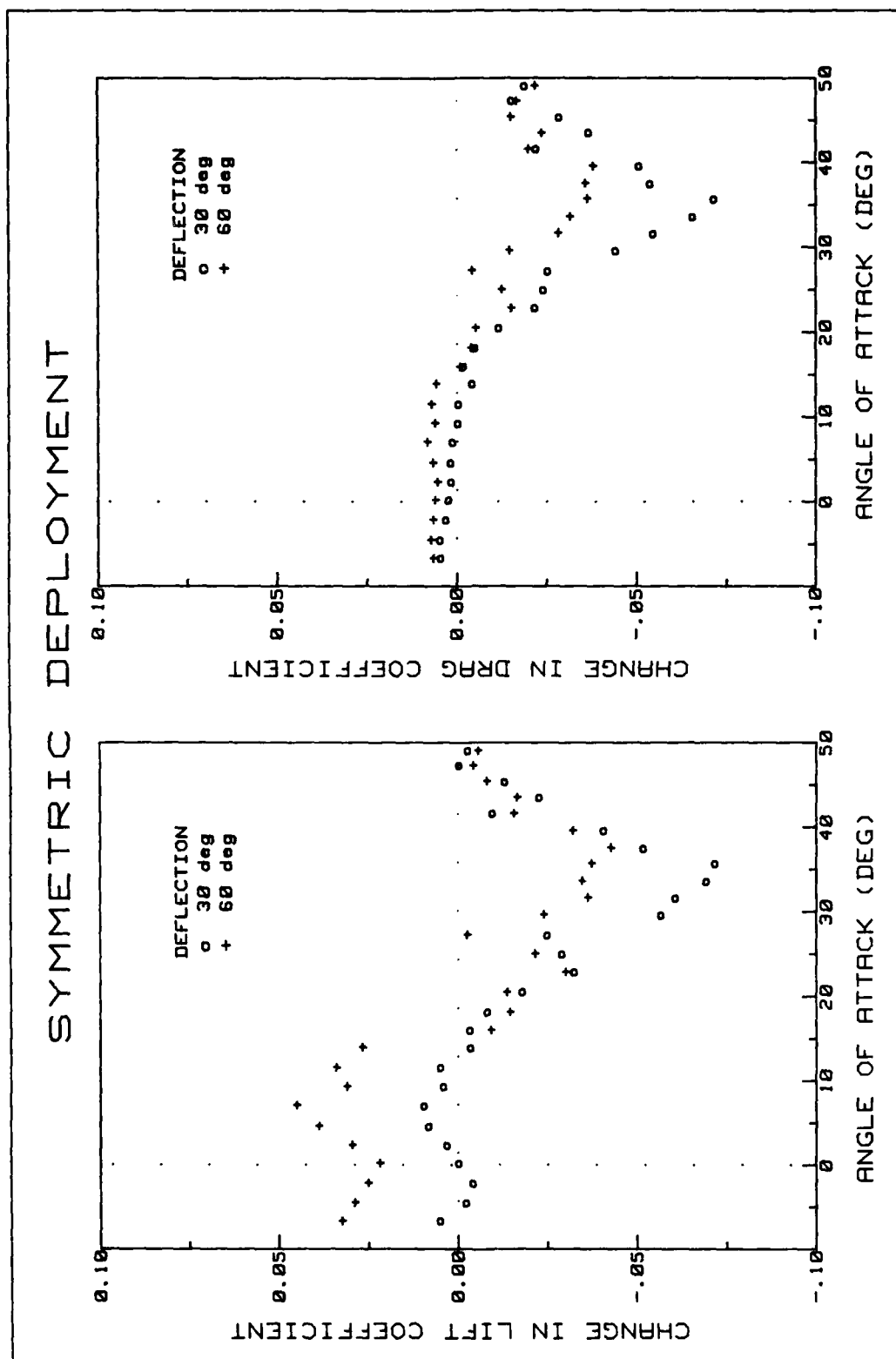


Figure 25. C2 Flap ΔC_L and ΔC_D for Various Deflection Angles (symmetric)

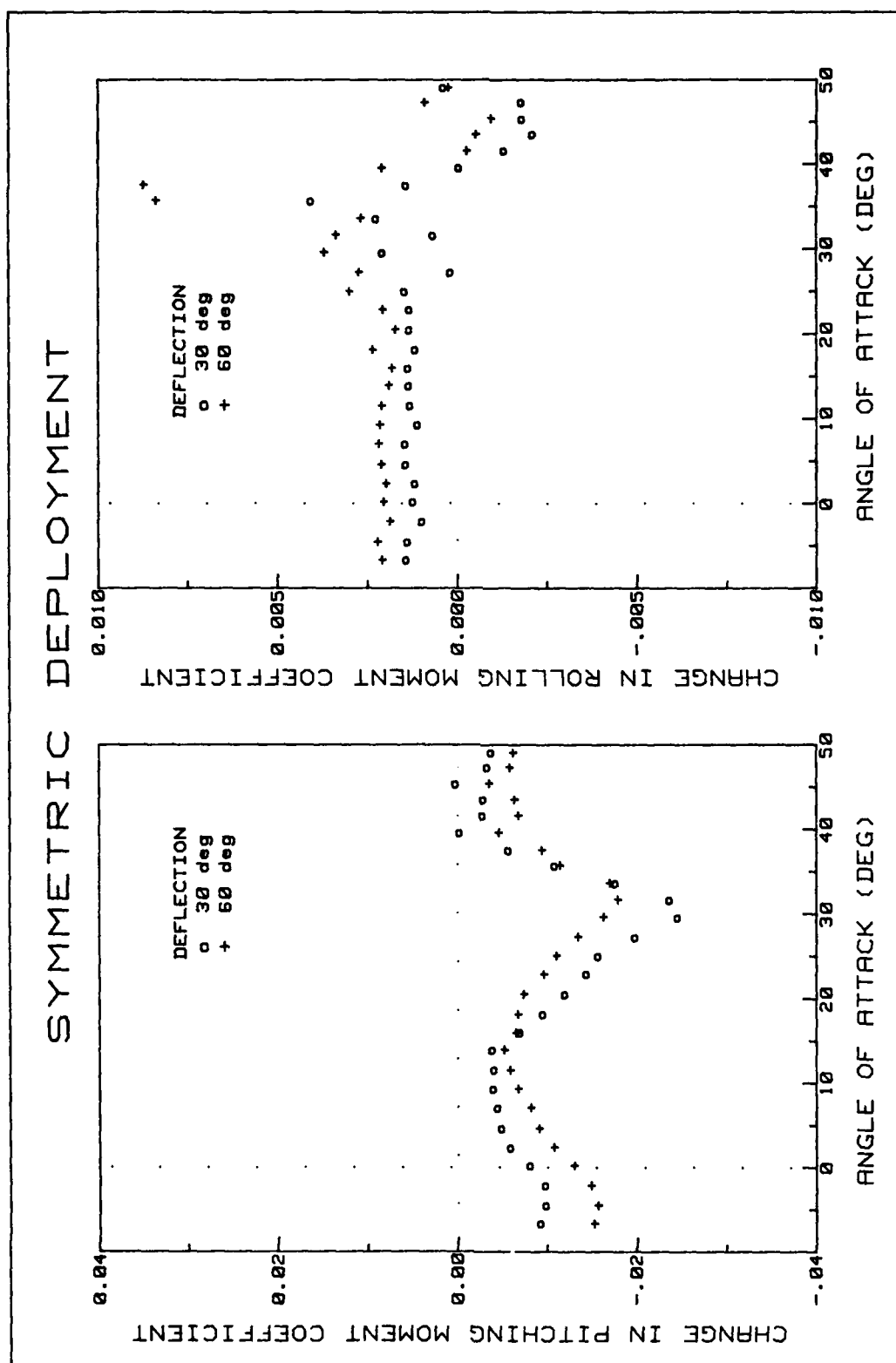


Figure 26. C2 Flap ΔC_m and ΔC_l for Various Deflection Angles (symmetric)

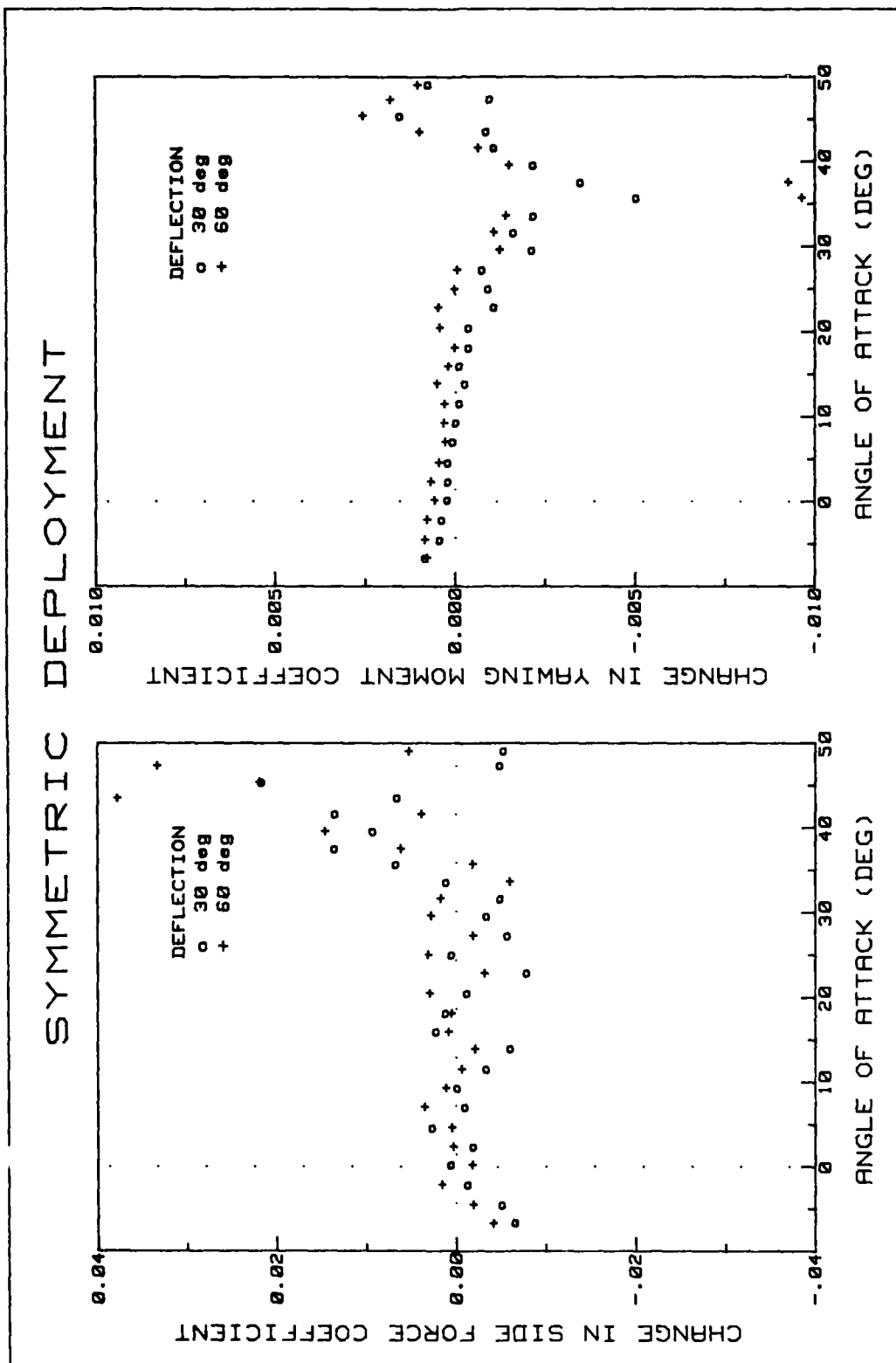


Figure 27. C2 Flap ΔC_Y and ΔC_N for Various Deflection Angles (symmetric)

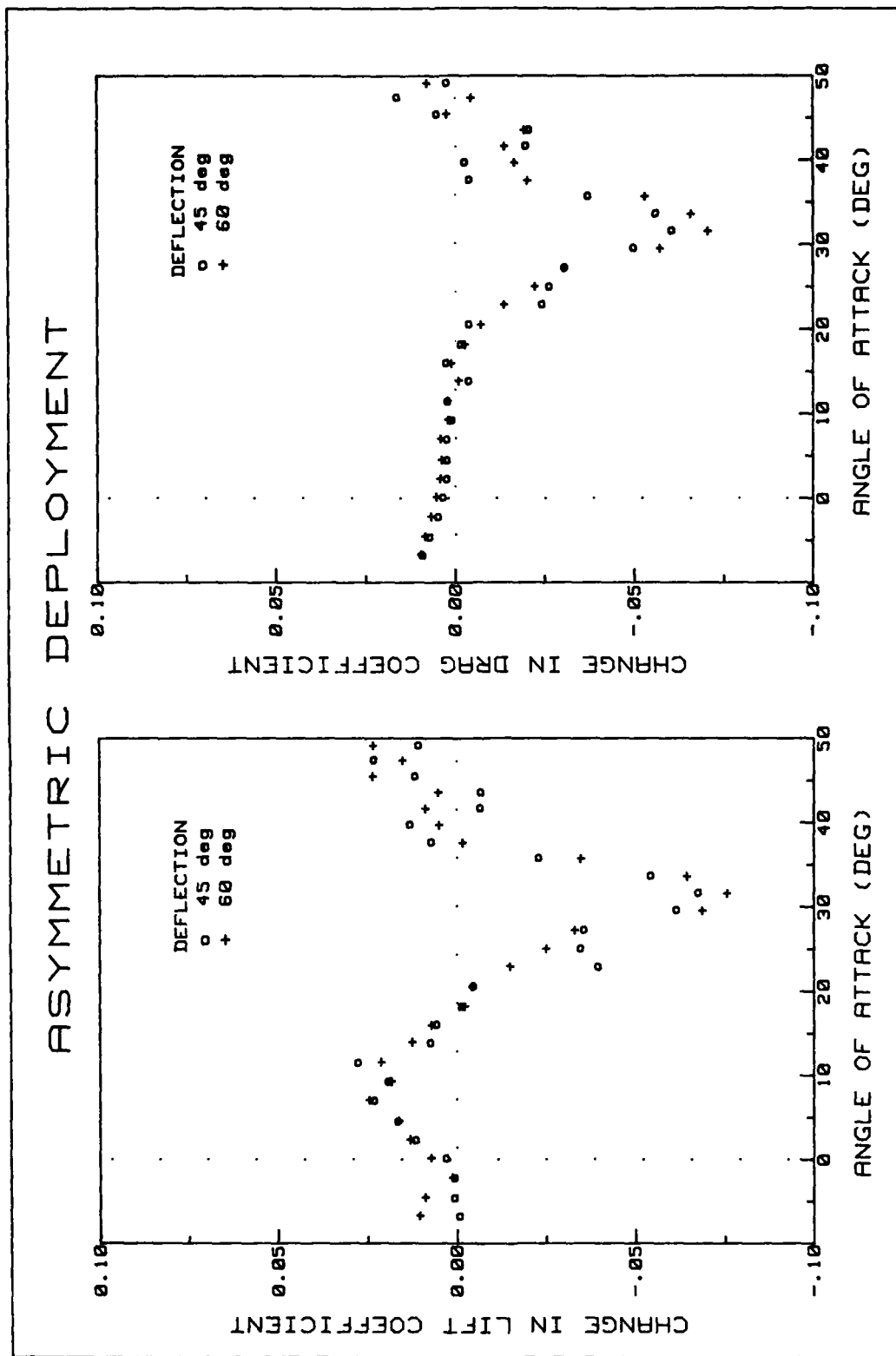


Figure 28. C3 Flap ΔC_L and ΔC_D for Various Deflection Angles (asymmetric)

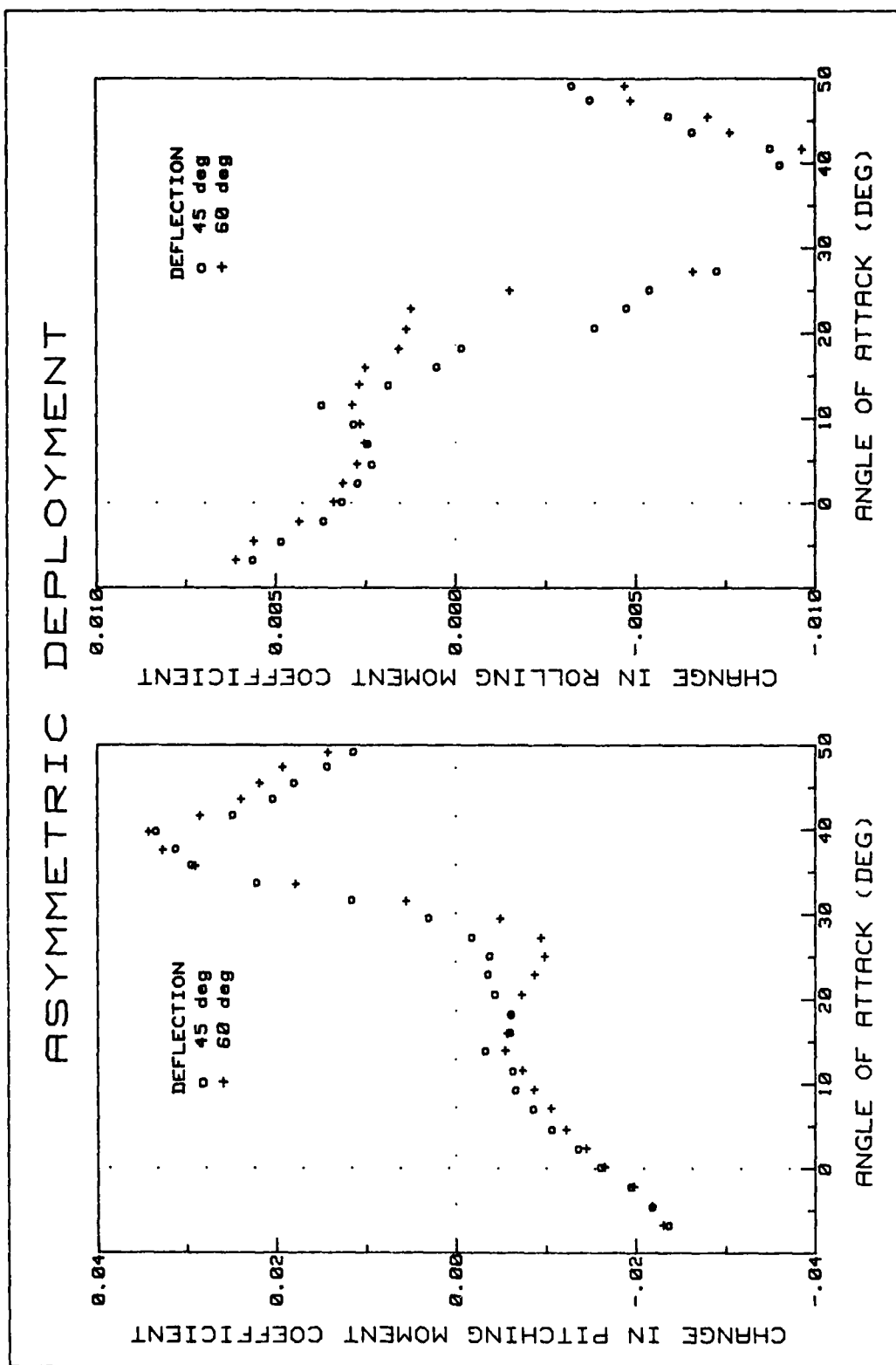


Figure 29. C3 Flap ΔC_m and ΔC_l for Various Deflection Angles (asymmetric)

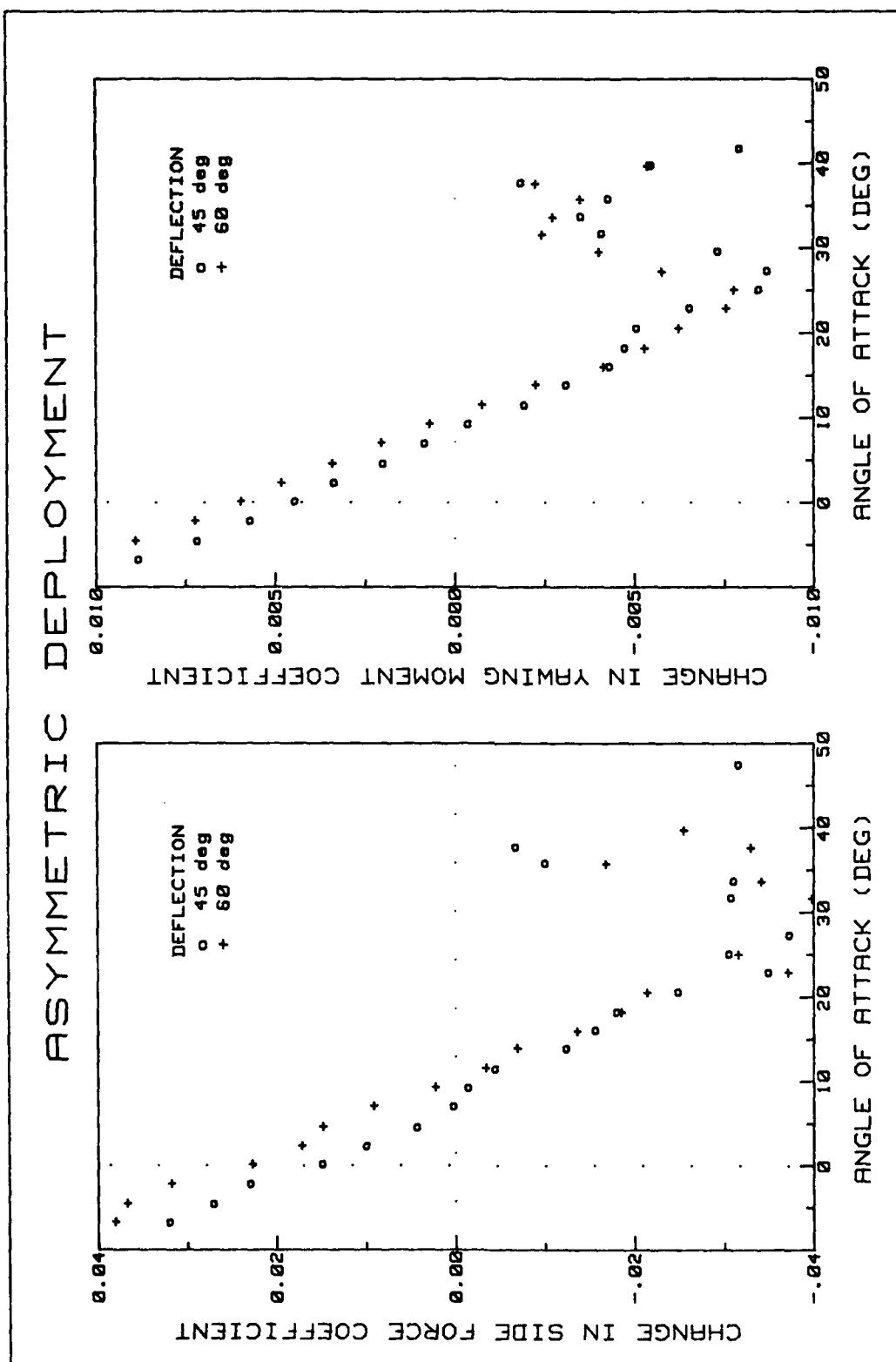


Figure 30. C3 Flap ΔC_y and ΔC_n for Various Deflection Angles (asymmetric)

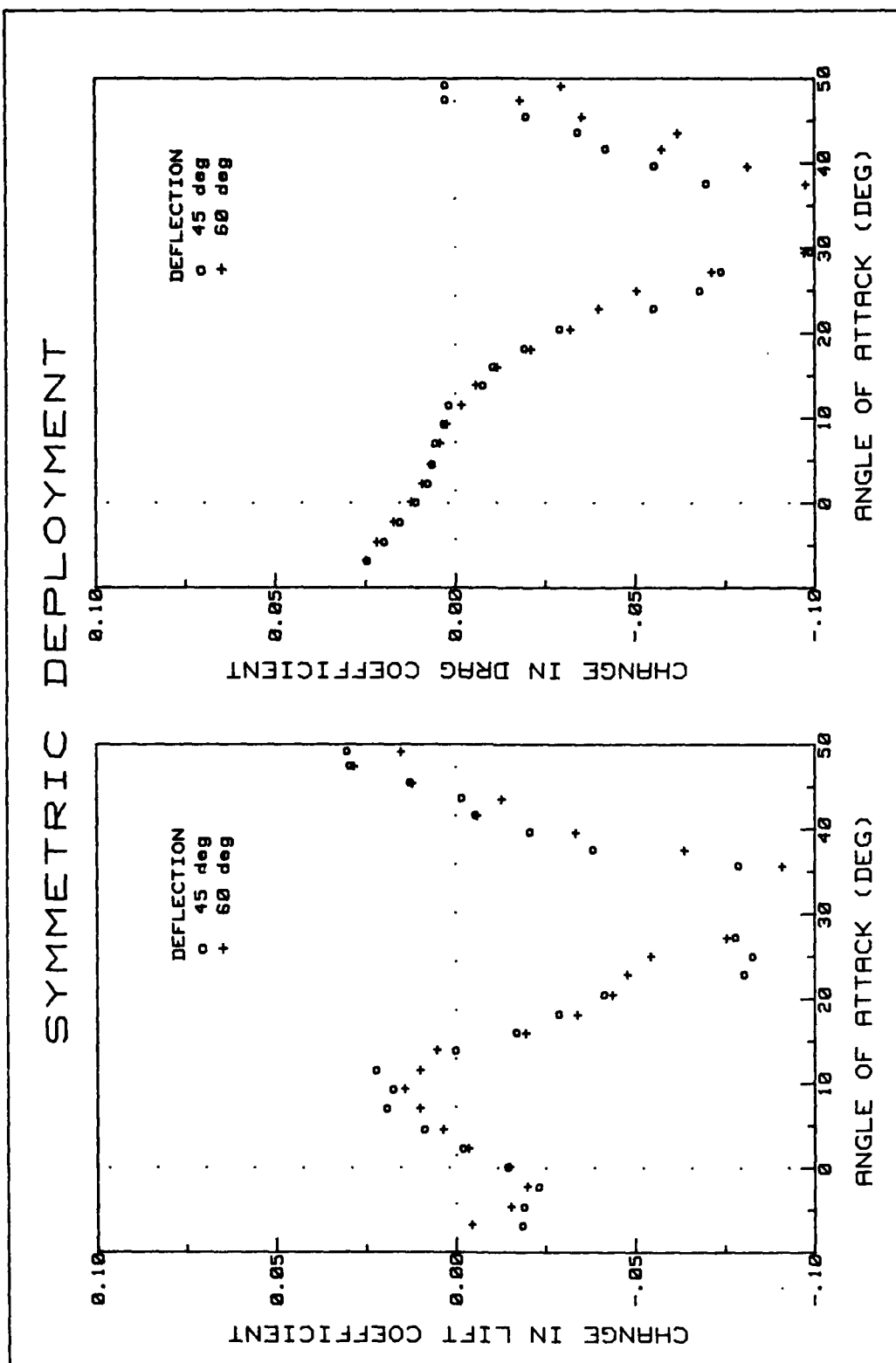


Figure 31. C3 Flap ΔC_L and ΔC_D for Various Deflection Angles (symmetric)

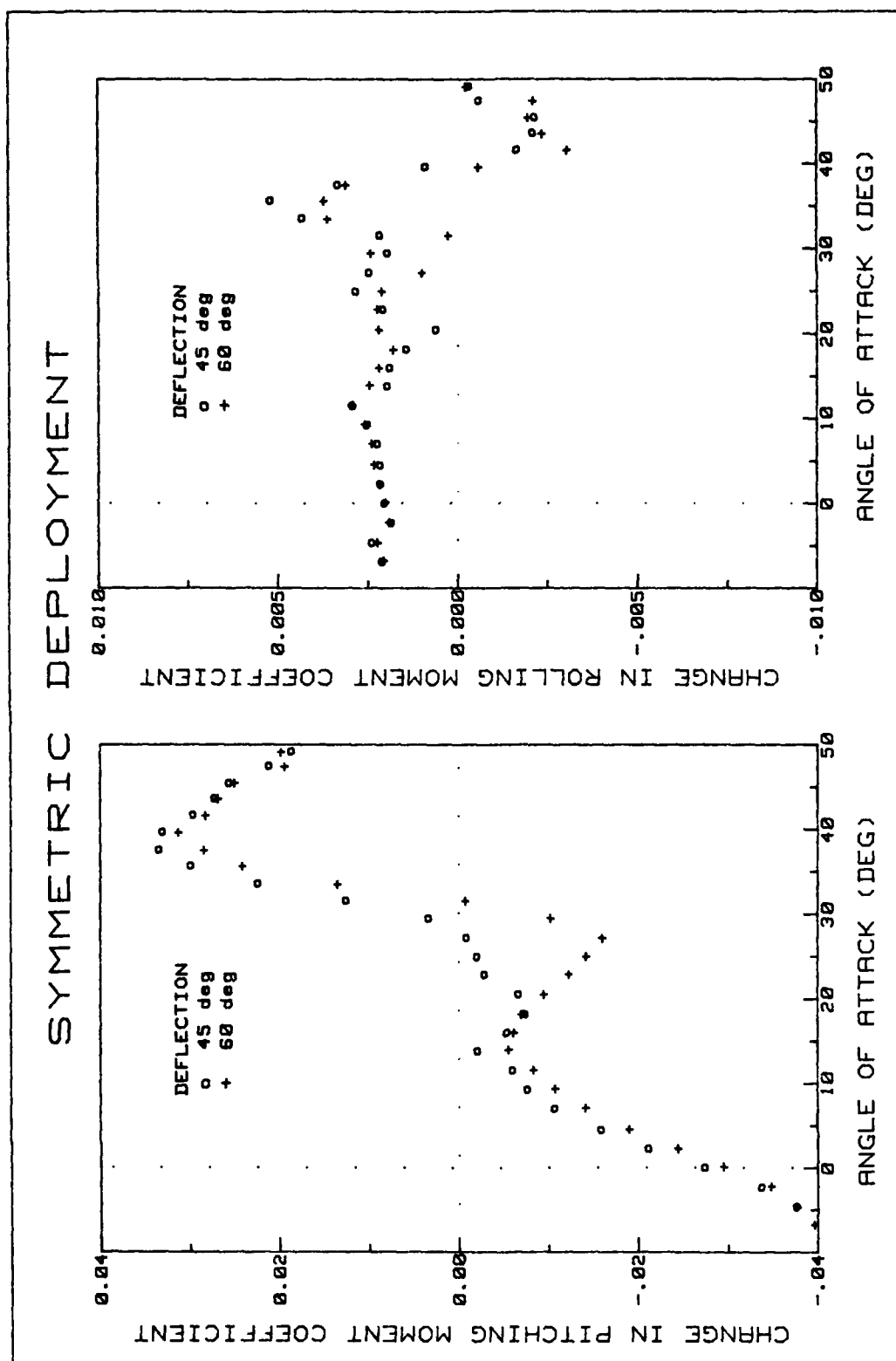


Figure 32. C3 Flap ΔC_m and ΔC_l for Various Deflection Angles (symmetric)

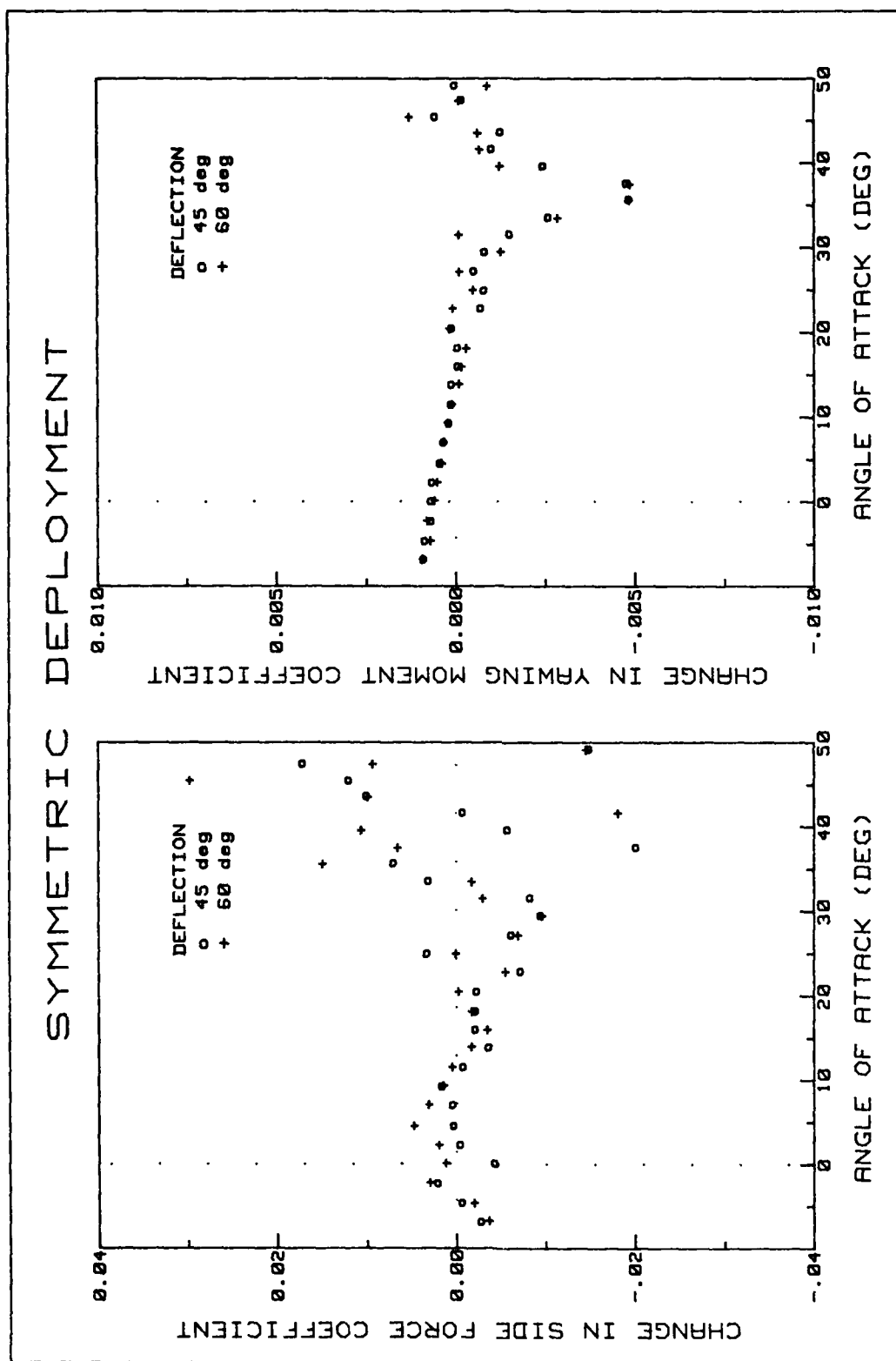


Figure 33. C3 Flap ΔC_Y and ΔC_n for Various Deflection Angles (symmetric)

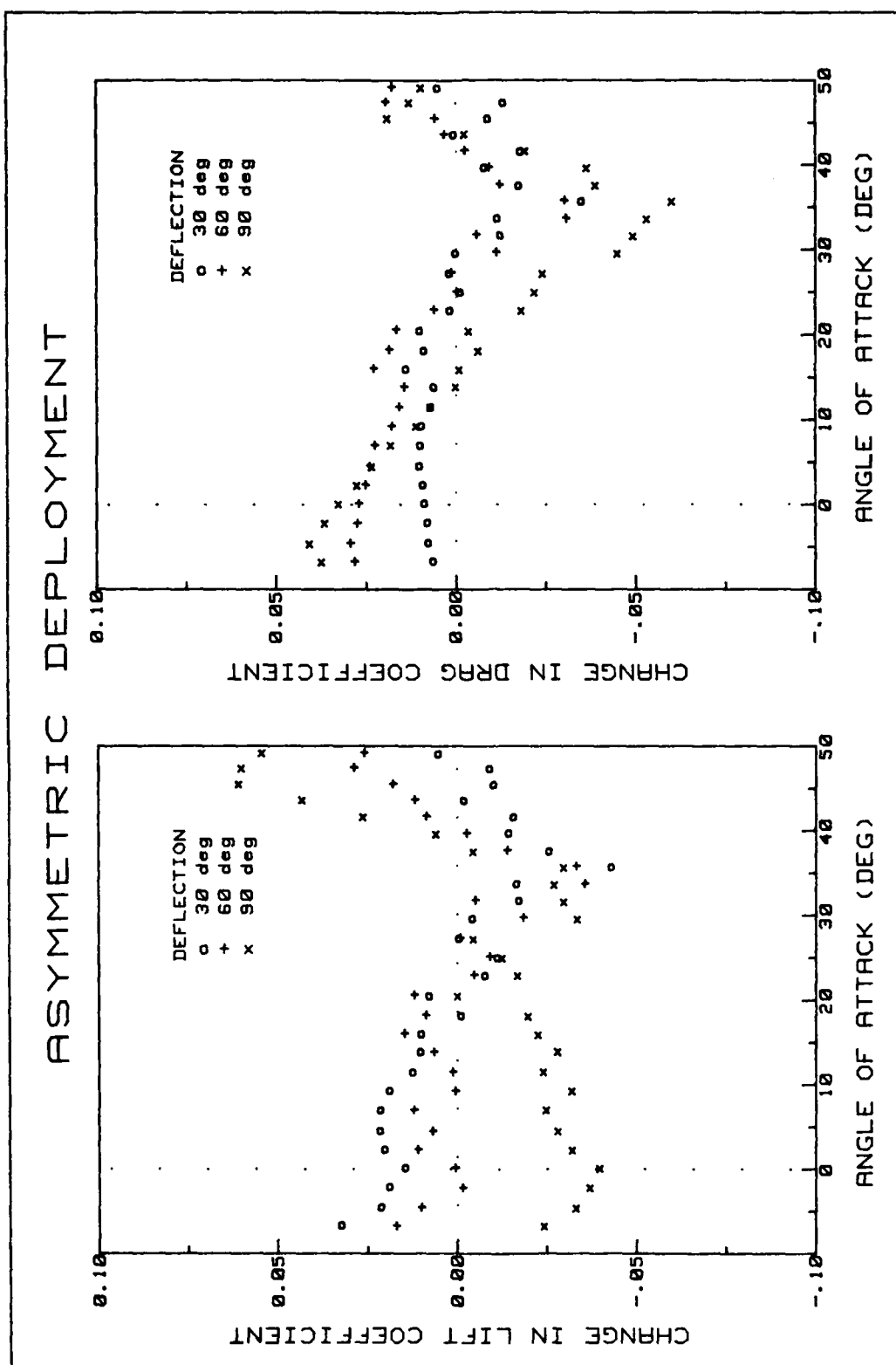


Figure 34. C4 Flap ΔC_L and ΔC_D for Various Deflection Angles (asymmetric)

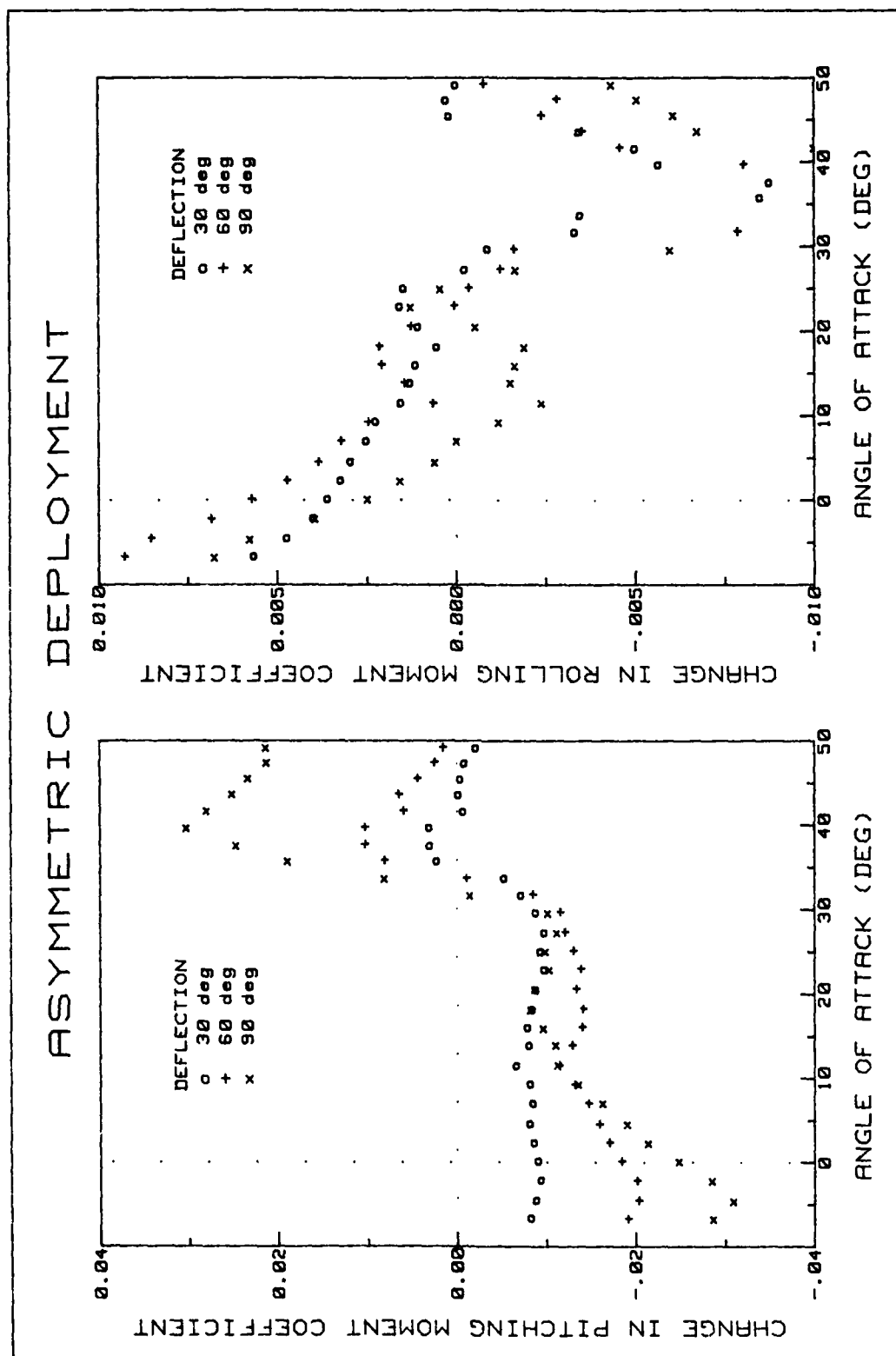


Figure 35. C4 Flap ΔC_m and ΔC_l for Various Deflection Angles (asymmetric)

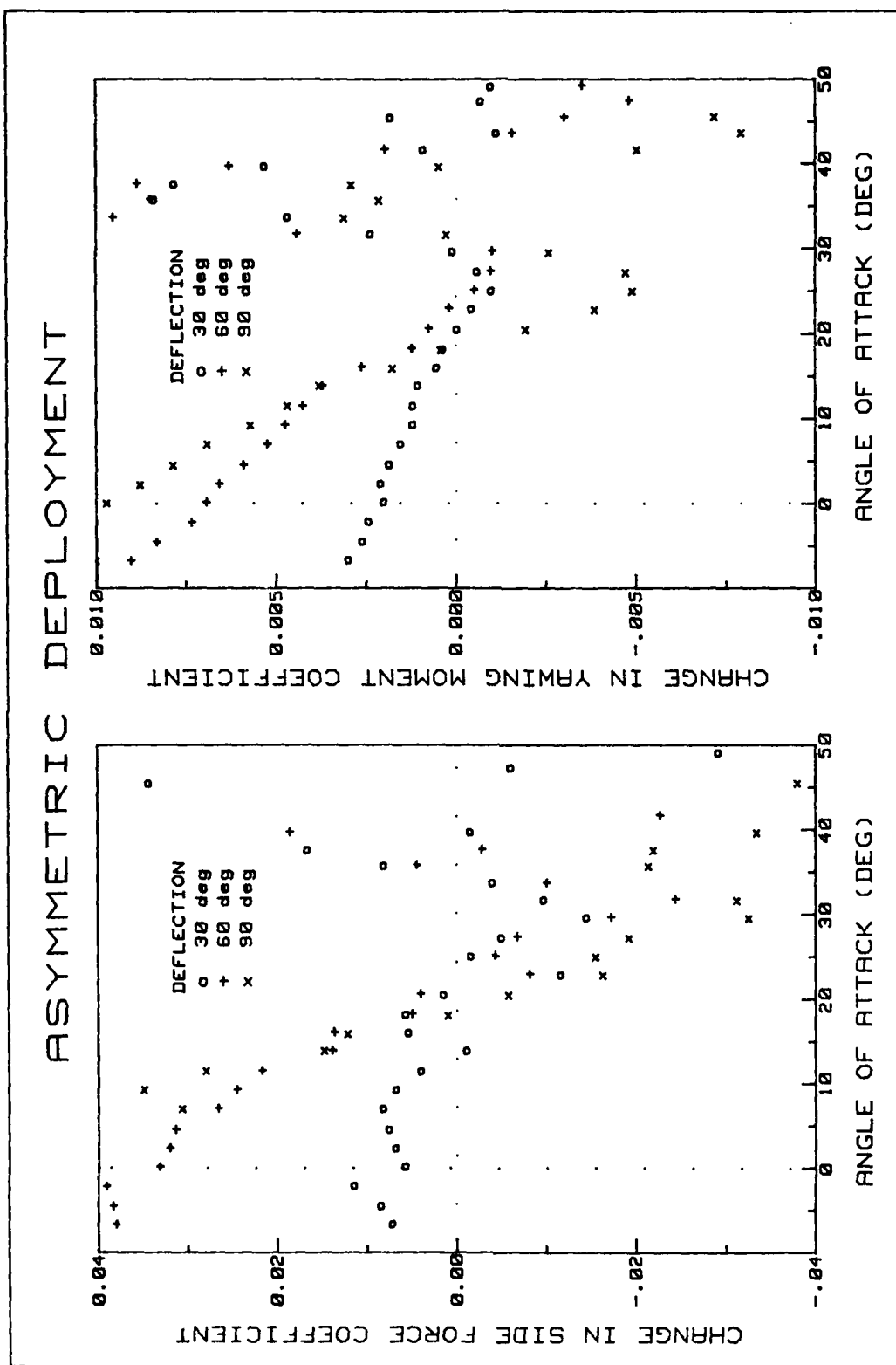


Figure 36. C4 Flap ΔC_y and ΔC_n for Various Deflection Angles (asymmetric)

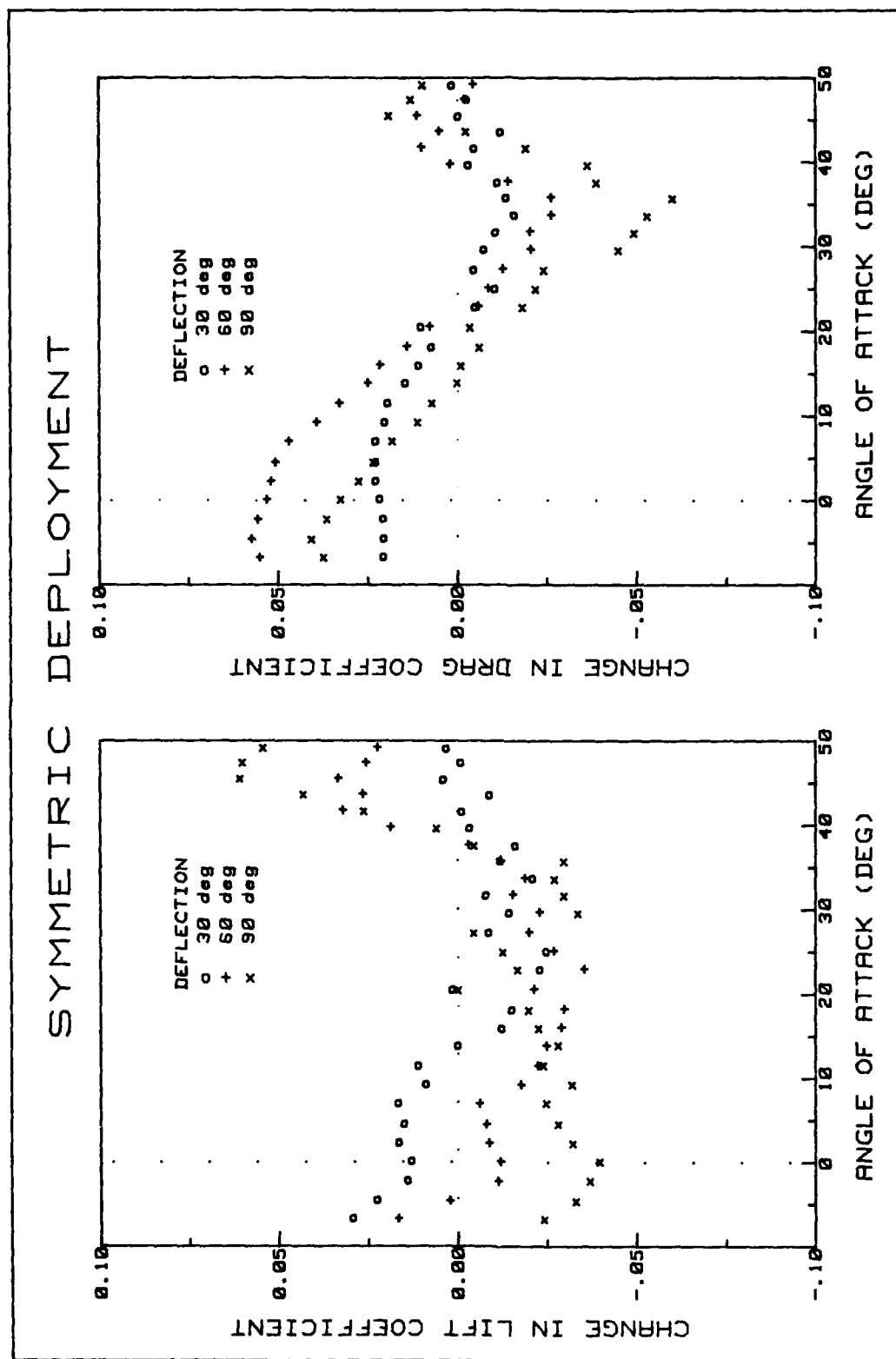


Figure 37. C4 Flap ΔC_L and ΔC_D for Various Deflection Angles (symmetric)

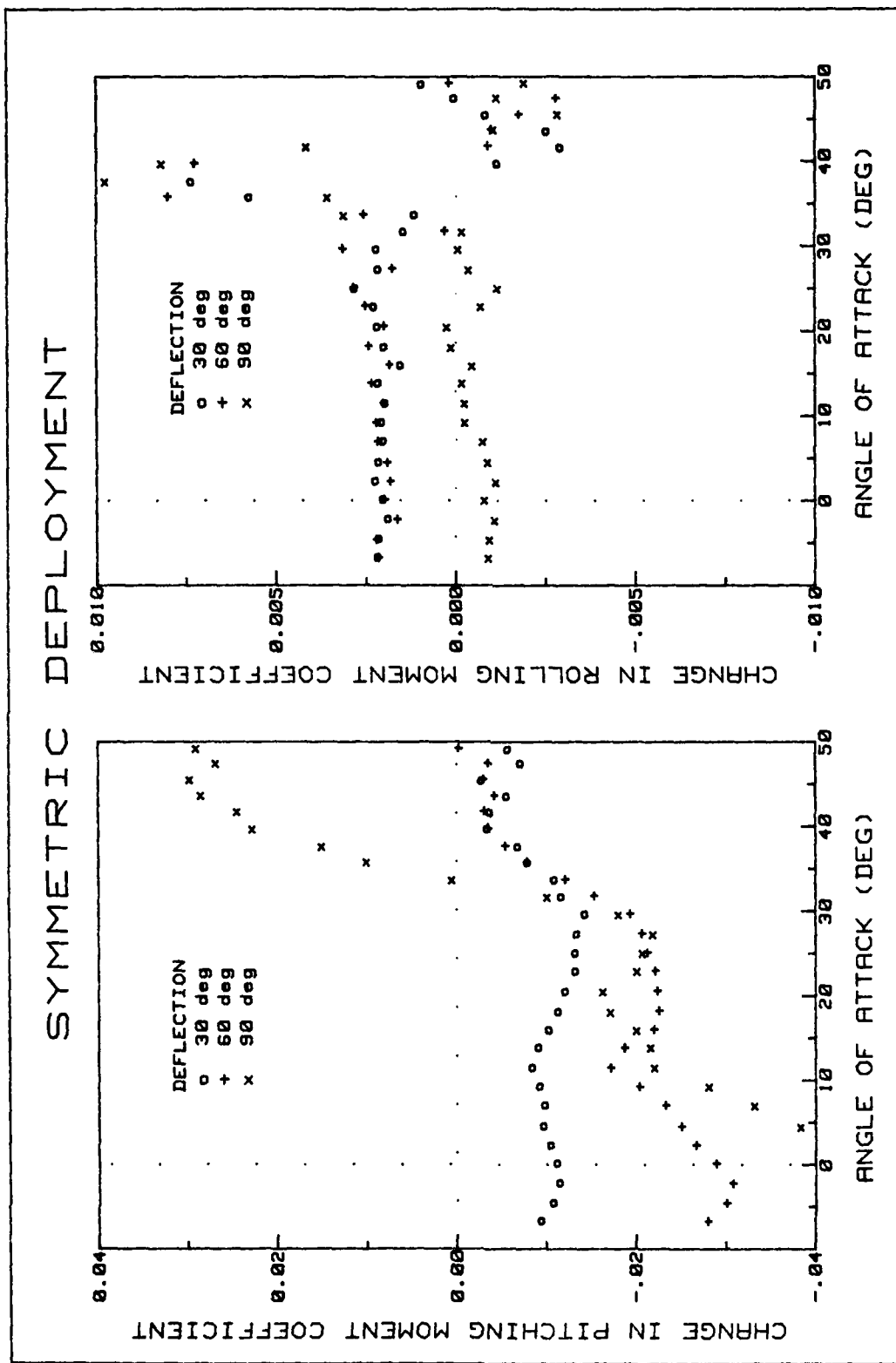


Figure 38. C4 Flap ΔC_m and ΔC_l for Various Deflection Angles (symmetric)

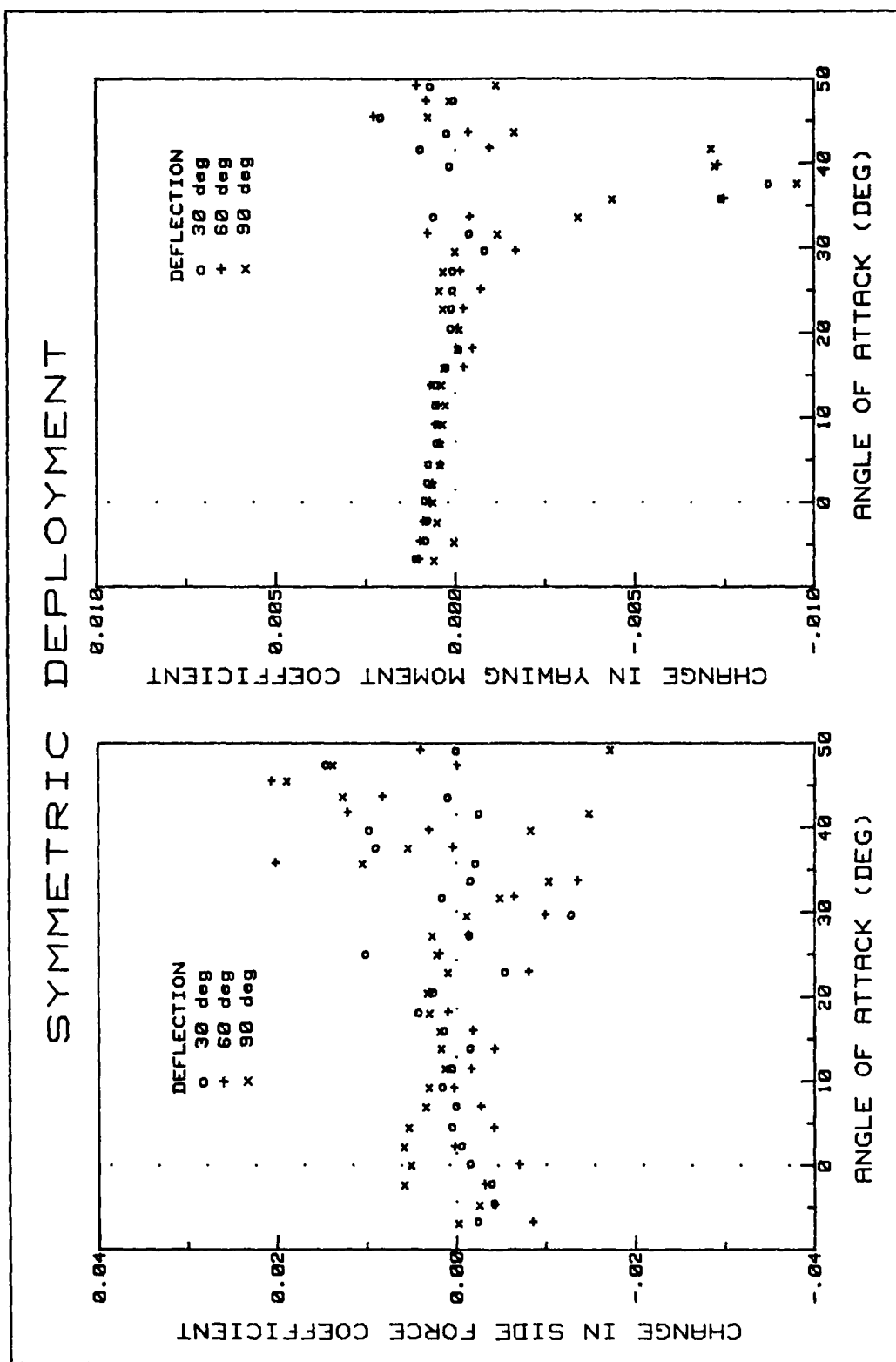


Figure 39. C4 Flap ΔC_Y and ΔC_N for Various Deflection Angles (symmetric)

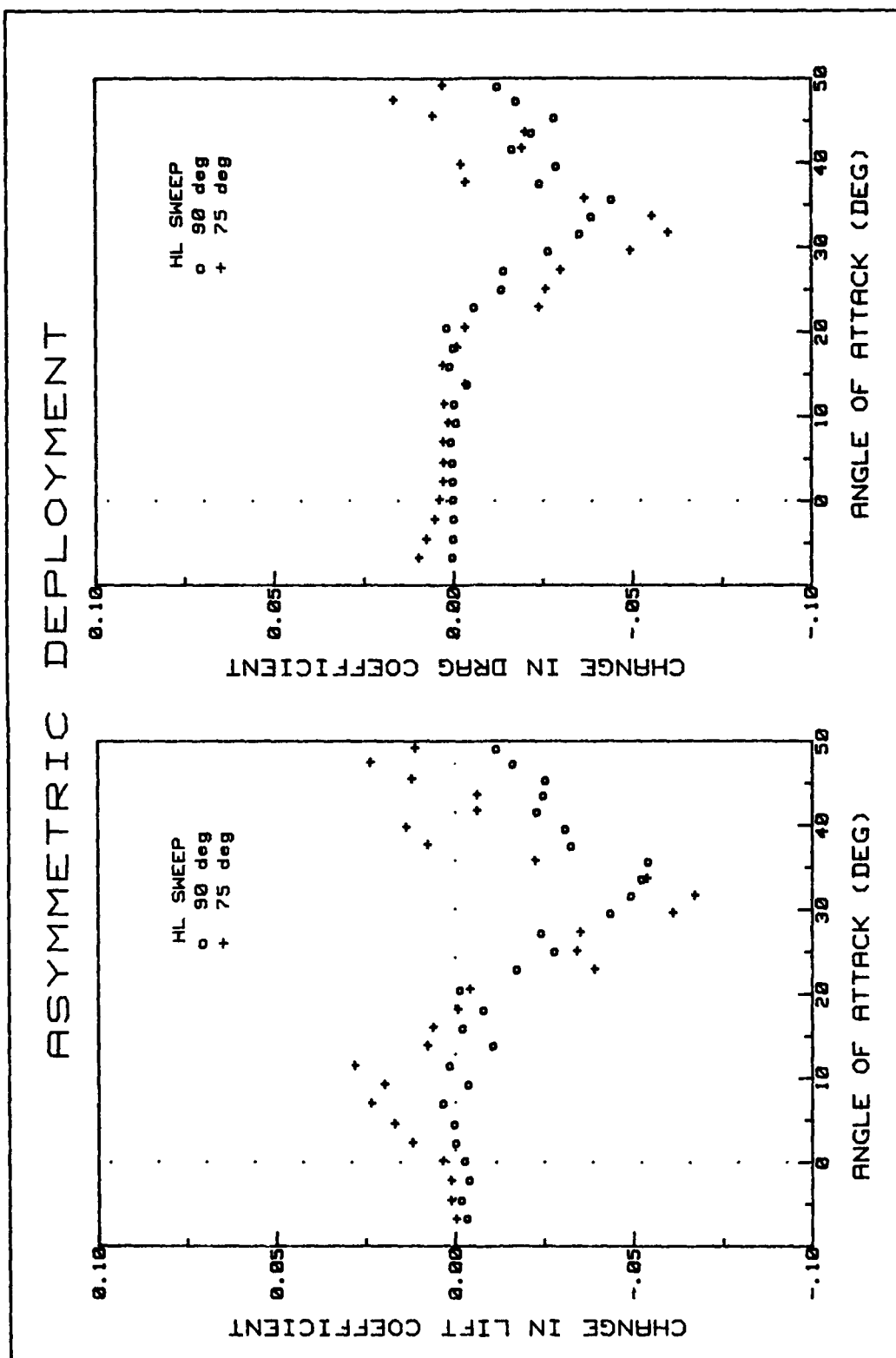


Figure 40. ΔC_L and ΔC_D for Various Sweep Angles at 45° Deflection (asymmetric)

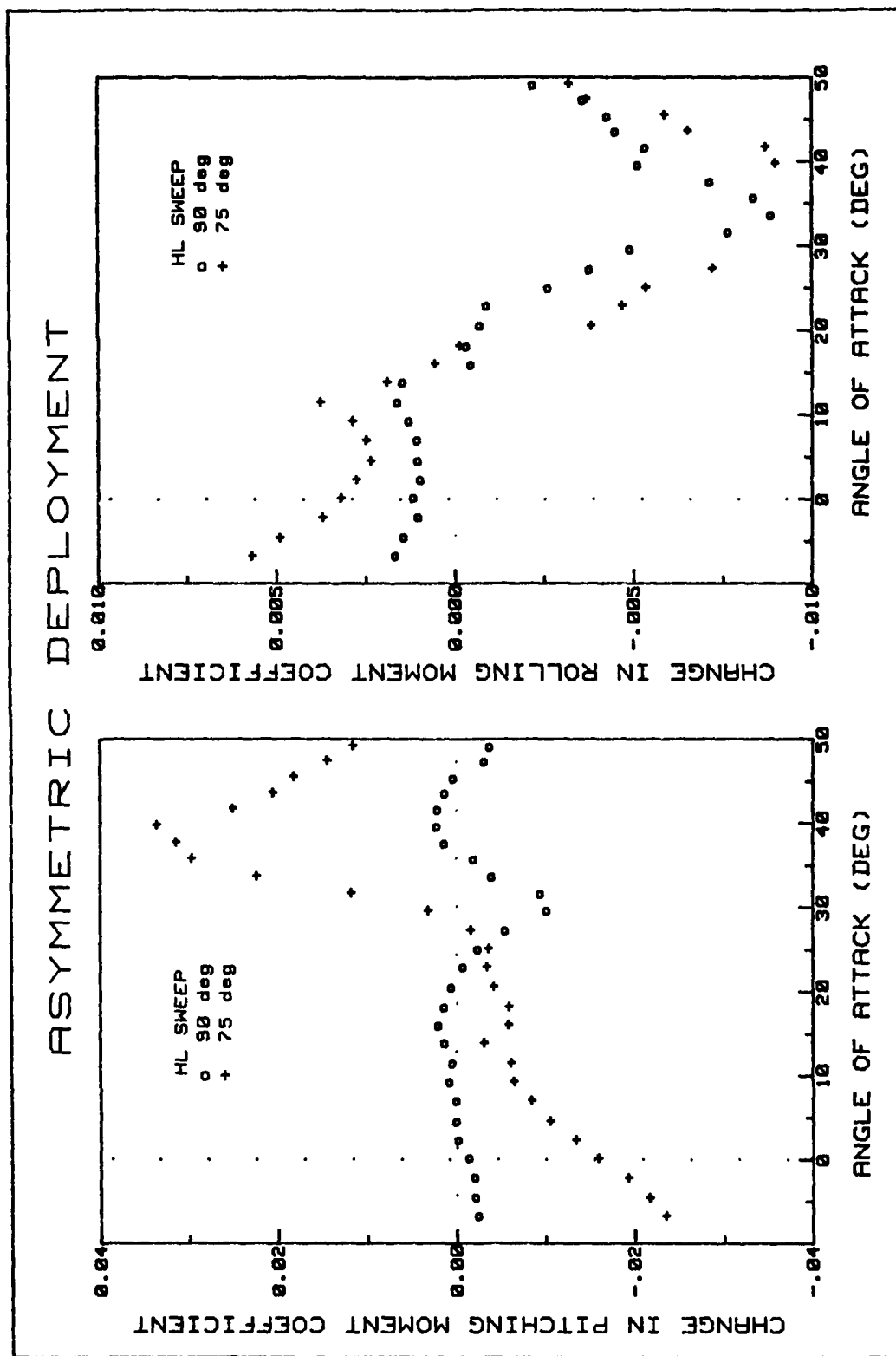


Figure 41. ΔC_m and ΔC_l for Various Sweep Angles at 45° Deflection (asymmetric)

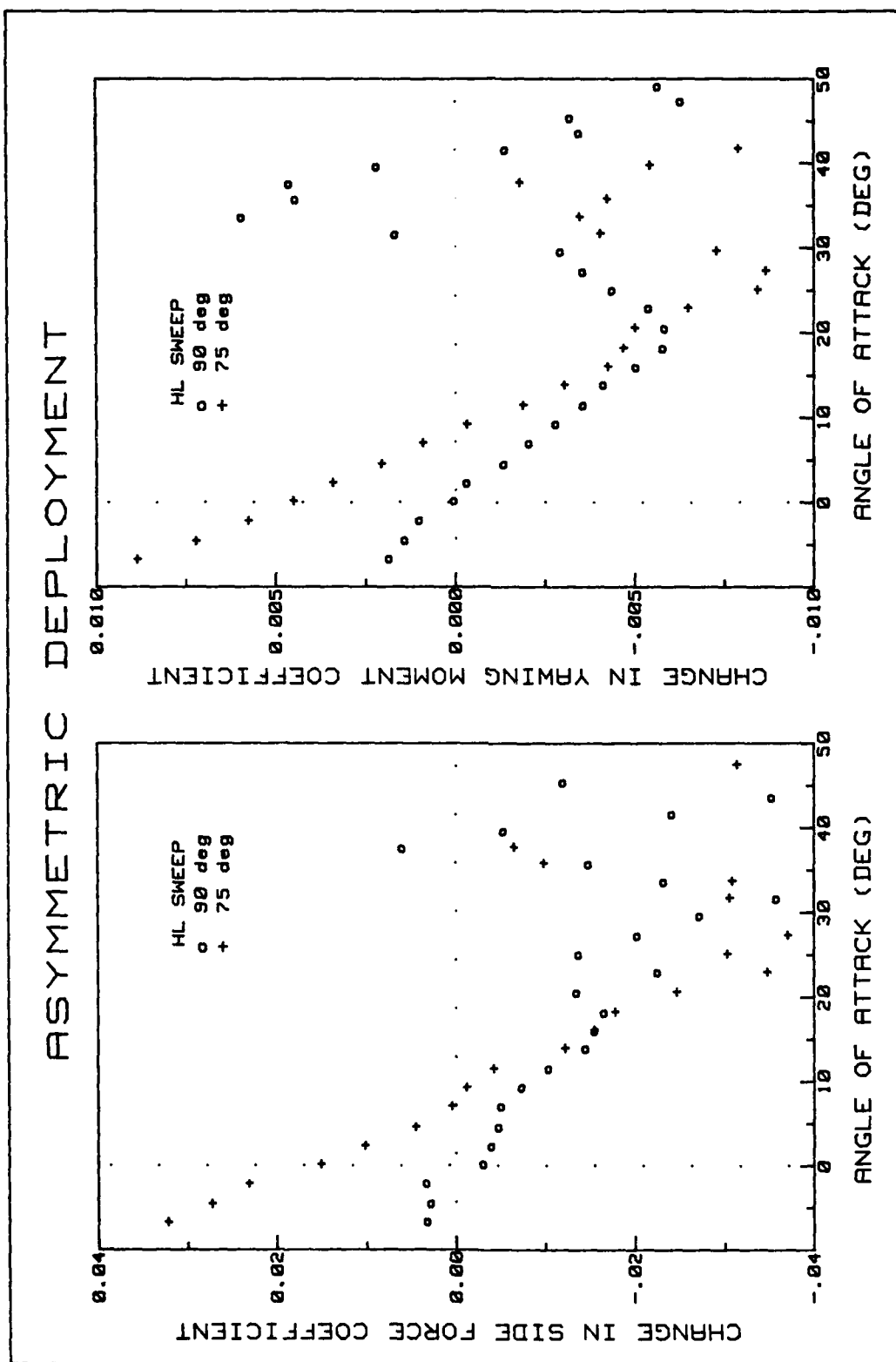


Figure 42. ΔC_y and ΔC_n for Various Sweep Angles at 45° Deflection (asymmetric)

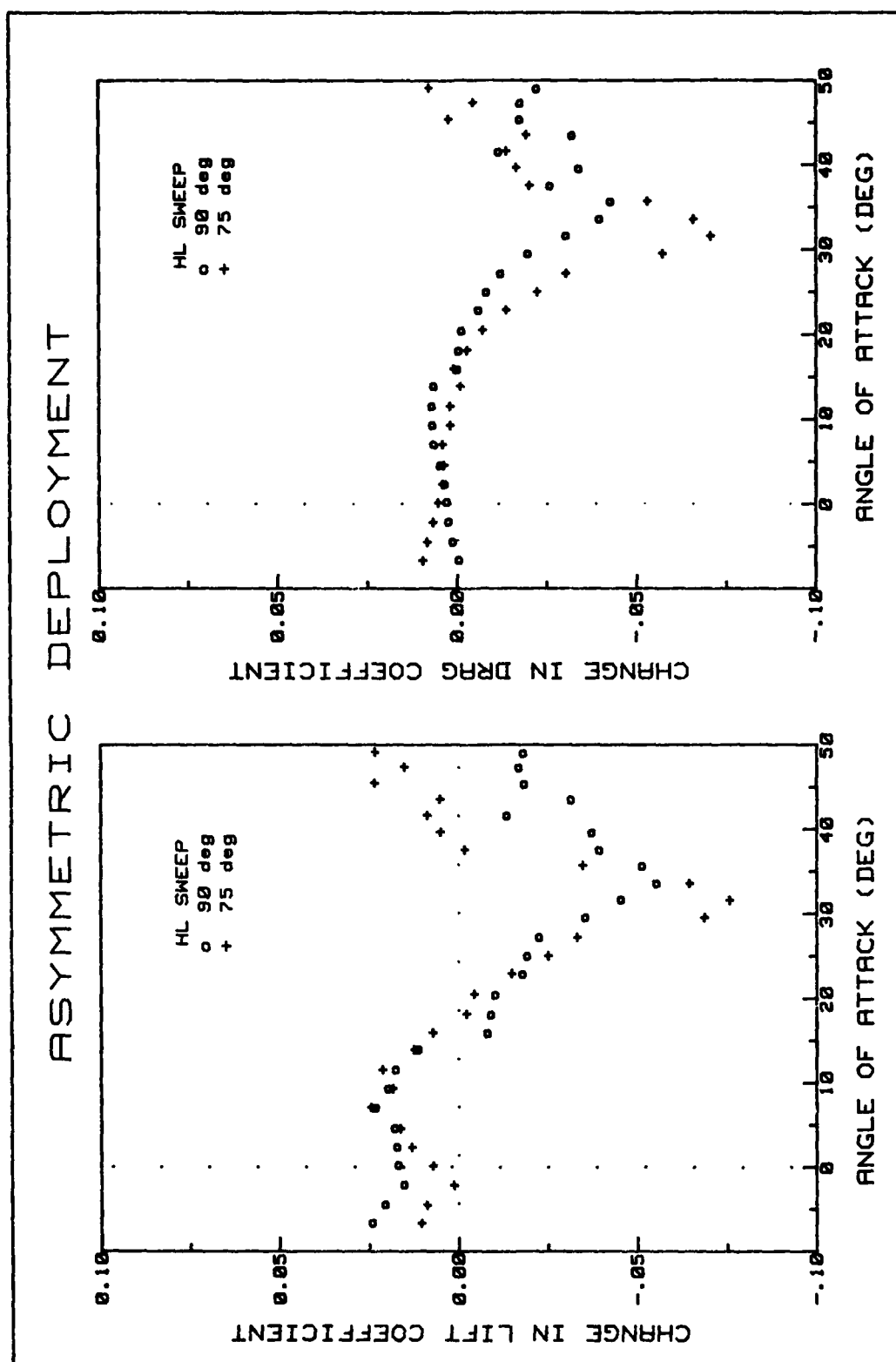


Figure 43. ΔC_L and ΔC_D for Various Sweep Angles at 60° Deflection (asymmetric)

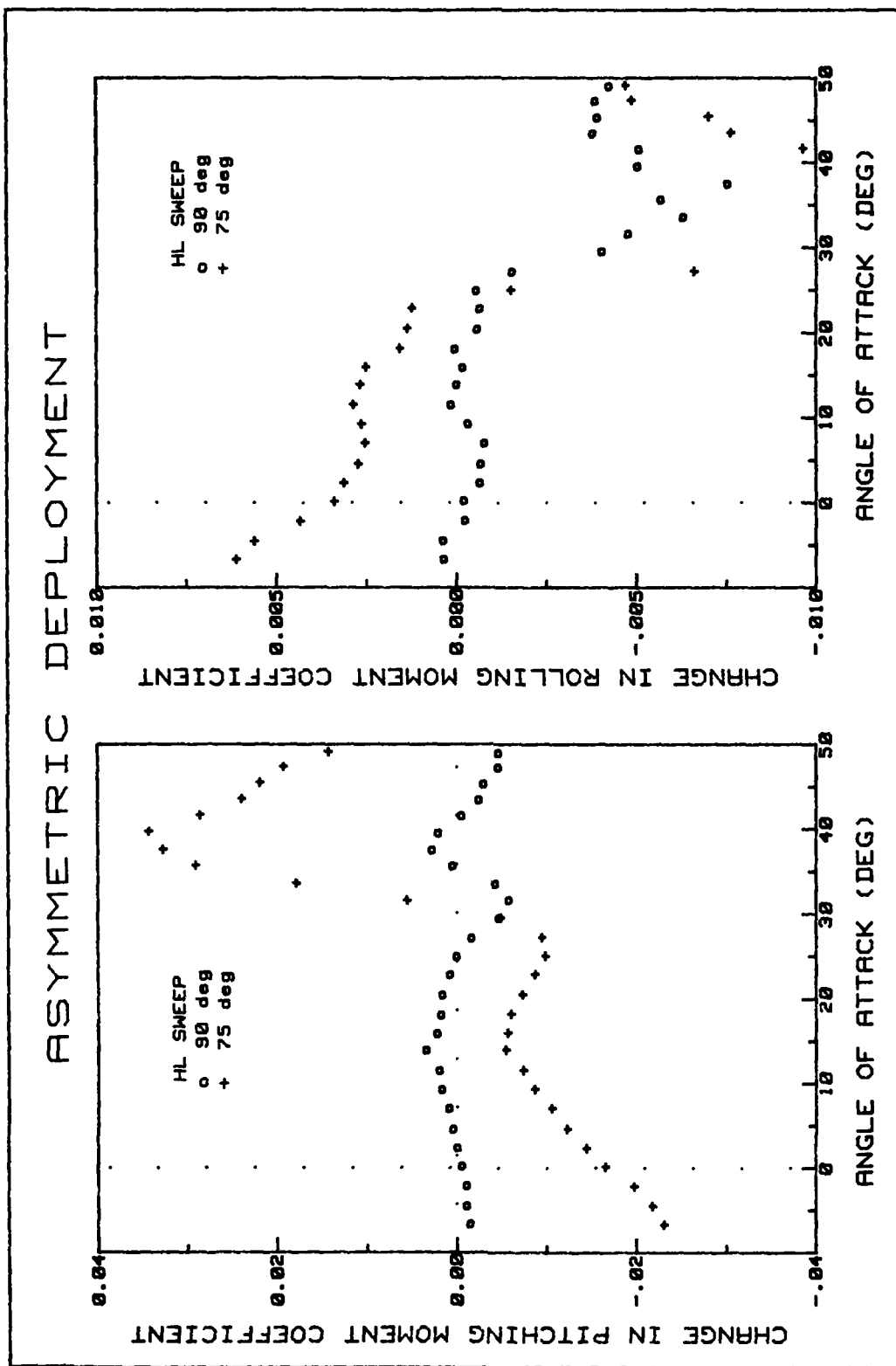


Figure 44. ΔC_m and ΔC_l for Various Sweep Angles at 60° Deflection (asymmetric)

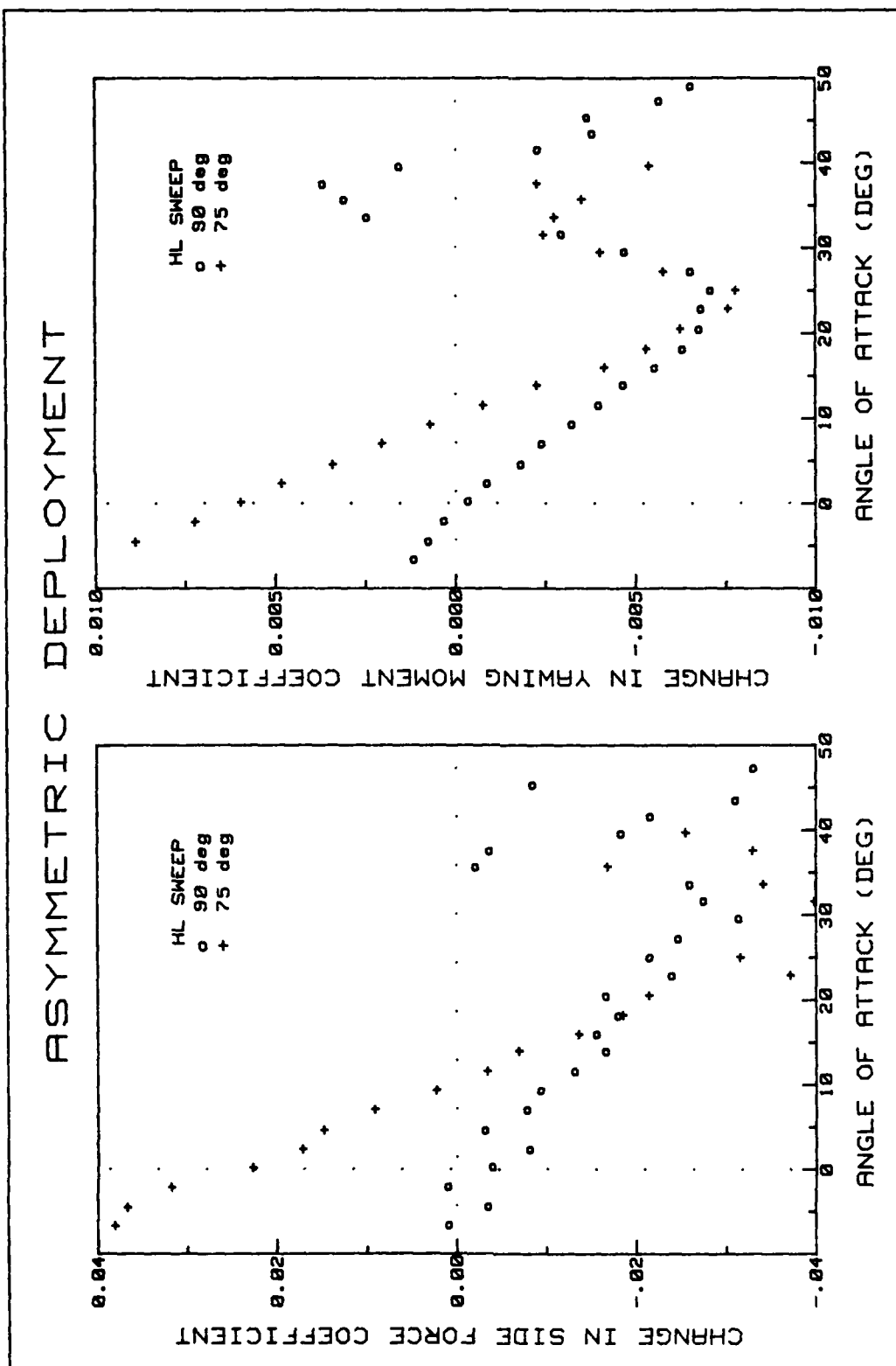


Figure 45. ΔC_y and ΔC_n for Various Sweep Angles at 60° Deflection (asymmetric)

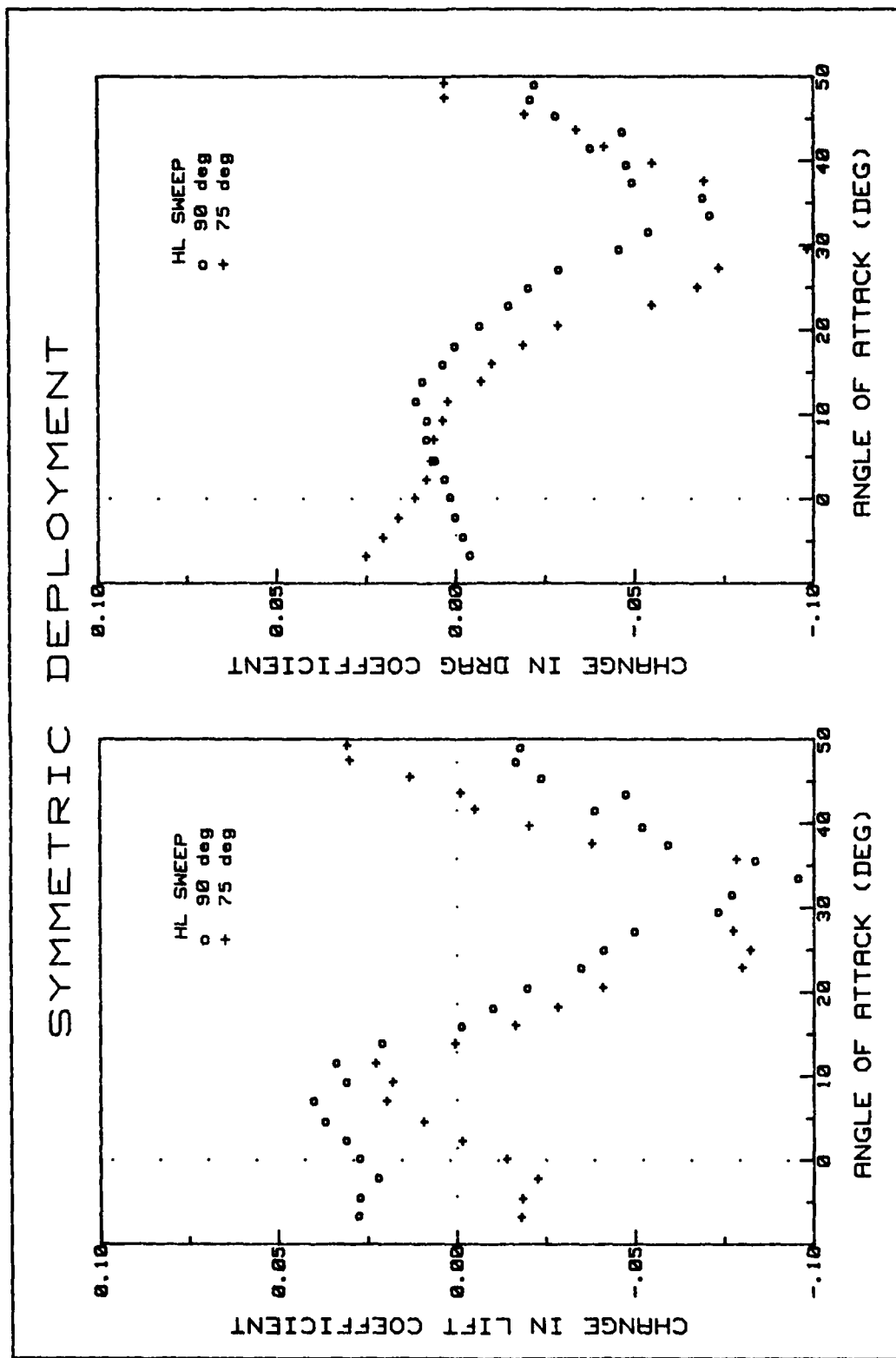


Figure 46. ΔC_L and ΔC_D for Various Sweep Angles at 45° Deflection (symmetric)

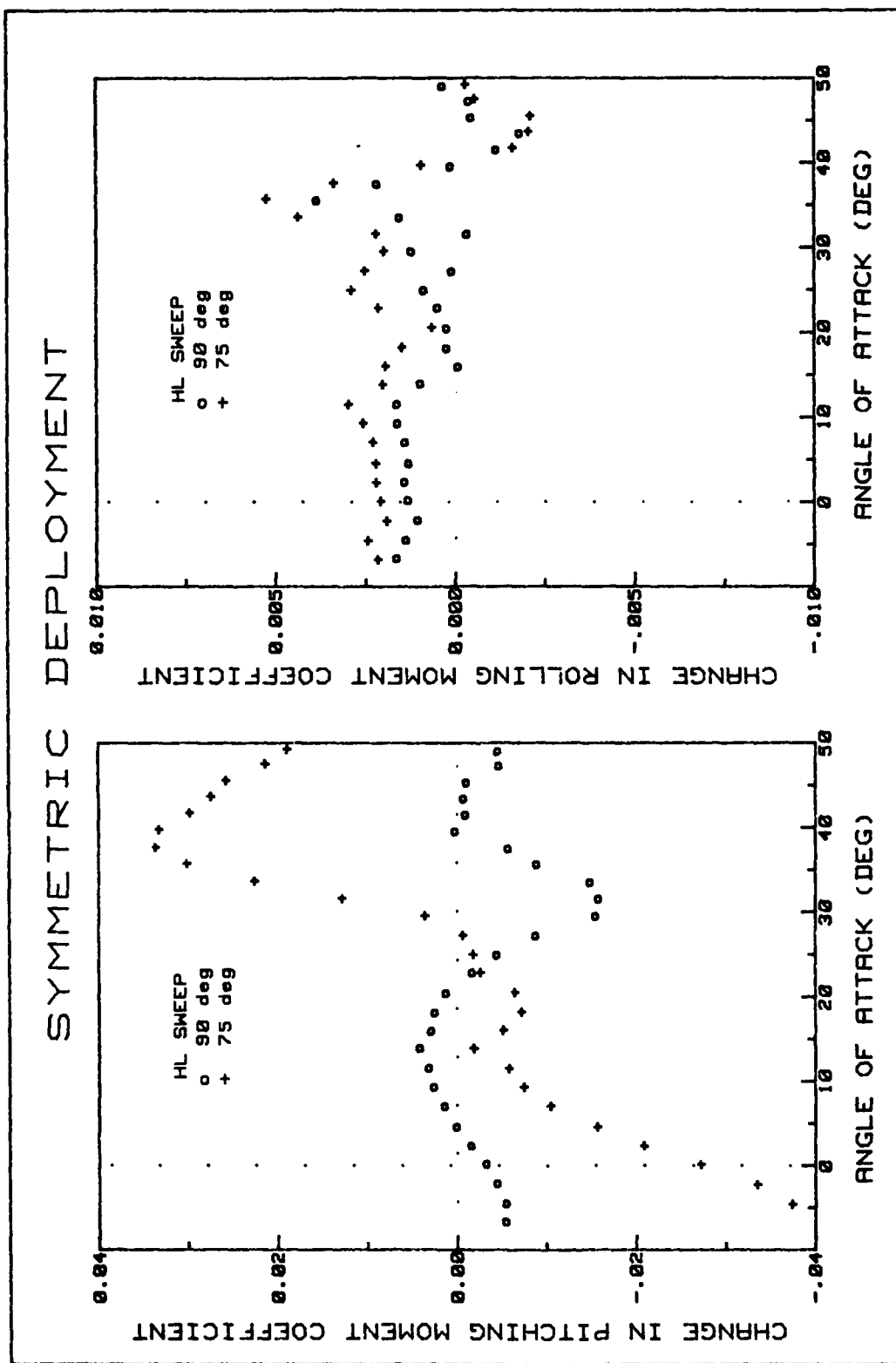


Figure 47. ΔC_m and ΔC_l for Various Sweep Angles at 45° Deflection (symmetric)

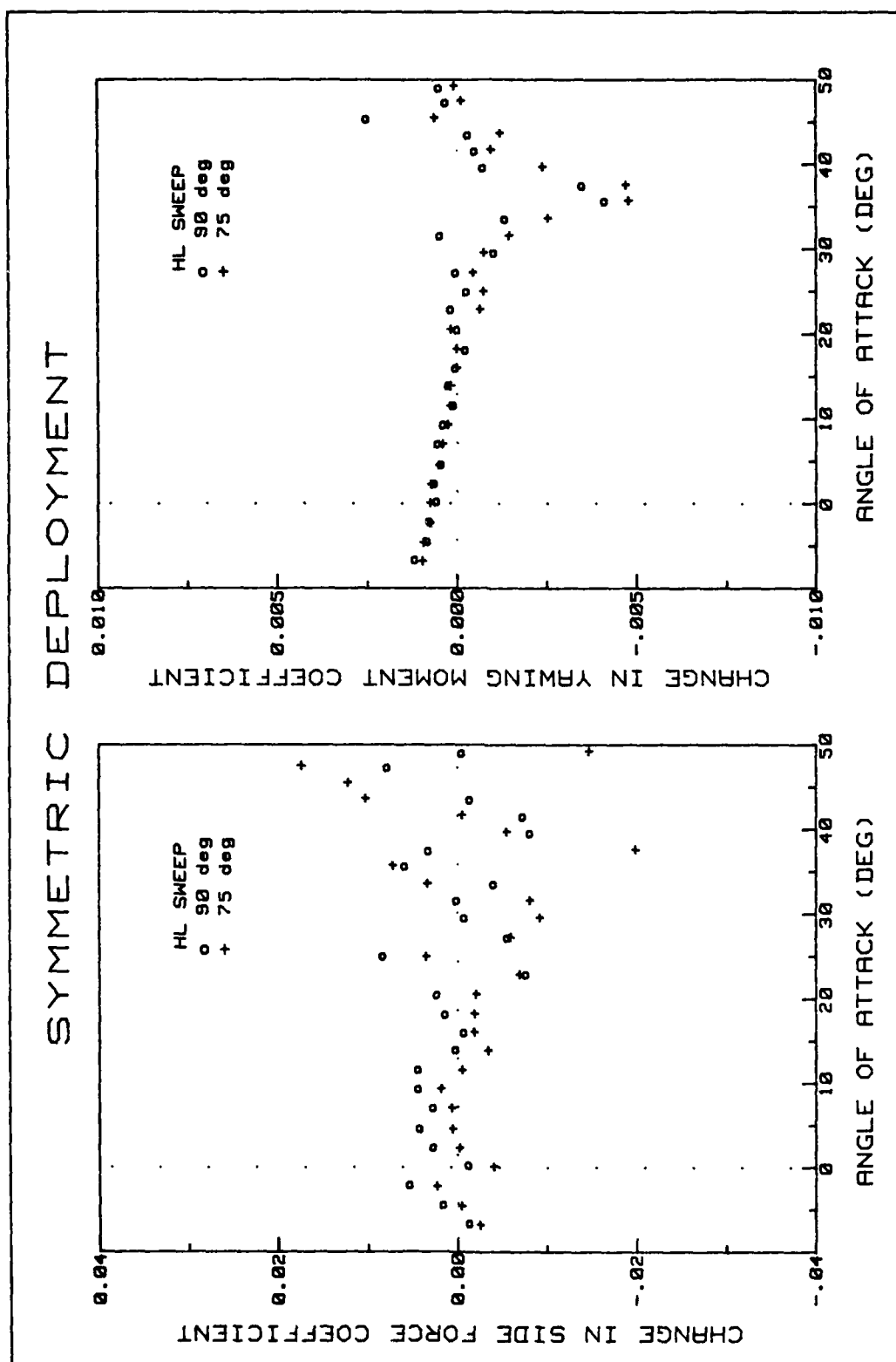


Figure 48. ΔC_Y and ΔC_n for Various Sweep Angles at 45° Deflection (symmetric)

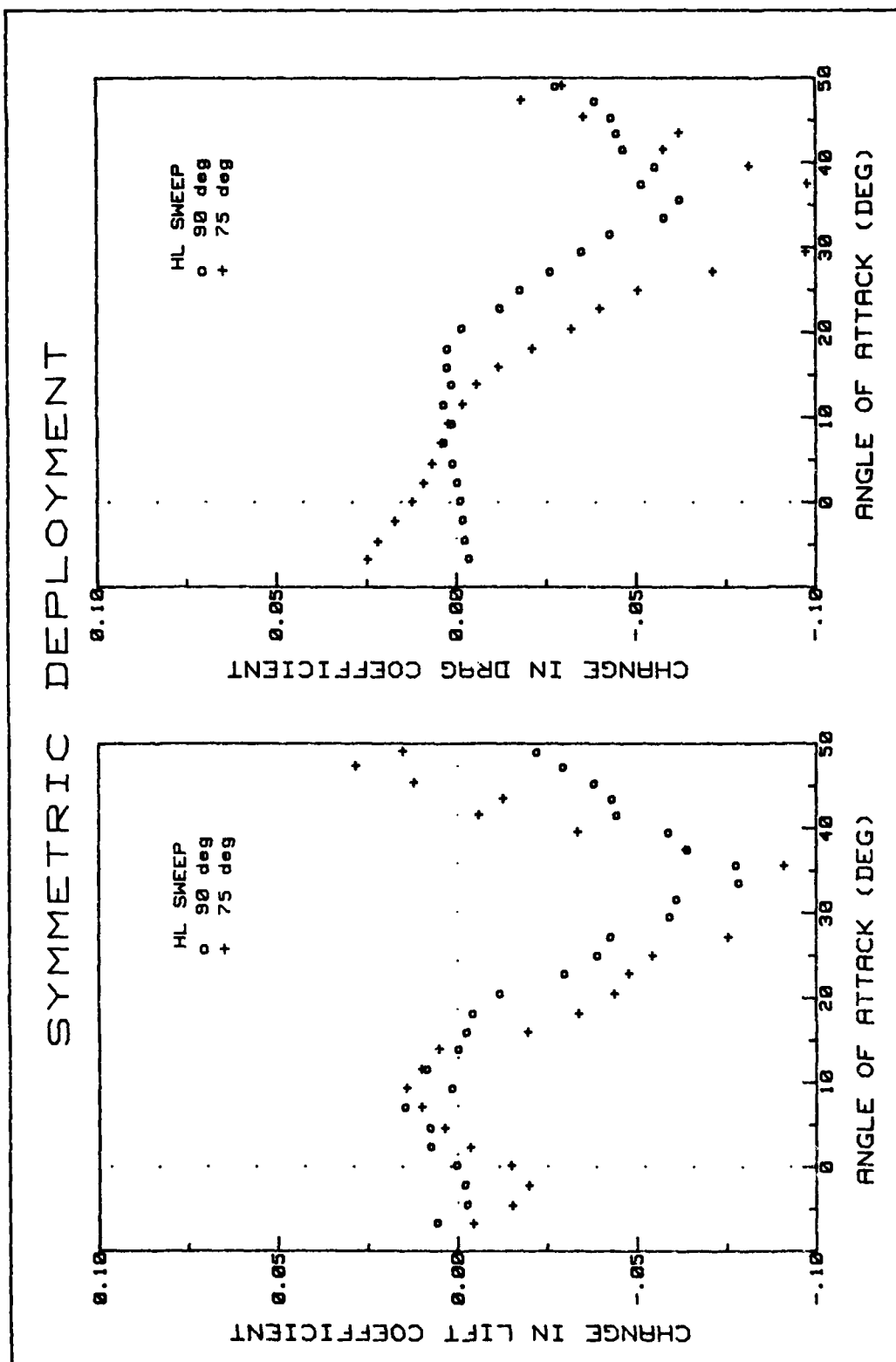


Figure 49. ΔC_L and ΔC_D for Various Sweep Angles at 60° Deflection (symmetric)

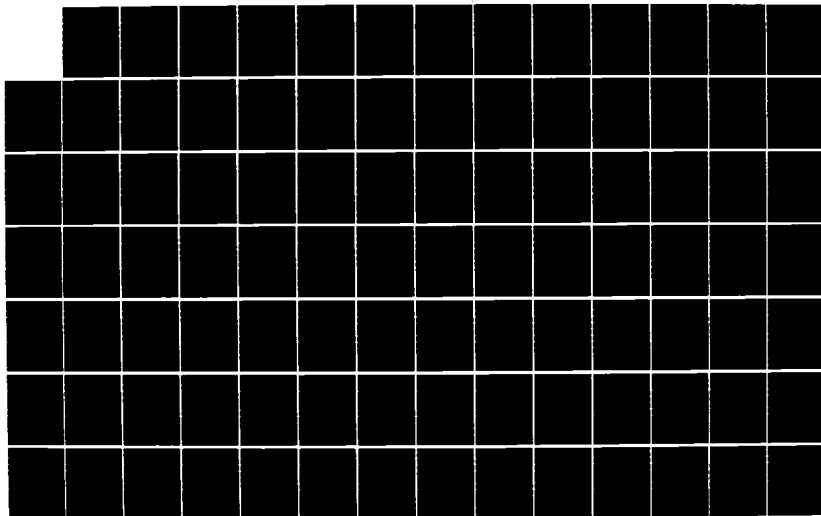
AD-A164 104

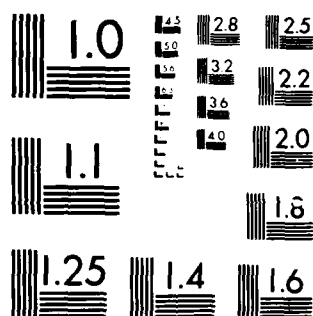
EXPERIMENTAL ASSESSMENT OF VORTEX RETAINING CAVITY
FLAPS FOR MANEUVERABIL. (U) AIR FORCE INST OF TECH
WRIGHT-PATTERSON AFB OH SCHOOL OF ENGI.. H C SMITH
DEC 85 AFIT/GAE/AA/85D-13 F/G 1/3

2/3

UNCLASSIFIED

NL





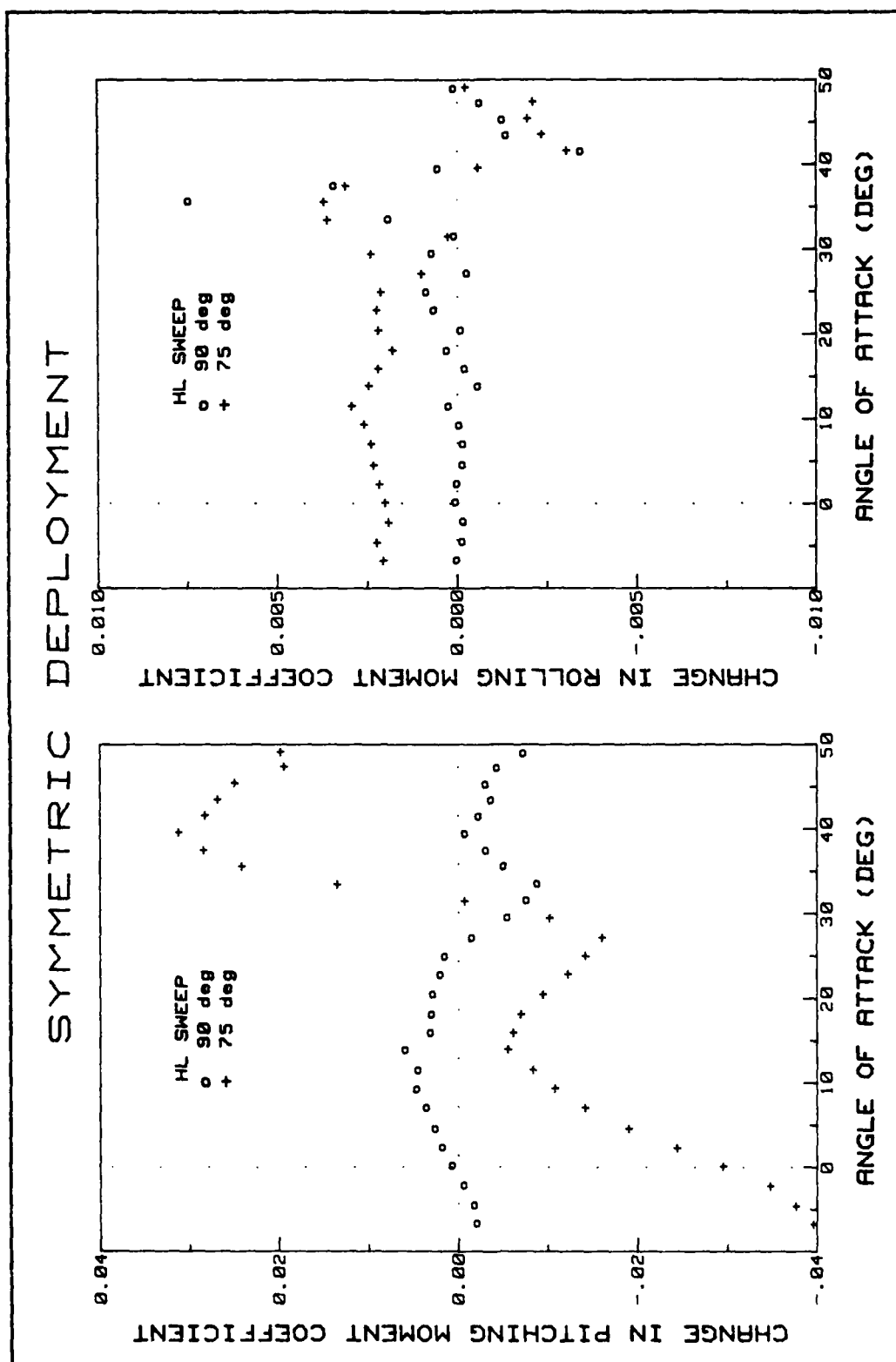


Figure 50. ΔC_m and ΔC_l for Various Sweep Angles at 60° Deflection (symmetric)

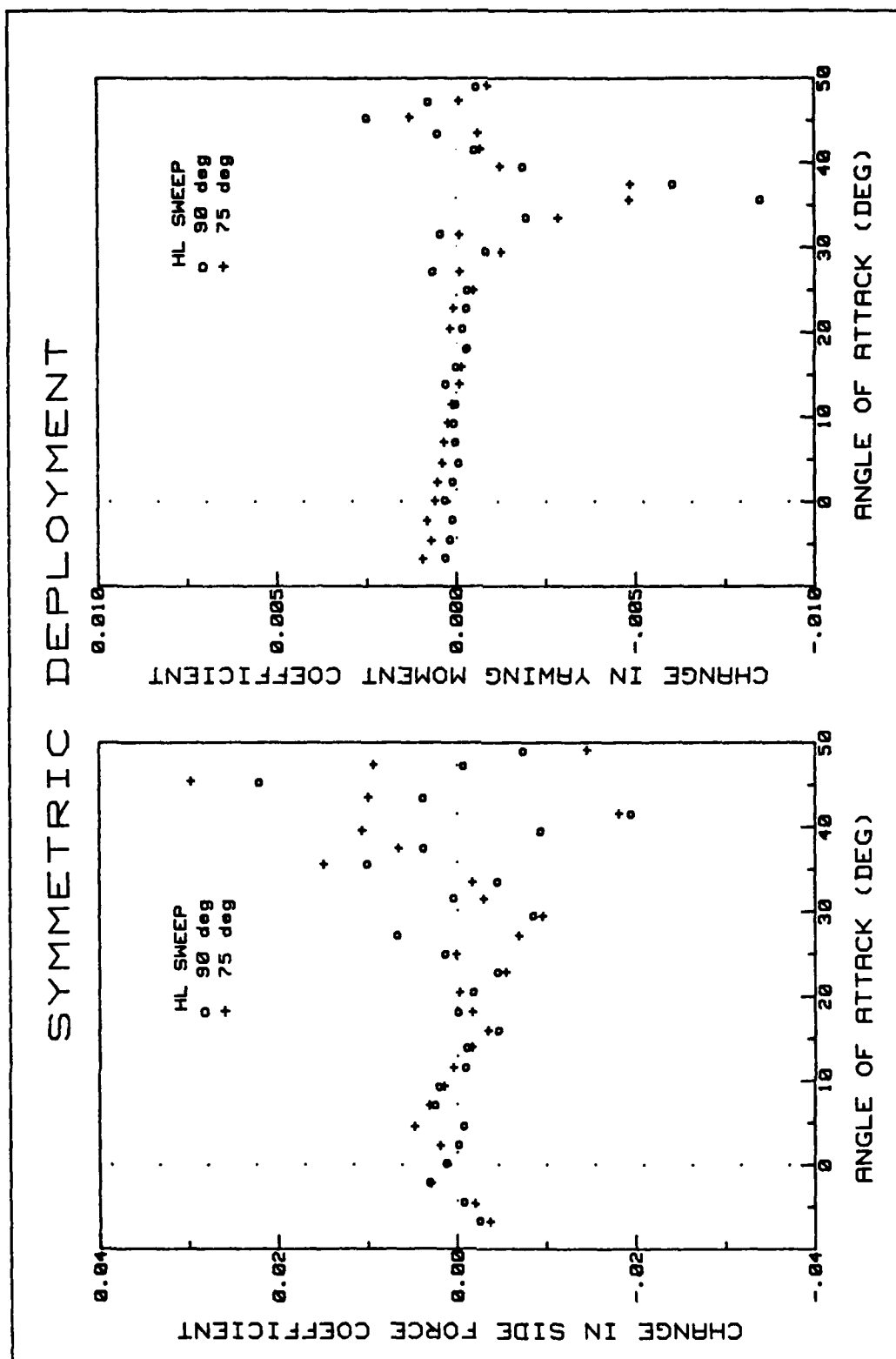


Figure 51. ΔC_Y and ΔC_n for Various Sweep Angles at 60° Deflection (symmetric)

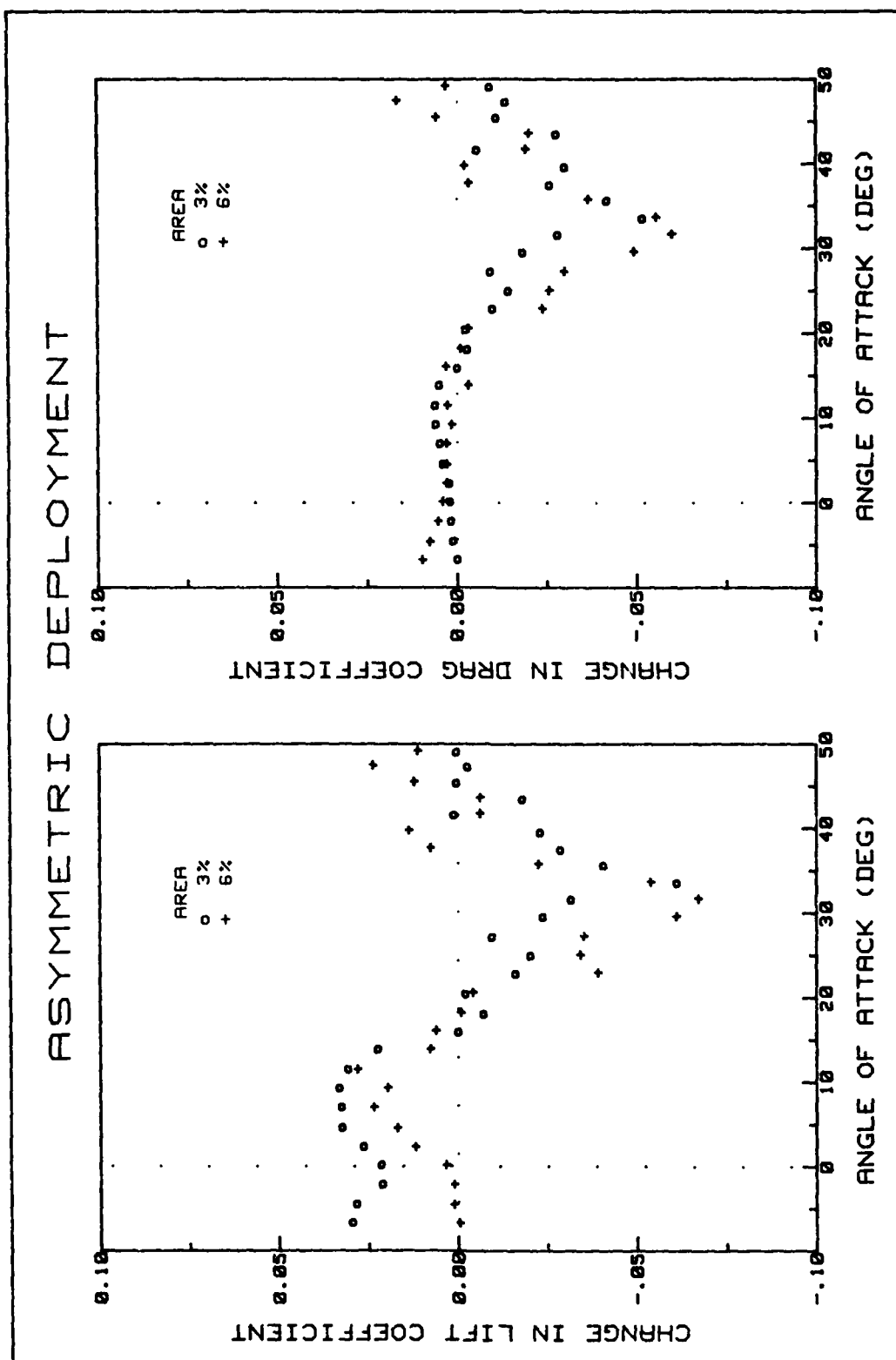


Figure 52. ΔC_L and ΔC_D for Various Flap Areas at 45° Deflection (asymmetric)

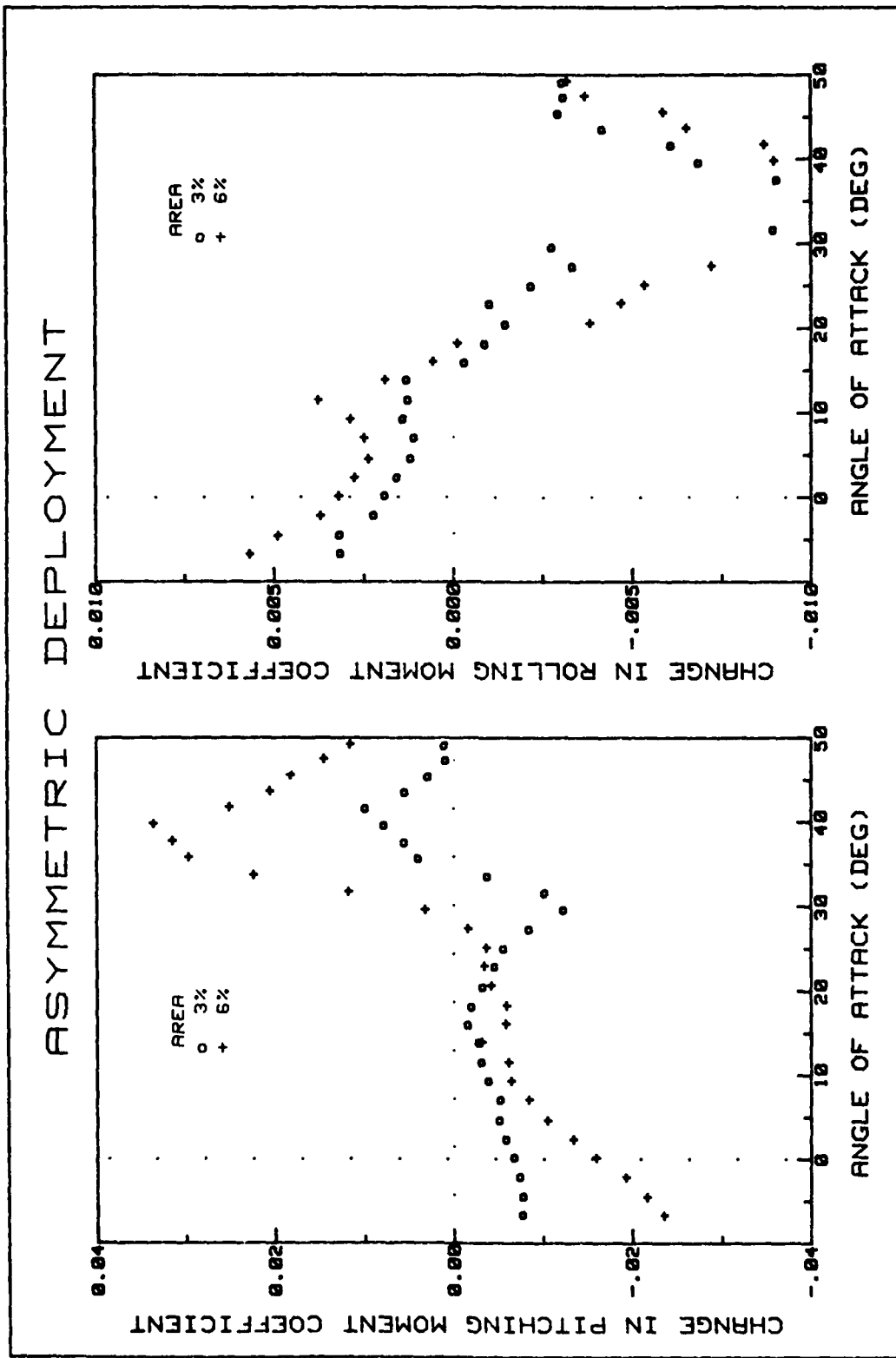


Figure 53. ΔC_m and ΔC_l for Various Flap Areas at 45° Deflection (asymmetric)

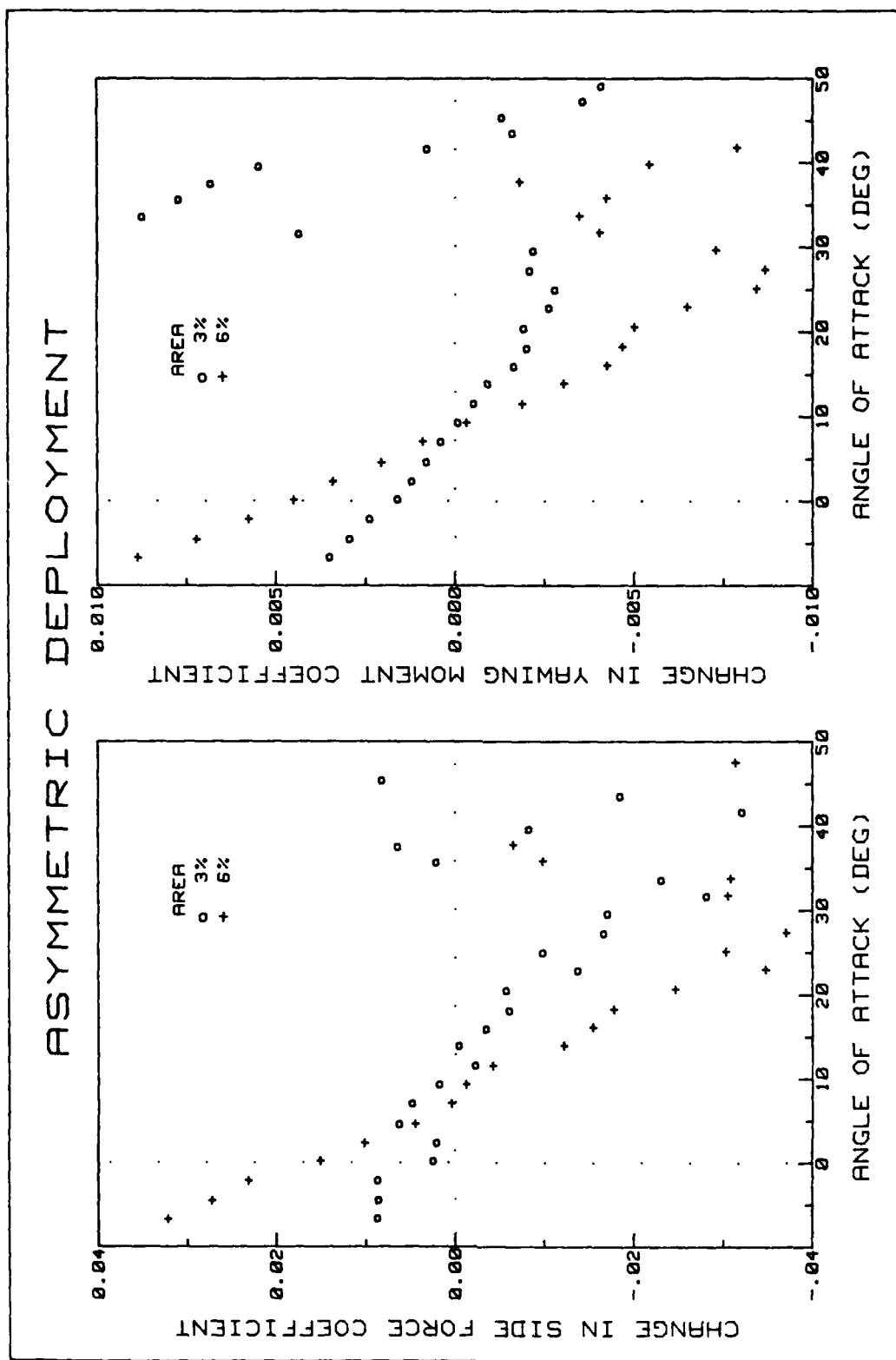


Figure 54. ΔC_y and ΔC_n for Various Flap Areas at 45° Deflection (asymmetric)

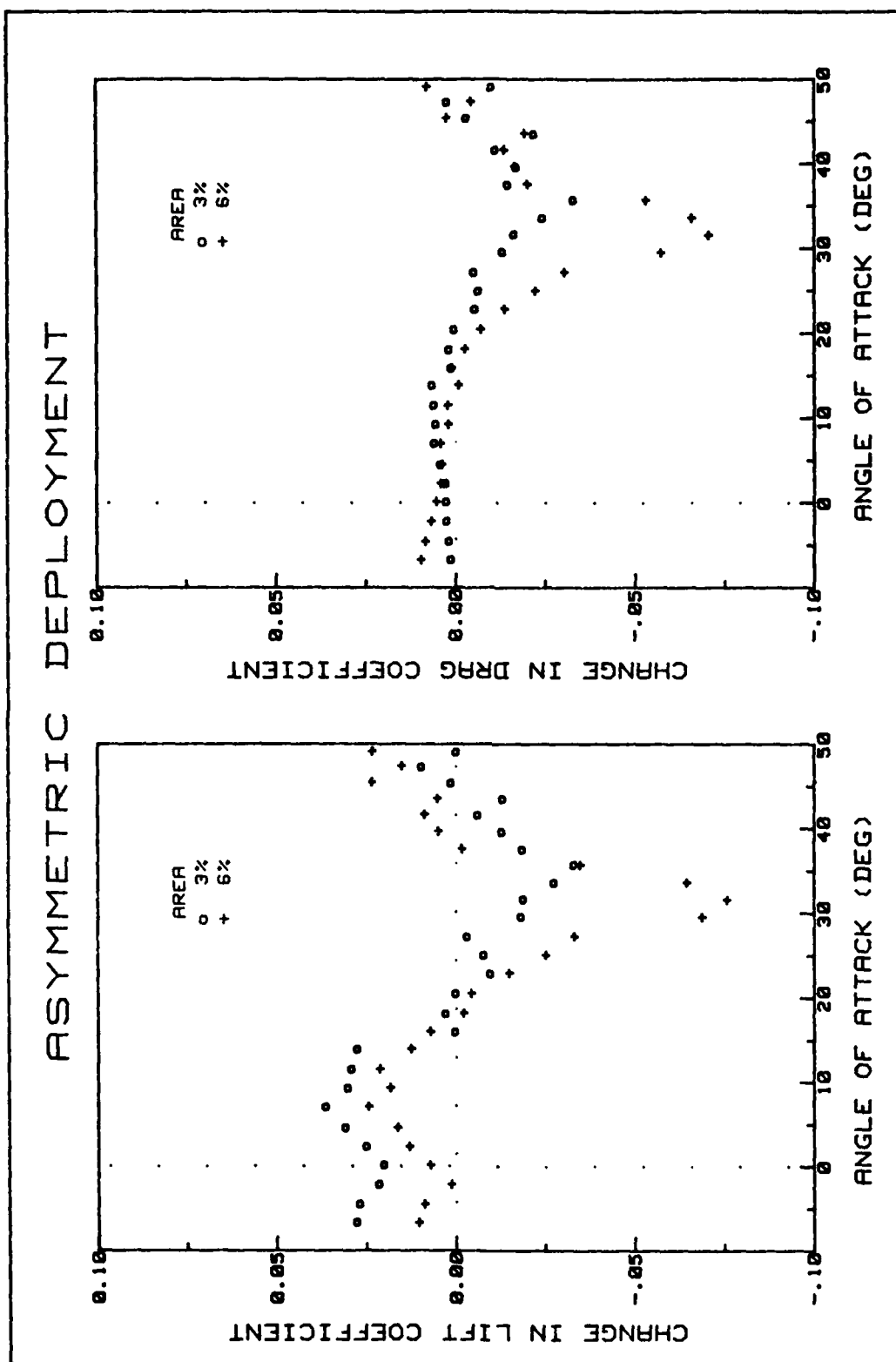


Figure 55. ΔC_L and ΔC_D for Various Flap Areas at 60° Deflection (asymmetric)

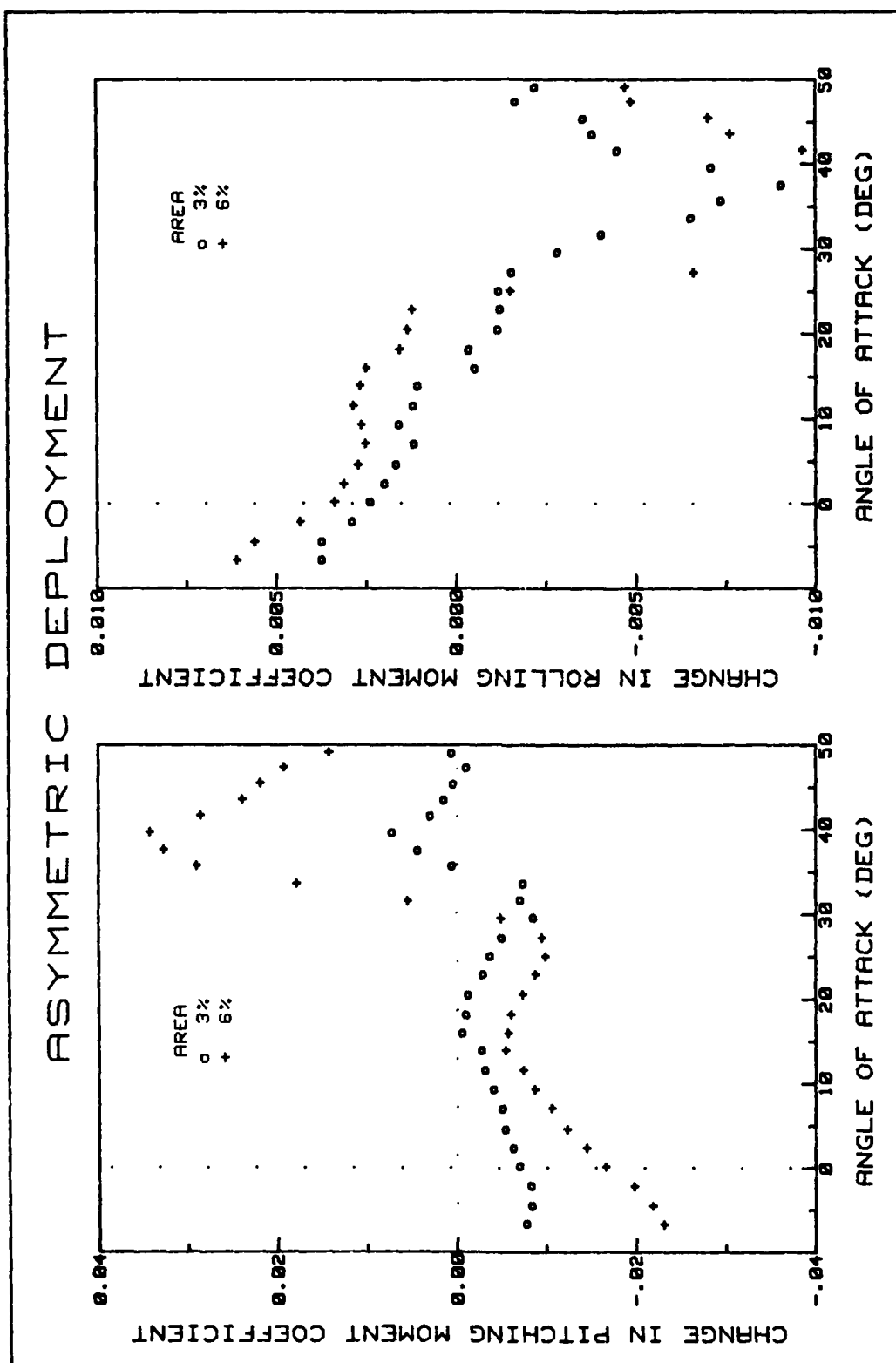


Figure 56. ΔC_m and ΔC_l for Various Flap Areas at 60° Deflection (asymmetric)

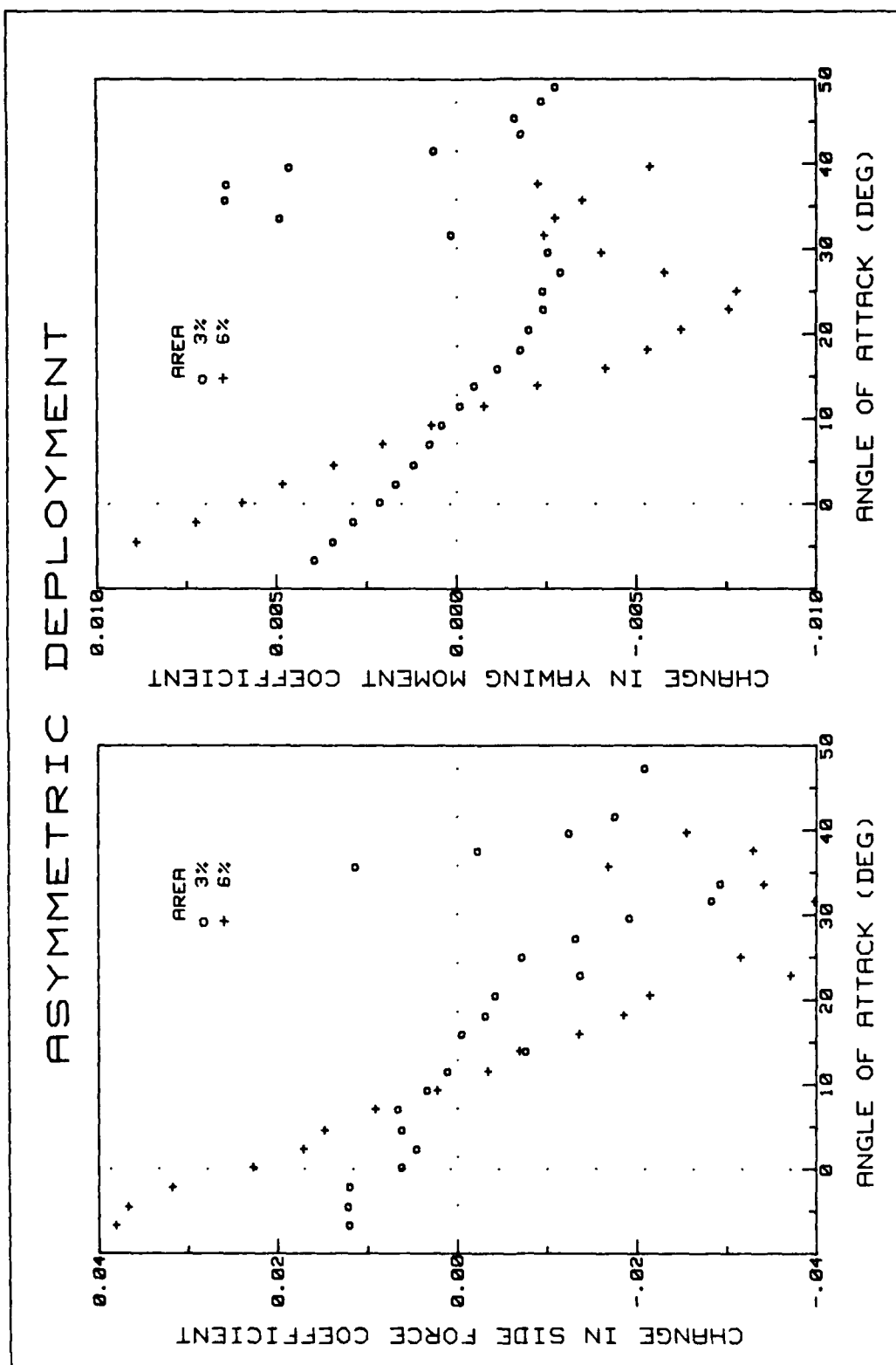


Figure 57. ΔC_Y and ΔC_n for Various Flap Areas at 60° Deflection (asymmetric)

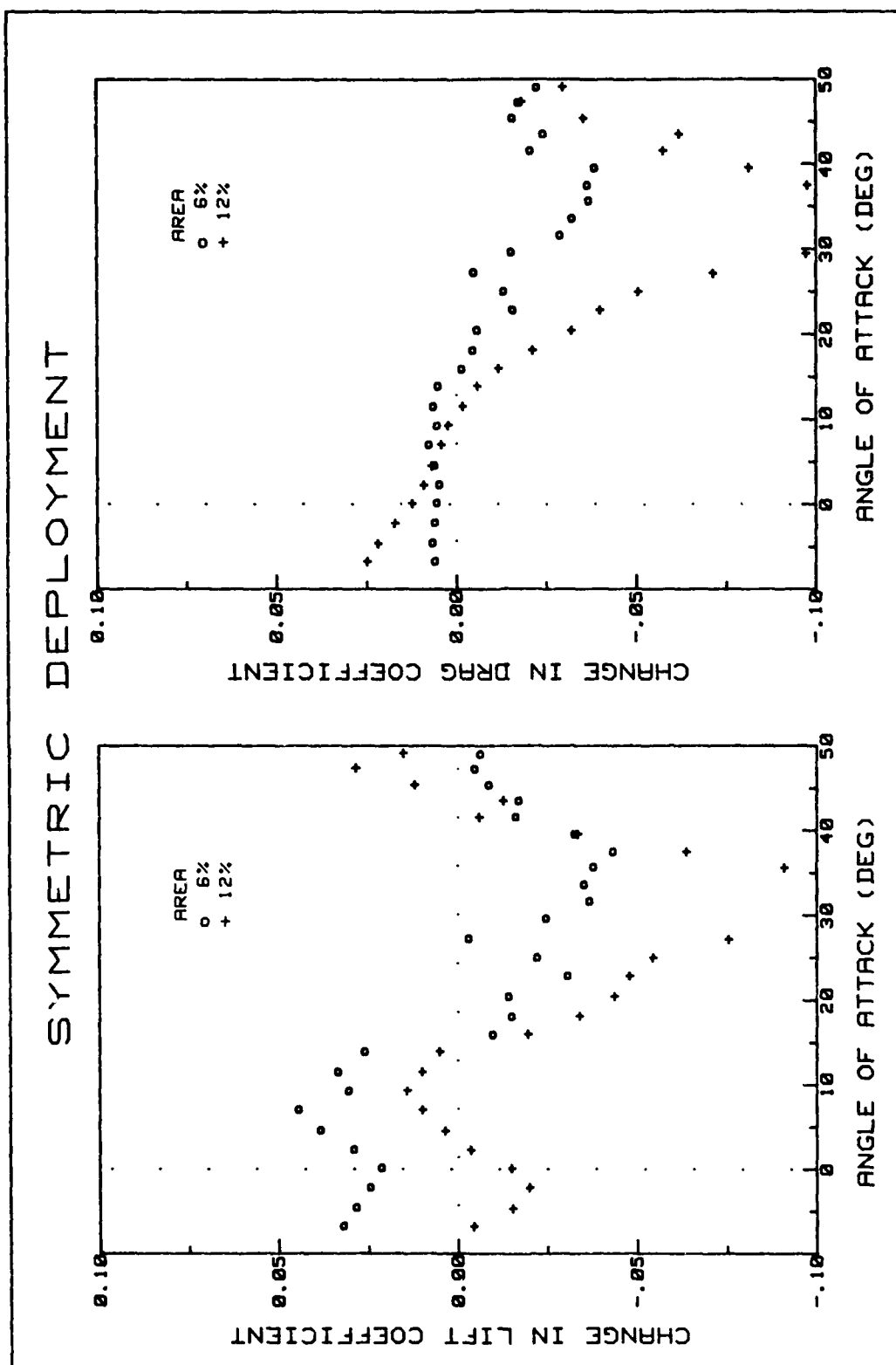


Figure 58. ΔC_L and ΔC_D for Various Flap Areas at 60° Deflection (symmetric)

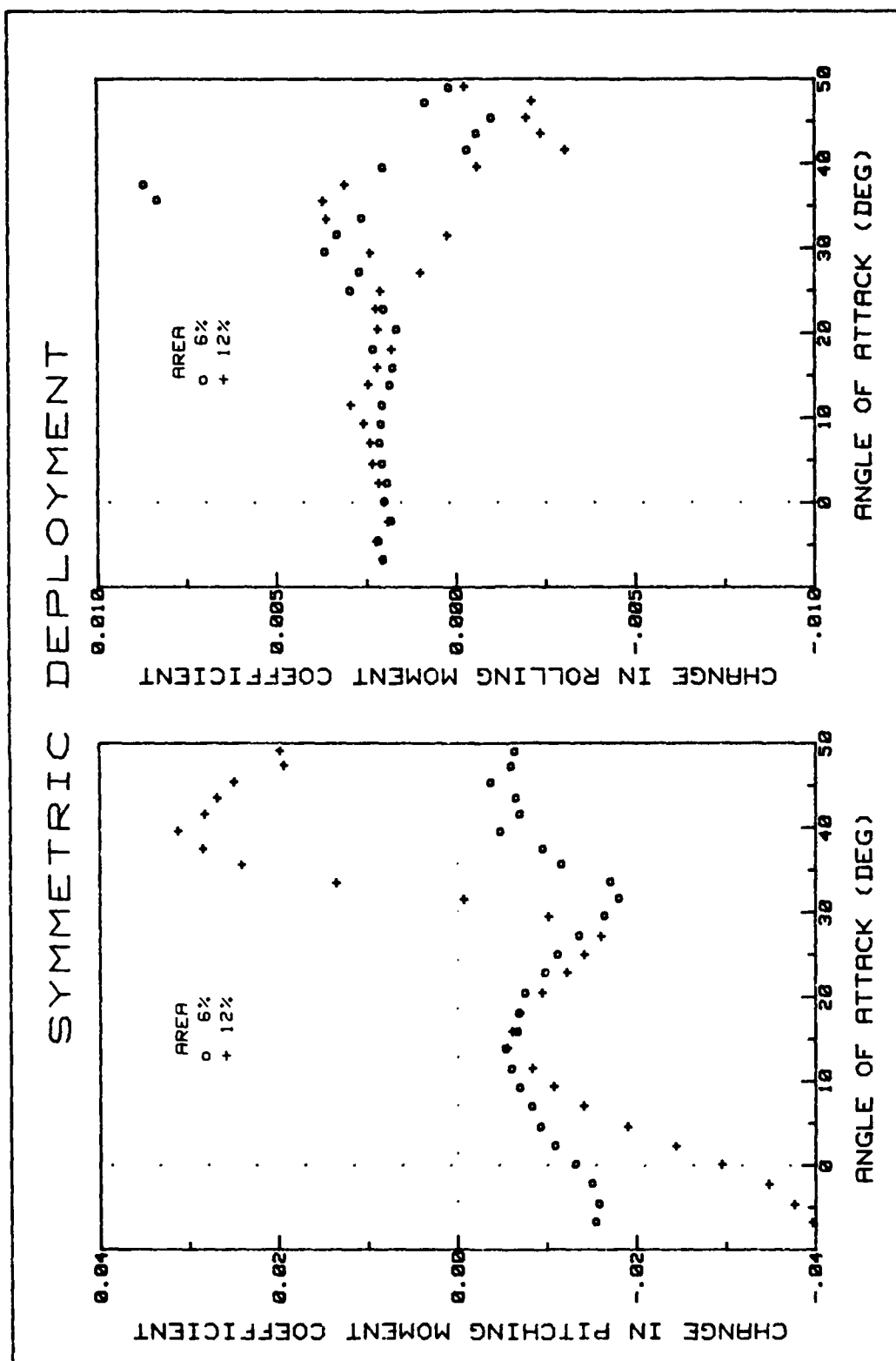


Figure 59. ΔC_m and ΔC_l for Various Flap Areas at 60° Deflection (symmetric)

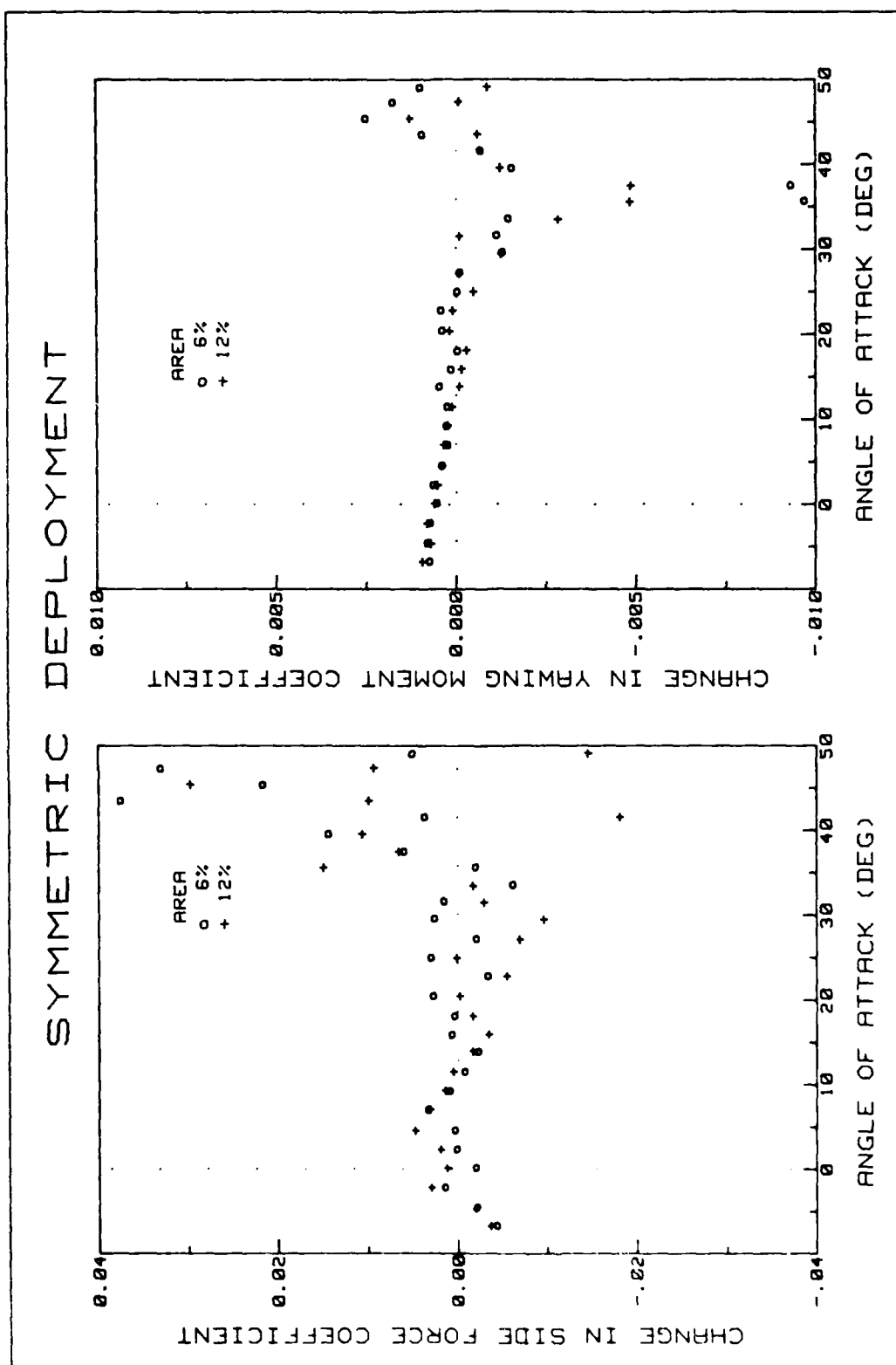


Figure 60. ΔC_Y and ΔC_n for Various Flap Areas at 60° Deflection (symmetric)

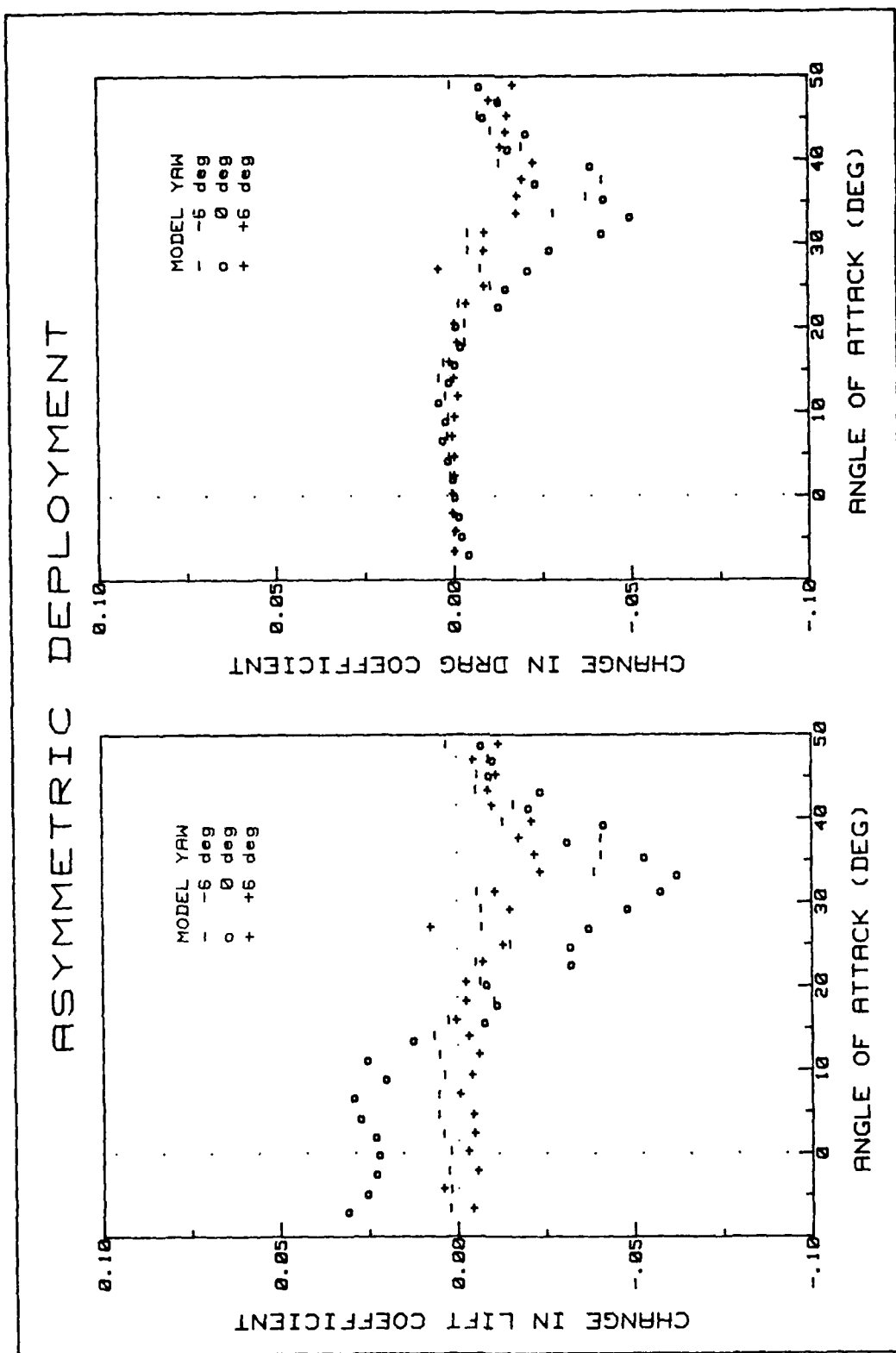


Figure 61. ΔC_L and ΔC_D for Various Yaw Angles at 60° Deflection (asymmetric)

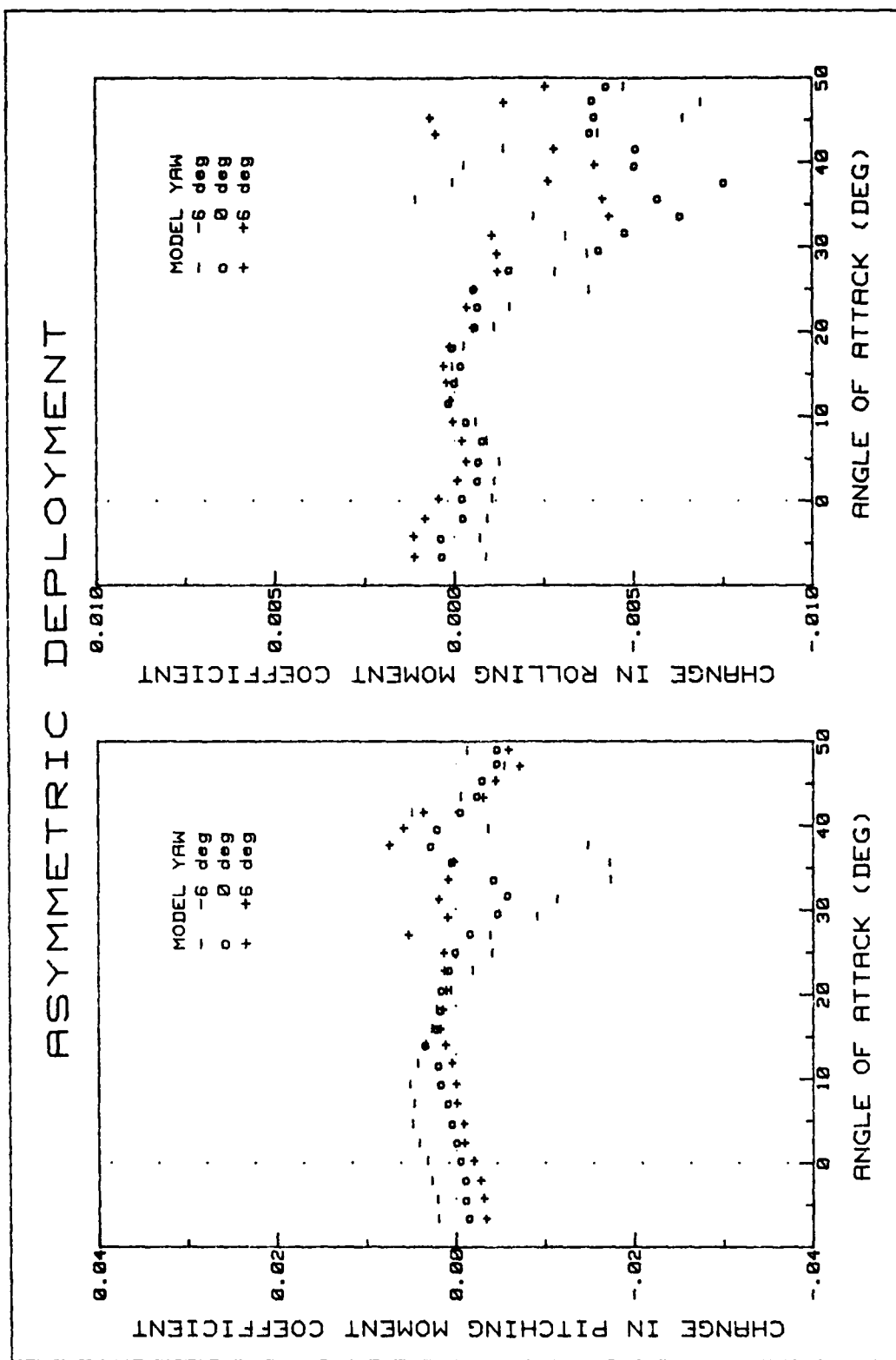


Figure 62. ΔC_m and ΔC_l for Various Yaw Angles at 60° Deflection (asymmetric)

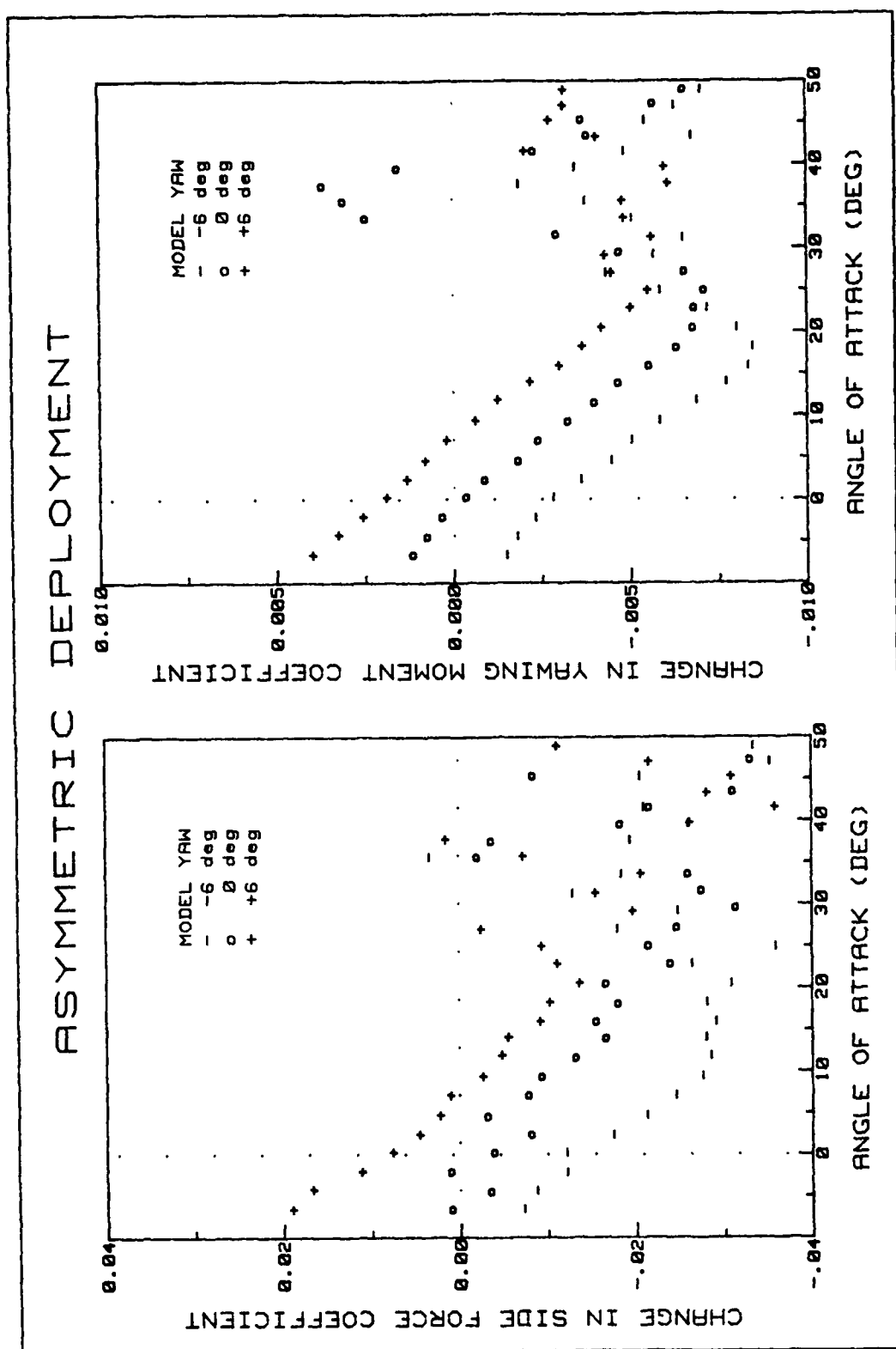


Figure 63. ΔC_Y and ΔC_n for Various Yaw Angles at 60° Deflection (asymmetric)

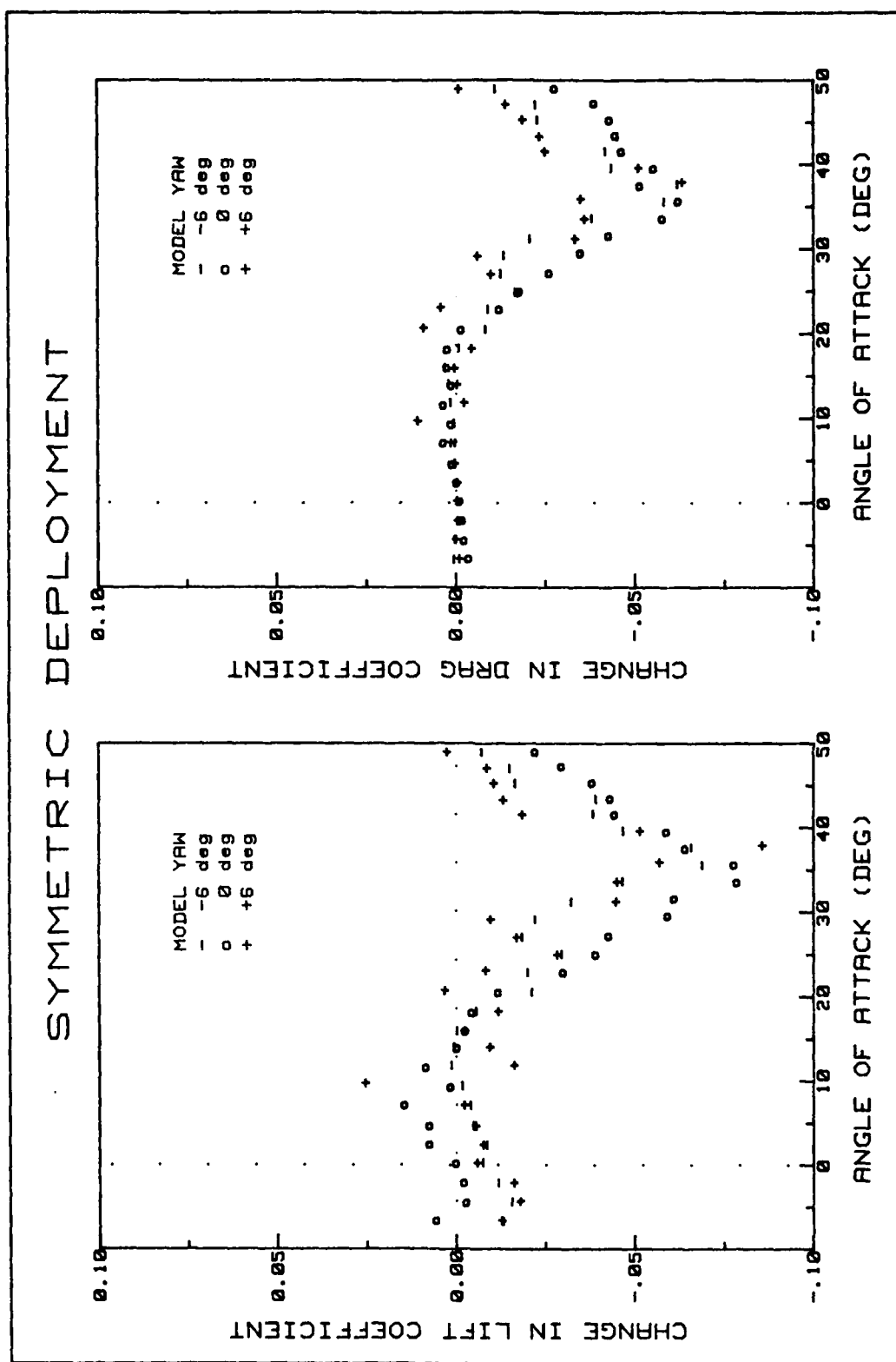


Figure 64. ΔC_L and ΔC_D for Various Yaw Angles at 60° Deflection (symmetric)

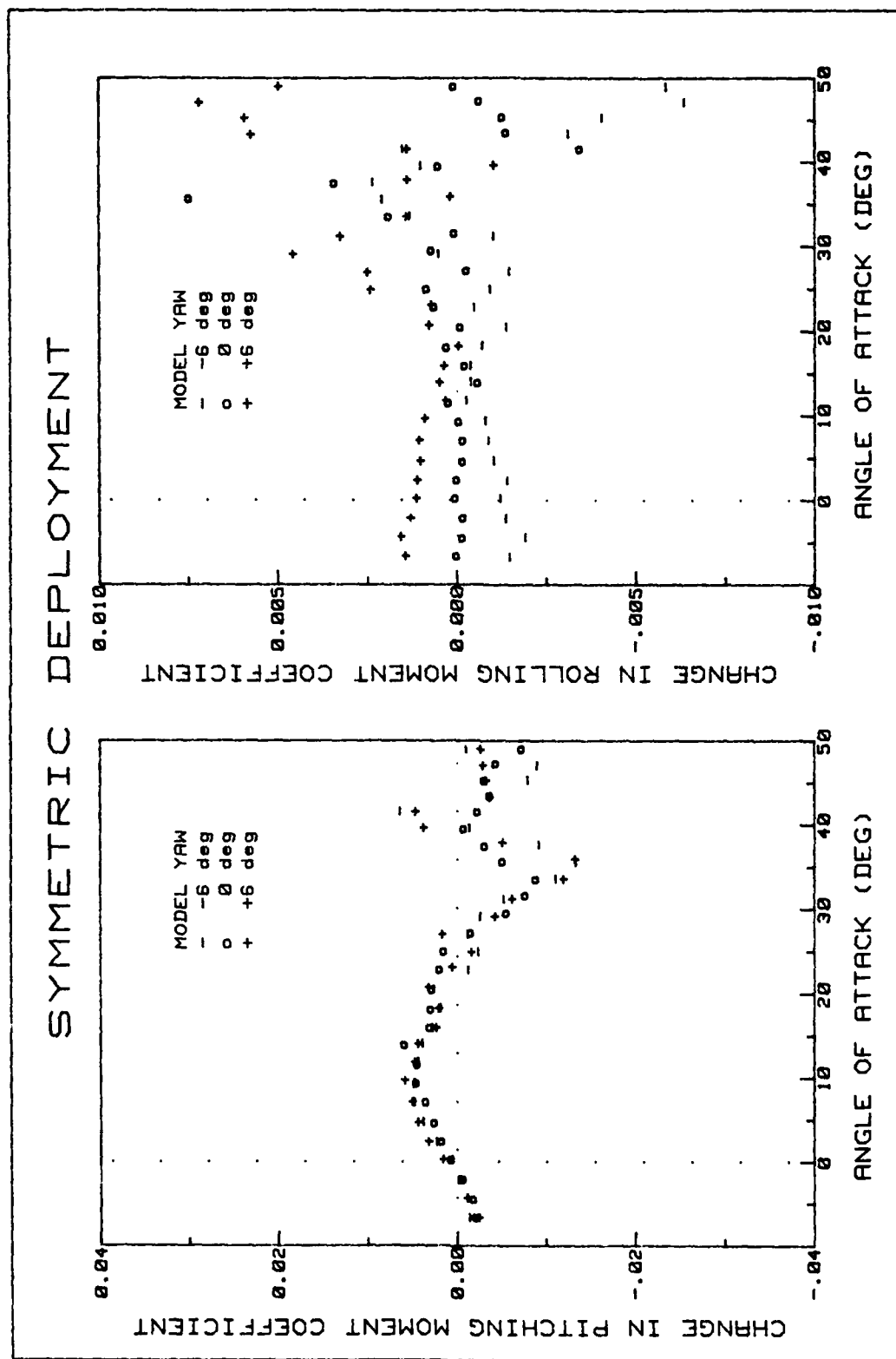


Figure 65. ΔC_m and ΔC_l for Various Yaw Angles at 60° Deflection (symmetric)

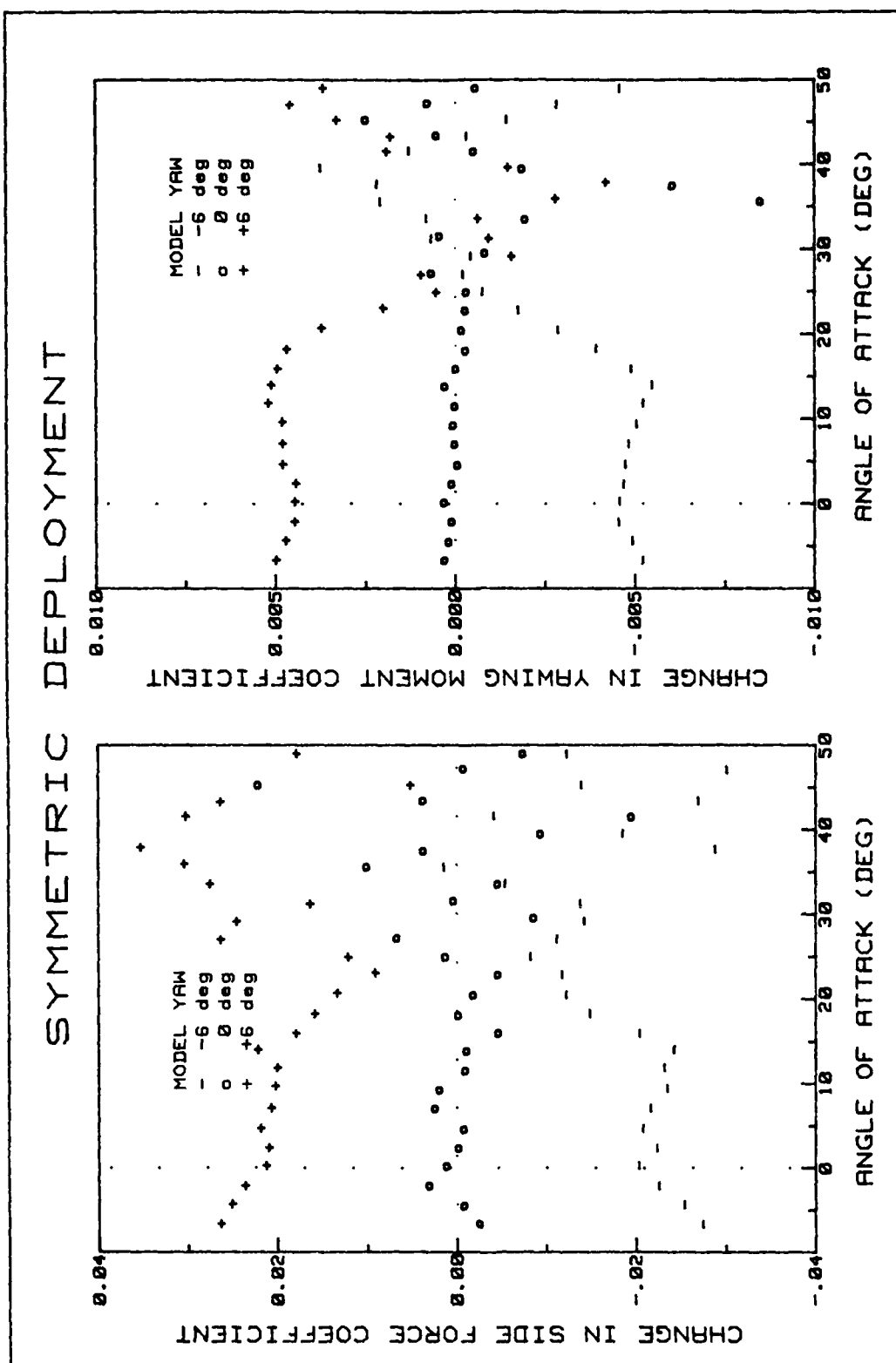


Figure 66. ΔC_Y and ΔC_n for Various Yaw Angles at 60° Deflection (symmetric)

VII. Conclusions and Recommendations

Conclusions

Based on the static test results presented in the last section, the maneuverability improvement of a delta wing fighter aircraft through the use of cavity flaps is feasible. Using both asymmetrical and symmetrical deployments, with a combination of cavity flap deflection angles, hinge line sweep angles and cavity flap surface areas, the longitudinal, lateral and directional moments of an aircraft can be modified for greater maneuverability. The amount of modification as shown in this study is very dependent on the parameters listed above.

Of the configurations tested, the maximum ΔC_m was 0.04 and occurred with a hinge line sweep angle of 75°, a cavity deflection angle of 45°, and a cavity flap surface area that was 12% of the total wing area. This change was with symmetrical deployment of the cavity flaps. The maximum ΔC_l was 0.01 from an asymmetrical cavity flap deployment. The hinge line sweep angle was 75°, a cavity flap deflection angle of 45°, and a cavity flap surface area that was 6% of the total wing area. The maximum ΔC_n of 0.007 also occurred with an asymmetrical cavity flap deployment. The hinge line sweep angle was 90°, a cavity flap deflection angle of 60°, and a cavity flap surface area equal to 6% of the total wing

area. The maximum decrease in C_D was 0.1 and occurred with symmetrical deployment of cavity flaps. Again, the hinge line sweep angle was 75° , and the angle of deflection was 60° . The cavity flap surface area was 12% of the total wing area.

These maximum changes seem to constitute a trend that can be used as a guideline in future cavity flap usage. Typical cavity flap deflection angles should be in the range of 45° to 60° . This creates a cavity that is large enough to develop and retain a vortex, yet small enough to prevent excessive stall on the cavity flap surface. The hinge line should not be along or parallel to the fuselage (except for yawing moment considerations) for maximum pitching and rolling moment changes. It is hard to say what the best hinge line sweep angle should be since only two angles, 75° and 90° , could be readily compared in this study with other parameters held constant. The cavity flap surface area should be as large as feasibly possible. To maximize the area and still have the cavity flap conformal to the lower wing surface, the entire area from fuselage to leading edge in the apex region should be used. This would require some type of mechanism that could pivot the cavity flap hinge line outward from the fuselage to give the flap a hinge line sweep angle less than 90° .

It seems that the future holds a promise for the cavity flap concept. Of course, a lot more experimental work must be accomplished before the concept can become a reality.

This study has shown that the cavity flap is a viable way to control and enhance the maneuverability of future delta wing fighter aircraft.

Recommendations

This study was a basic look at the cavity flap concept and its influence on the maneuverability of delta wing aircraft. It seems that very little experimental work has been done in this area, therefore, this investigation here had only a few guidelines available to work from. This would imply that there are a lot of questions left unanswered. And indeed, there are. One item left undetermined was the best cavity flap hinge line sweep angle for maneuverability enhancement. This could best be answered with more experimental work concentrating on sweep angles.

The experimental work accomplished here focused on such parameters as deflection angle, sweep angle, and area. A few scattered test runs were conducted that looked at placement of cavity flaps relative to the wing. A more extensive study should address this parameter. Another thing to look at would be the shape of the cavity flaps themselves. Optimizing the shapes of cavity flaps for maximum maneuverability with minimal loss in lift should prove worthy of investigation.

Appendix A

Test Data Plots

This appendix contains plots for the data collected during this study. As mentioned in section IV, "Procedures and Analysis", the full α sweep for each cavity flap configuration was actually accomplished in two separate data runs. The low α sweep ranged from -6° to 26° , while the high α sweep ranged from 14° to 46° . The latter was conducted with a $+20^\circ$ prebend of the sting. This overlapping of α 's in the two data runs allowed for checking the influence of the sting's prebend on the data collected in the test section. The actual α 's ranged from -6° to 49° because of sting deflections and is evident in the data plots.

The plots presented here show continuous data points over the full α sweep without any overlapping. The overlapping points were not plotted so trends in the data could be readily distinguished. The first 10 data points, α 's from -6° to 14° , were taken from the low α sweep, while the remaining 17 data points, α 's from 16° to 49° , were taken from the high α sweep.

Figures A1 through A6 contain plots of the data taken for the model baseline before cavity flap configurations were added. The plots in figures A1 and A2 are for 0° of yaw, the plots in figures A3 and A4 are for $+6^\circ$ of yaw, and

the plots in figures A5 and A6 are for -6° of yaw.

The remaining figures, A7 through A108, can be grouped into sets of three to review the data for each cavity flap configuration. Each figure title identifies the data by a specific cavity flap configuration and its type of deployment. All figures are for 0° of yaw unless otherwise noted. All asymmetric deployments were done from the left wing for consistency. The first two figures consist of four plots each while the third figure consists of six plots. Plots in the first figure are C_L versus α , C_D versus α , C_D versus C_L (the drag polar), and L/D versus C_L . Plots in the second figure are C_v versus α , C_i versus α , C_m versus α , and C_n versus α . The force and moment data in the first two figures were compared against the respective model baseline data (Figures A1-A6). These differences are plotted in the third figure of each set and consist of the change in C_L versus α , the change in C_D versus α , the change in C_v versus α , the change in C_i versus α , the change in C_m versus α , and the change in C_n versus α .

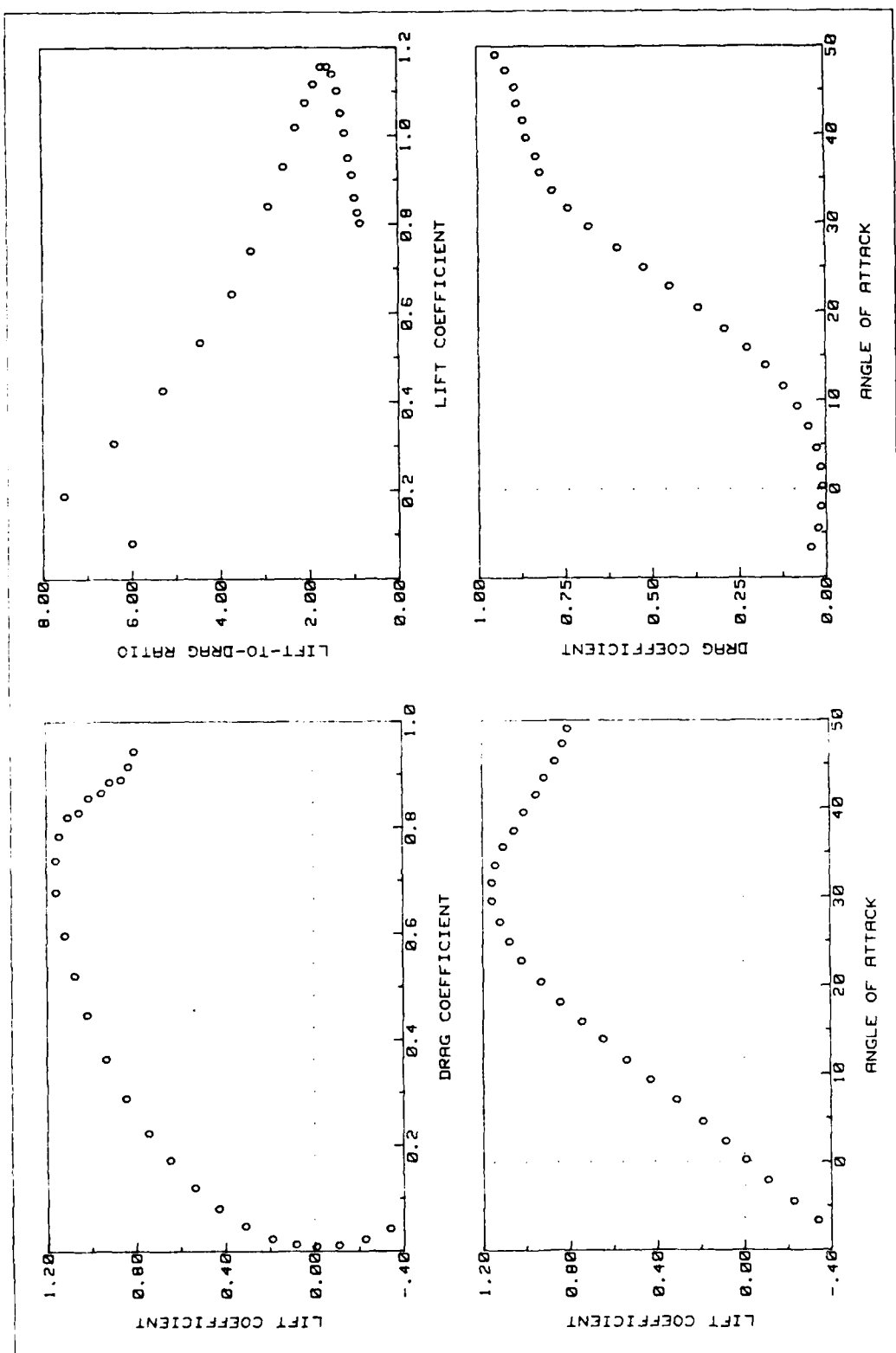


Fig A1. Model Baseline Lift and Drag Data (no cavity flaps)

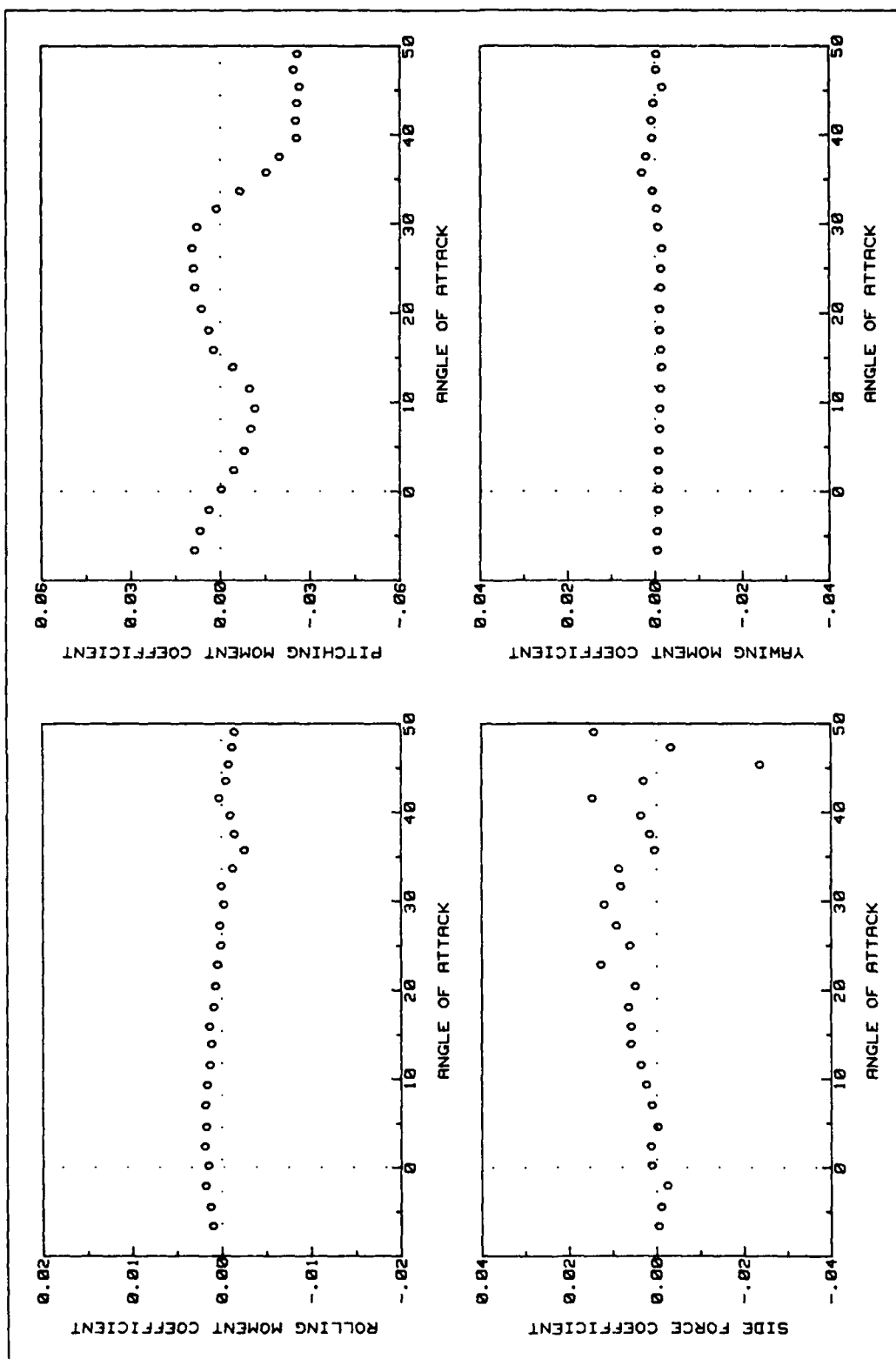


Fig A2. Model 1 Baseline Side Force and Moments Data (no cavity flaps)

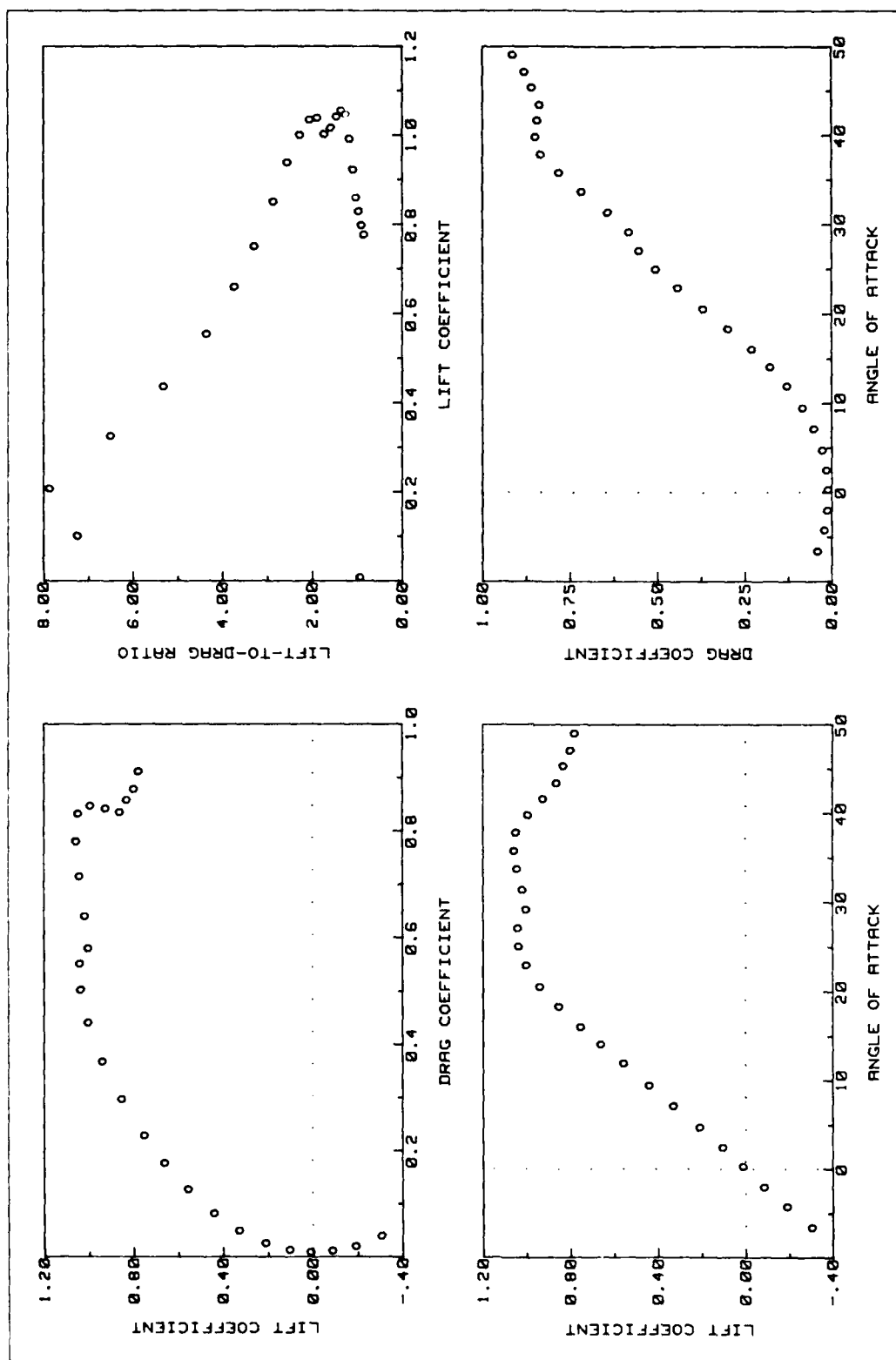


Fig A3. Model Baseline Lift and Drag Data (+6 deg yaw)

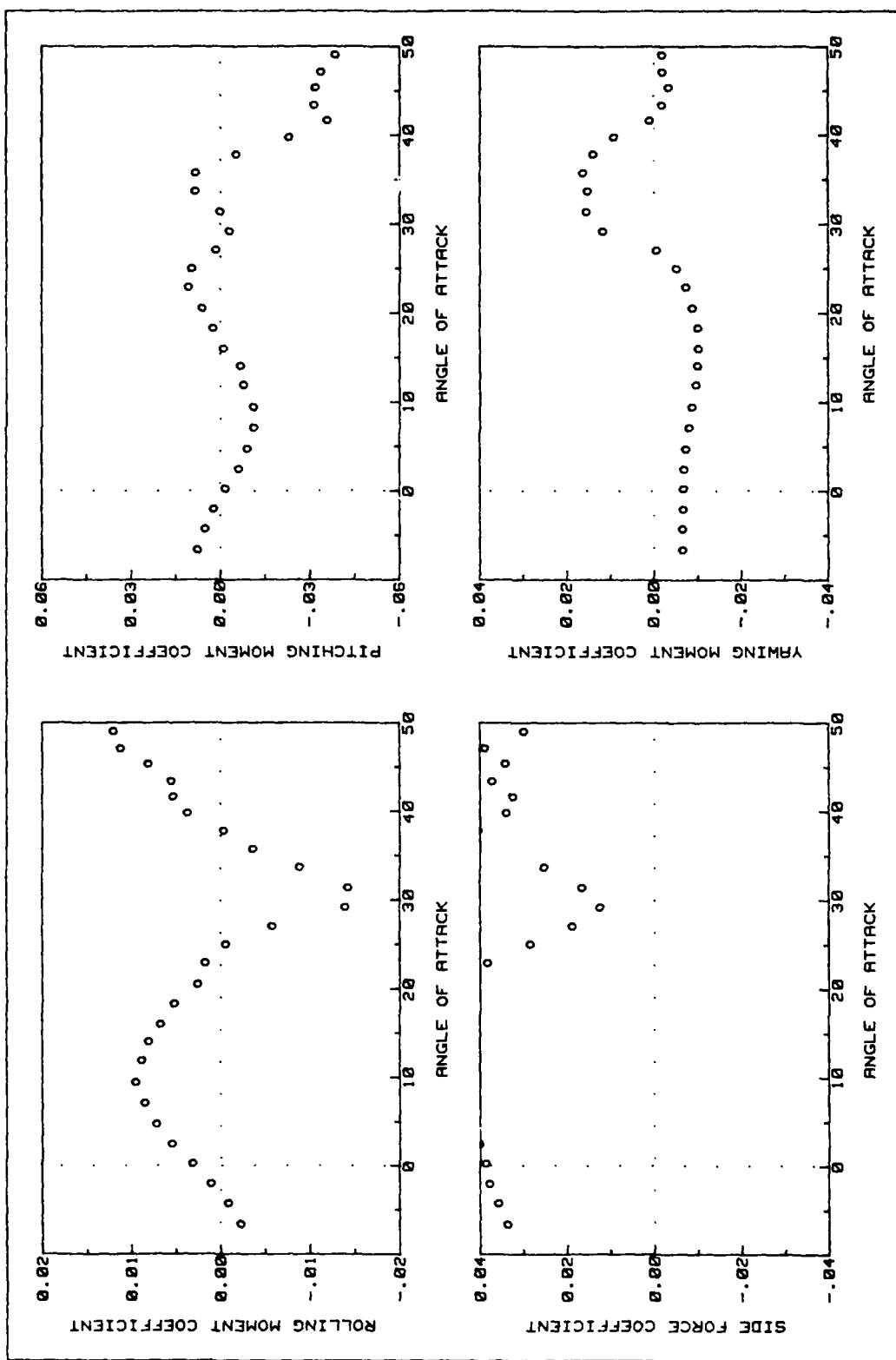


Fig A4. Model Baseline Side Force and Moments Data (+6 deg yaw)

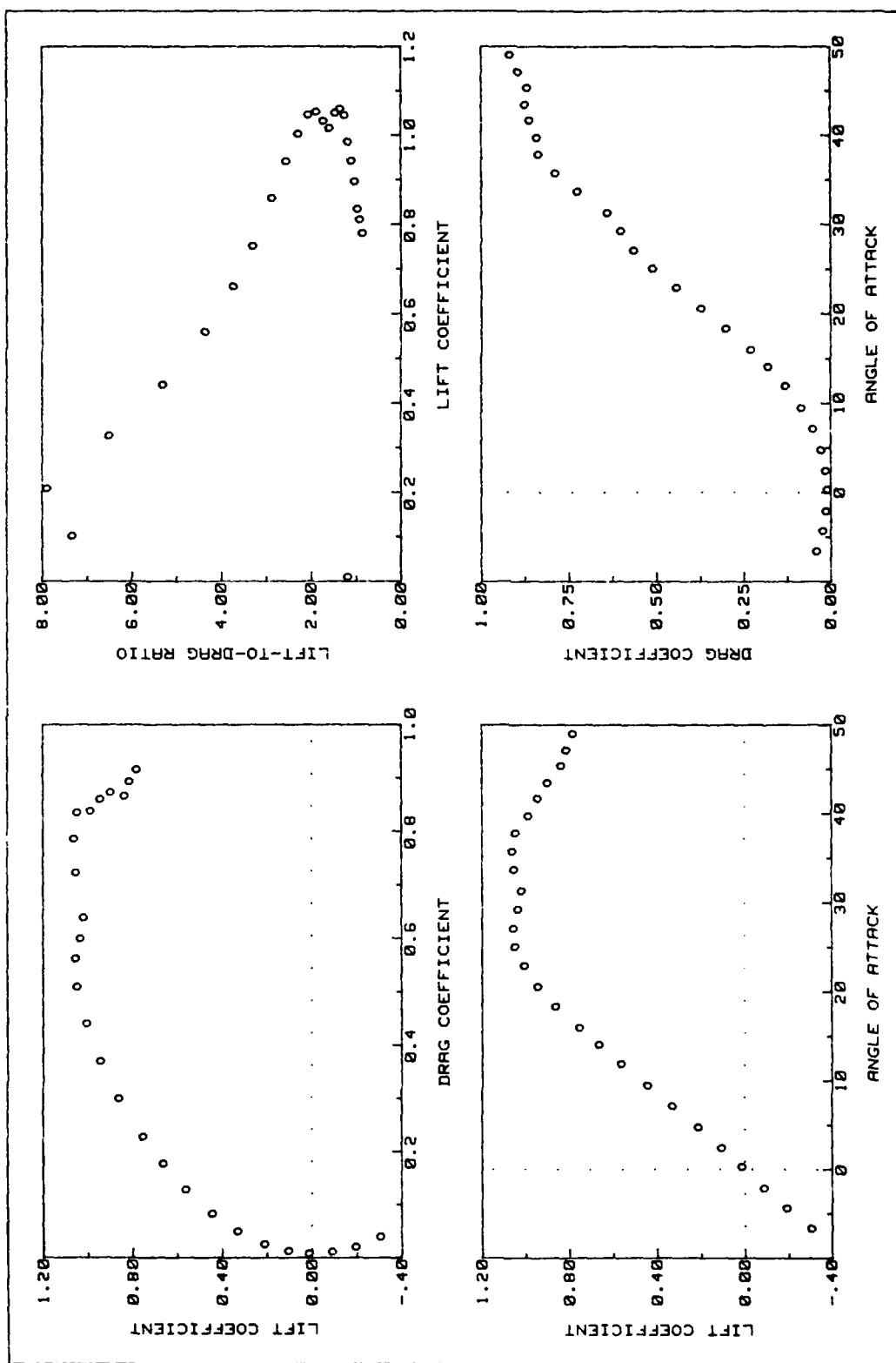


Fig A5. Model Baseline Lift and Drag Data (-6 deg yaw)

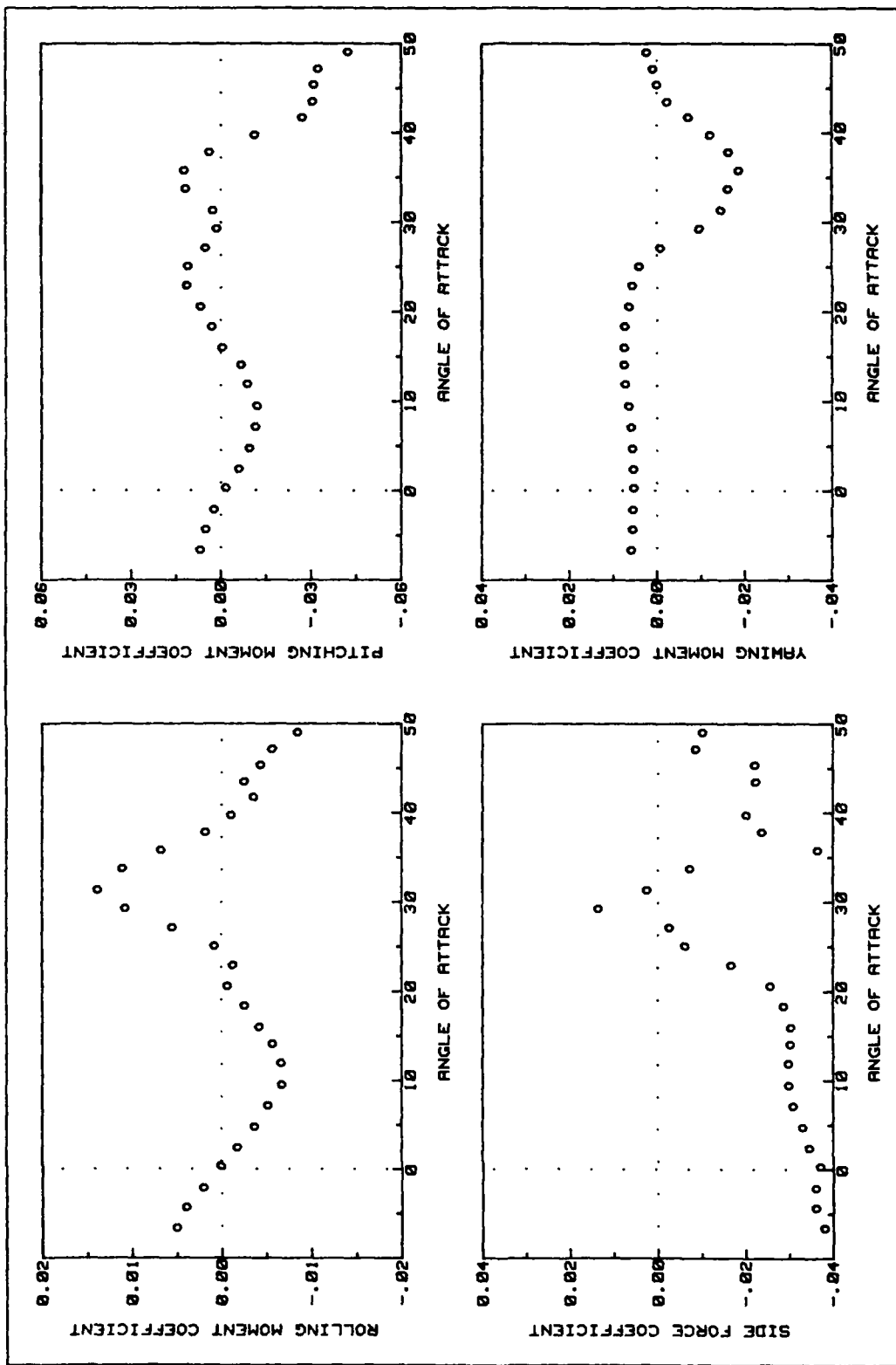


Fig A6. Model Baseline Side Force and Moments Data (-6 deg yaw)

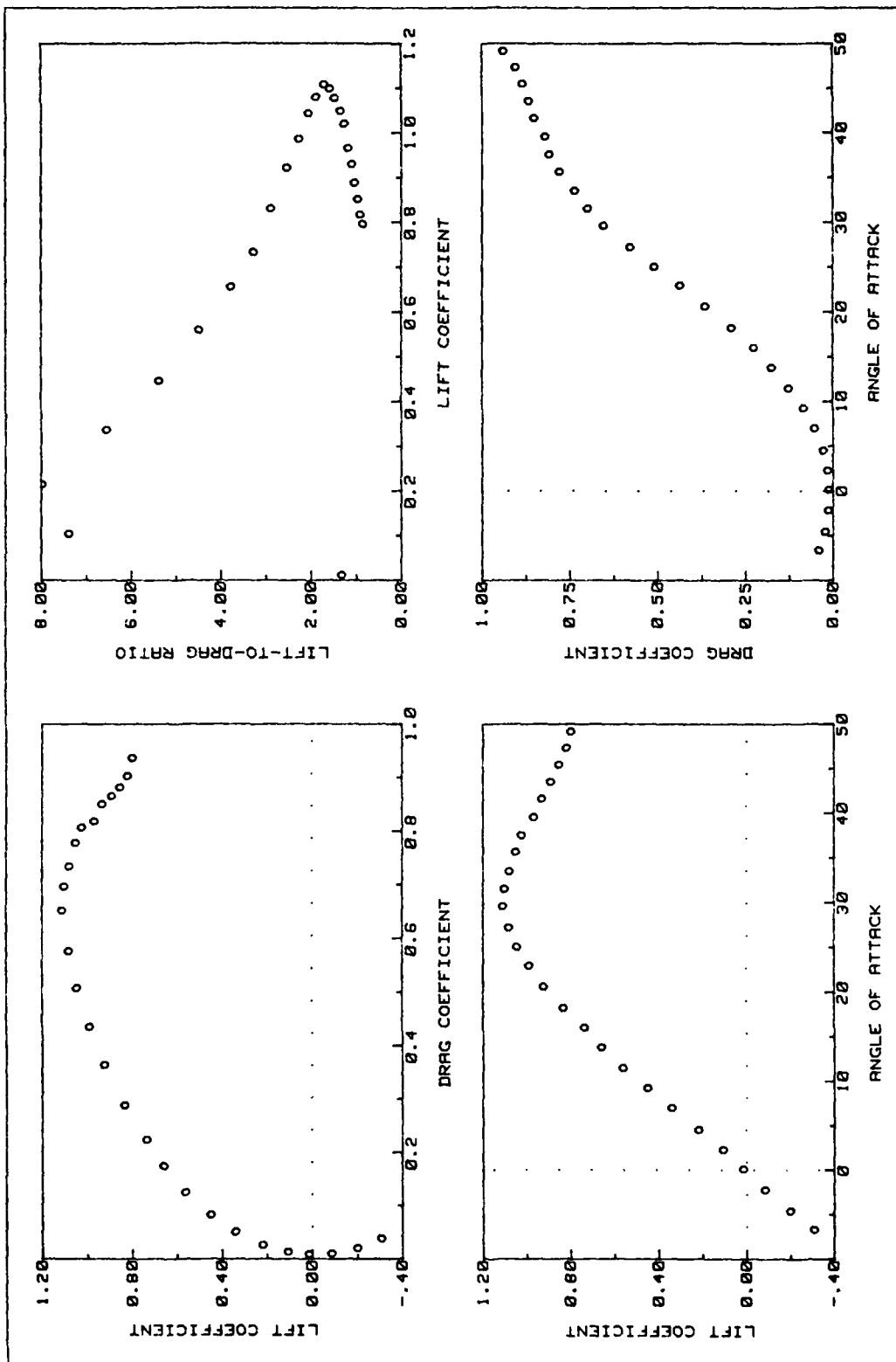


Fig A7. C1 Flap Lift and Drag Data (deployed 30 deg asymmetric)

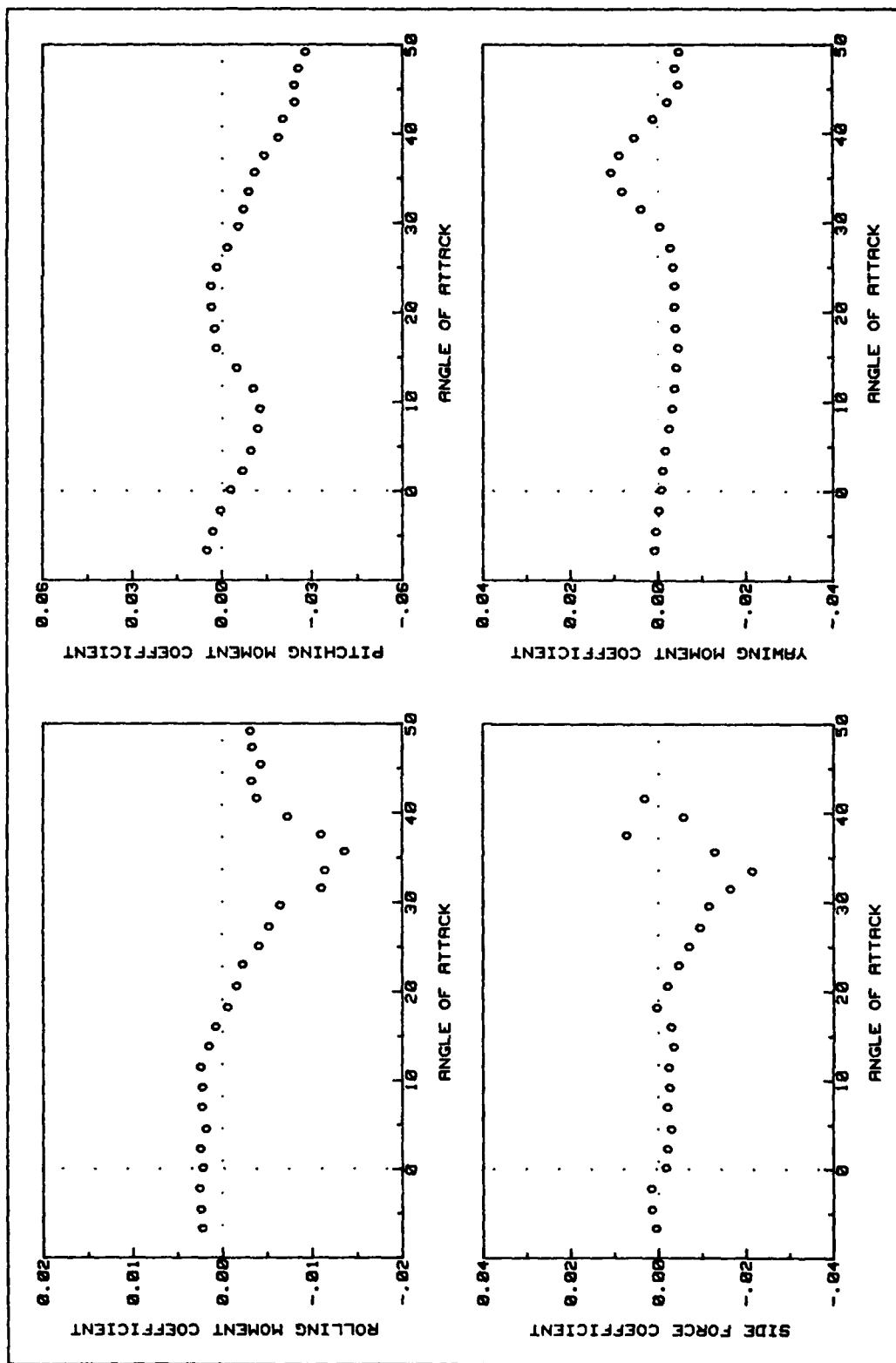


Fig A8. C1 Flap Side Force and Moments Data (deployed 30 deg asymmetric)

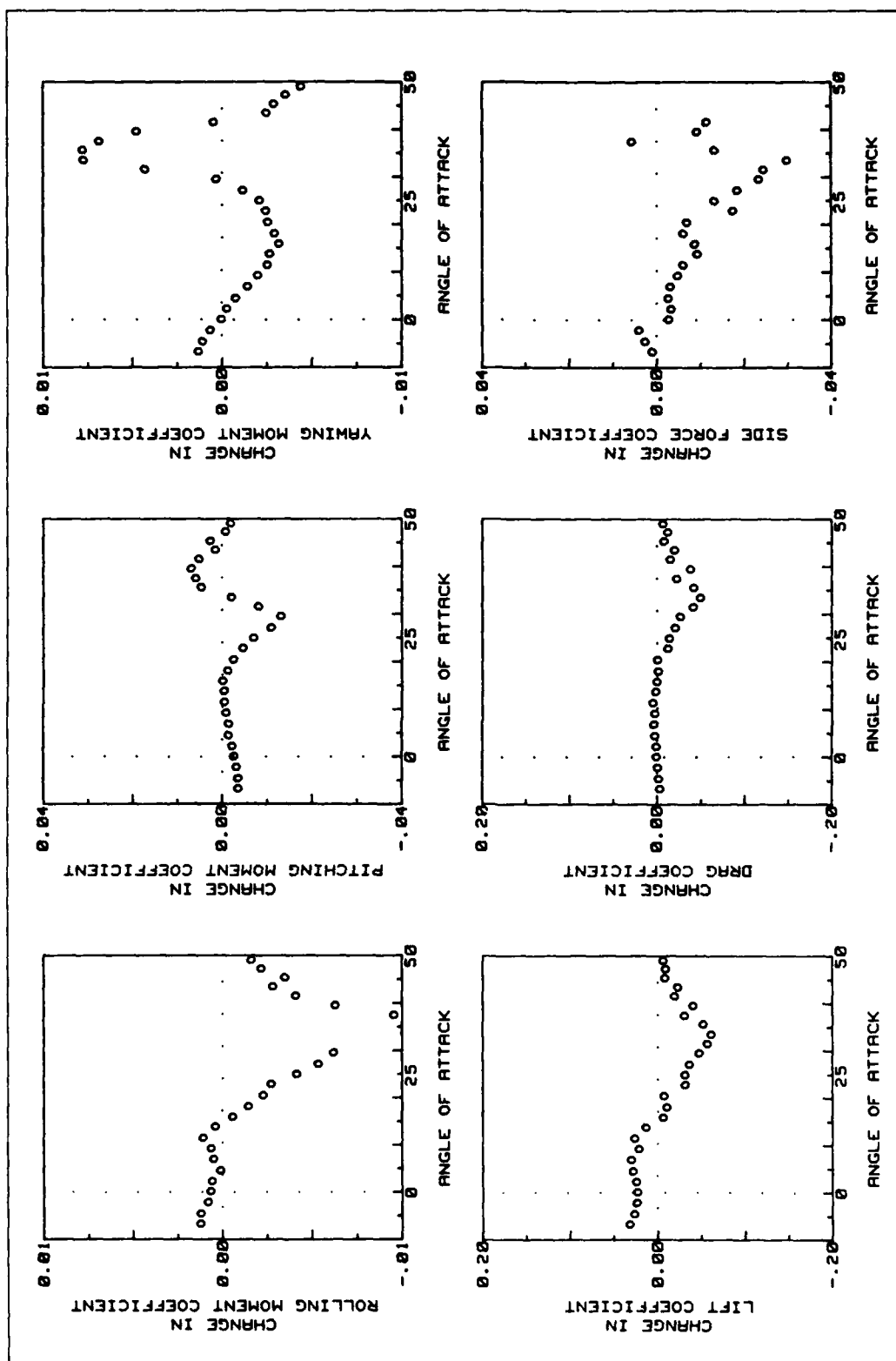


Fig A9. C1 Flap Force and Moment Changes (deployed 30 deg asymmetric)

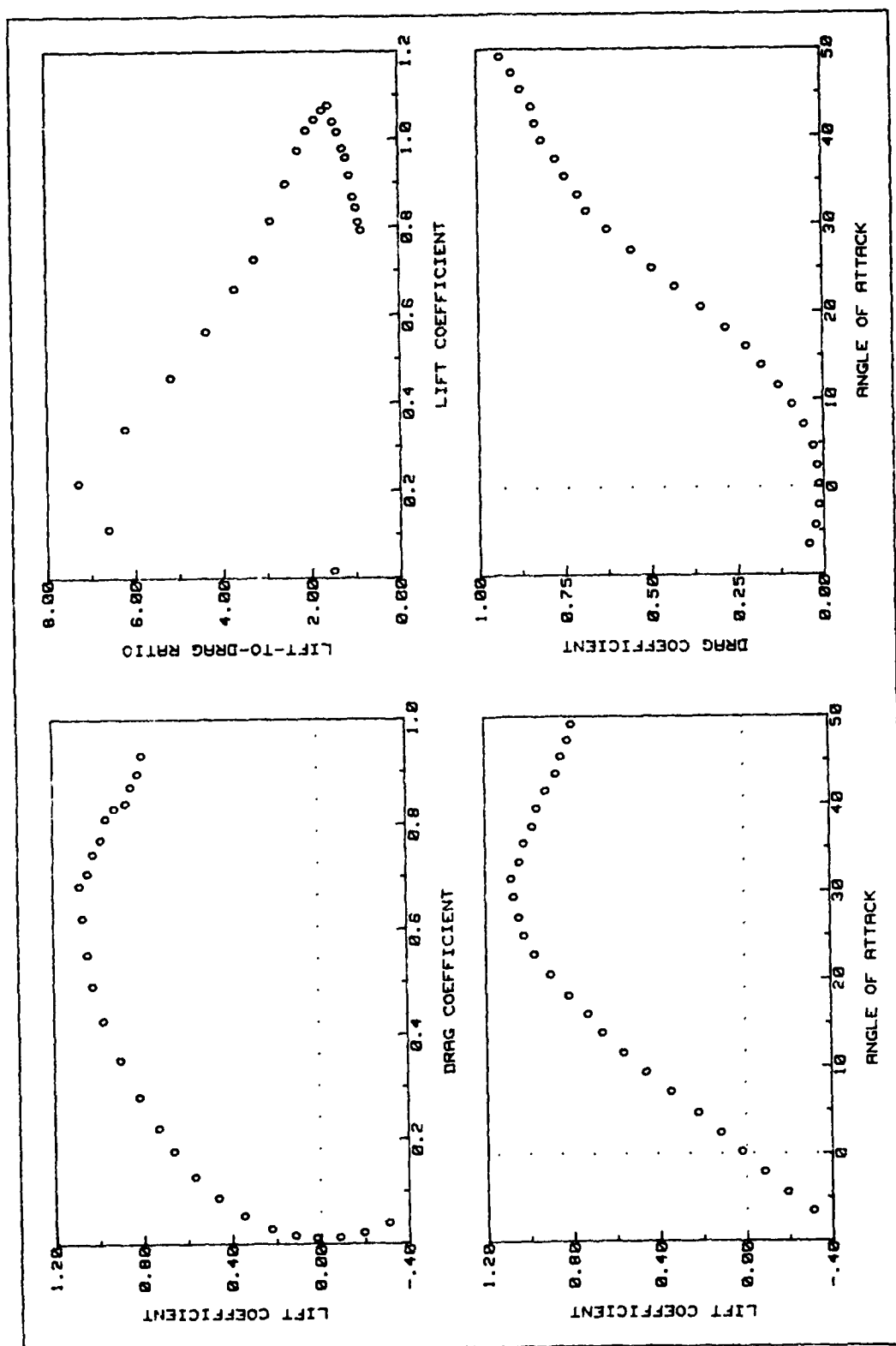


Fig A10. C1 Flap Lift and Drag Data (deployed 30 deg symmetric)

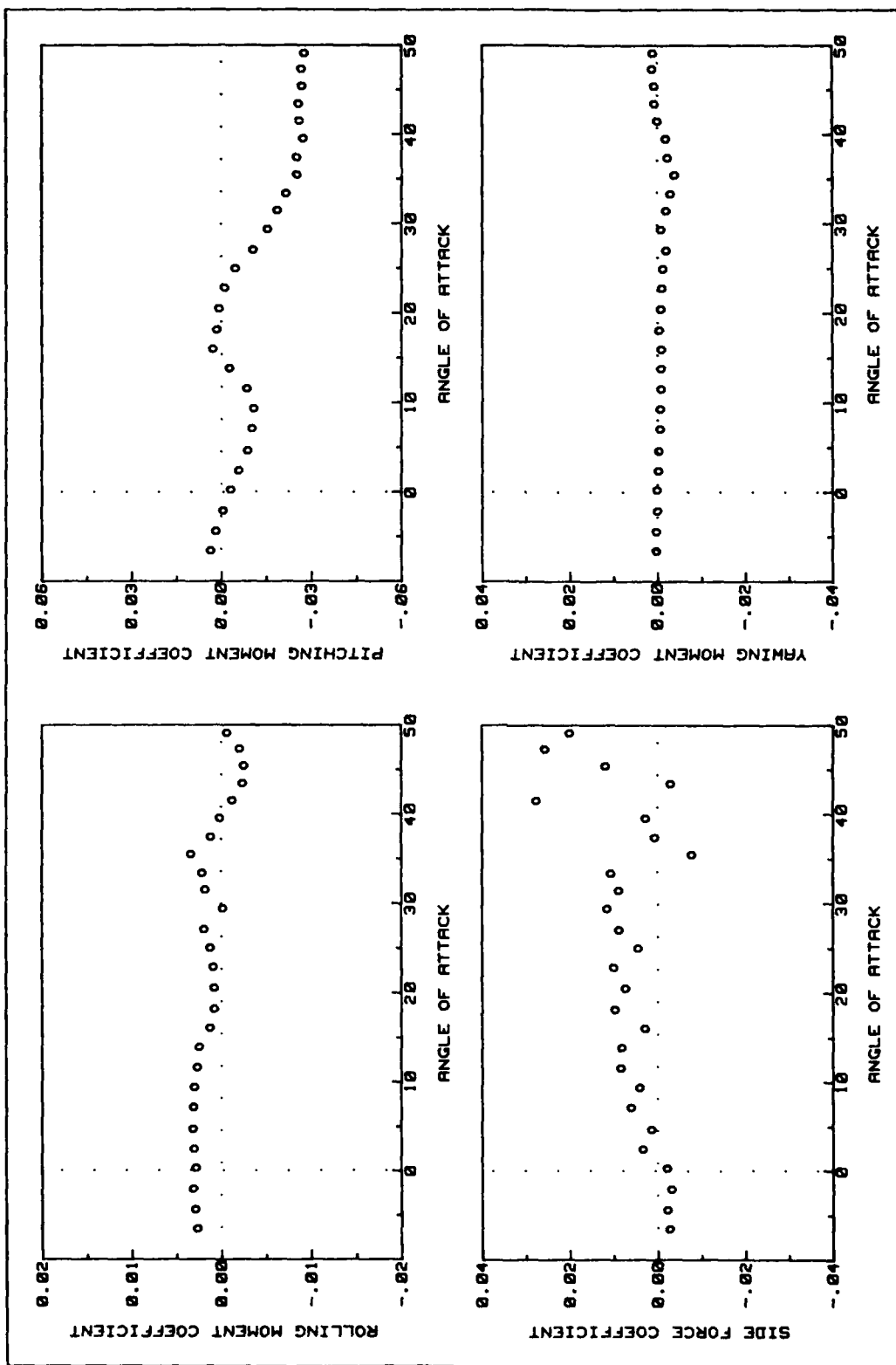


Fig A11. C1 Flap Side Force and Moments Data (deployed 30 deg symmetric)

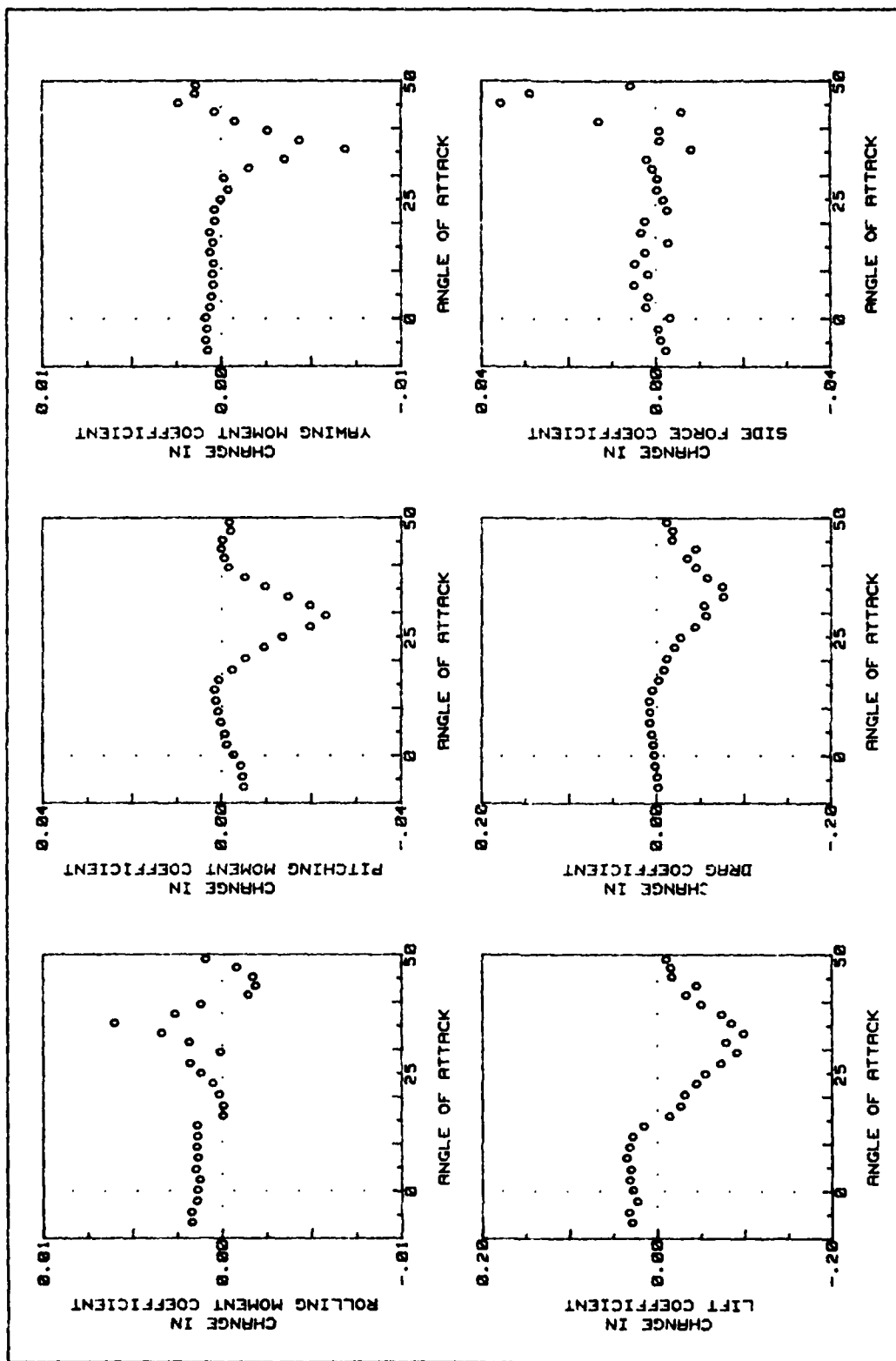


Fig A12. C1 Flap Force and Moment Changes (deployed 30 deg symmetric)

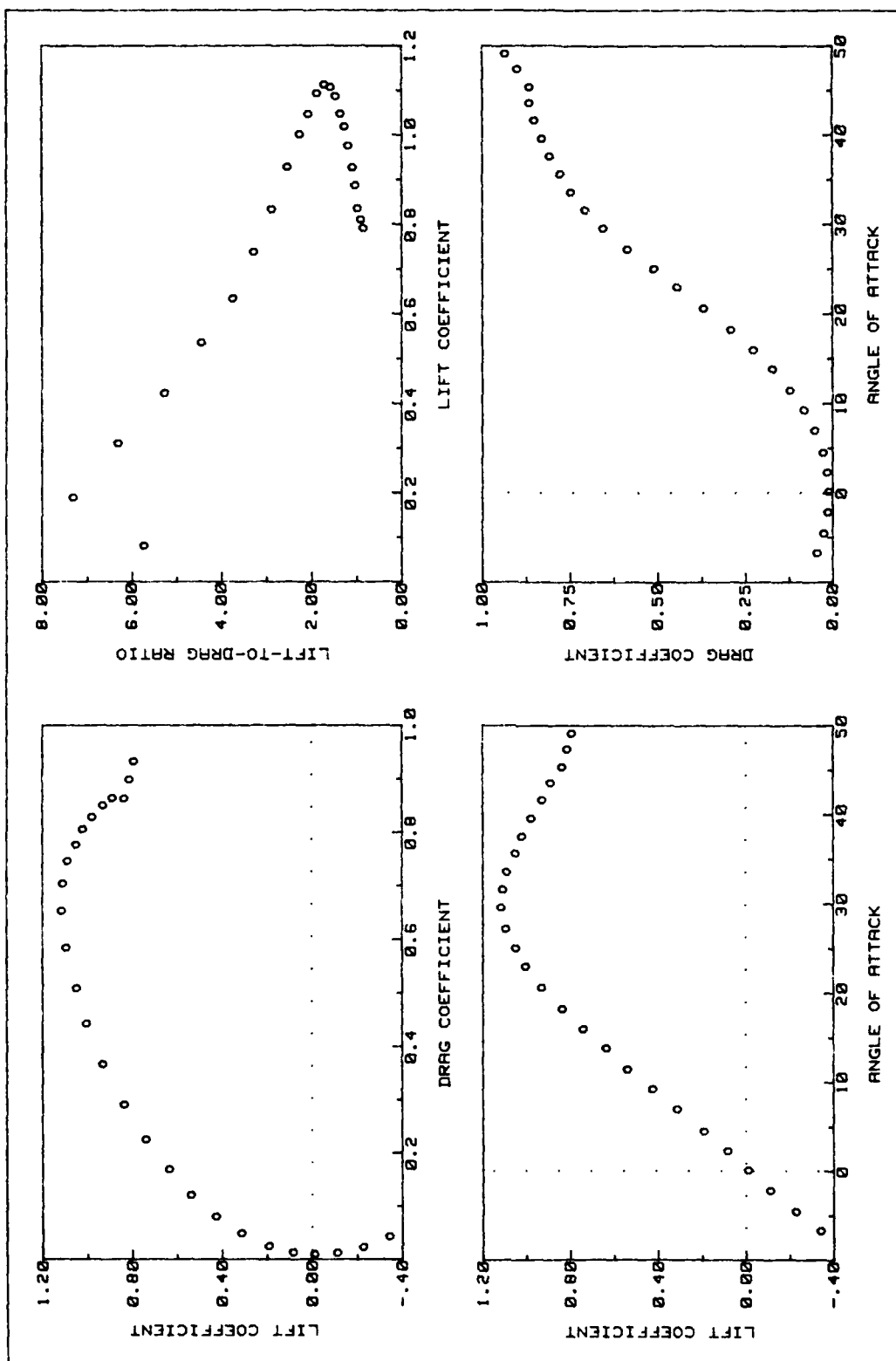


Fig A13. C1 Flap Lift and Drag Data (deployed 45 deg asymmetric)

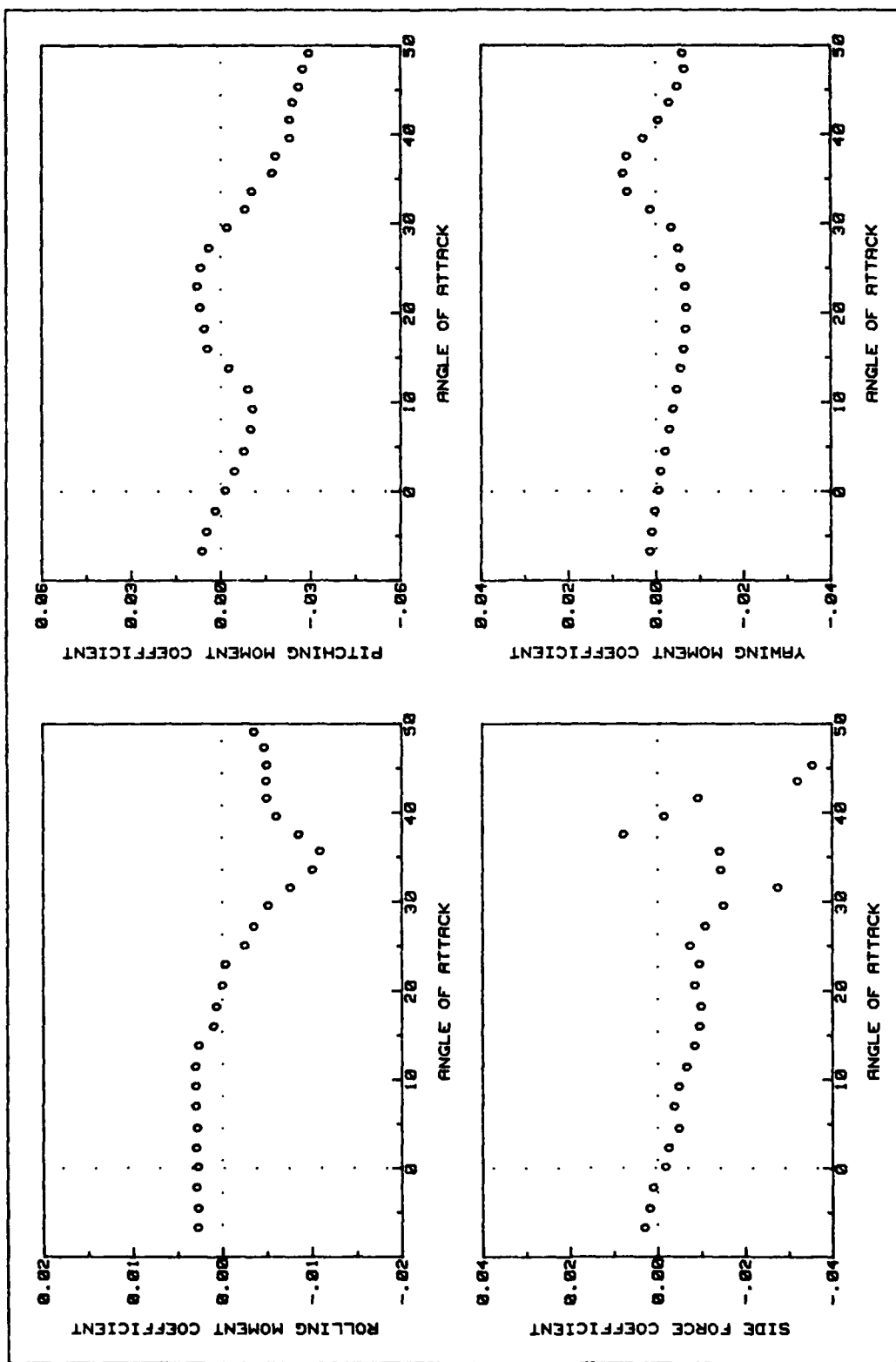


Fig A14. C1 Flap Side Force and Moments Data (deployed 45 deg asymmetric)

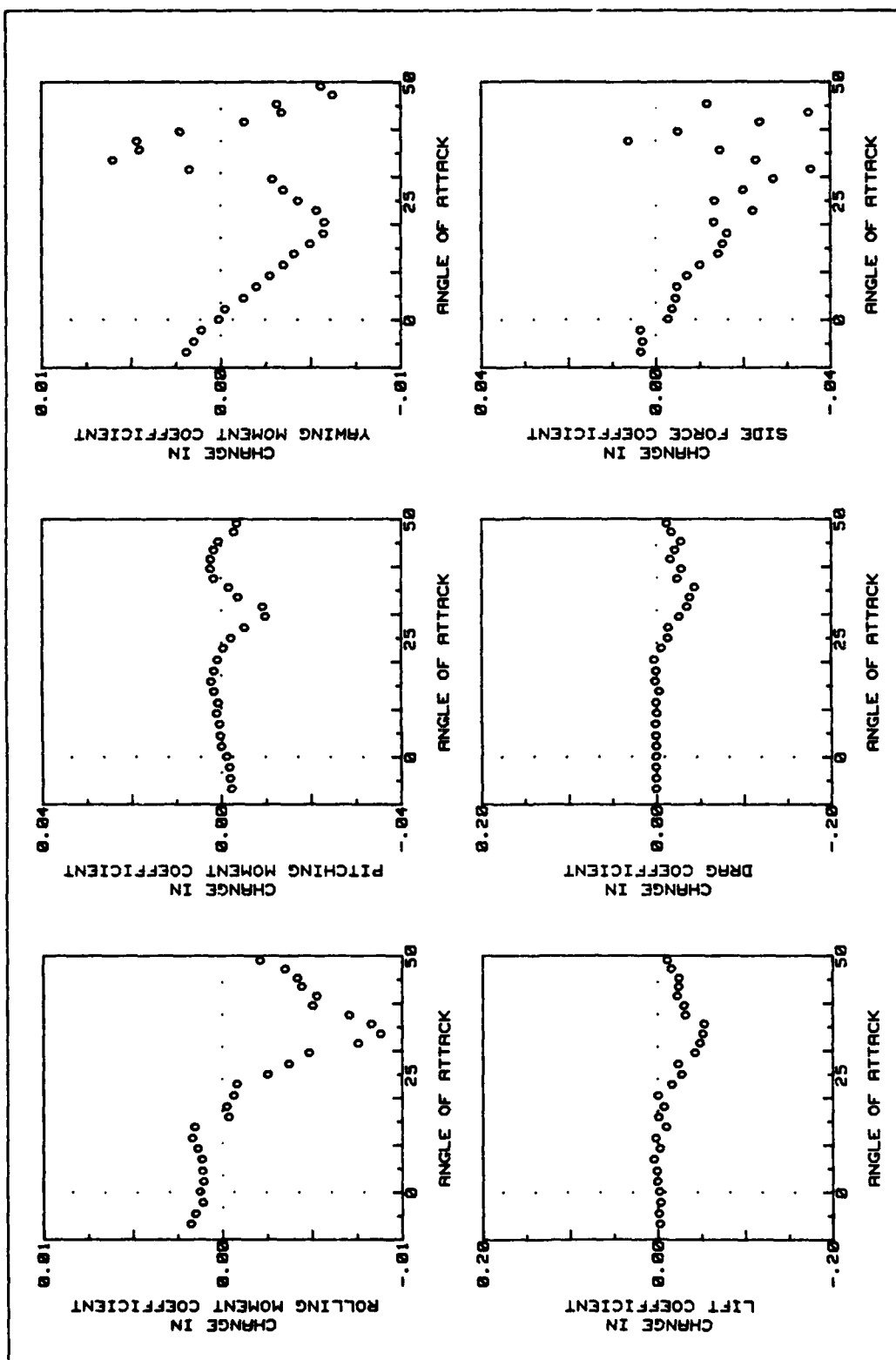


Fig A15. C1 Flap Force and Moment Changes (deployed 45 deg asymmetric)

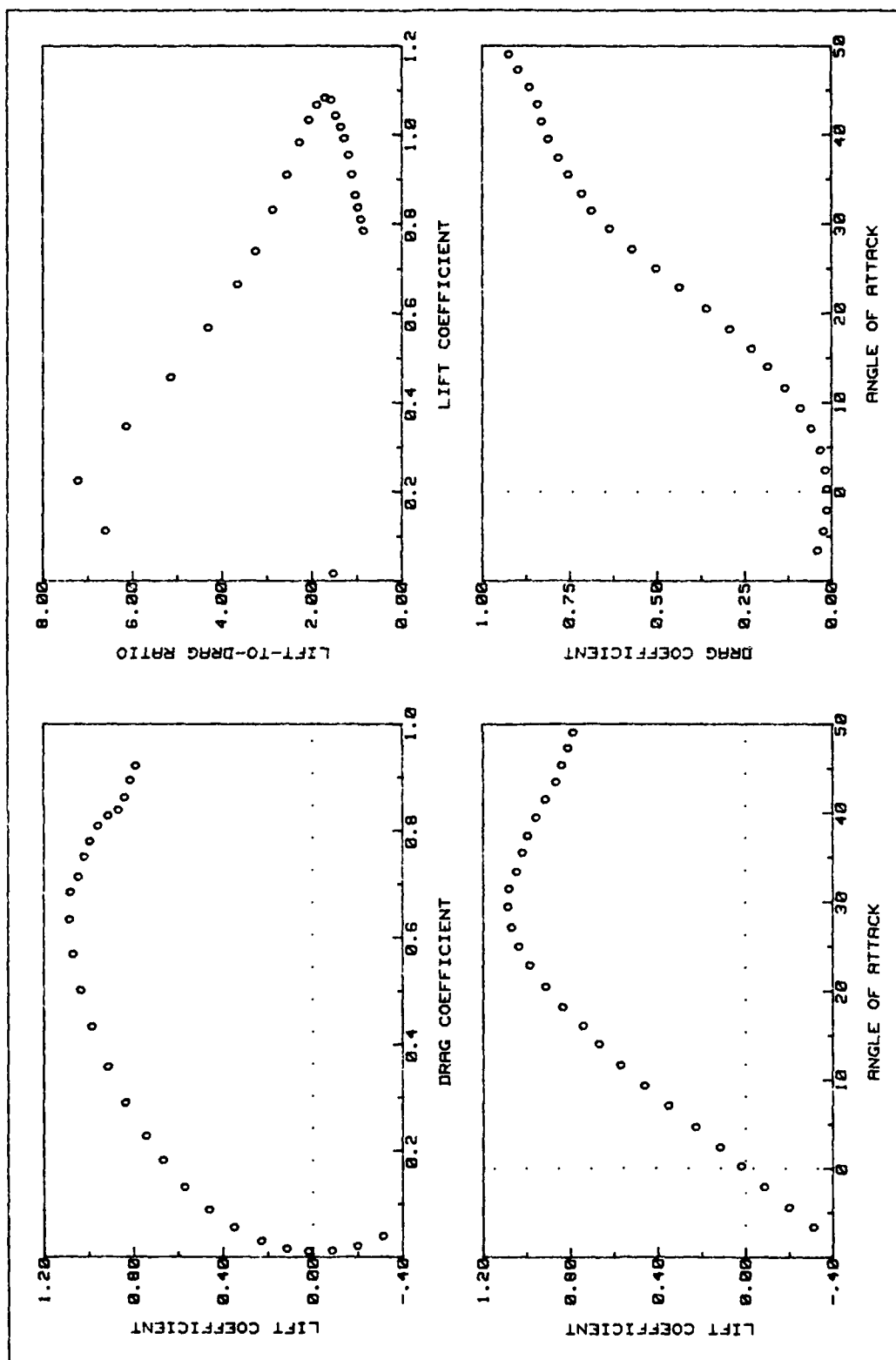


Fig A16. C1 Flap Lift and Drag Data (deployed 45 deg symmetric)

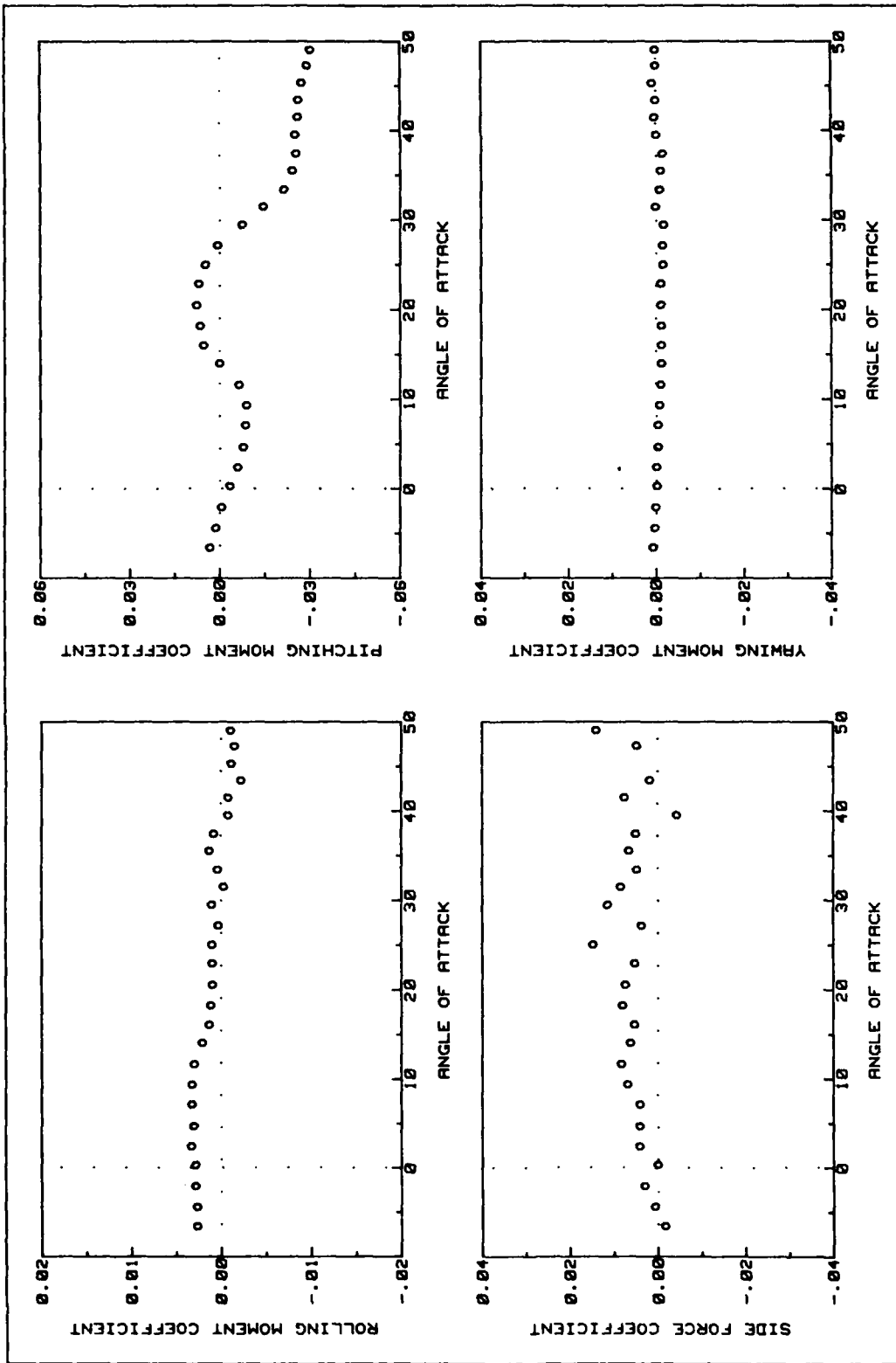


Fig A17. C1 Flap Side Force and Moments Data (deployed 45 deg symmetric)

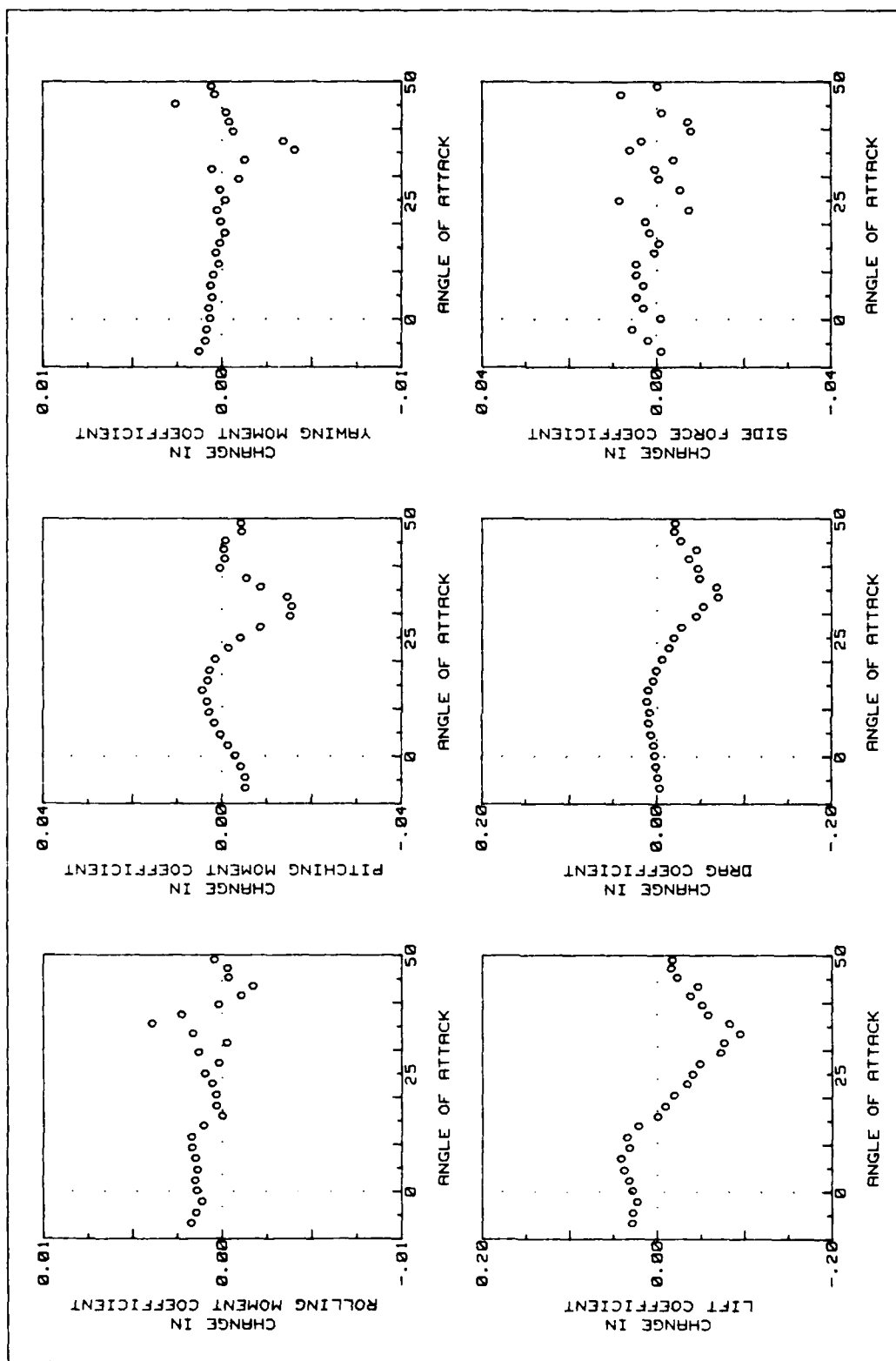


Fig A18. C1 Flap Force and Moment Changes (deployed 45 deg symmetric)

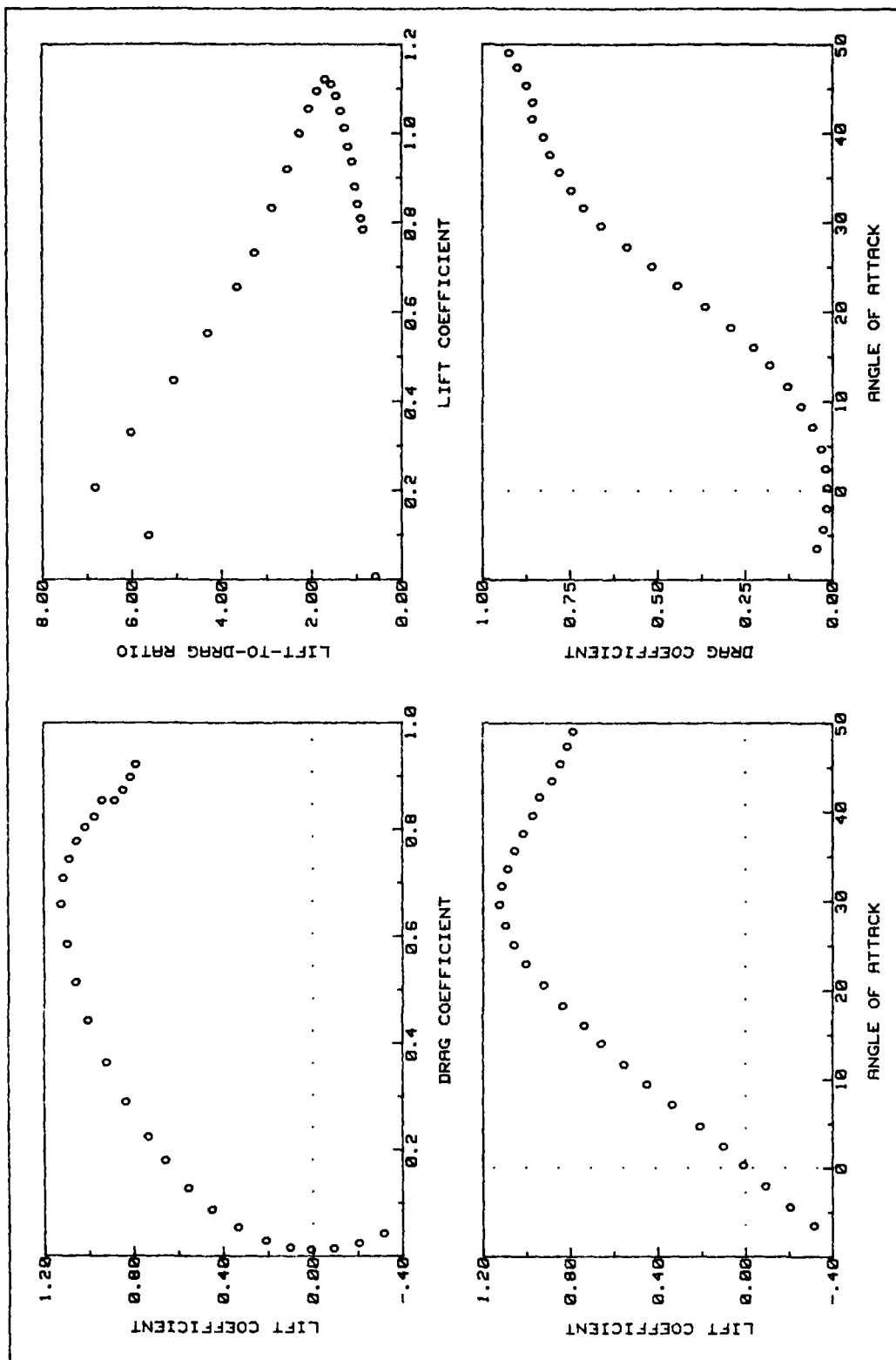


Fig A19. C1 Flap Lift and Drag Data (deployed 60 deg asymmetric)

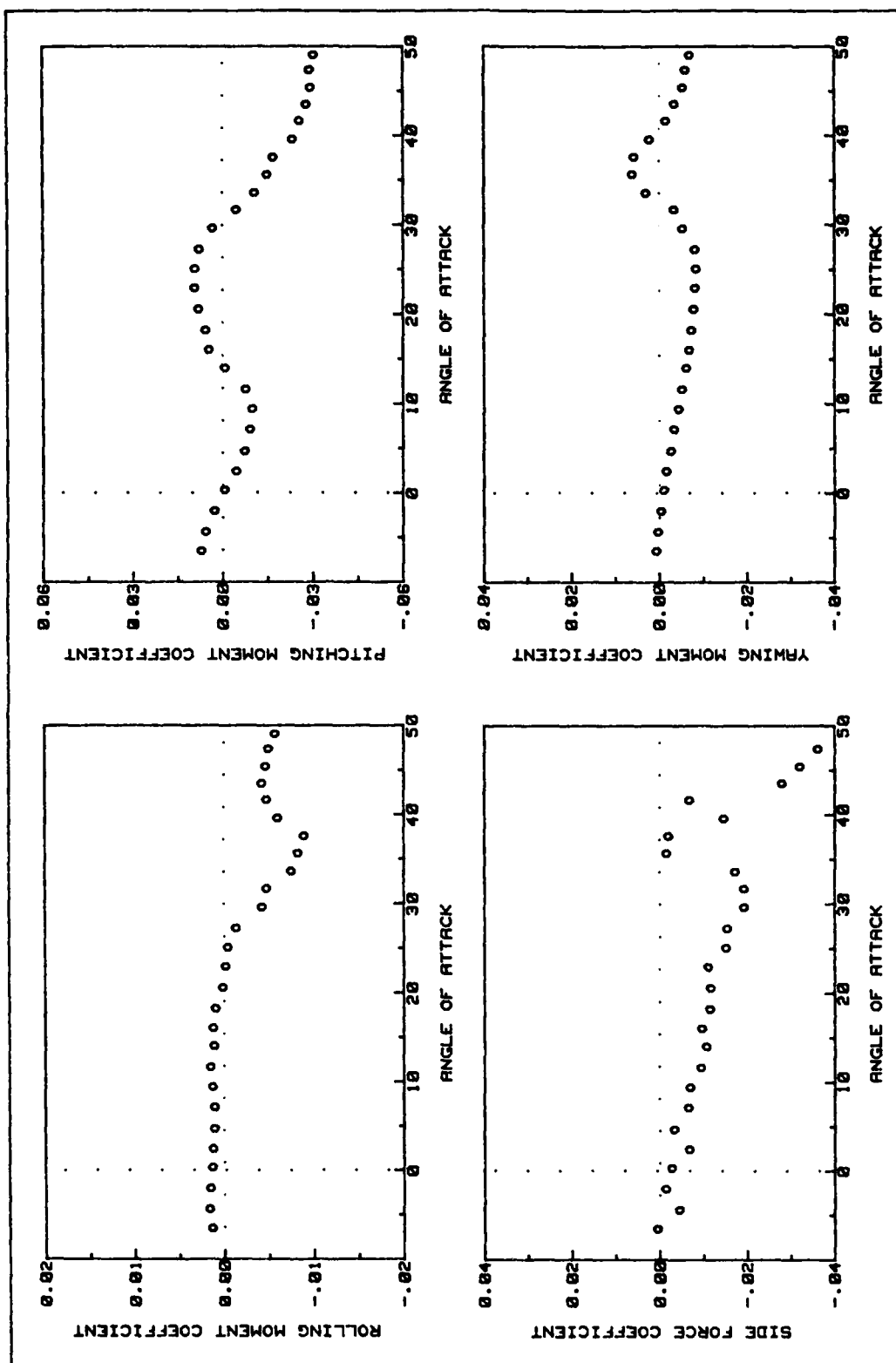


Fig A20. C1 Flap Side Force and Moments Data (deployed 60 deg asymmetric)

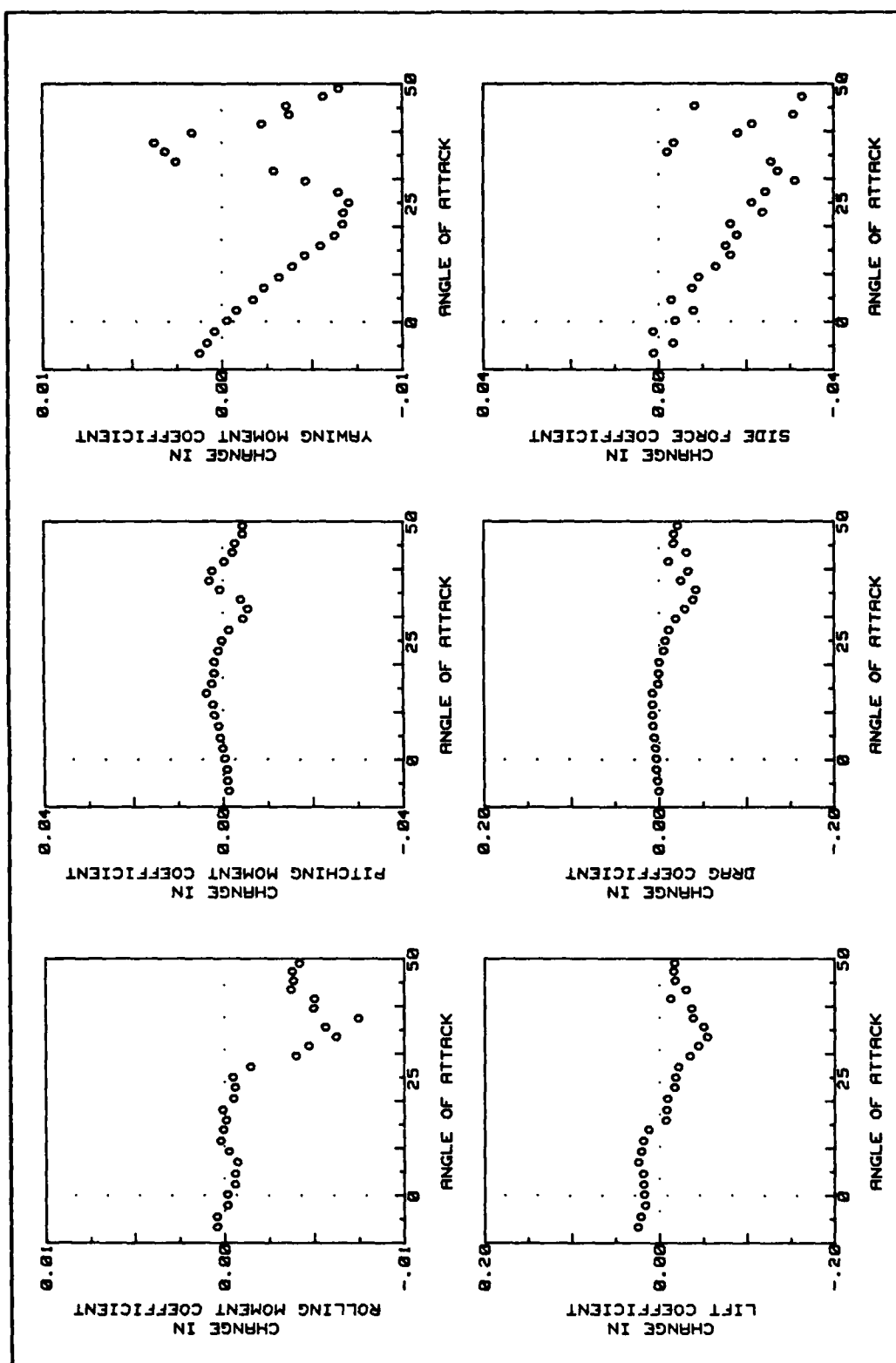


Fig A21. C1 Flap Force and Moment Changes (deployed 60 deg asymmetric)

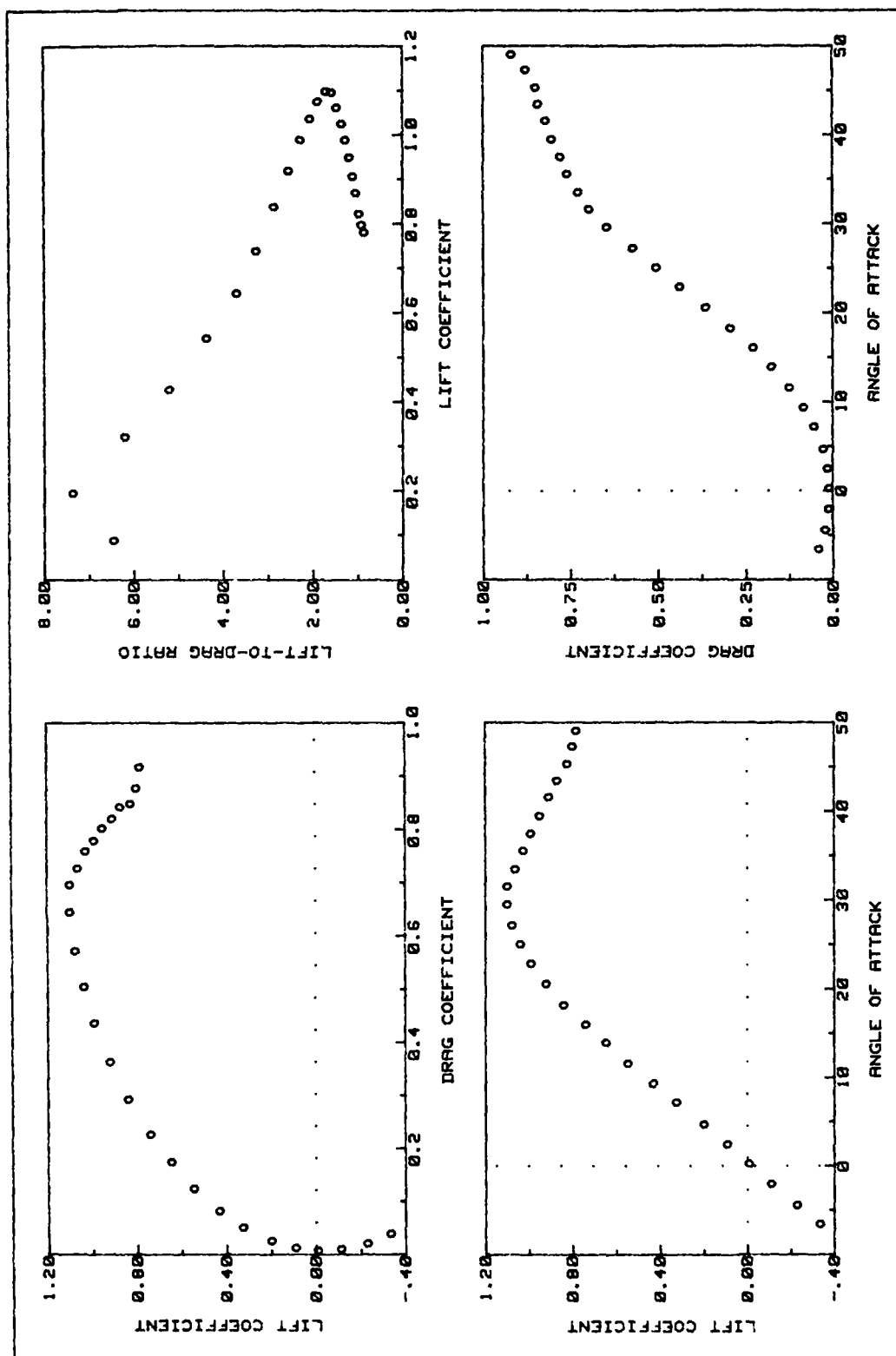


Fig A22. C1 Flap Lift and Drag Data (deployed 60 deg symmetric)

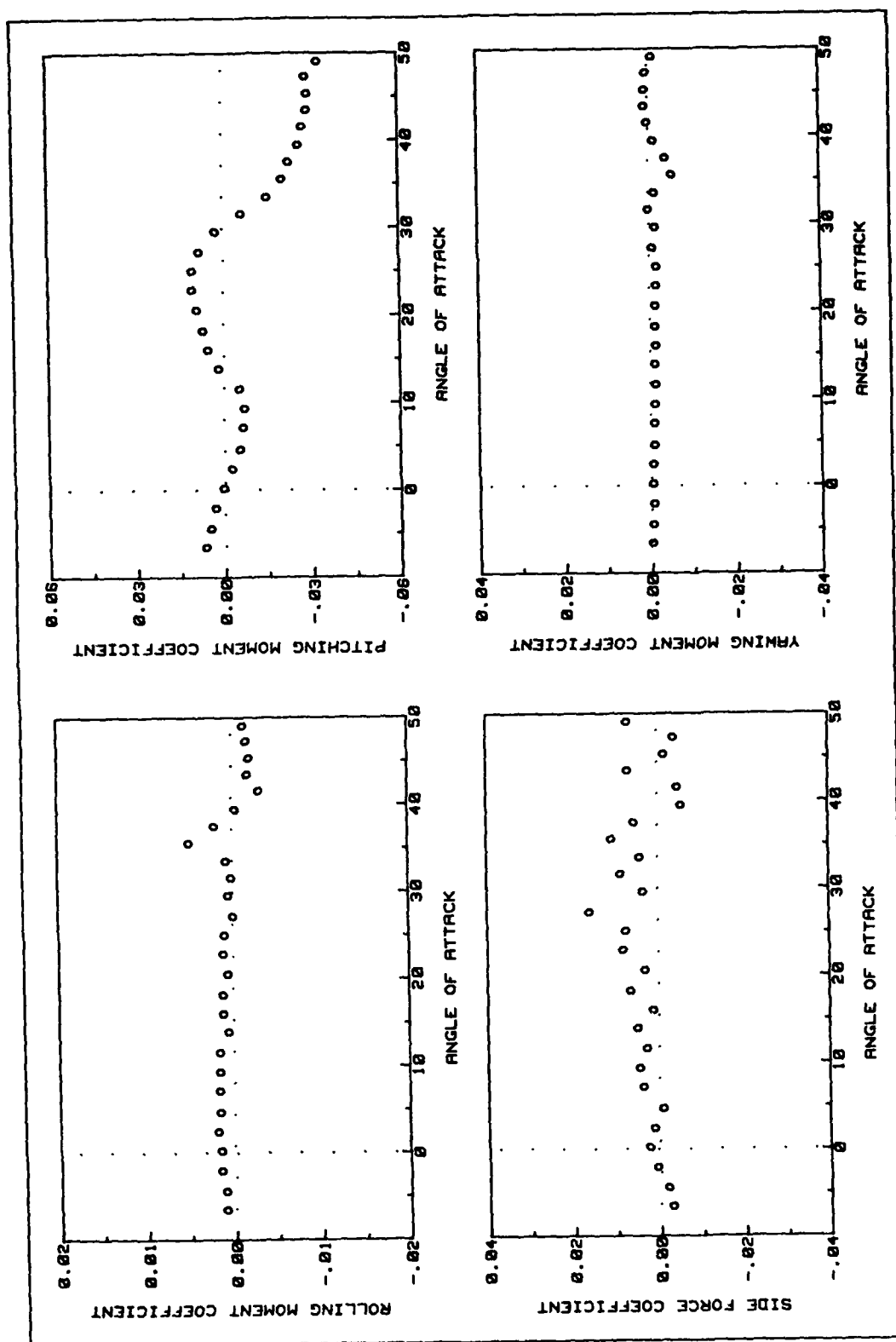


Fig A23. C1 Flap Side Force and Moments Data (deployed 60 deg symmetric)

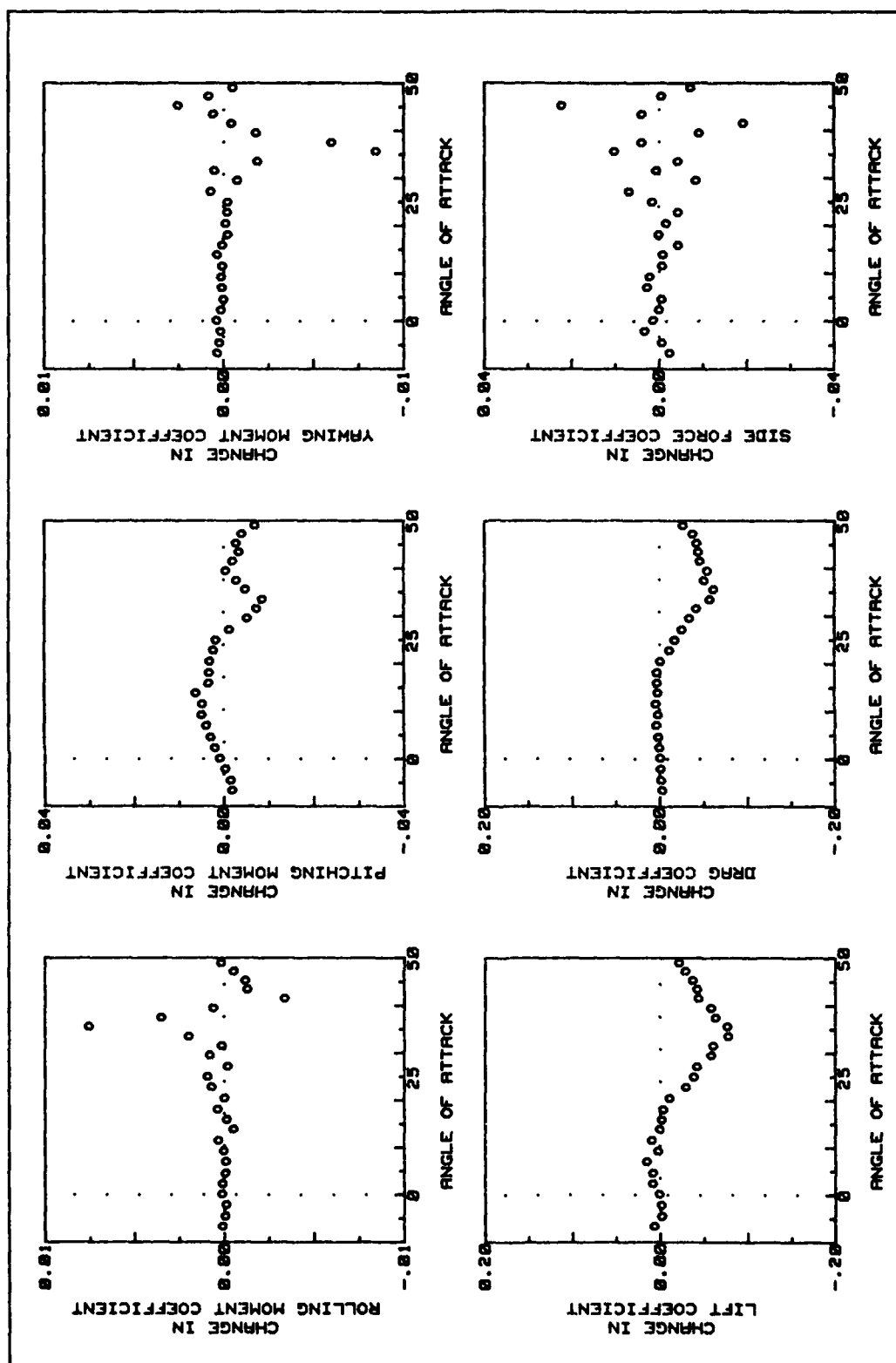


Fig A24. C1 Flap Force and Moment Changes (deployed 60 deg symmetric)

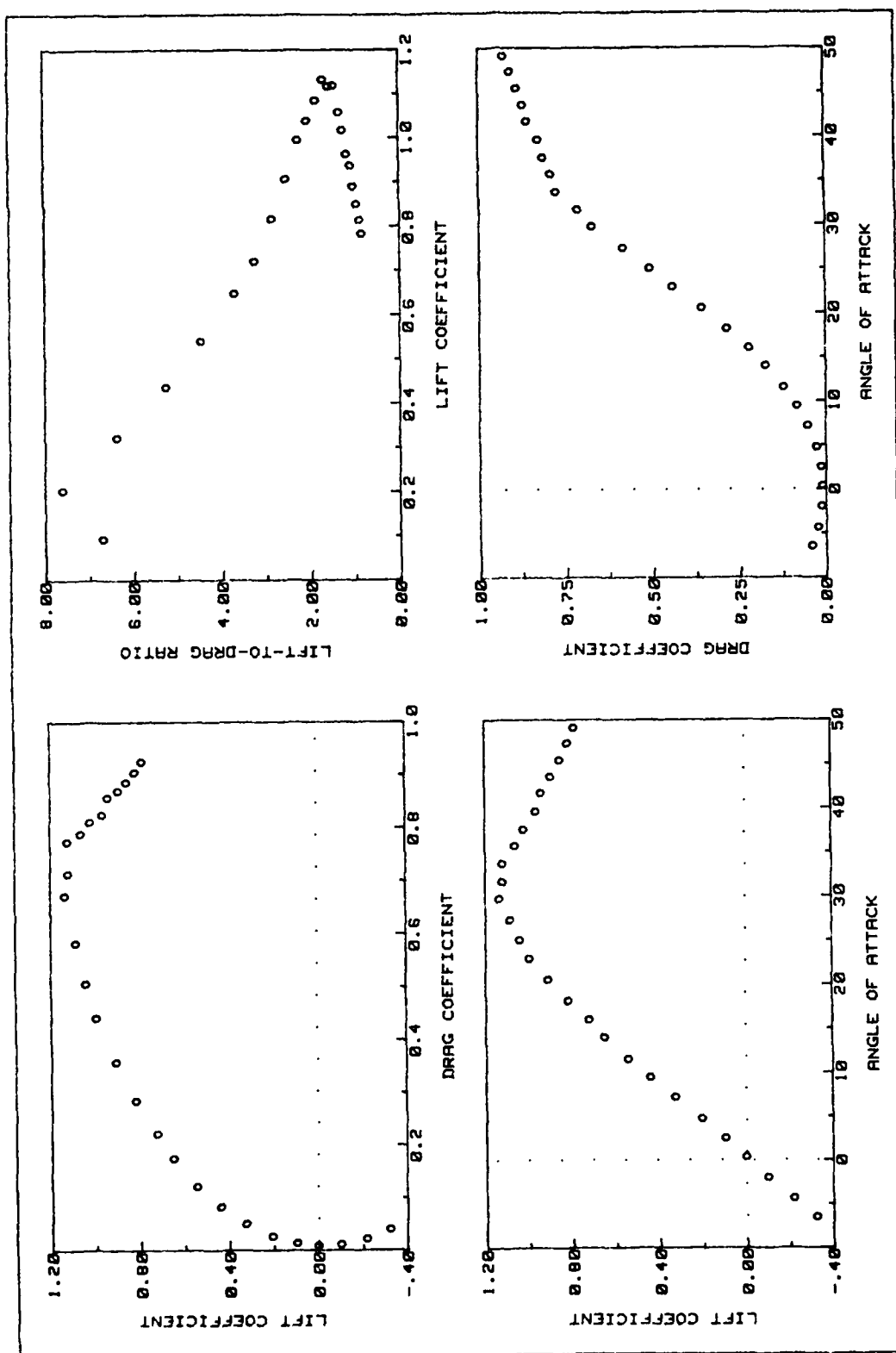


Fig A25. C1 Flap Lift and Drag Data (deployed 75 deg aysmmetric)

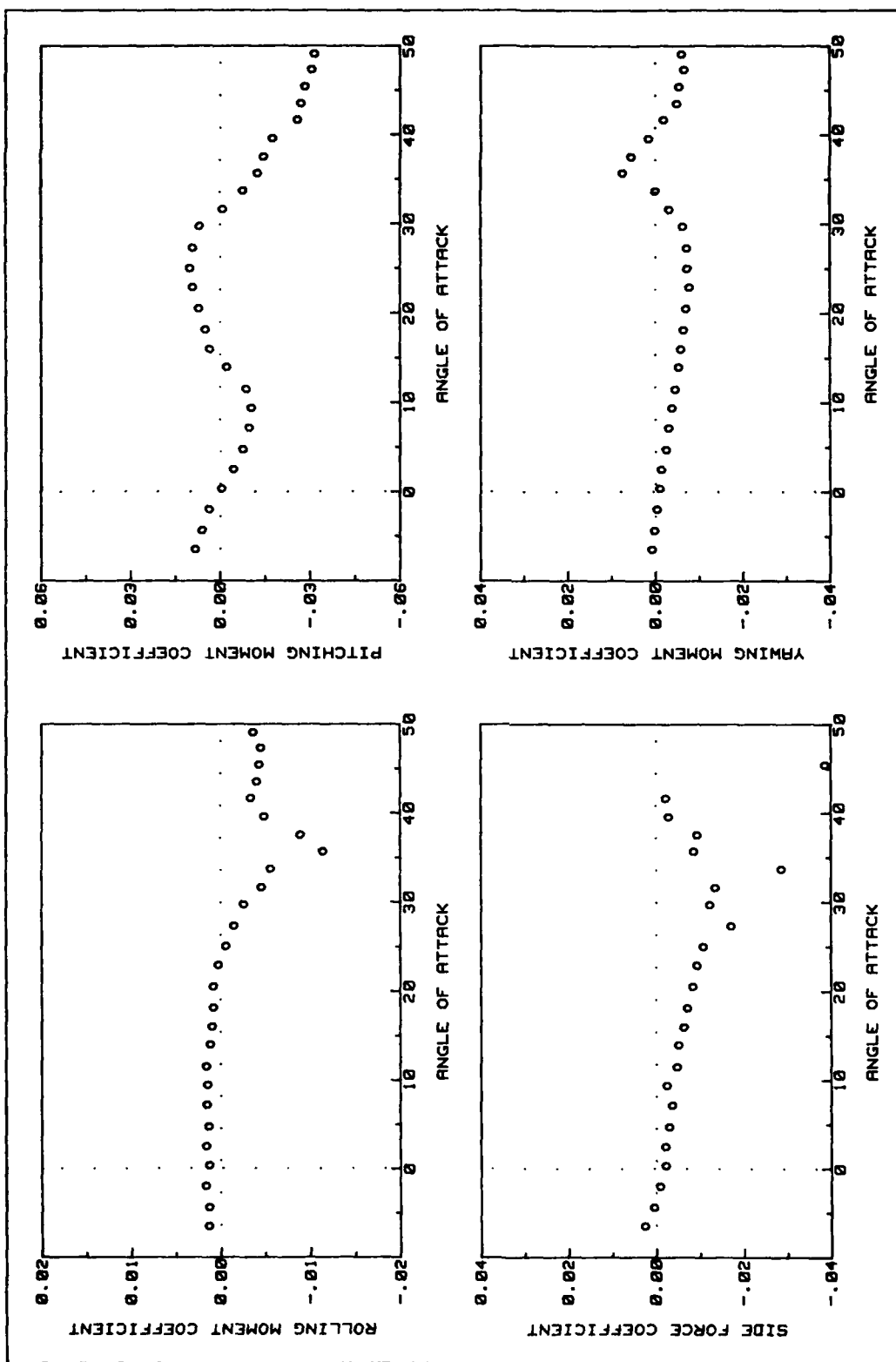


Fig A26. C1 Flap Side Force and Moments Data (deployed 75 deg asymmetric)

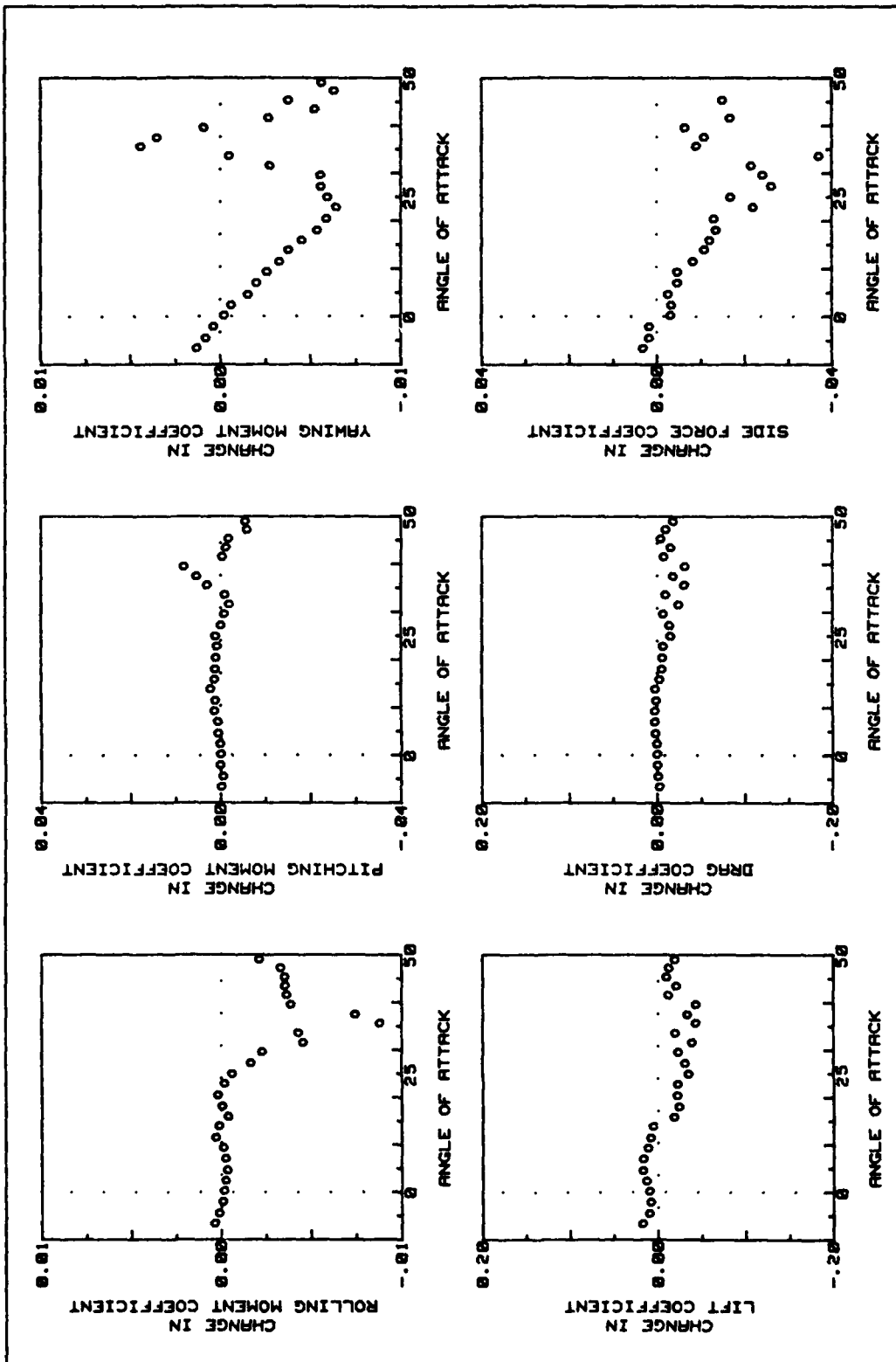


Fig A27. C1 Flap Force and Moment Changes (deployed 75 deg asymmetric)

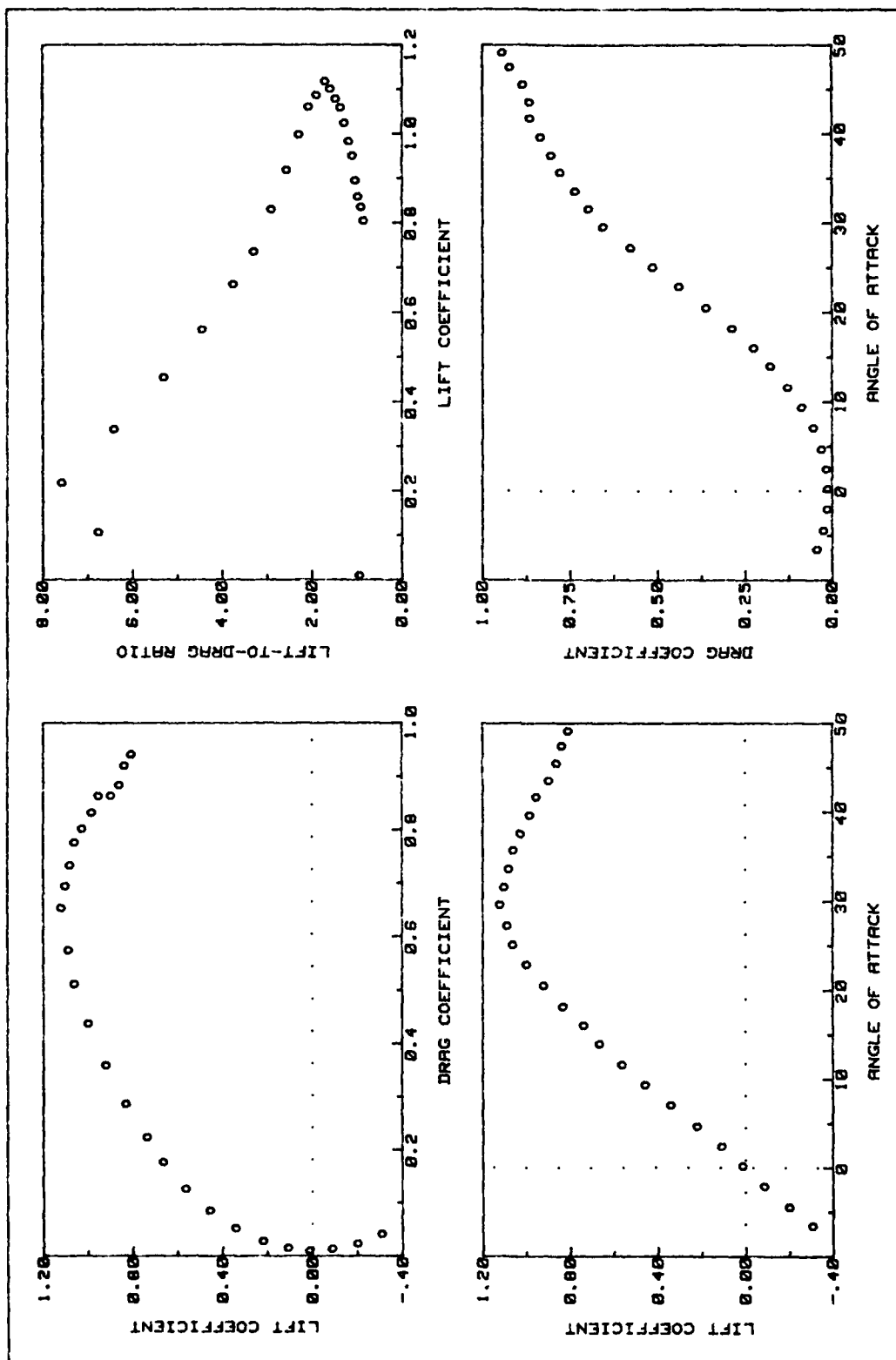


Fig A28. C2 Flap Lift and Drag Data (deployed 30 deg asymmetric)

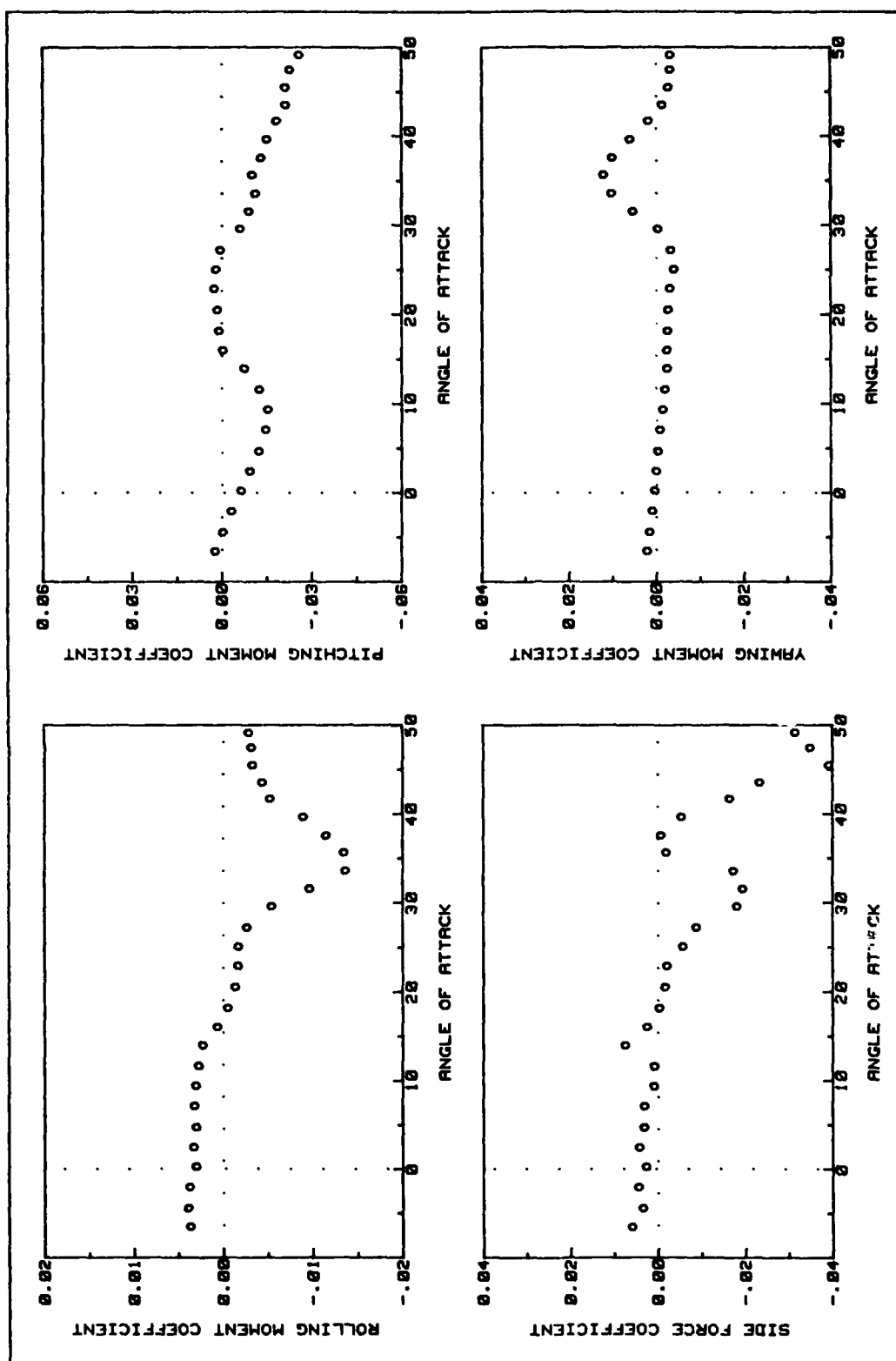


Fig A29. C2 Flap Side Force and Moments Data (deployed 30 deg asymmetric)

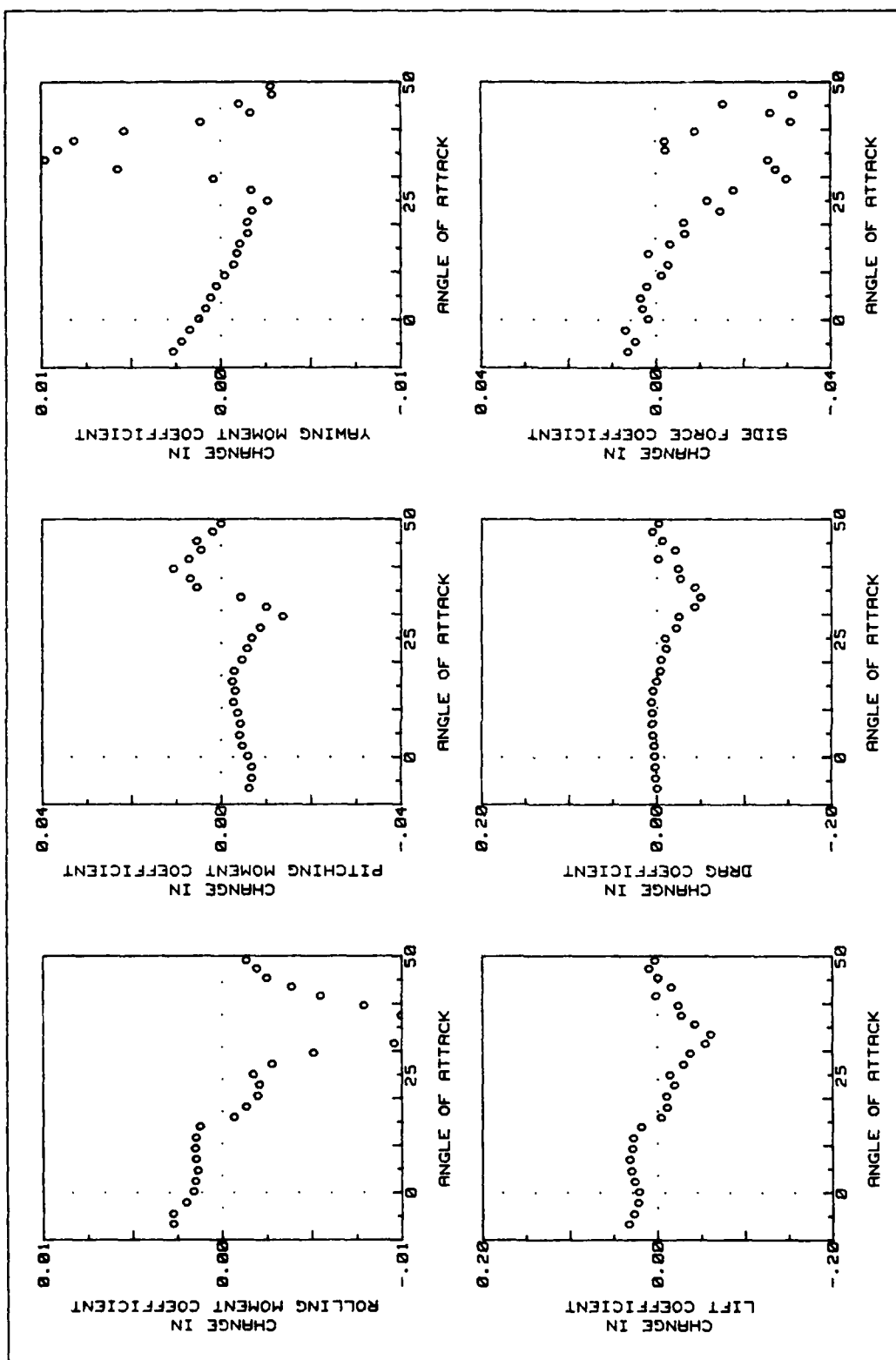


Fig A30. C2 Flap Force and Moment Changes (deployed 30 deg asymmetric)

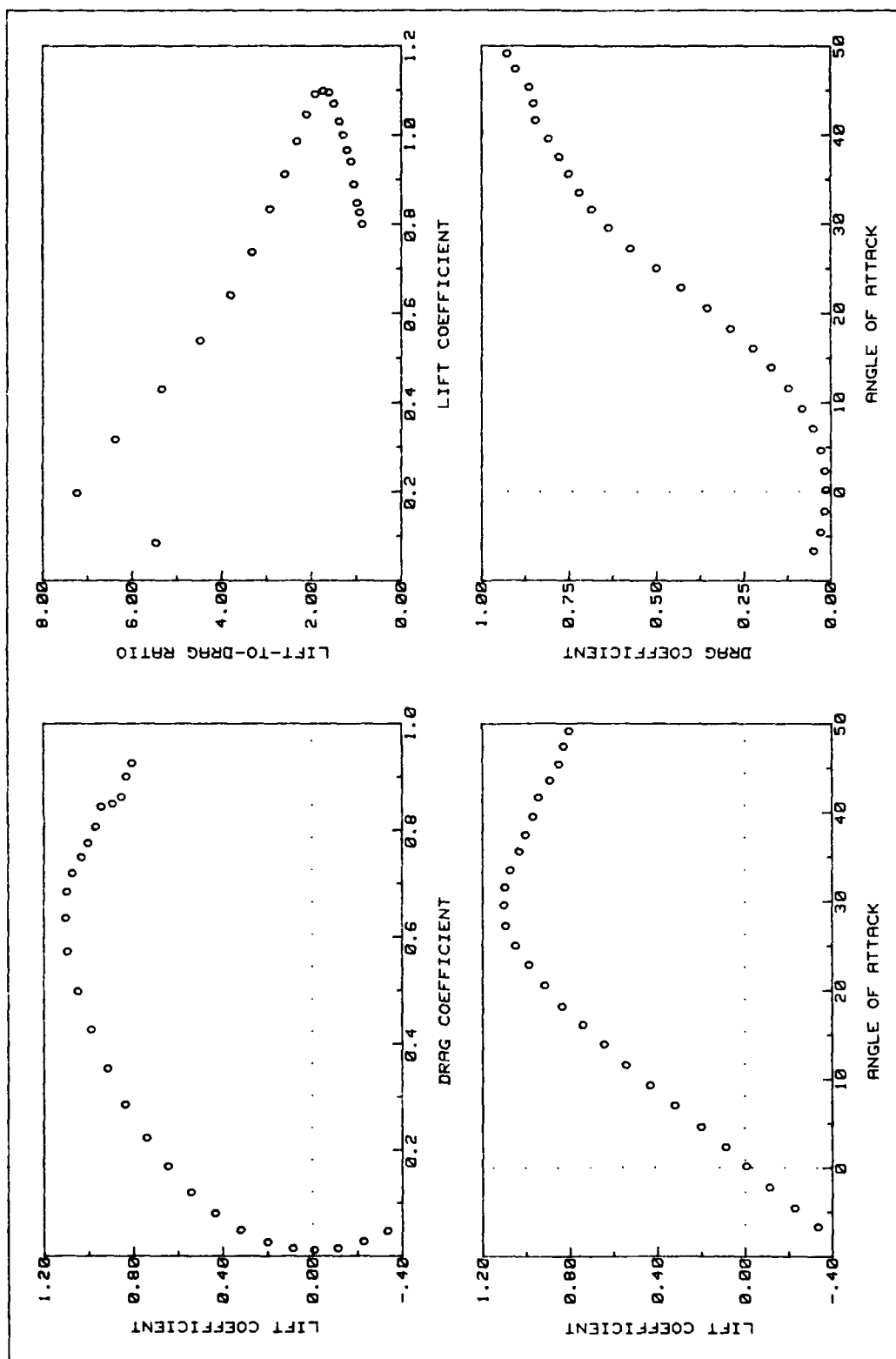


Fig A31. C2 Flap Lift and Drag Data (deployed 30 deg symmetric)

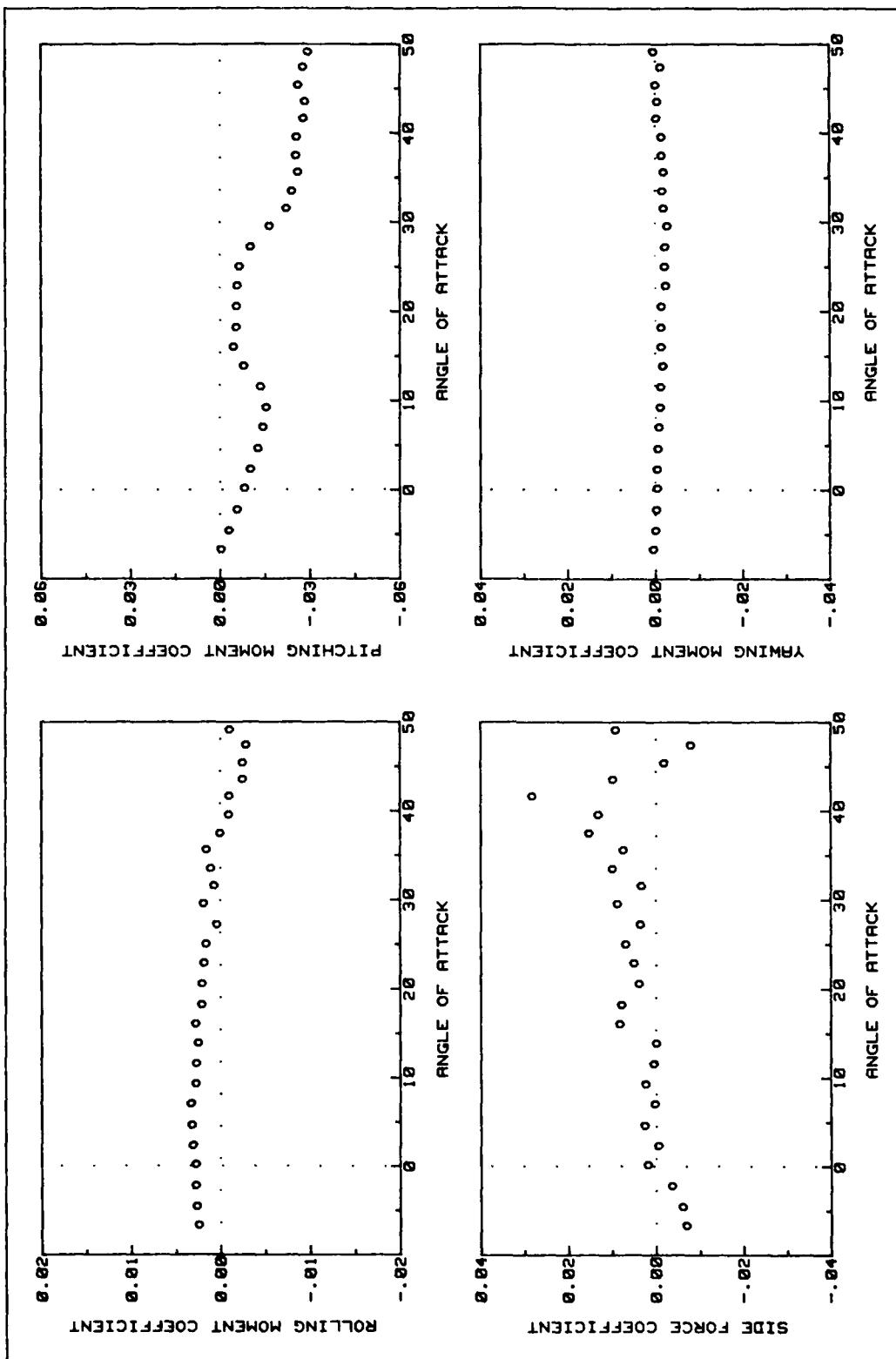


Fig A32. C2 Flap Side Force and Moments Data (deployed 30 deg symmetric)

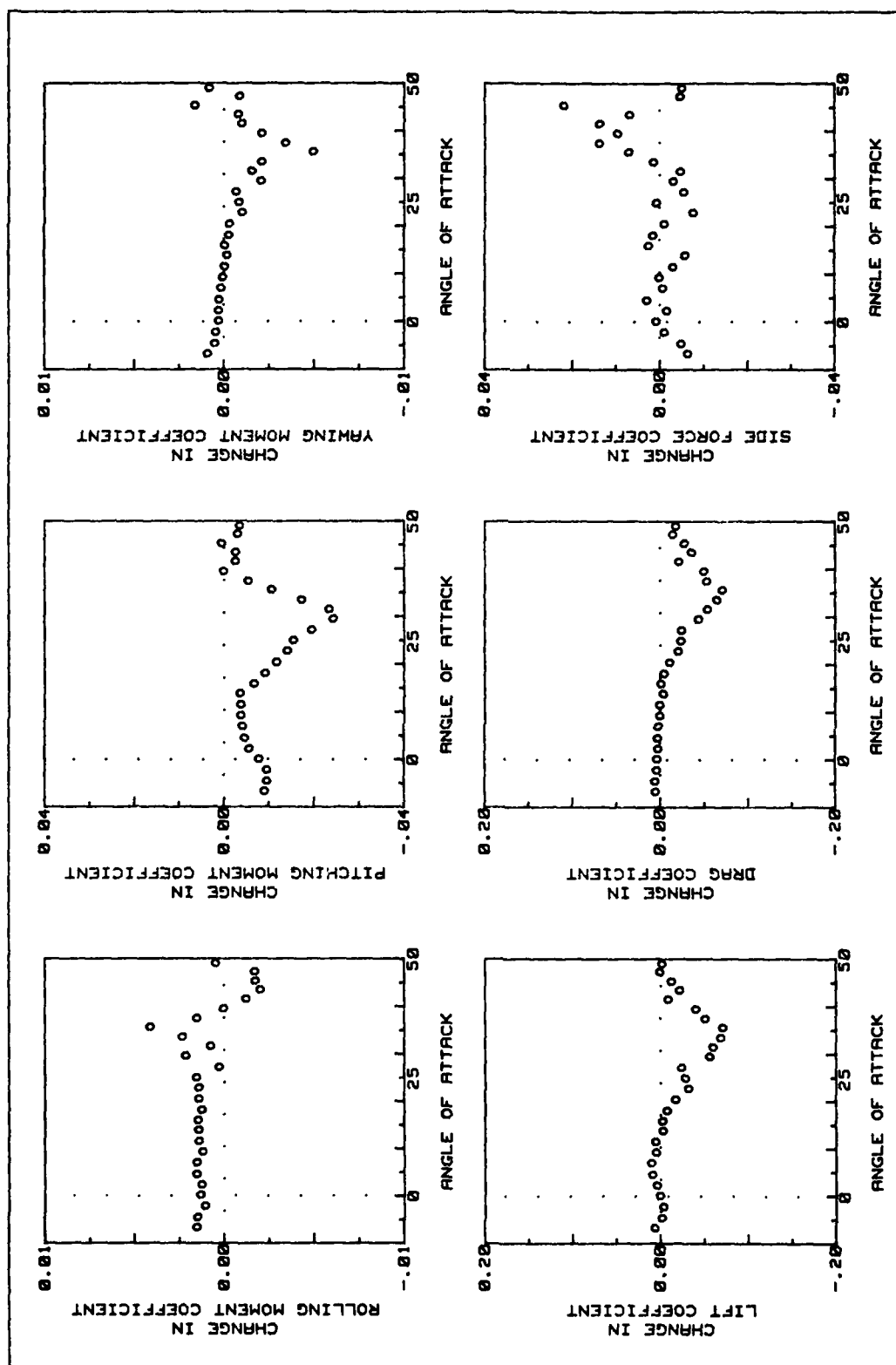


Fig A33. C2 Flap Force and Moment Changes (deployed 30 deg symmetric)

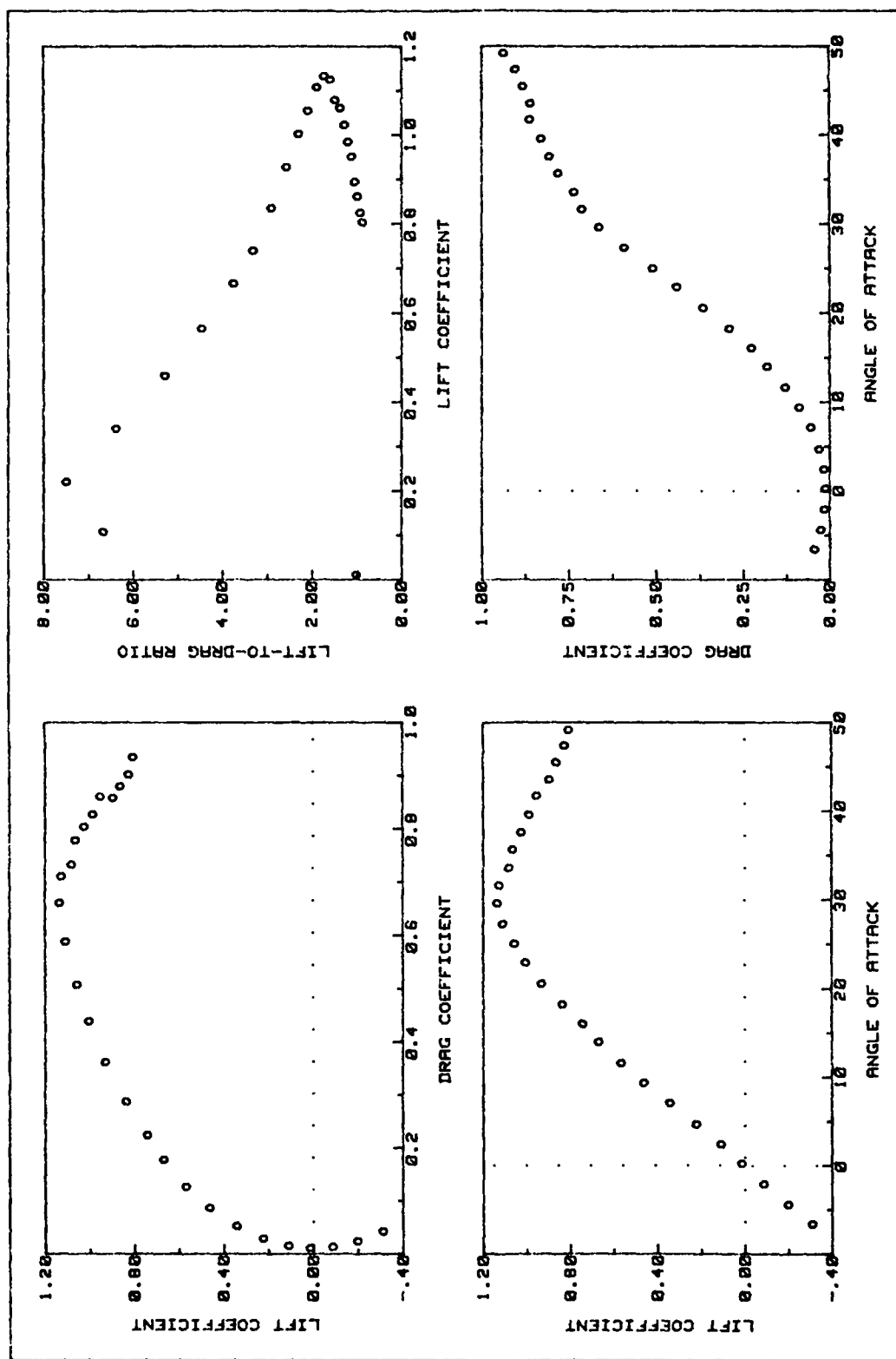


Fig A34. C2 Flap Lift and Drag Data (deployed 45 deg asymmetric)

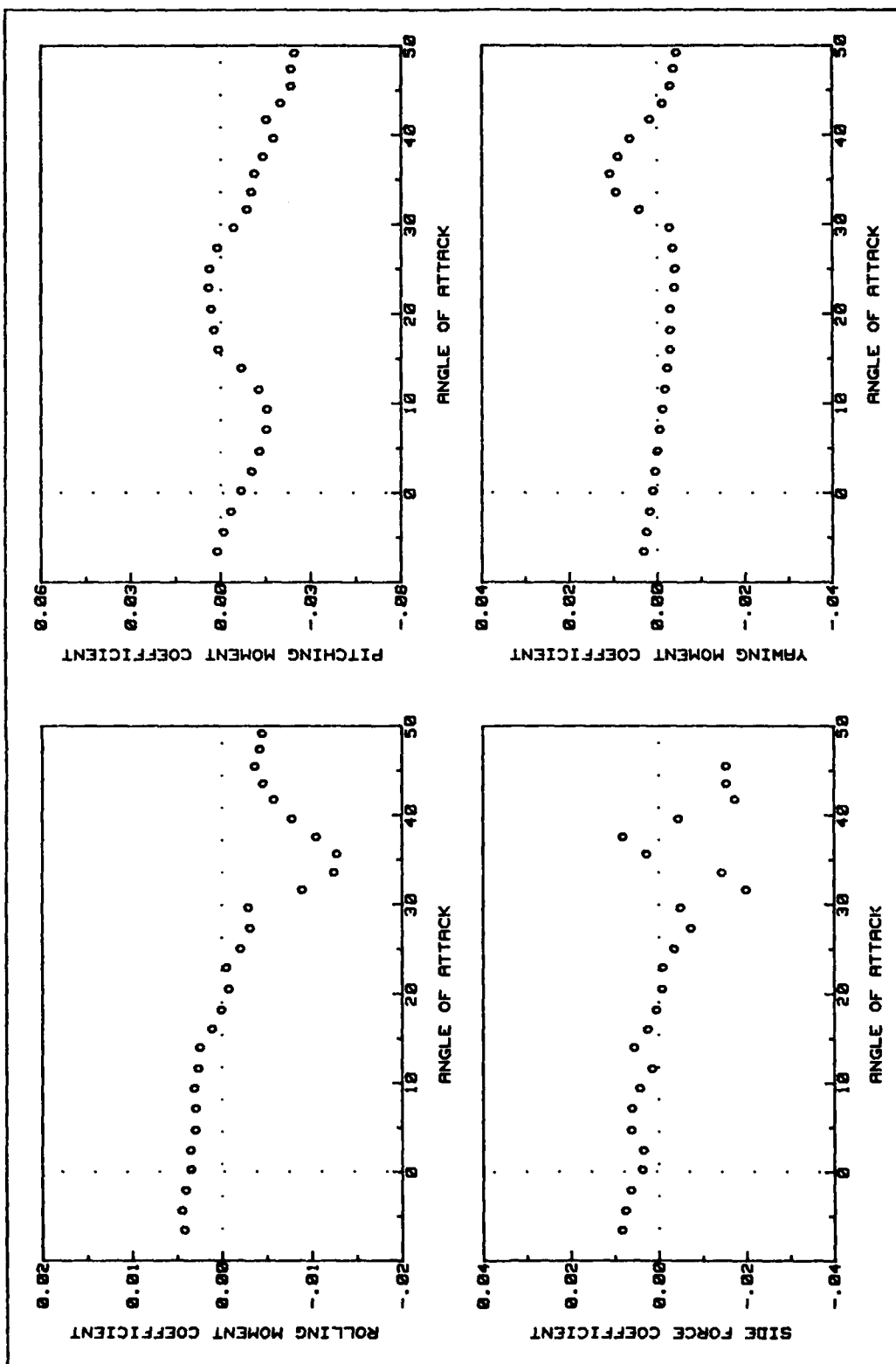


Fig A35. C2 Flap Side Force and Moments Data (deployed 45 deg asymmetric)

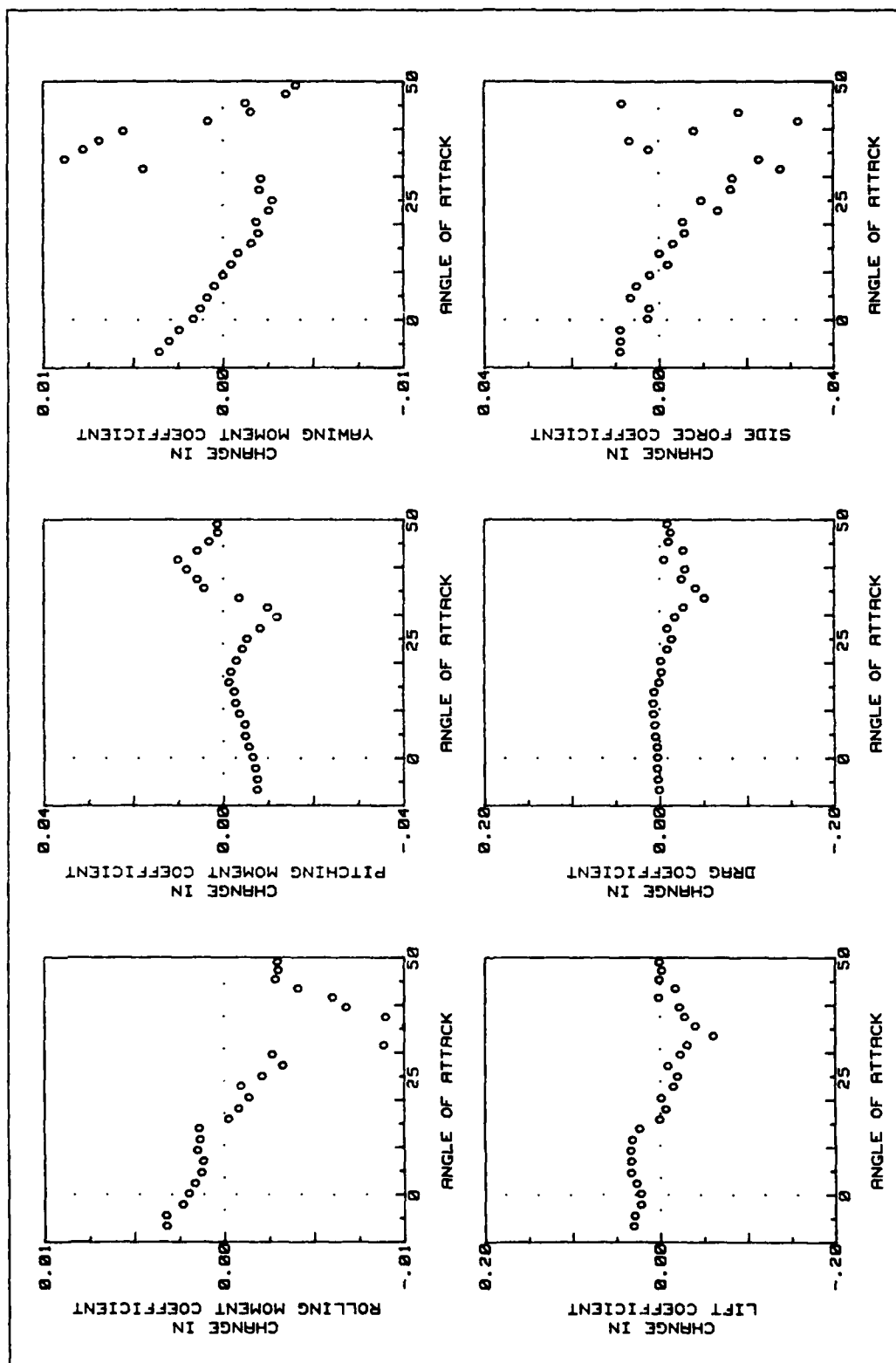


Fig A36. C2 Flap Force and Moment Changes (deployed 45 deg asymmetric)

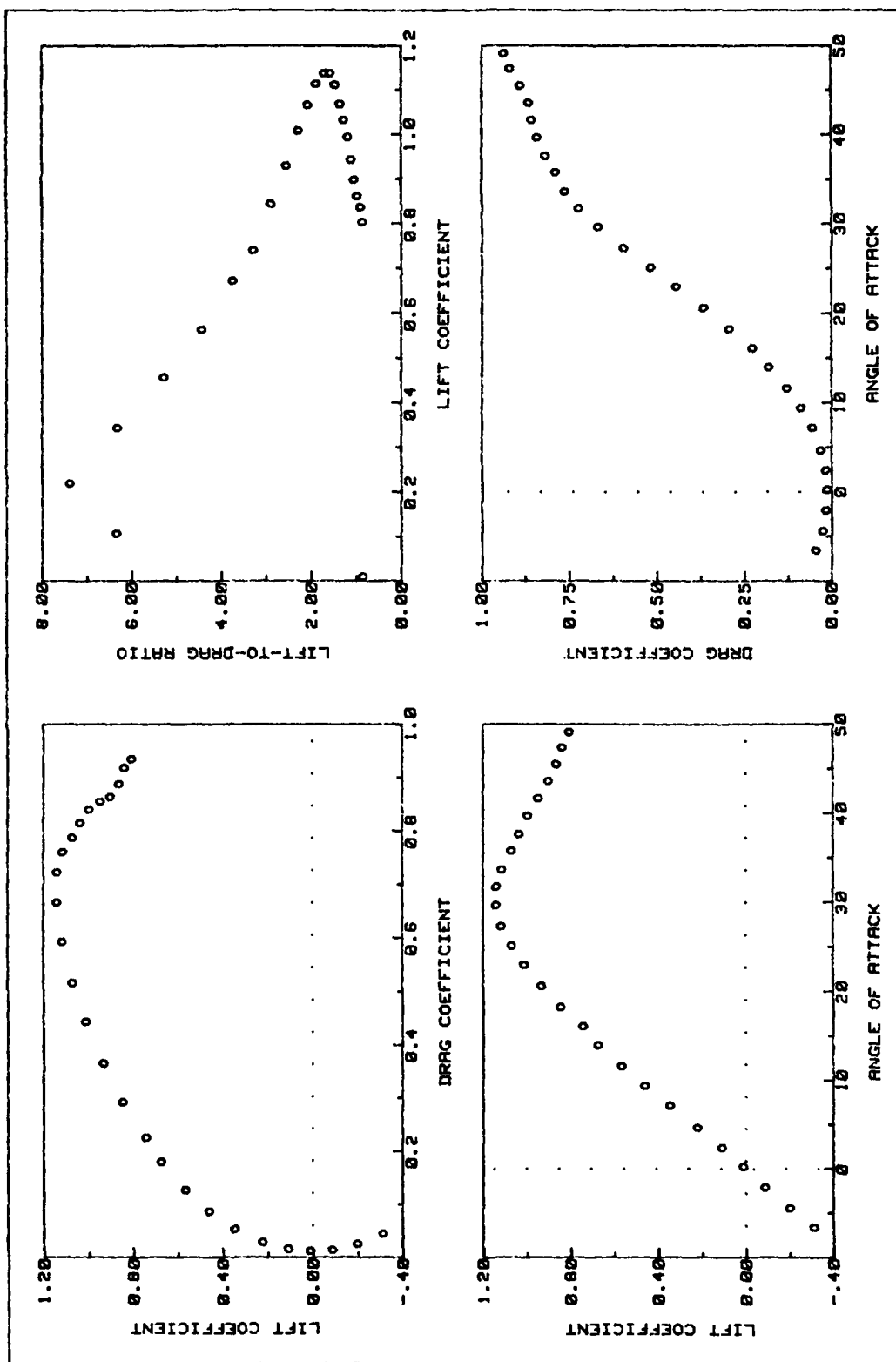


Fig A37. C2 Flap Lift and Drag Data (deployed 60 deg asymmetric)

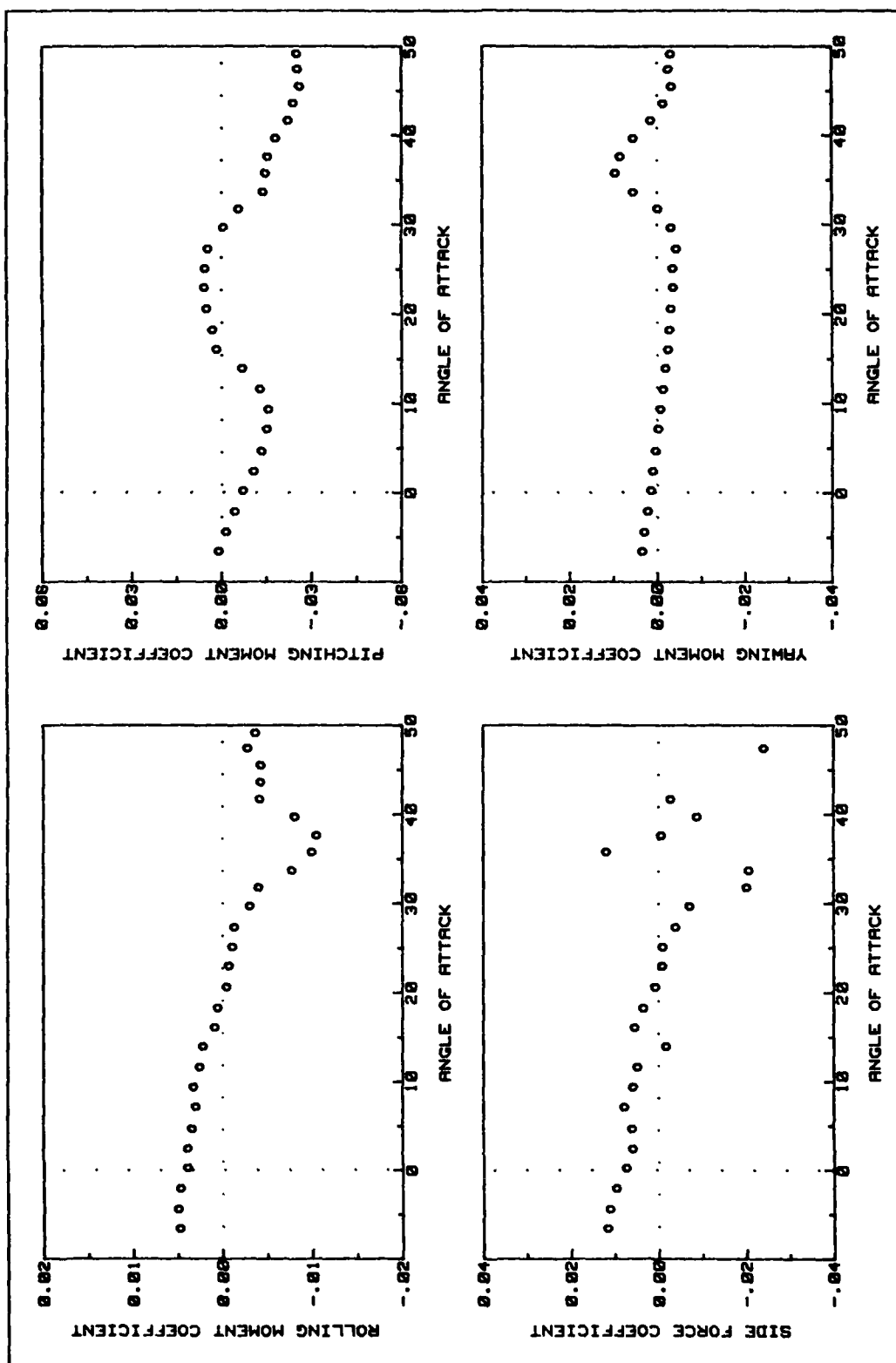


Fig A38. C2 Flap Side Force and Moments Data (deployed 60 deg asymmetric)

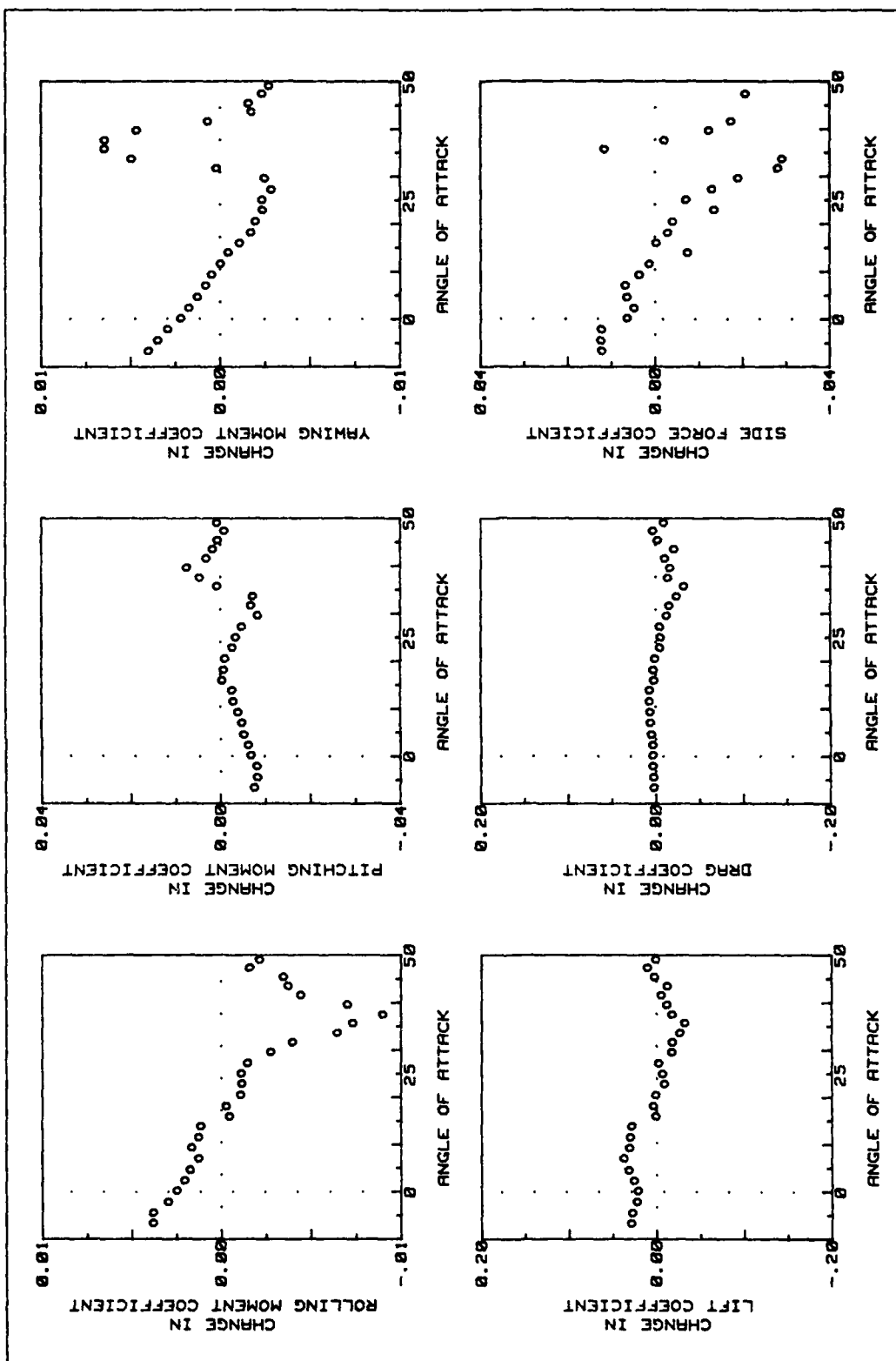


Fig A39. C2 Flap Force and Moment Changes (deployed 60 deg asymmetric)

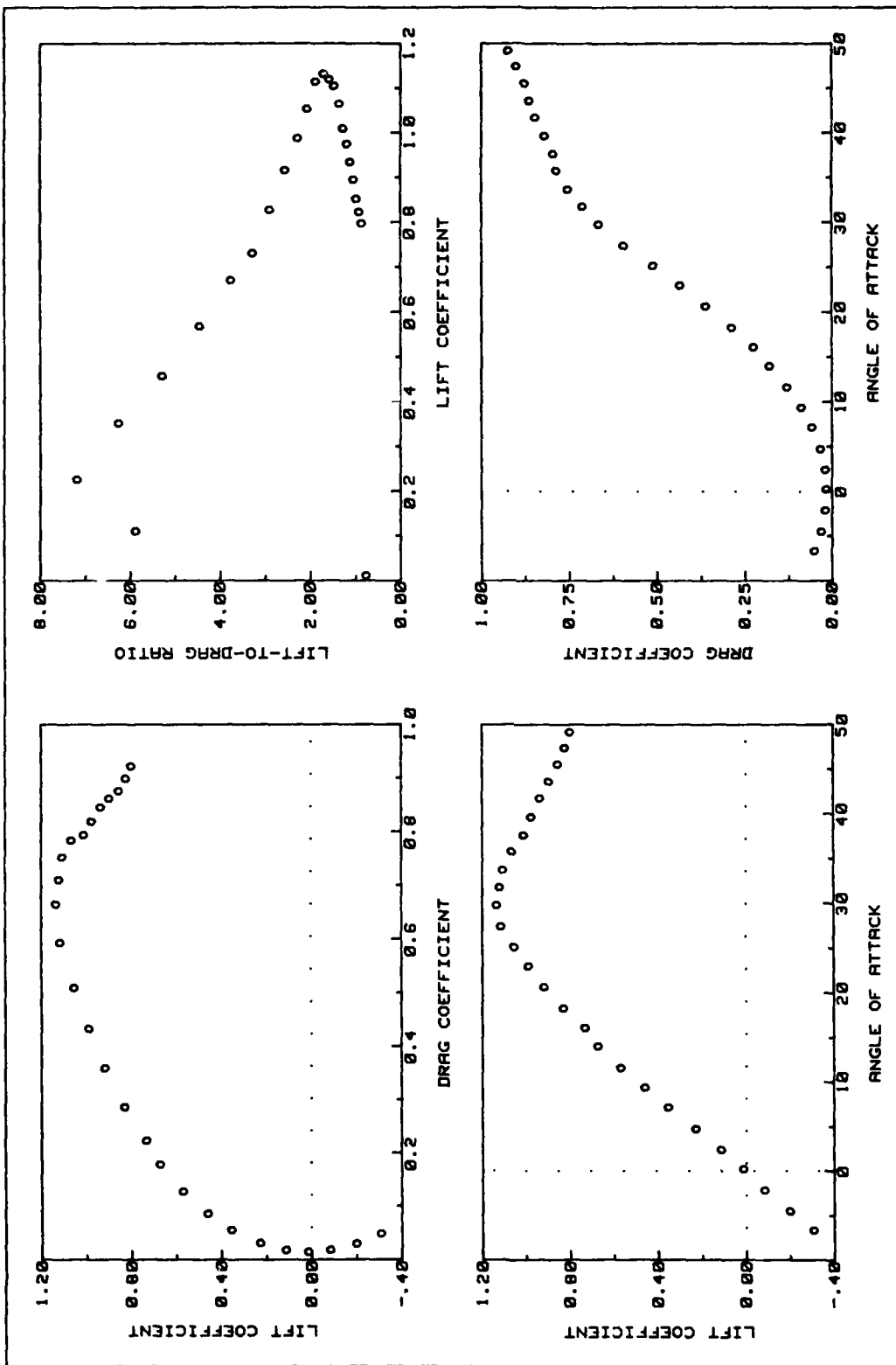


Fig A40. C2 Flap Lift and Drag Data (deployed 60 deg symmetric)

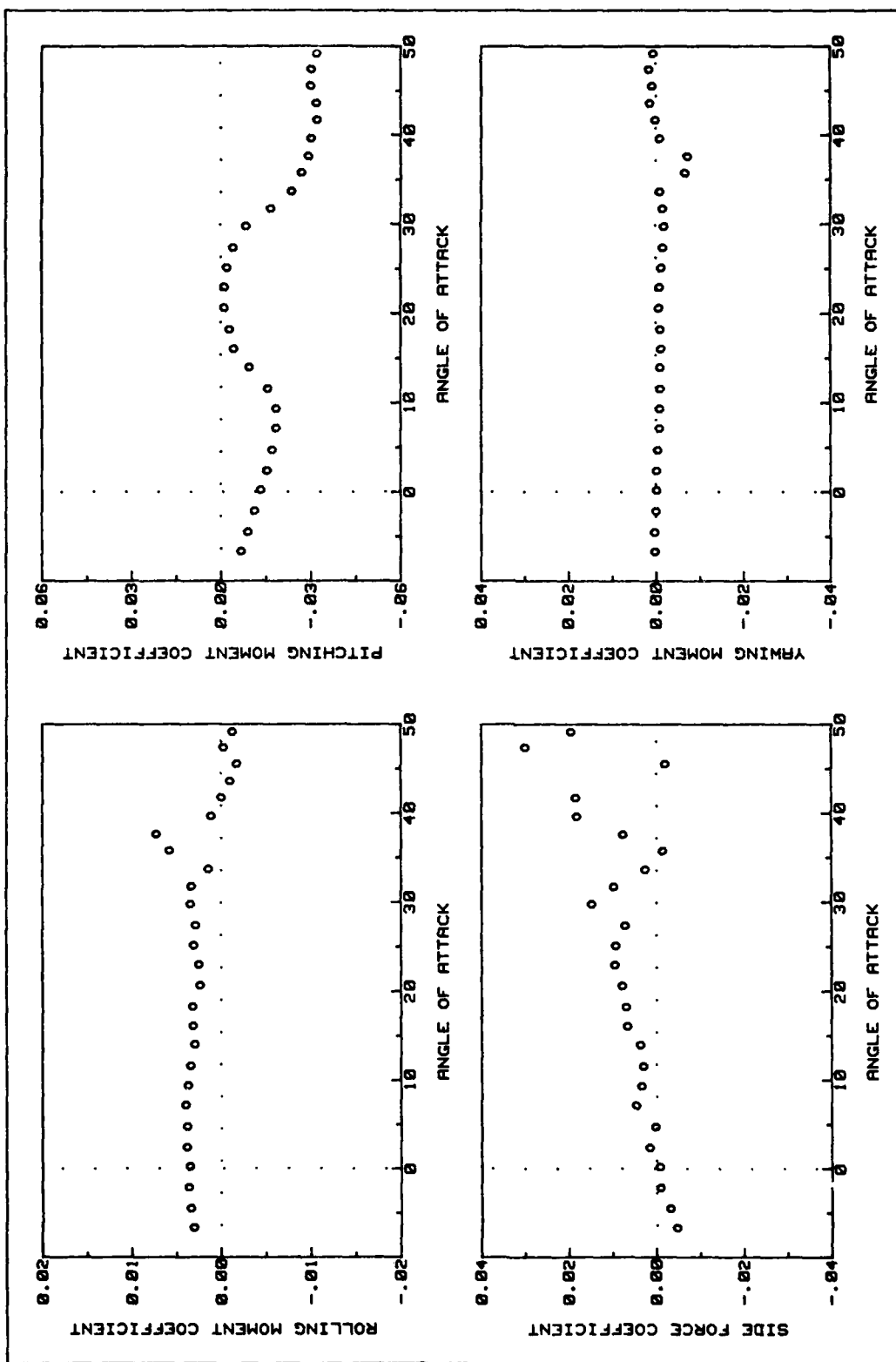


Fig A41. C2 Flap Side Force and Moments Data (deployed 60 deg symmetric)

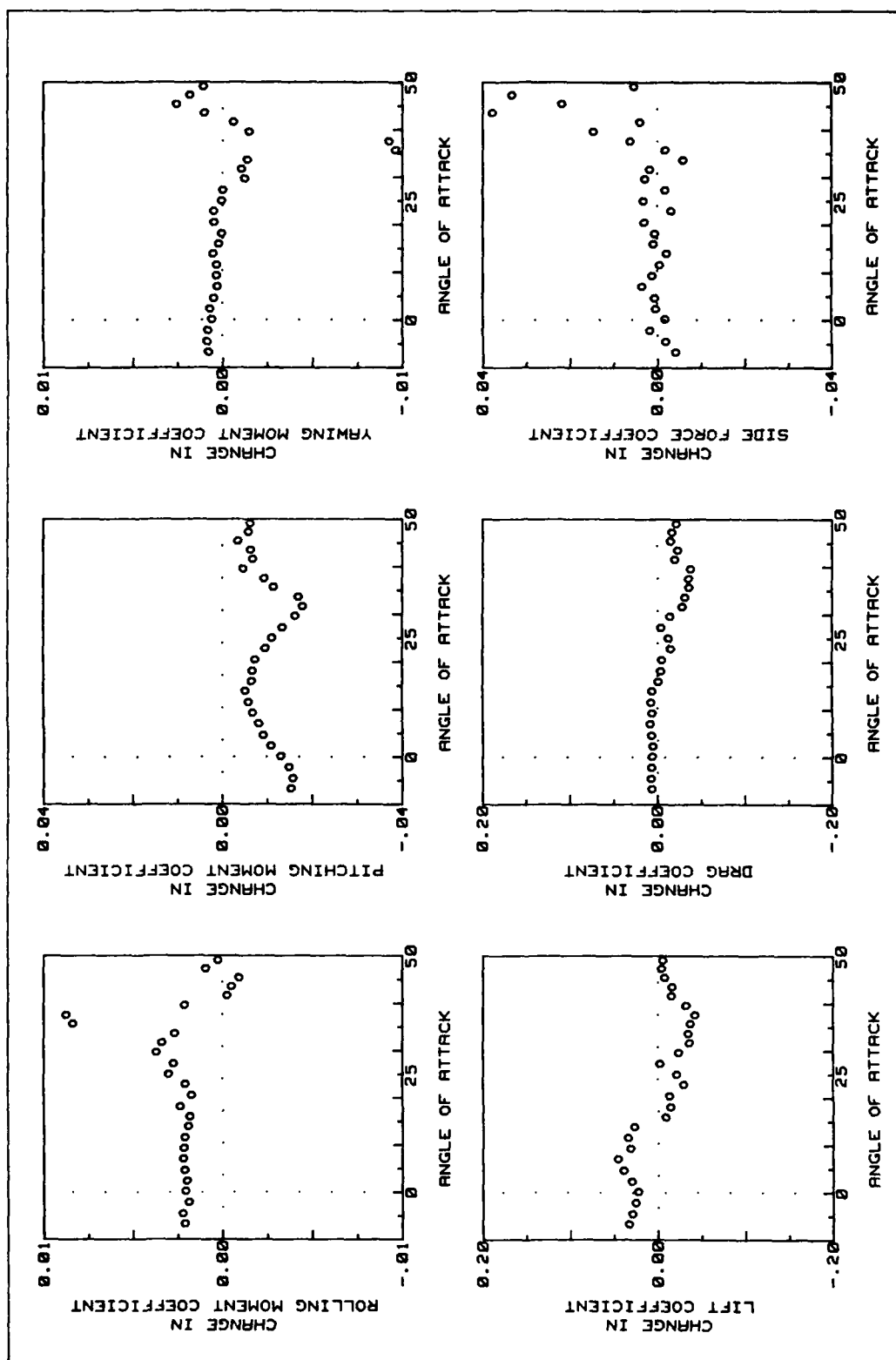


Fig A42. C2 Flap Force and Moment Changes (deployed 60 deg symmetric)

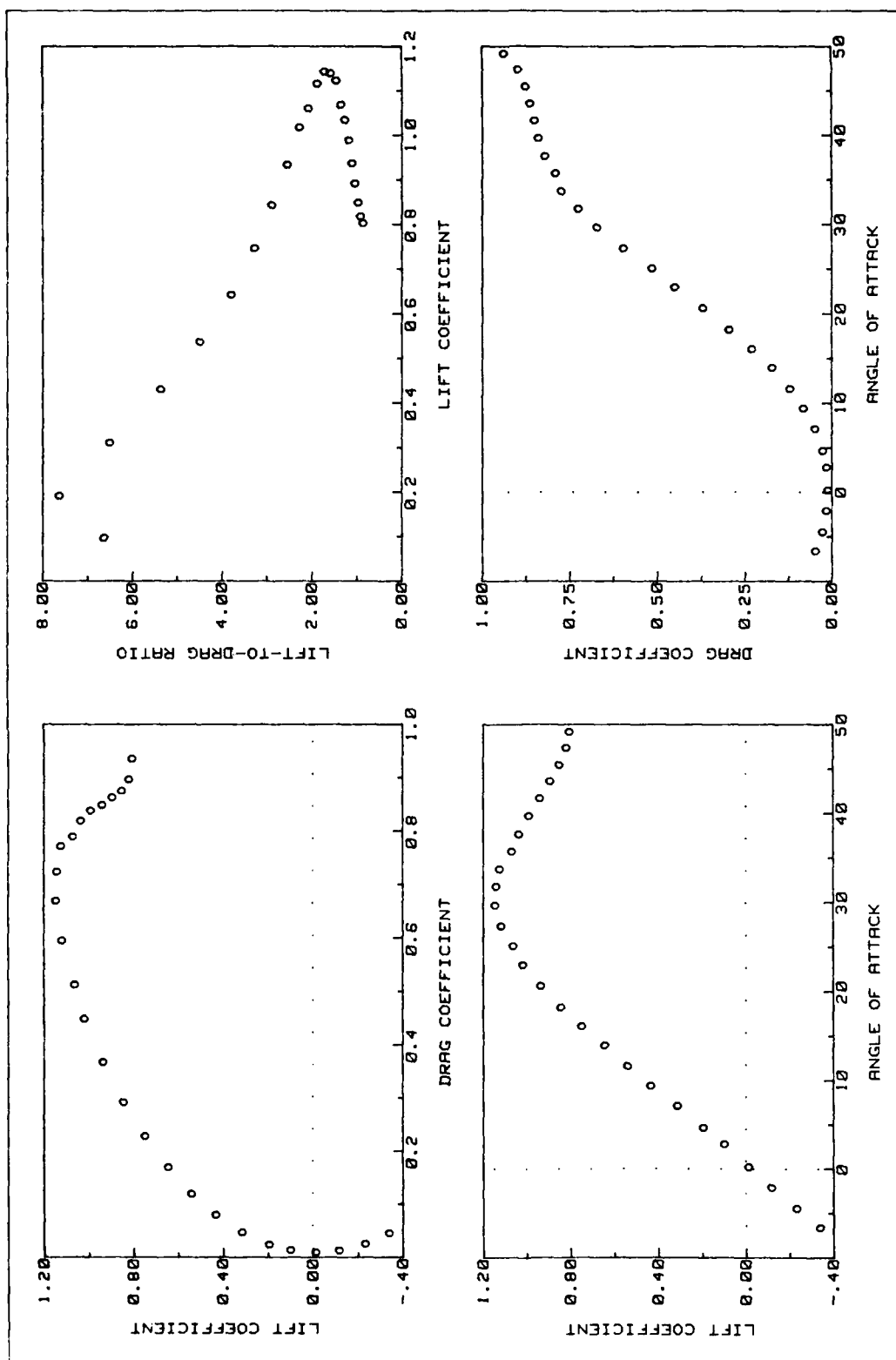


Fig A43. C2 Flap Lift and Drag Data (deployed 75 deg asymmetric)

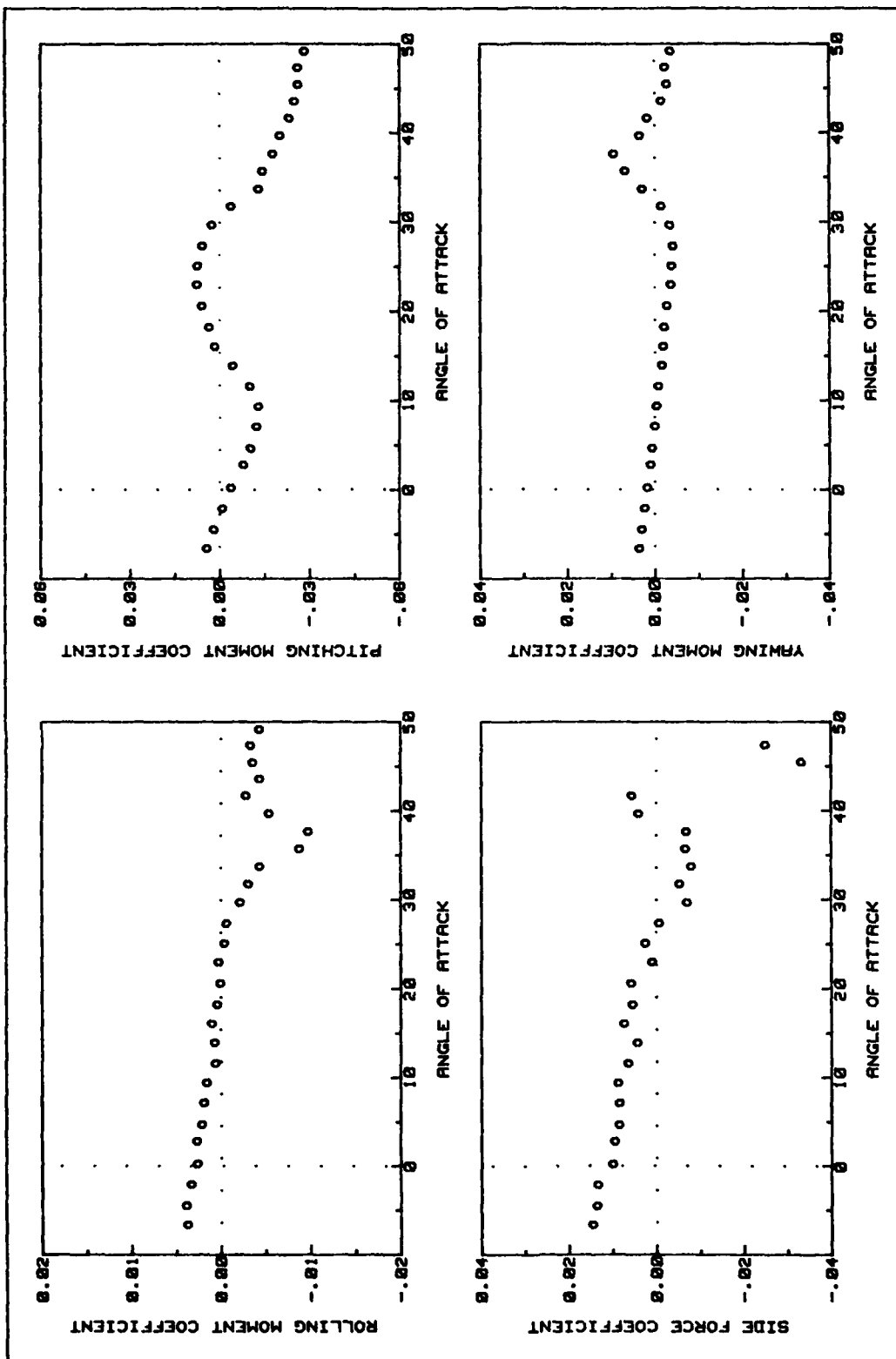


Fig R44. C2 Flap Side Force and Moments Data (deployed 75 deg asymmetric)

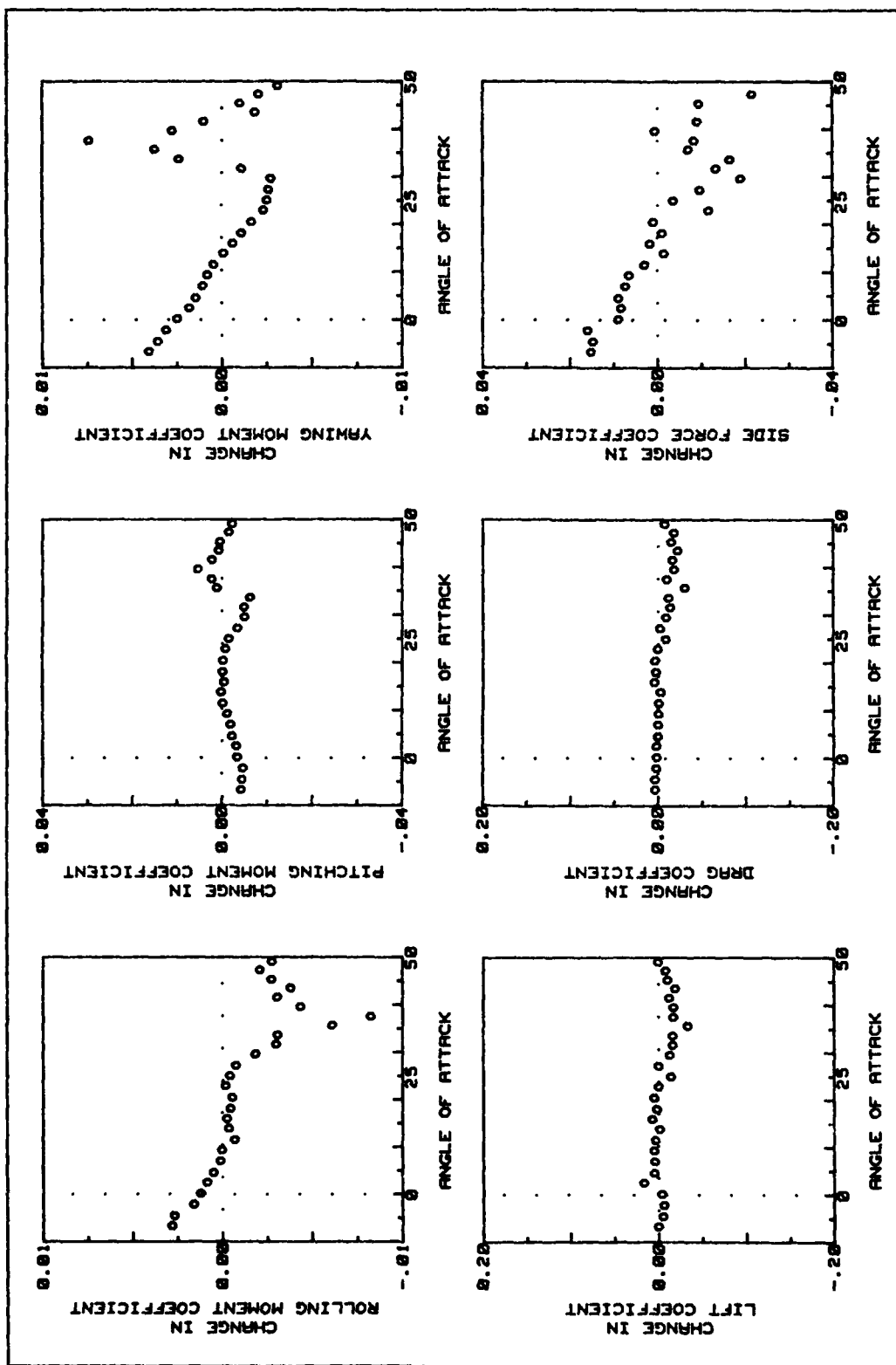


Fig A45. C2 Flap Force and Moment Changes (deployed 75 deg asymmetric)

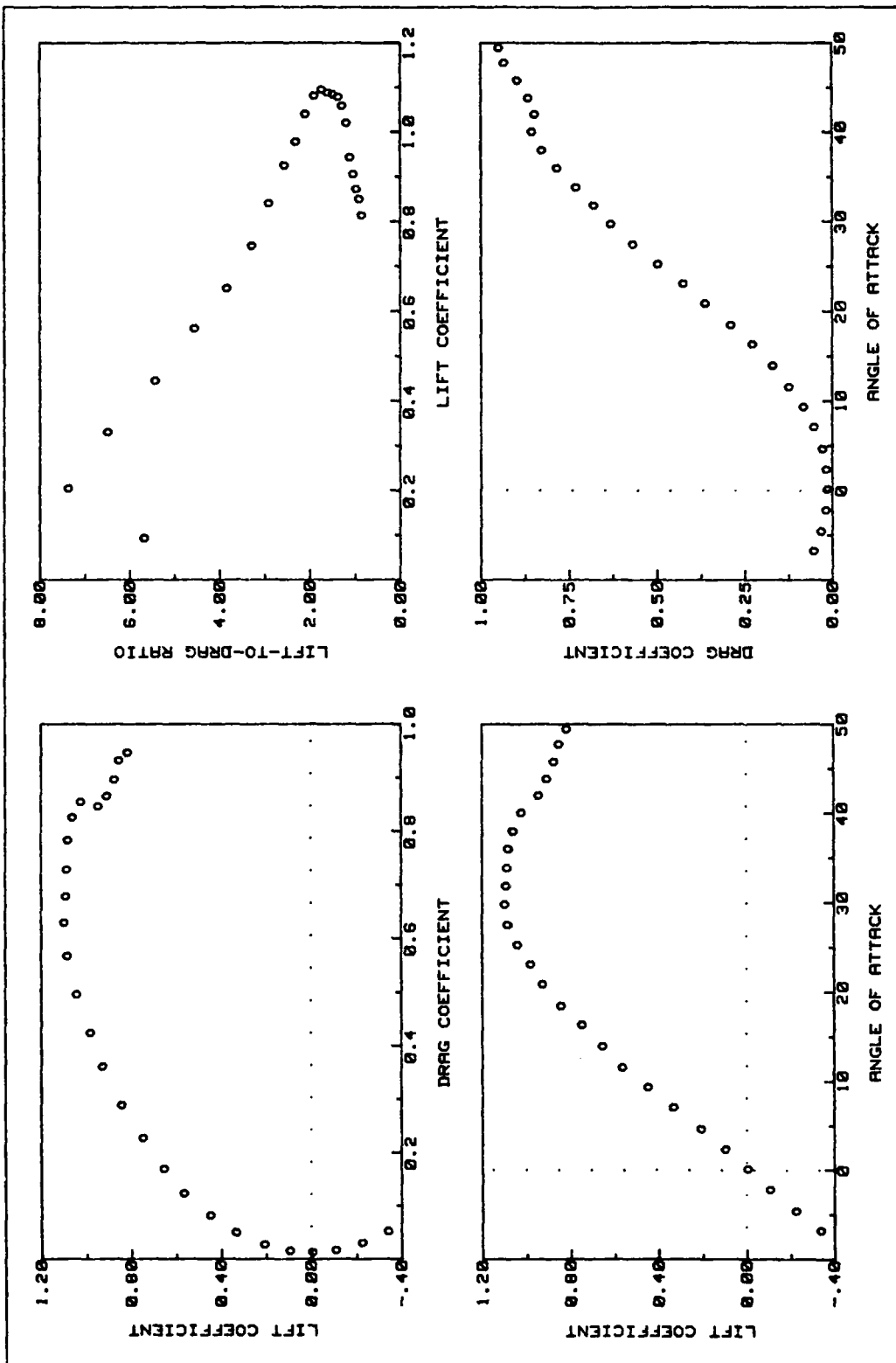


Fig A46. C3 Flap Lift and Drag Data (deployed 45 deg asymmetric)

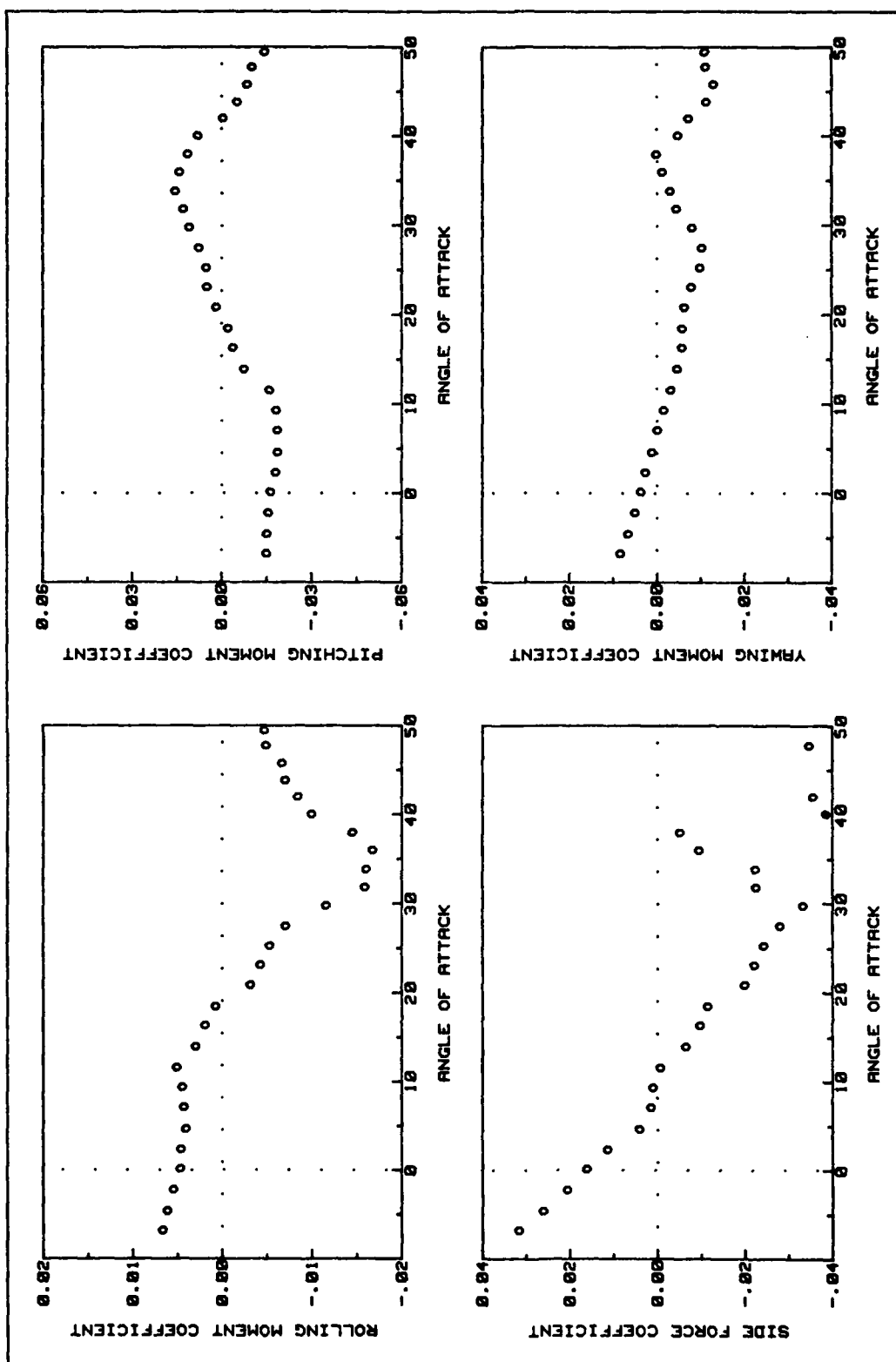


Fig A47. C3 Flap Side Force and Moments Data (deployed 45 deg asymmetric)

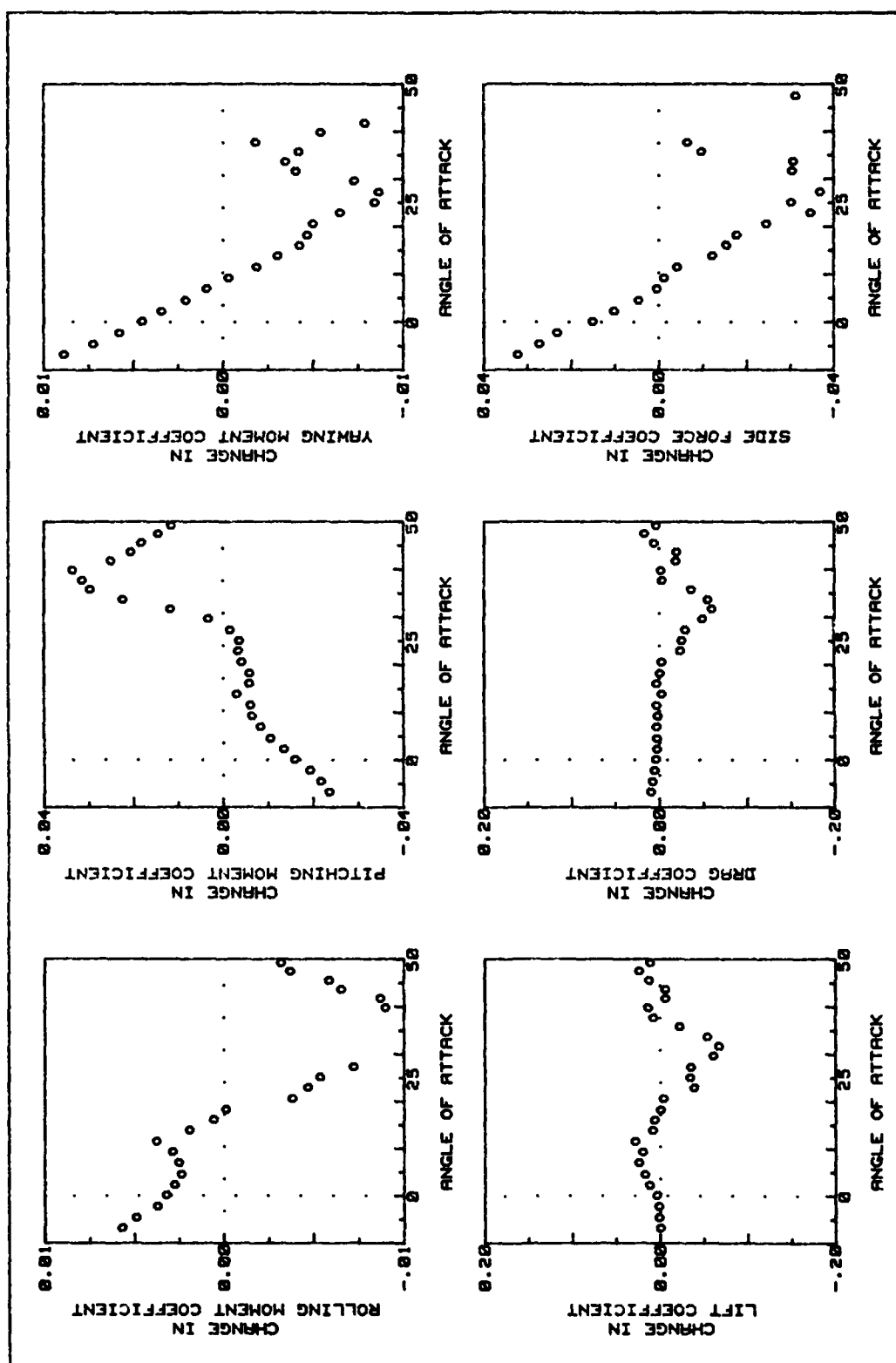


Fig A48. C3 Flap Force and Moment Changes (deployed 45 deg asymmetric)

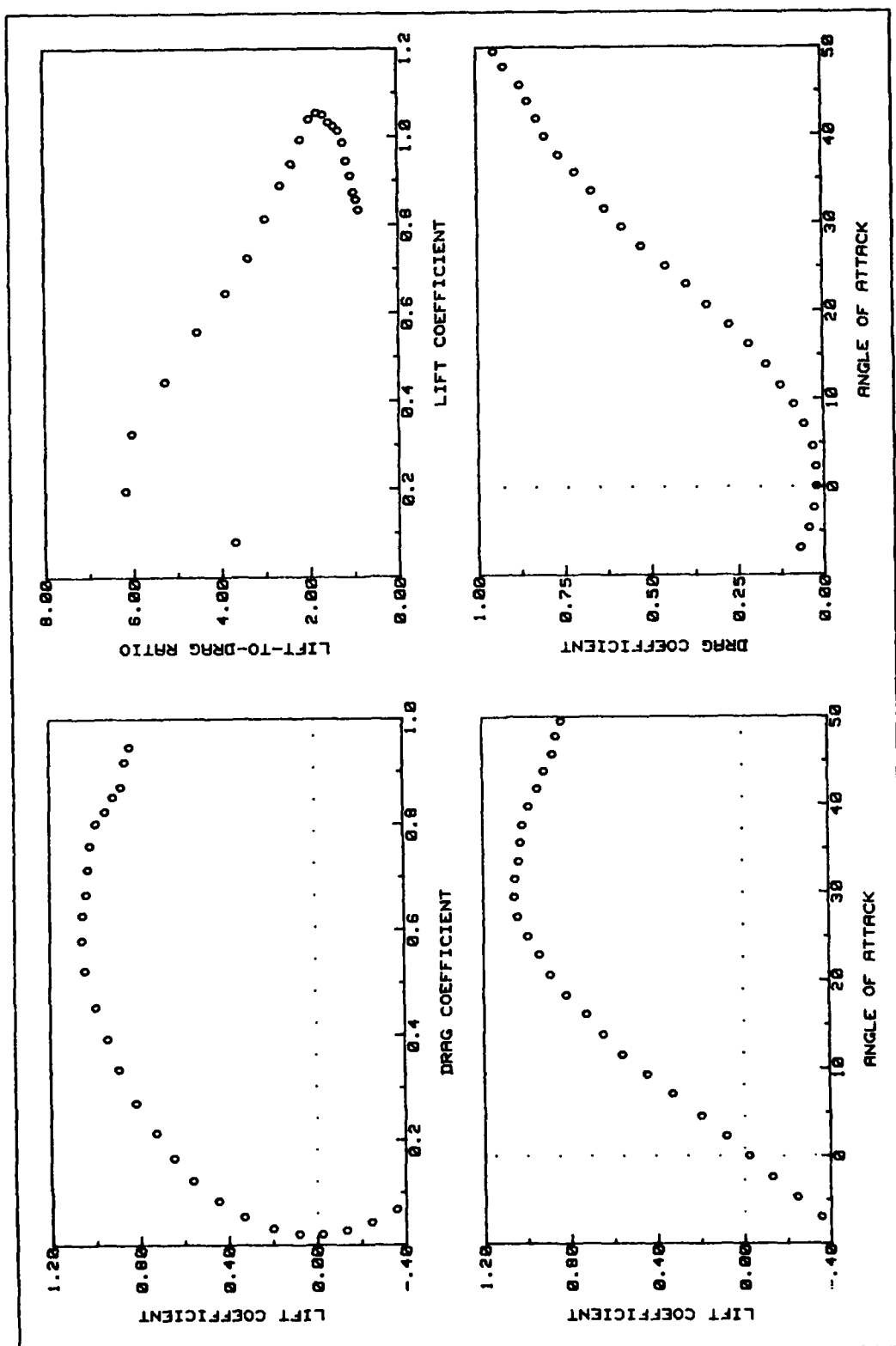


Fig A49. C3 Flap Lift and Drag Data (deployed 45 deg symmetric)

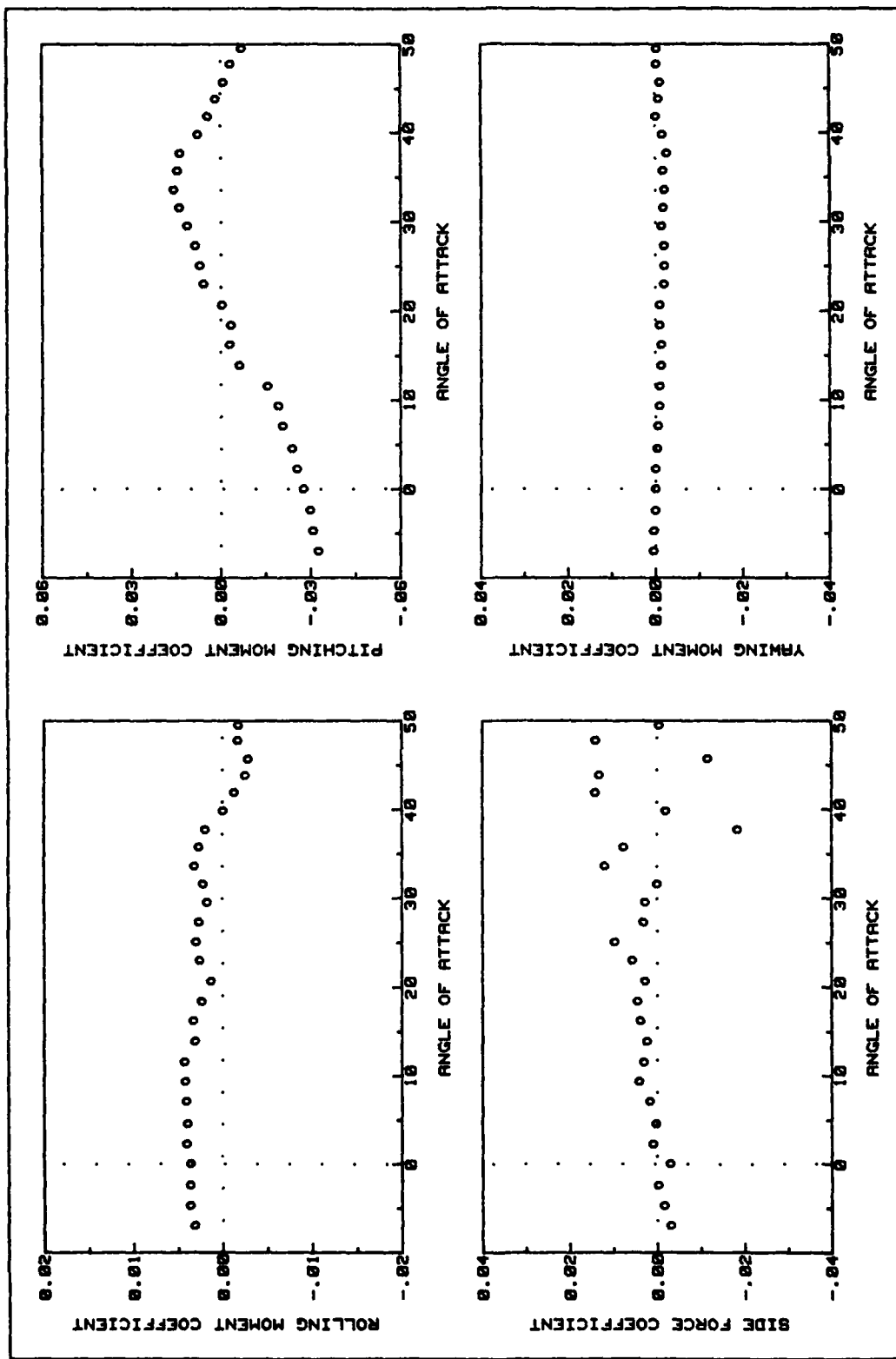


Fig A50. C3 Flap Side Force and Moments Data (deployed 45 deg symmetric)

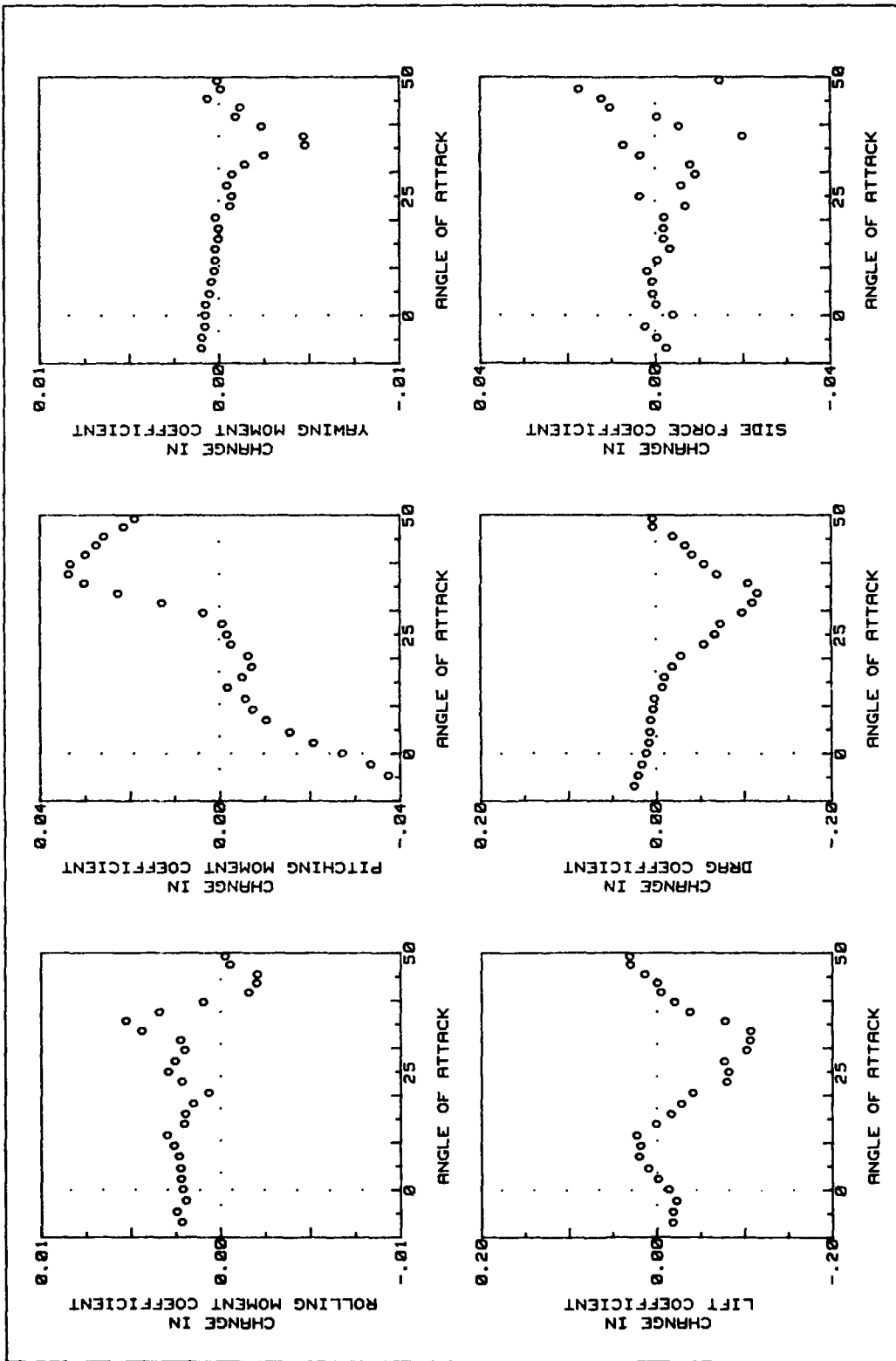


Fig A51. C3 Flap Force and Moment Changes (deployed 45 deg symmetric)

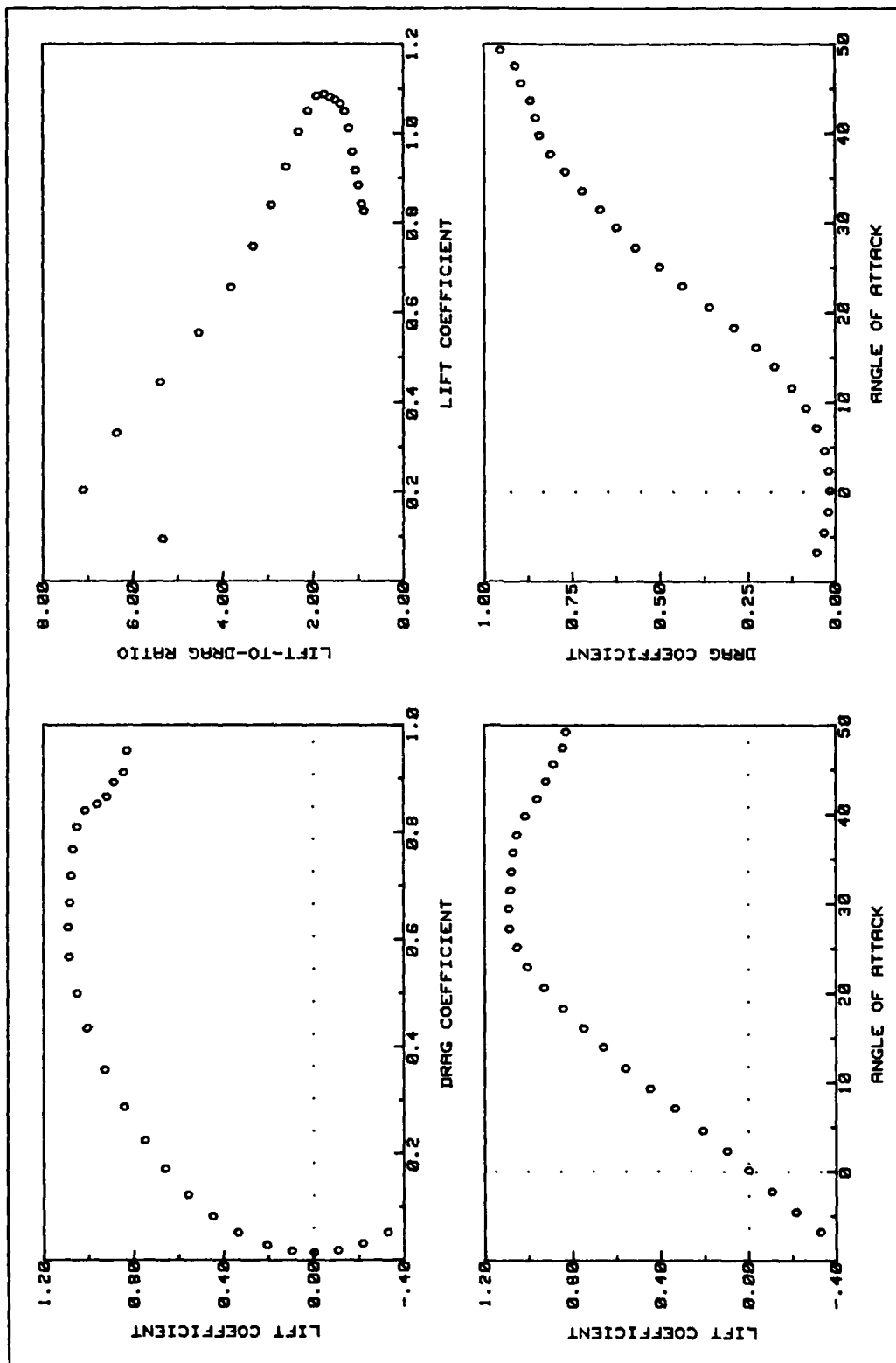


Fig A52. C3 Flap Lift and Drag Data (deployed 60 deg asymmetric)

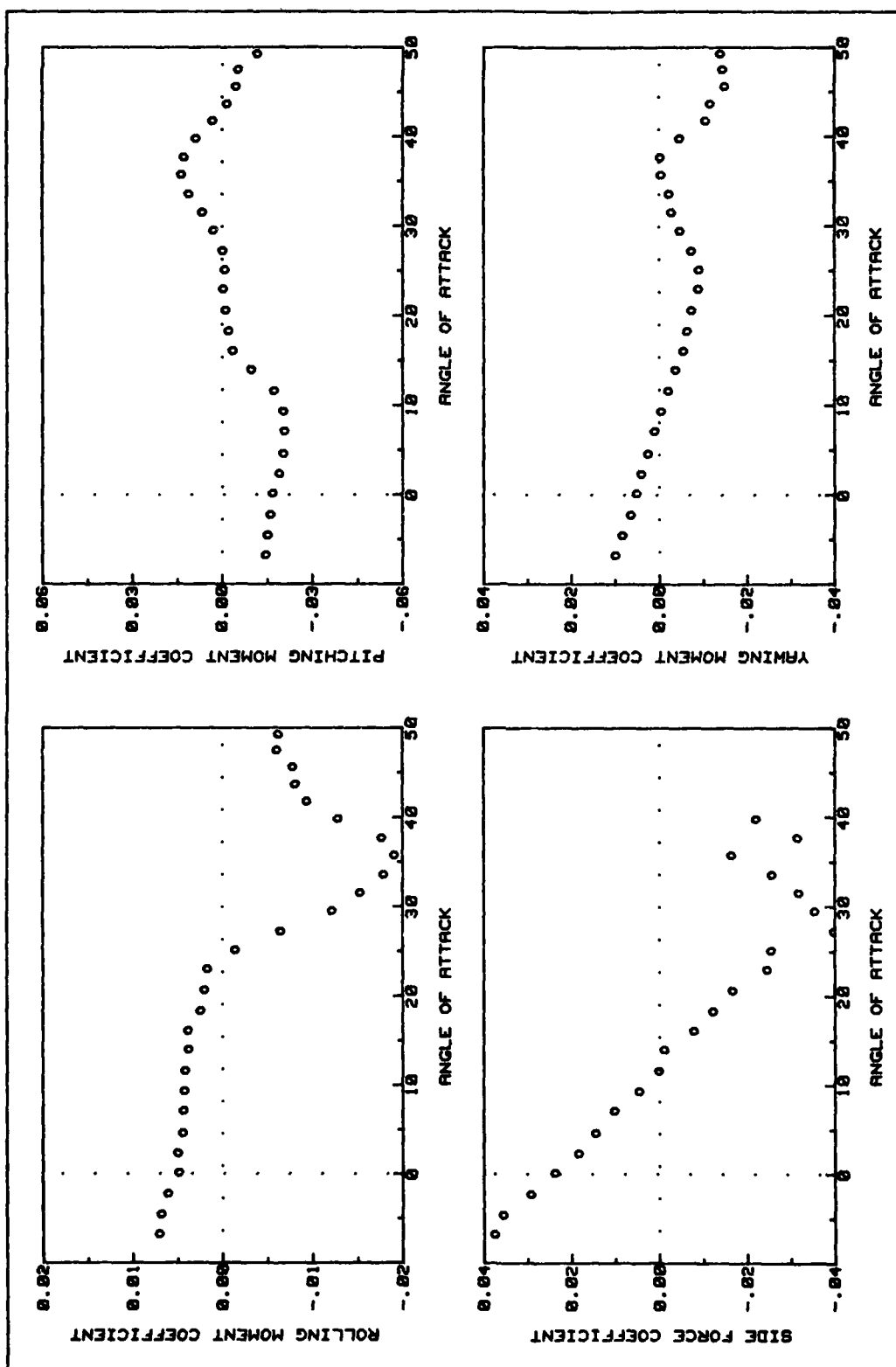


Fig A53. C3 Flap Side Force and Moments Data (deployed 60 deg asymmetric)

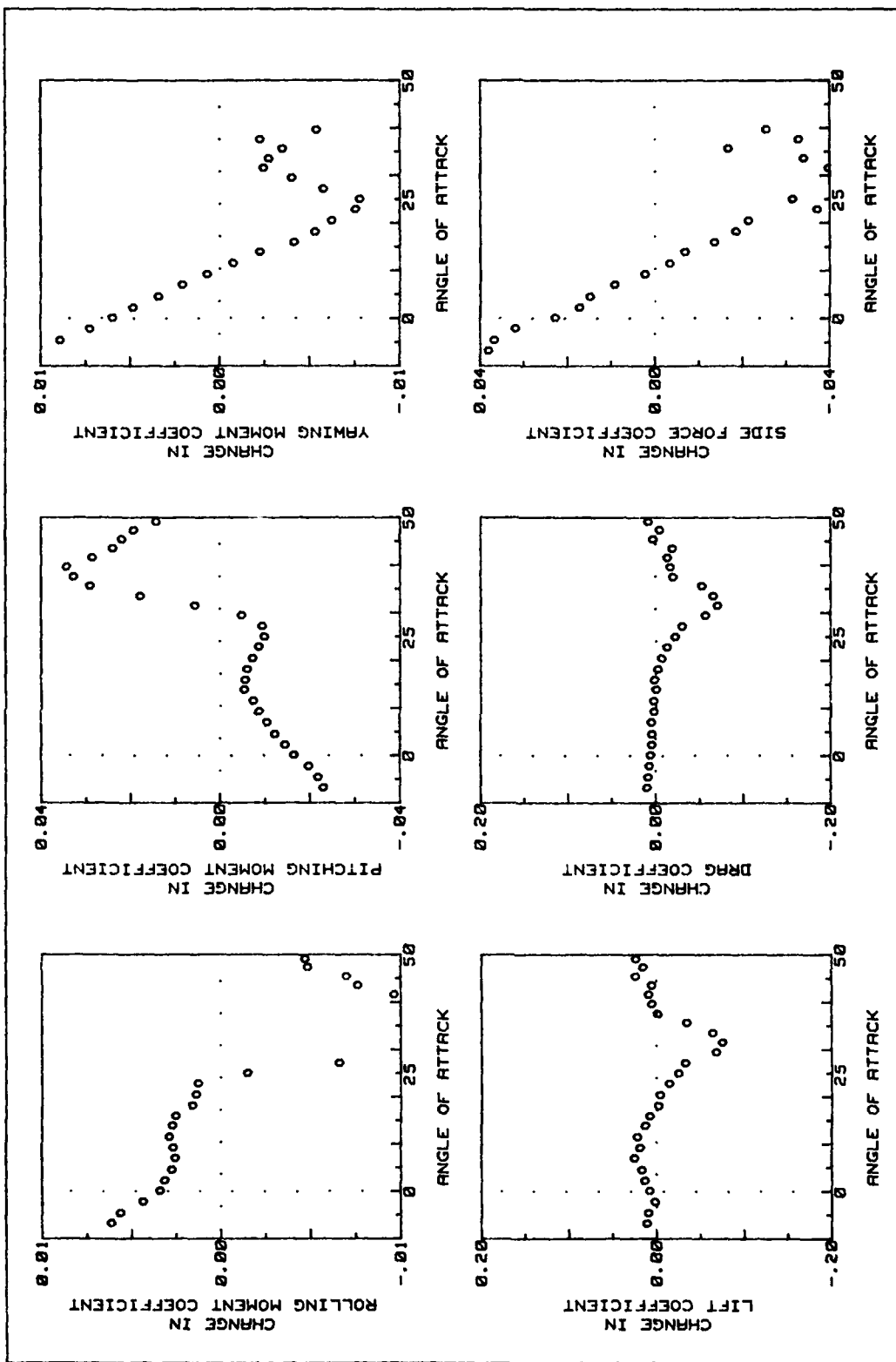


Fig A54. C3 Flap Force and Moment Changes (deployed 60 deg asymmetric)

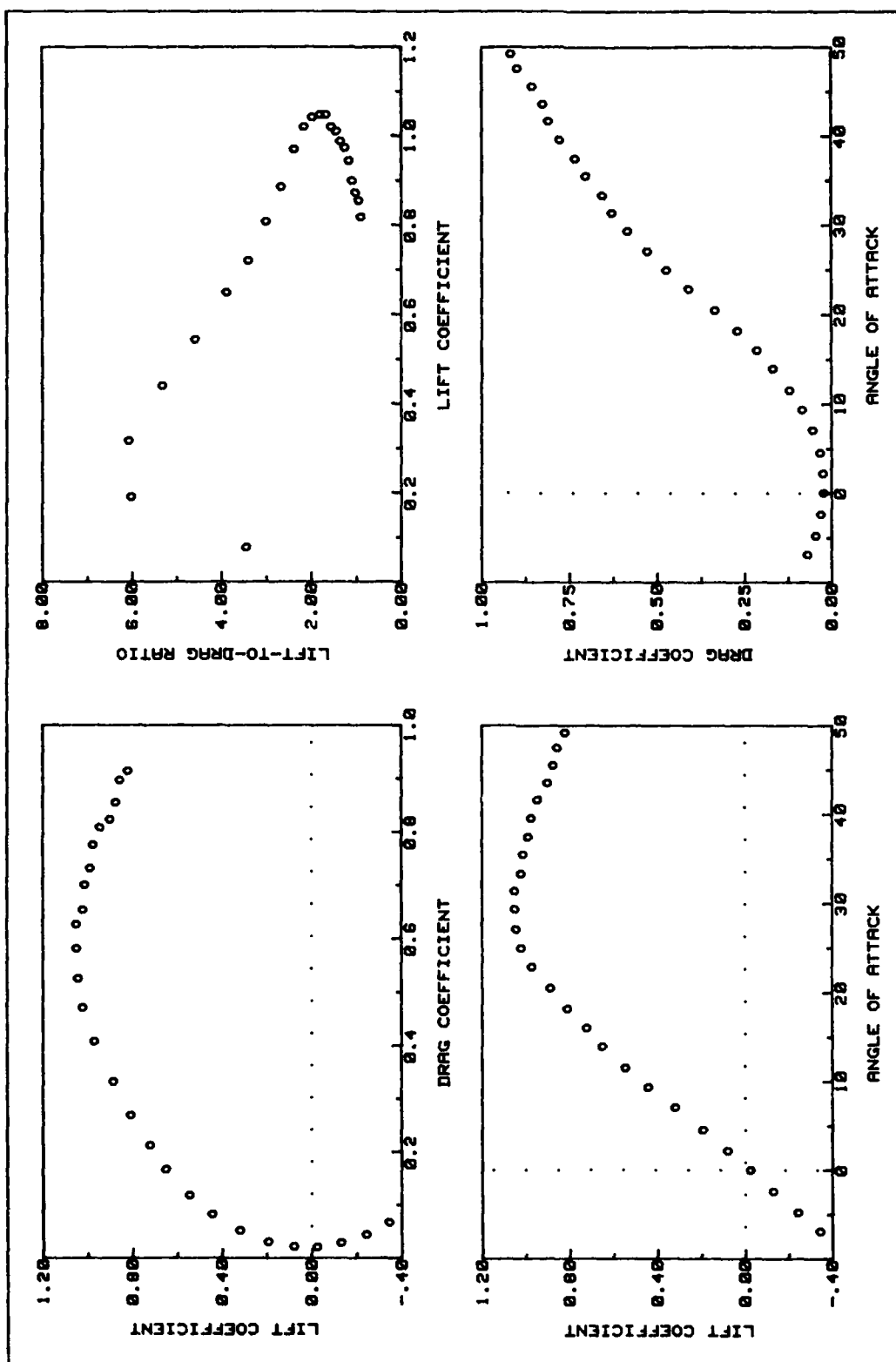


Fig A55. C3 Flap Lift and Drag Data (deployed 60 deg symmetric)

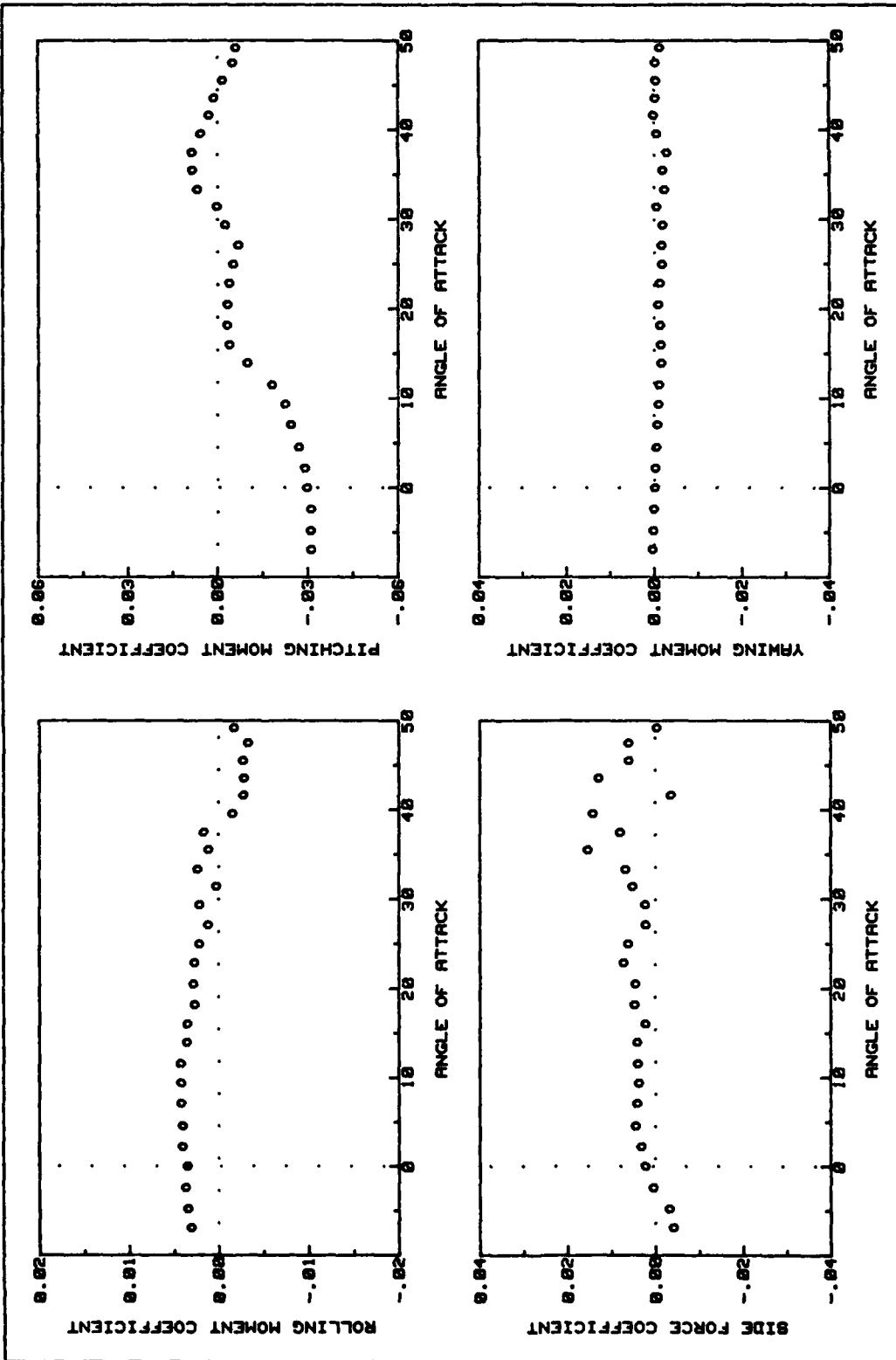


Fig A56. C3 Flap Side Force and Moments Data (deployed 60 deg symmetric)

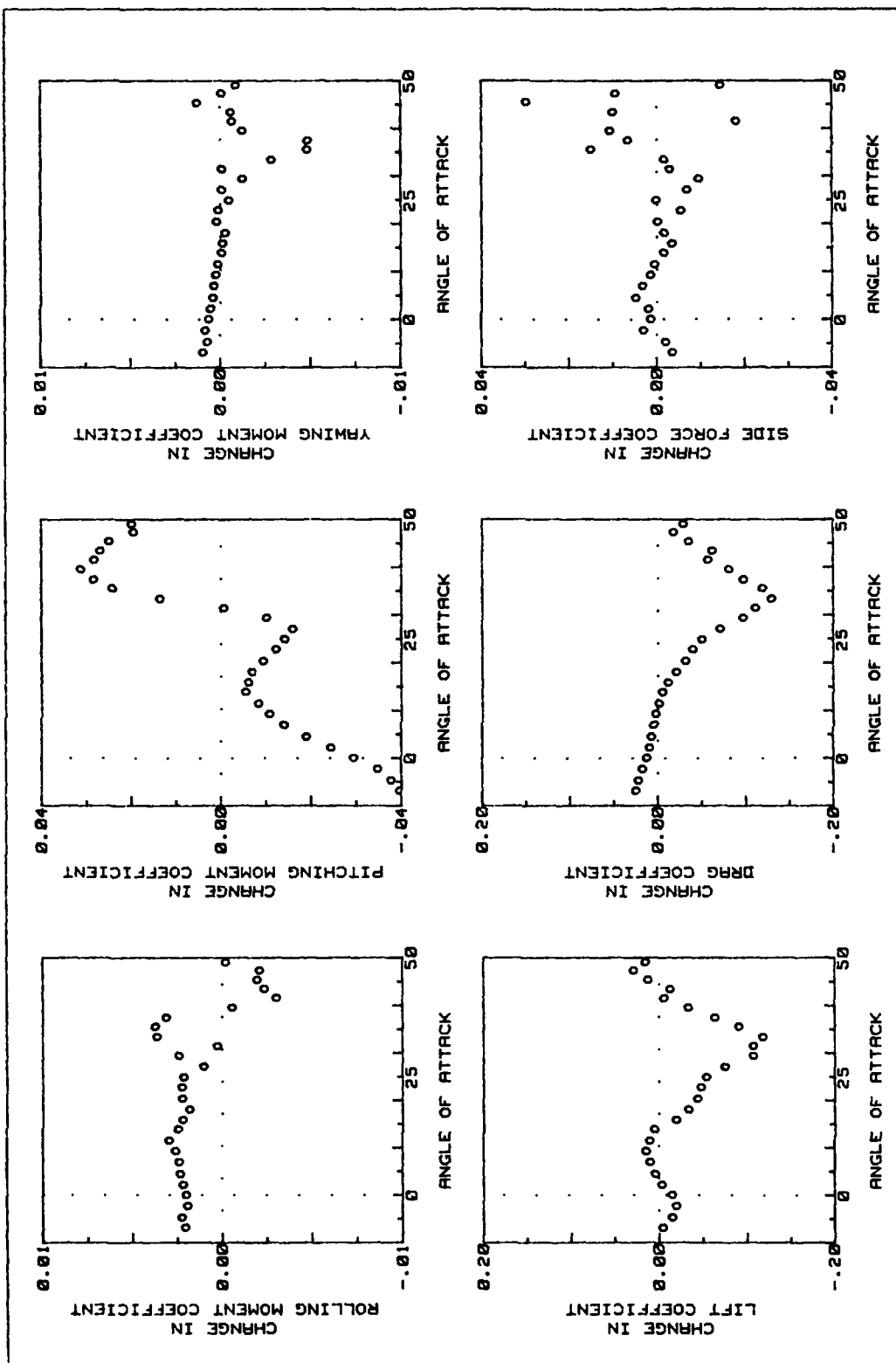


Fig A57. C3 Flap Force and Moment Changes (deployed 60 deg symmetric)

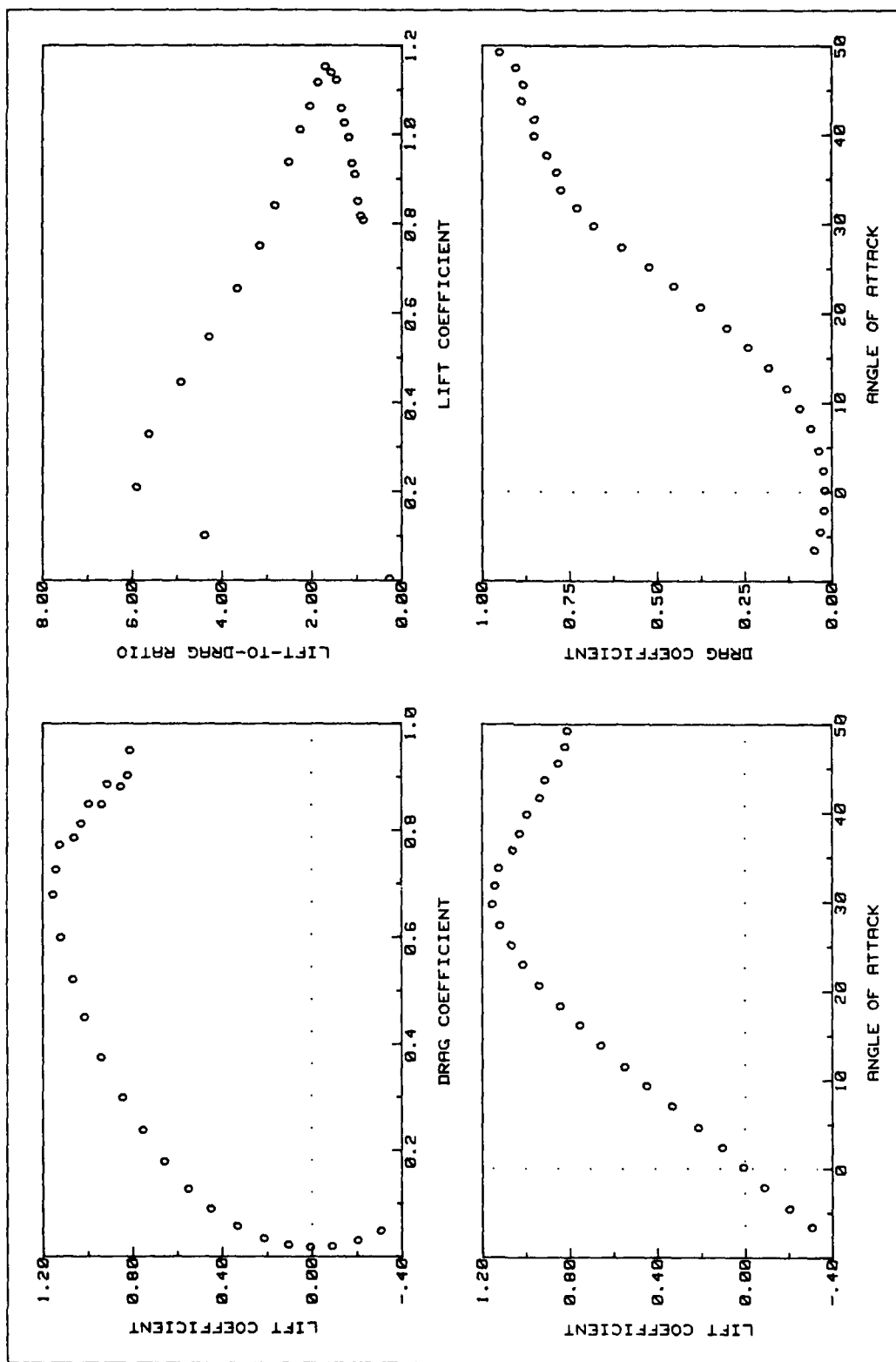


Fig A58. C4 Flap Lift and Drag Data (deployed 30 deg asymmetric)

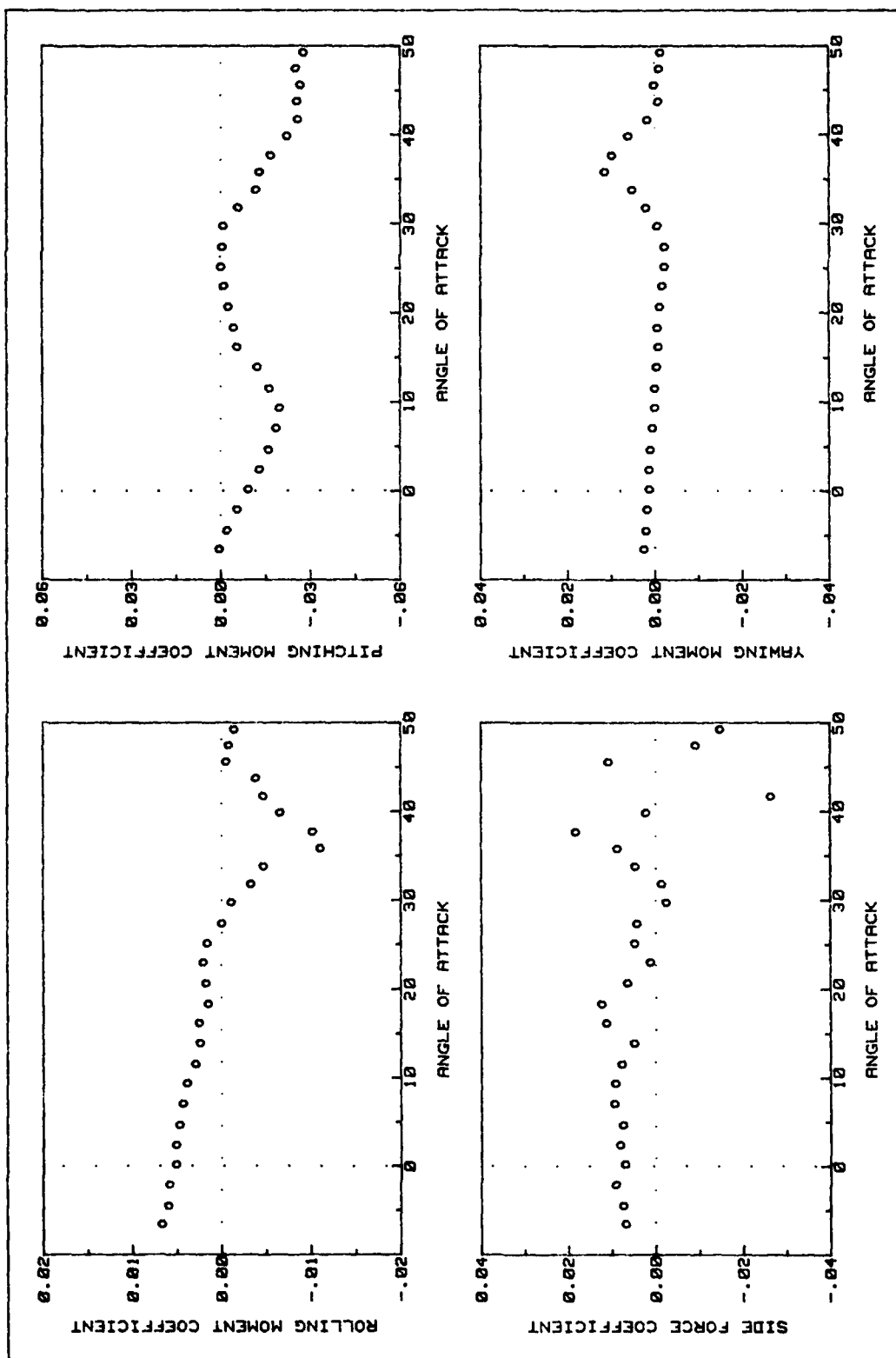


Fig A59. C4 Flap Side Force and Moments Data (deployed 30 deg asymmetric)

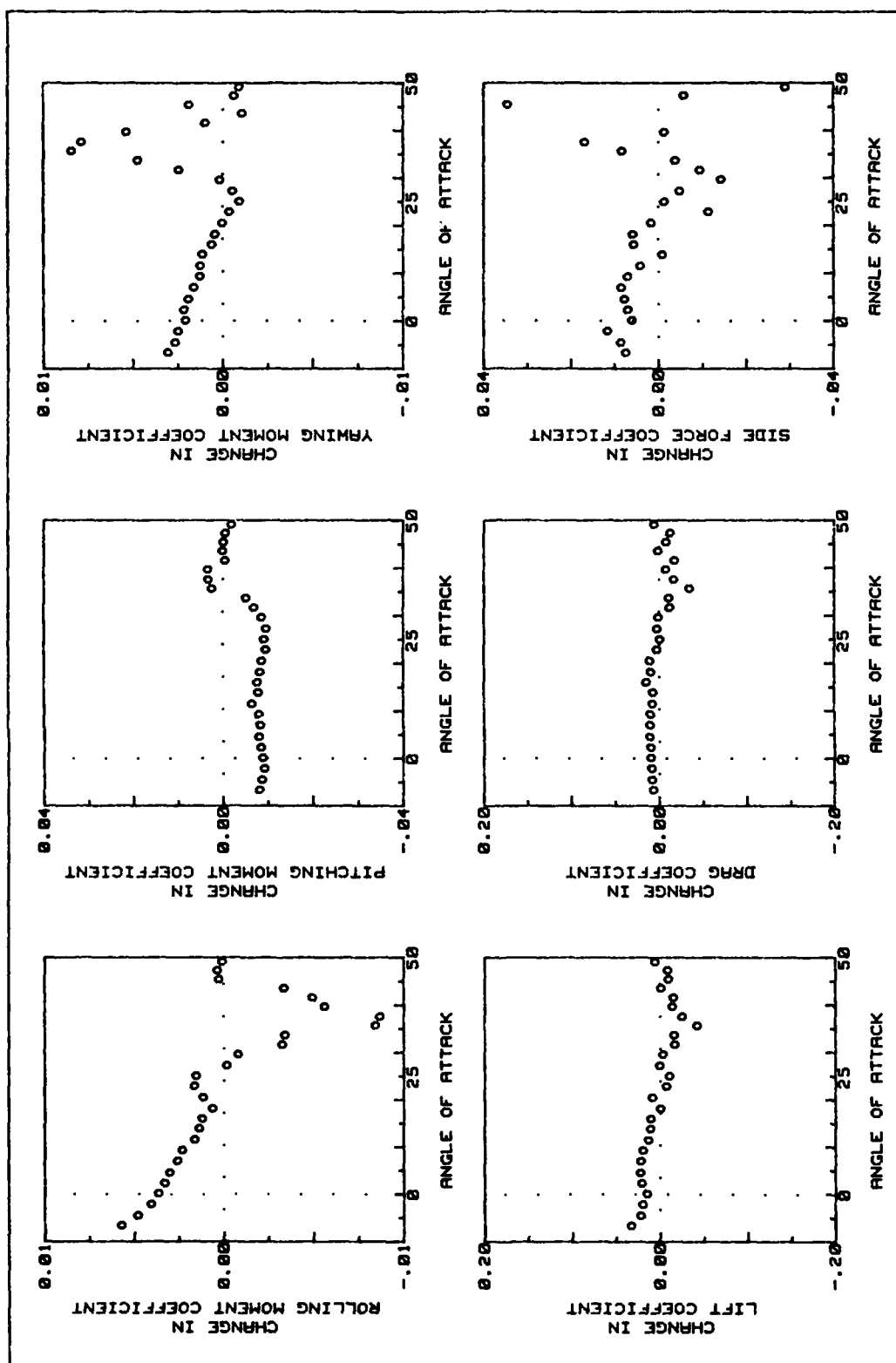


Fig A60. C4 Flap Force and Moment Changes (deployed 30 deg asymmetric)

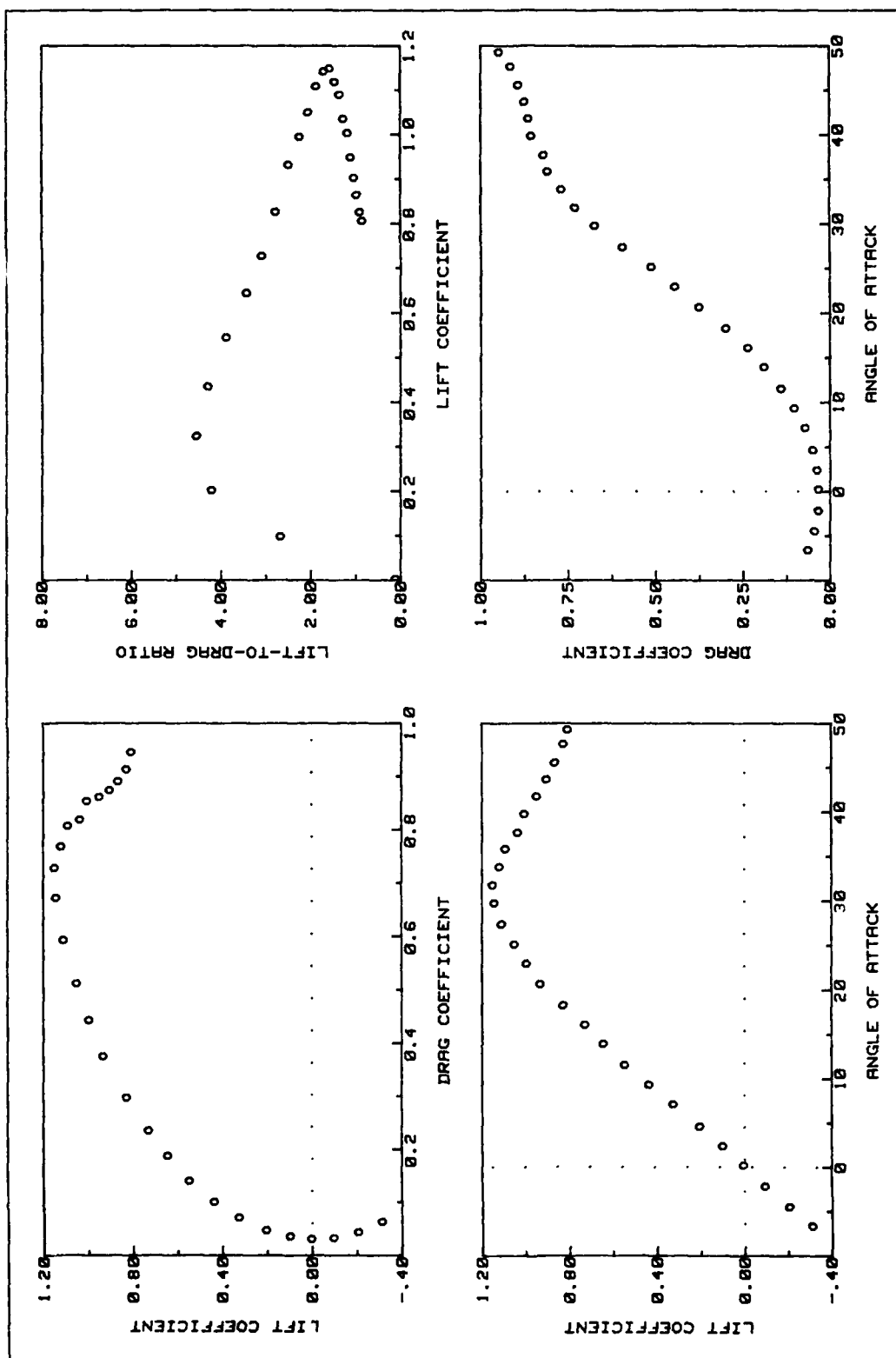


Fig A61. C4 Flap Lift and Drag Data (deployed 30 deg symmetric)

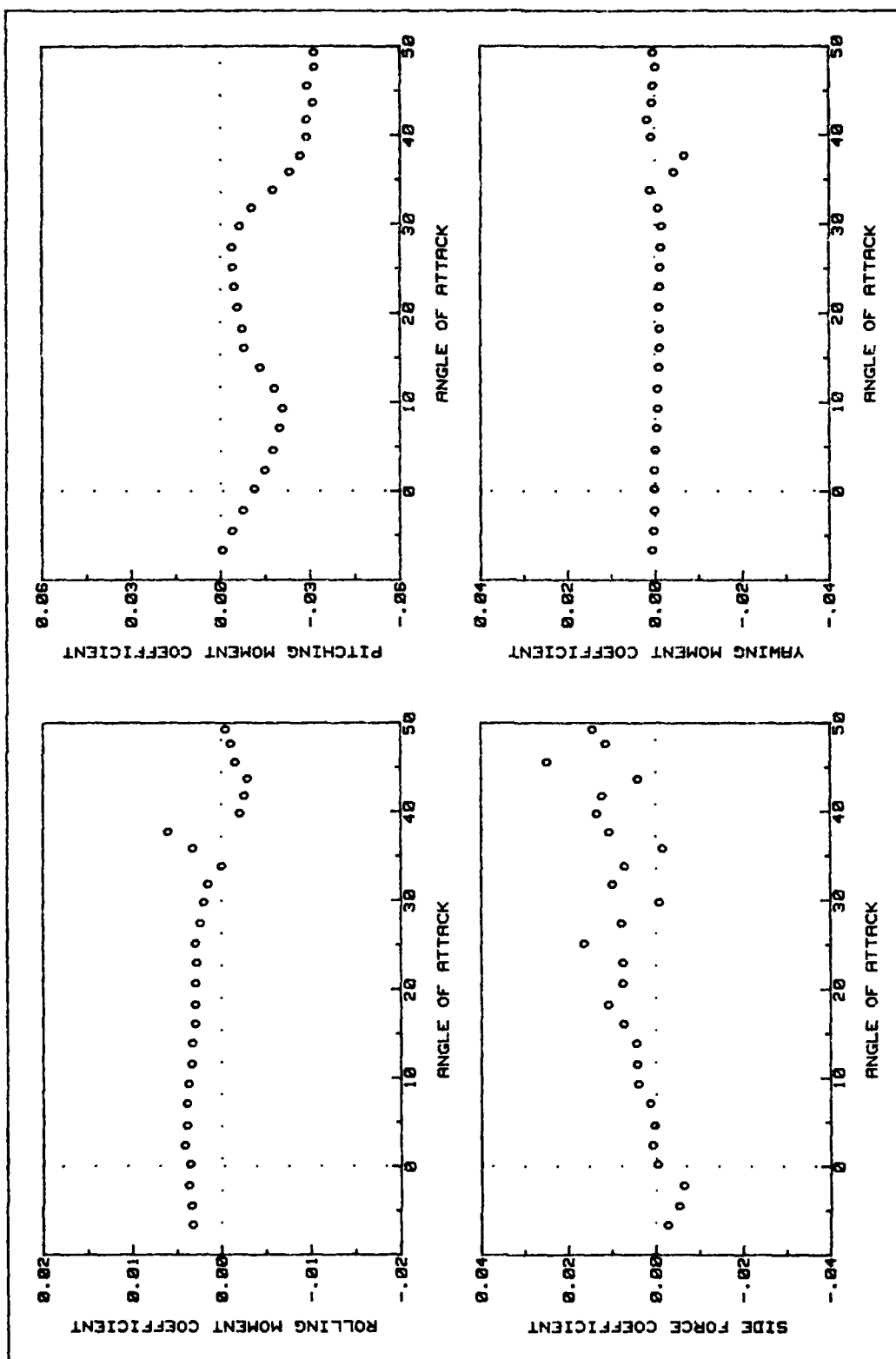


Fig A62. C4 Flap Side Force and Moments Data (deployed 30 deg symmetric)

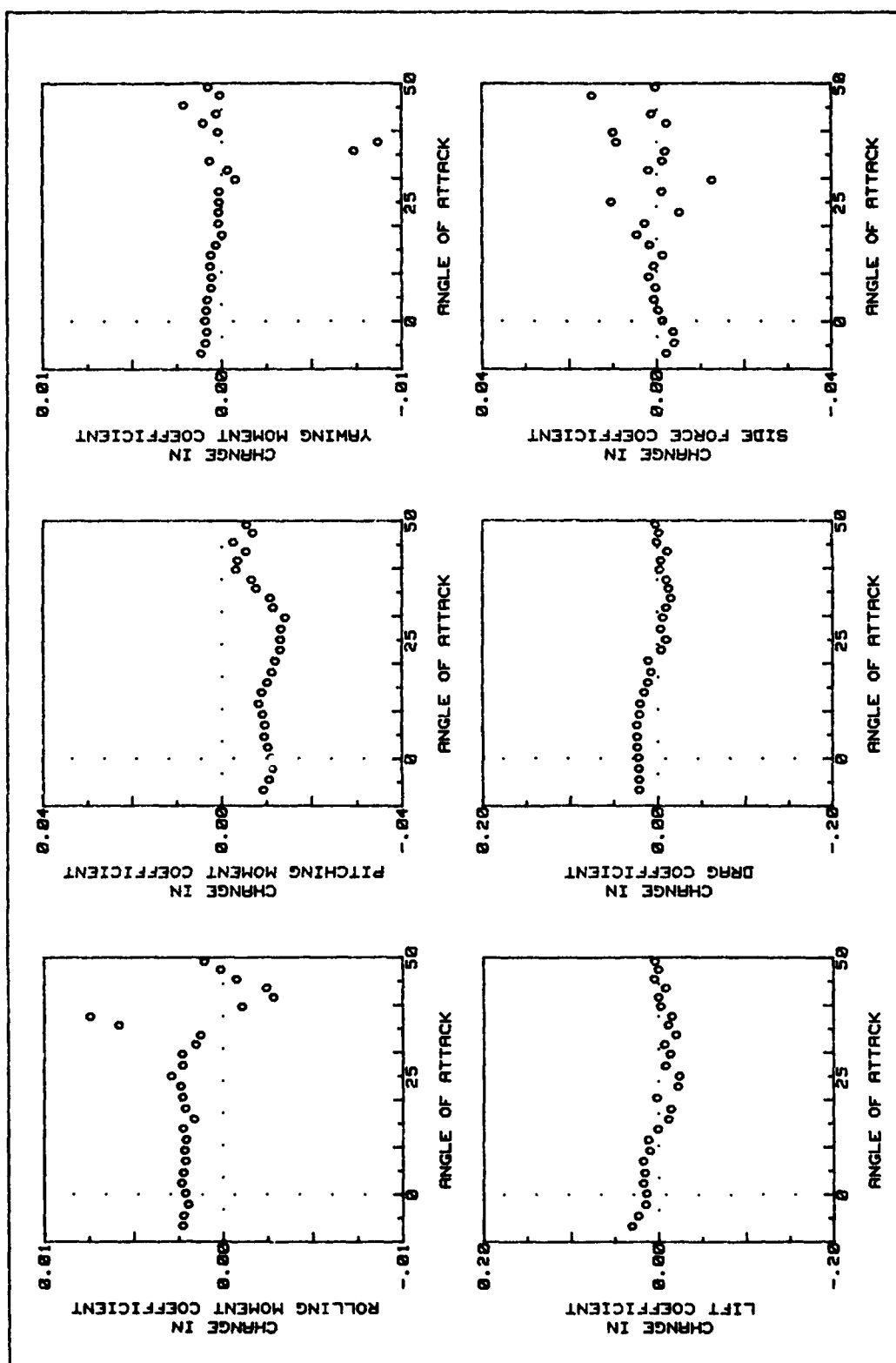


Fig A63. C4 Flap Force and Moment Changes (deployed 30 deg symmetric)

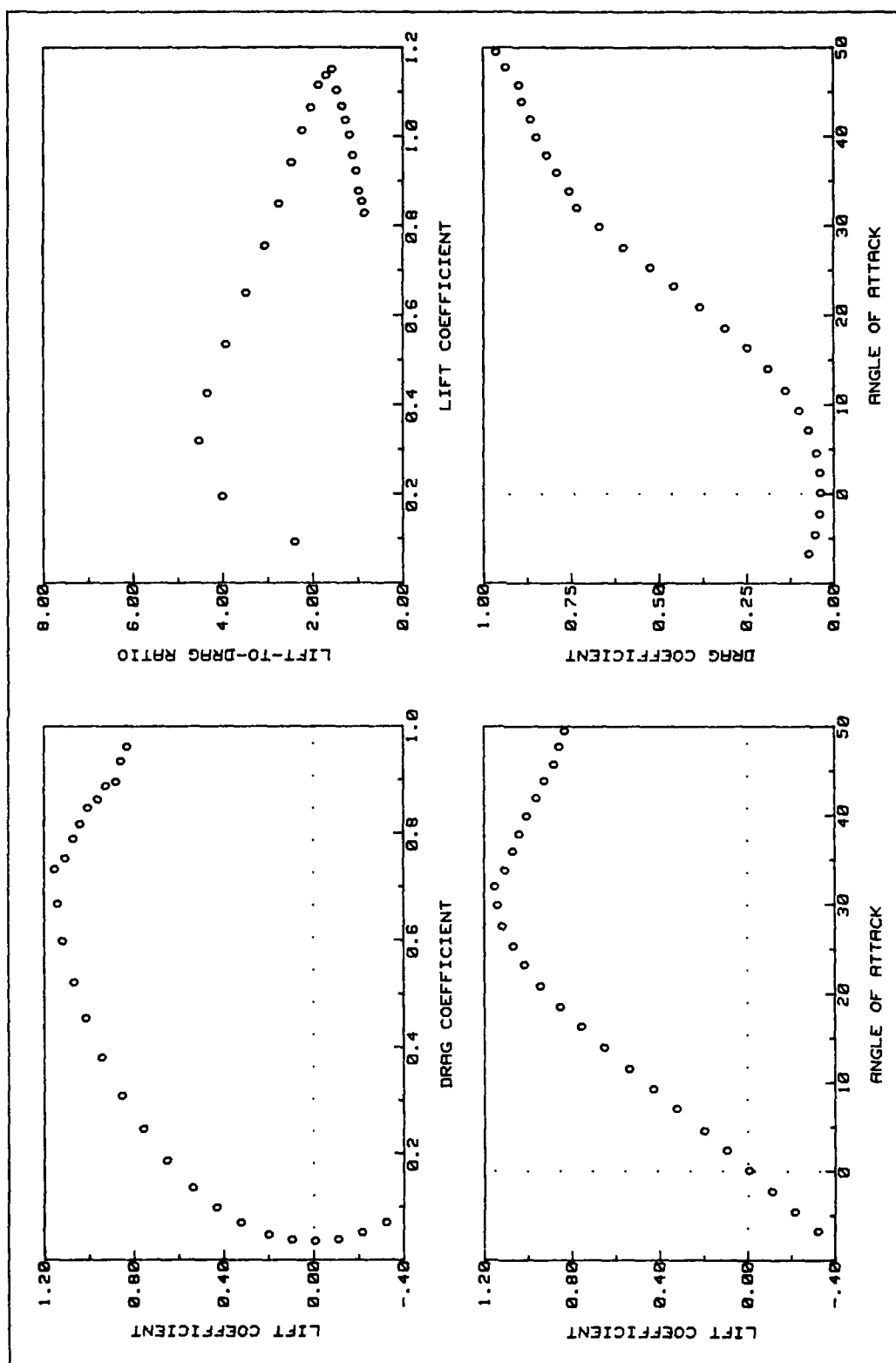


Fig A64. C4 Flap Lift and Drag Data (deployed 60 deg asymmetric)

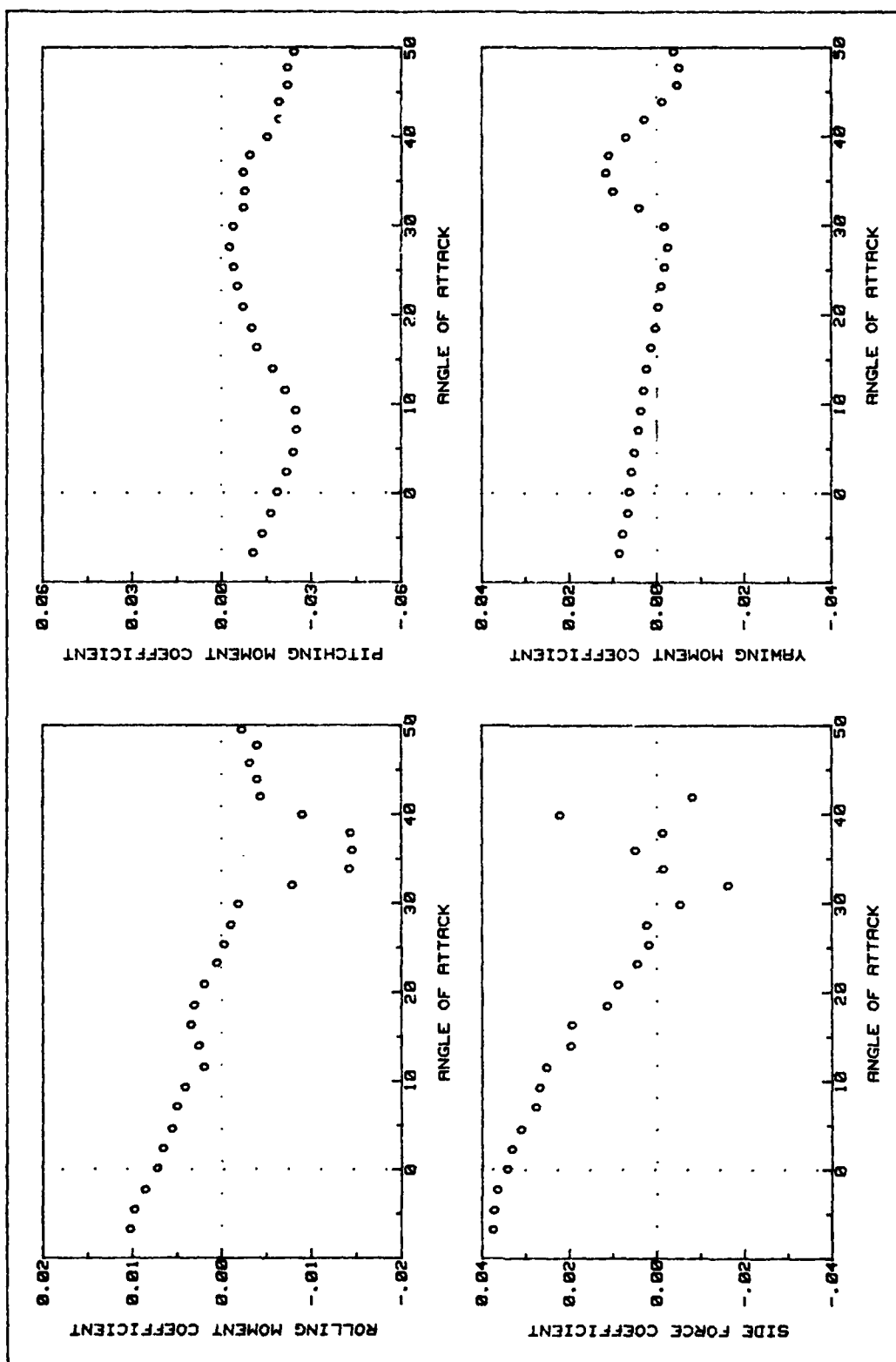


Fig A65. C4 Flap Side Force and Moments Data (deployed 60 deg asymmetric)

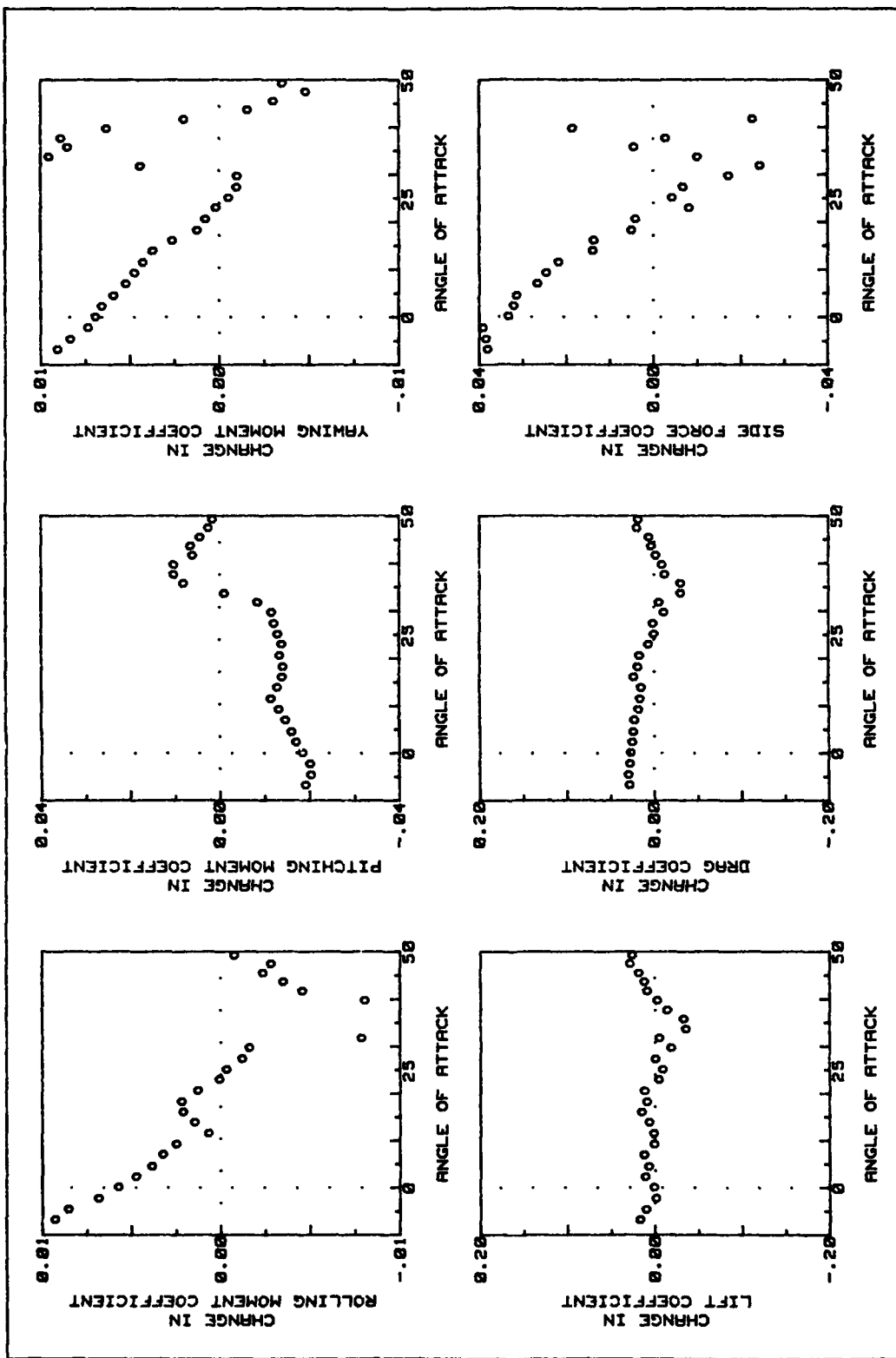


Fig A66. C4 Flap Force and Moment Changes (deployed 60 deg asymmetric)

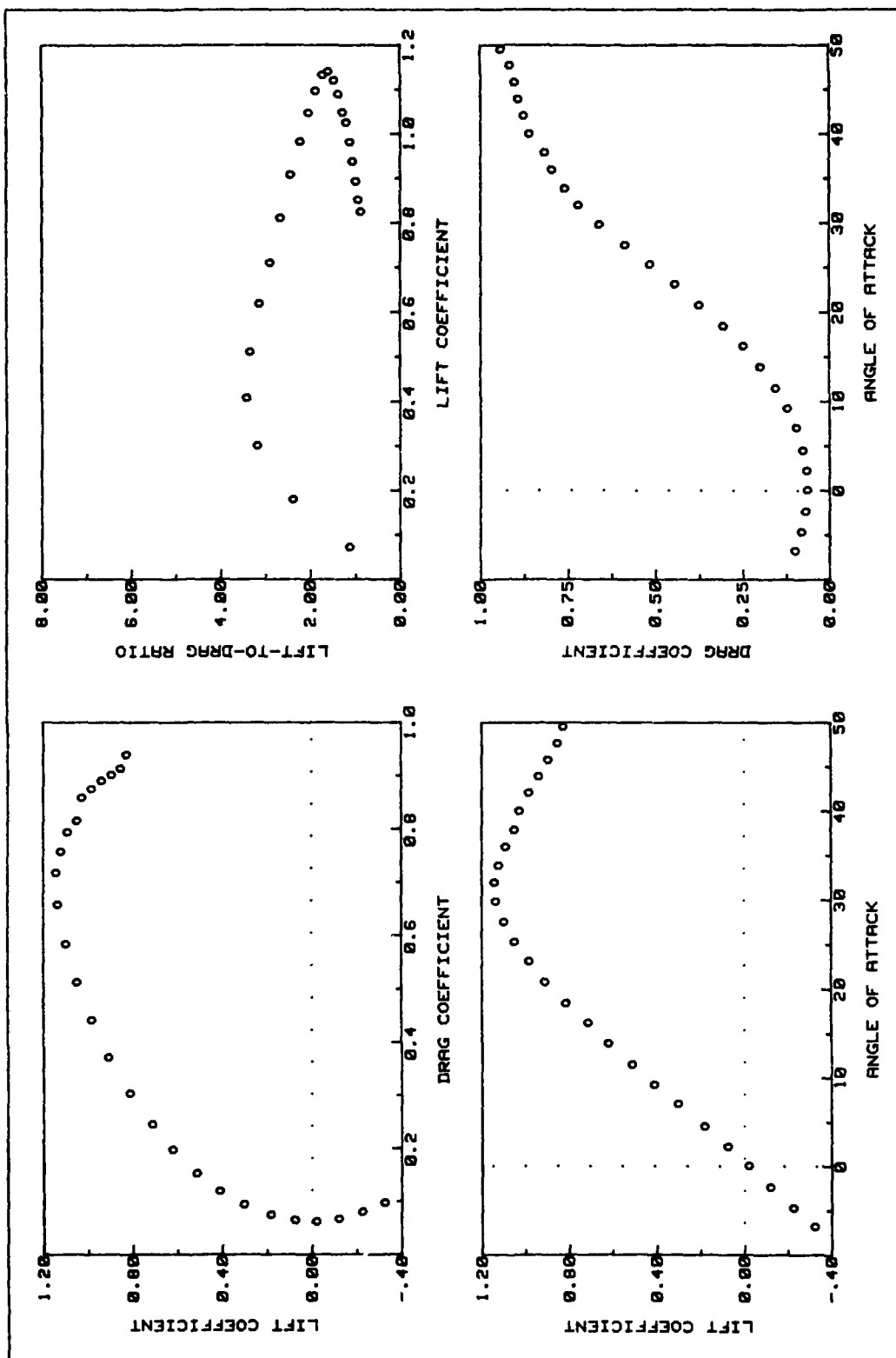


Fig A67. C4 Flap Lift and Drag Data (deployed 60 deg symmetric)

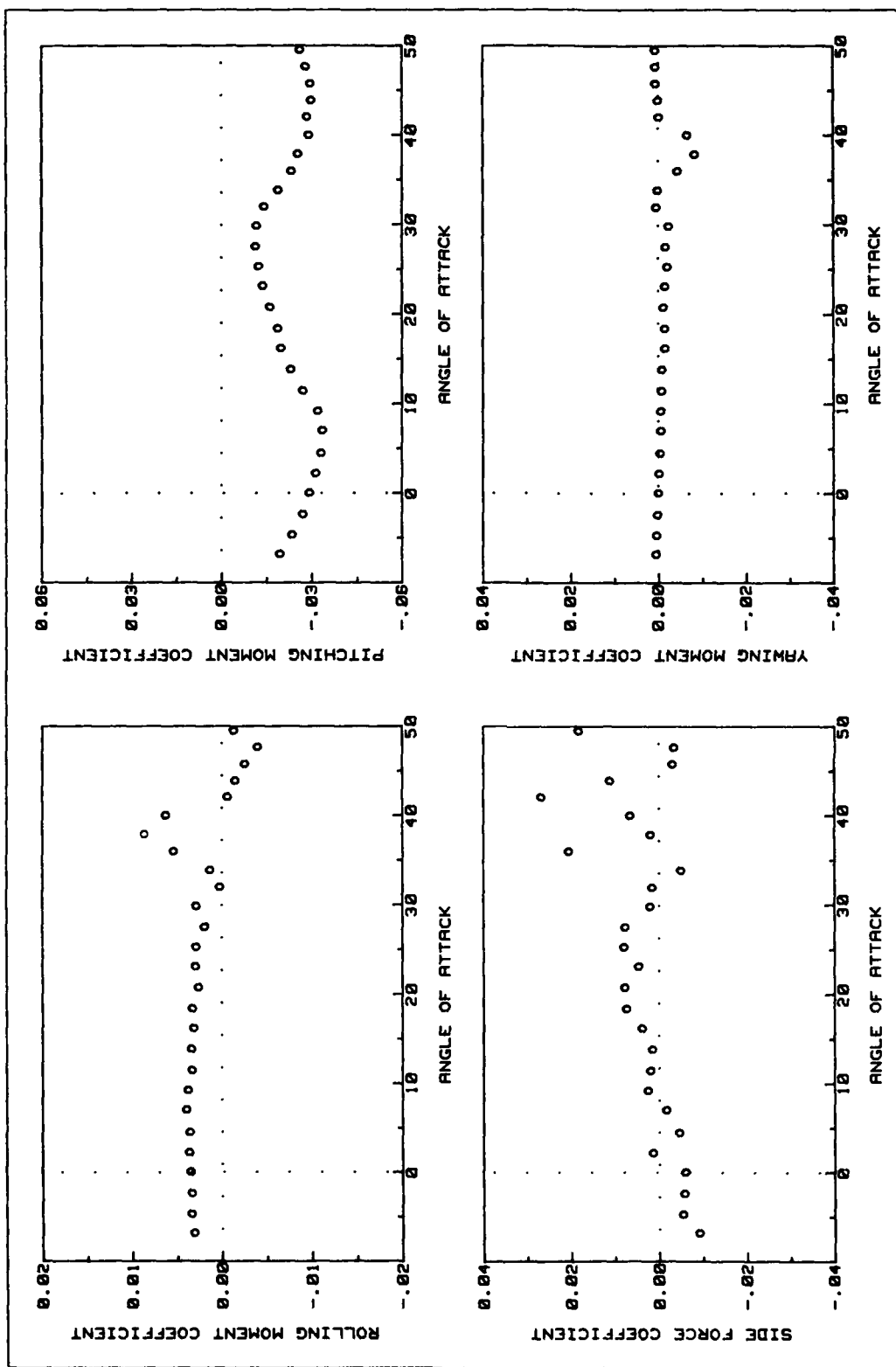


Fig A68. C4 Flap Side Force and Moments Data (deployed 60 deg symmetric)

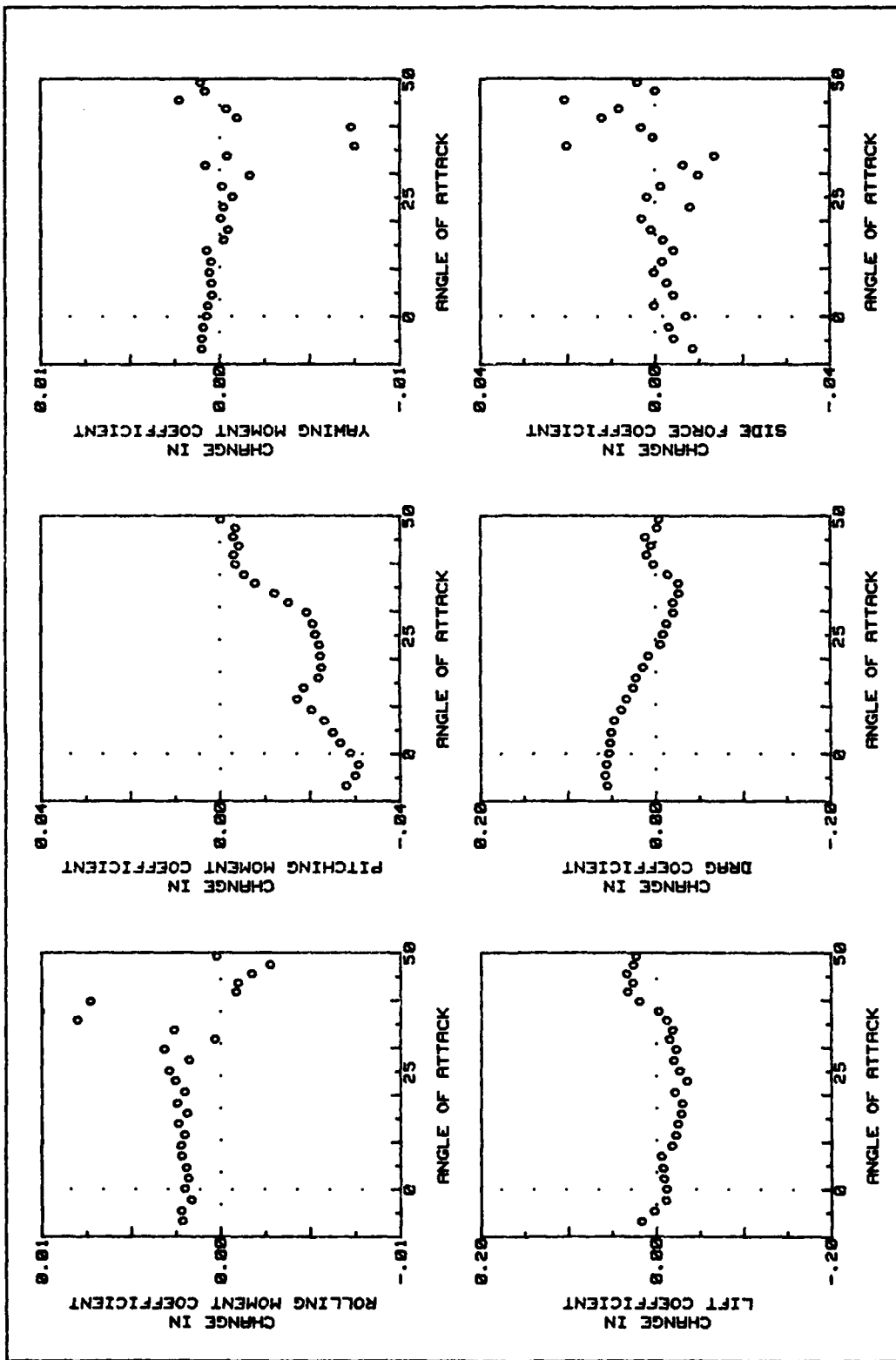


Fig A69. C4 Flap Force and Moment Changes (deployed 60 deg symmetric)

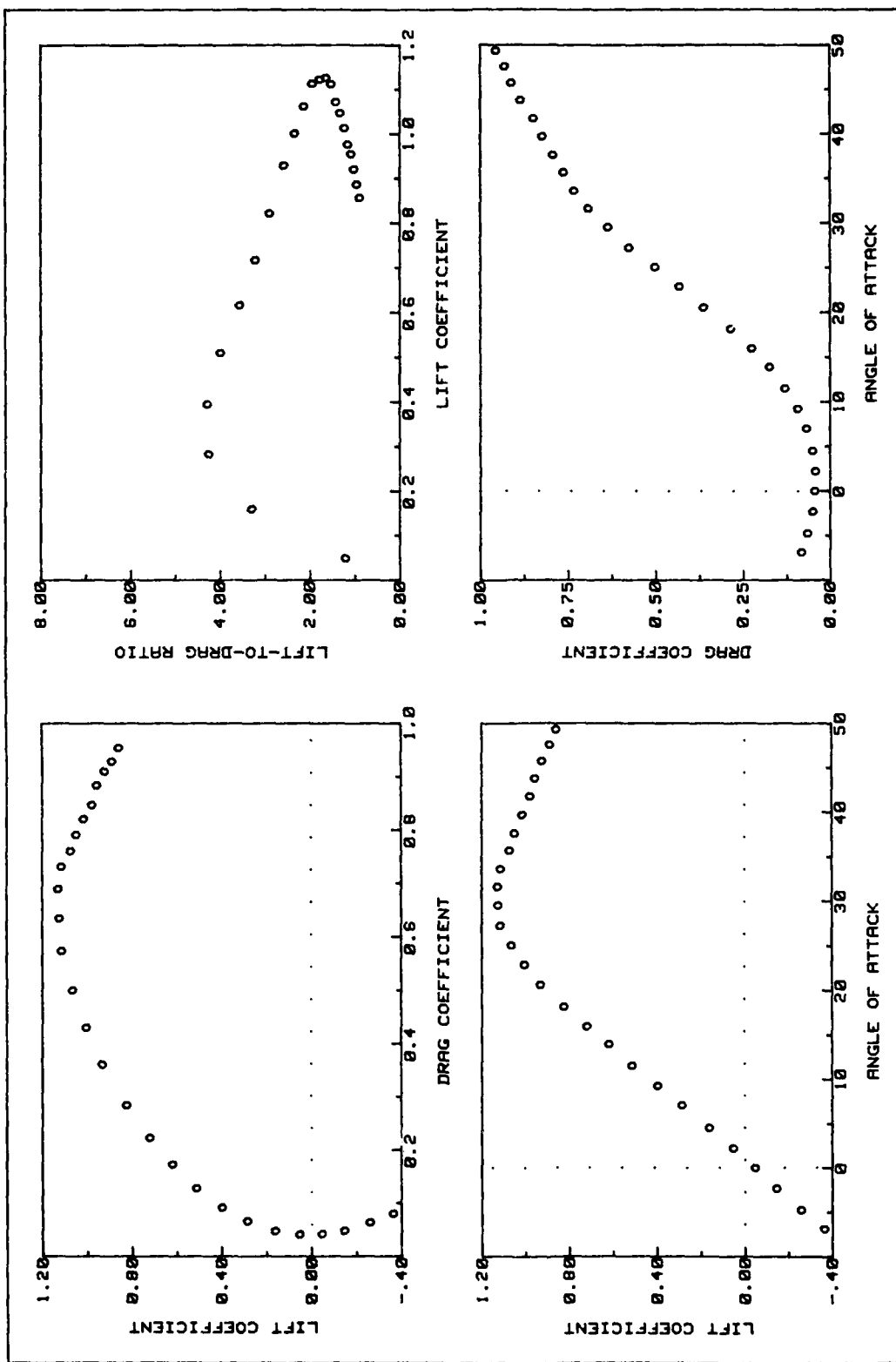


Fig A70. C4 Flap Lift and Drag Data (deployed 90 deg asymmetric)

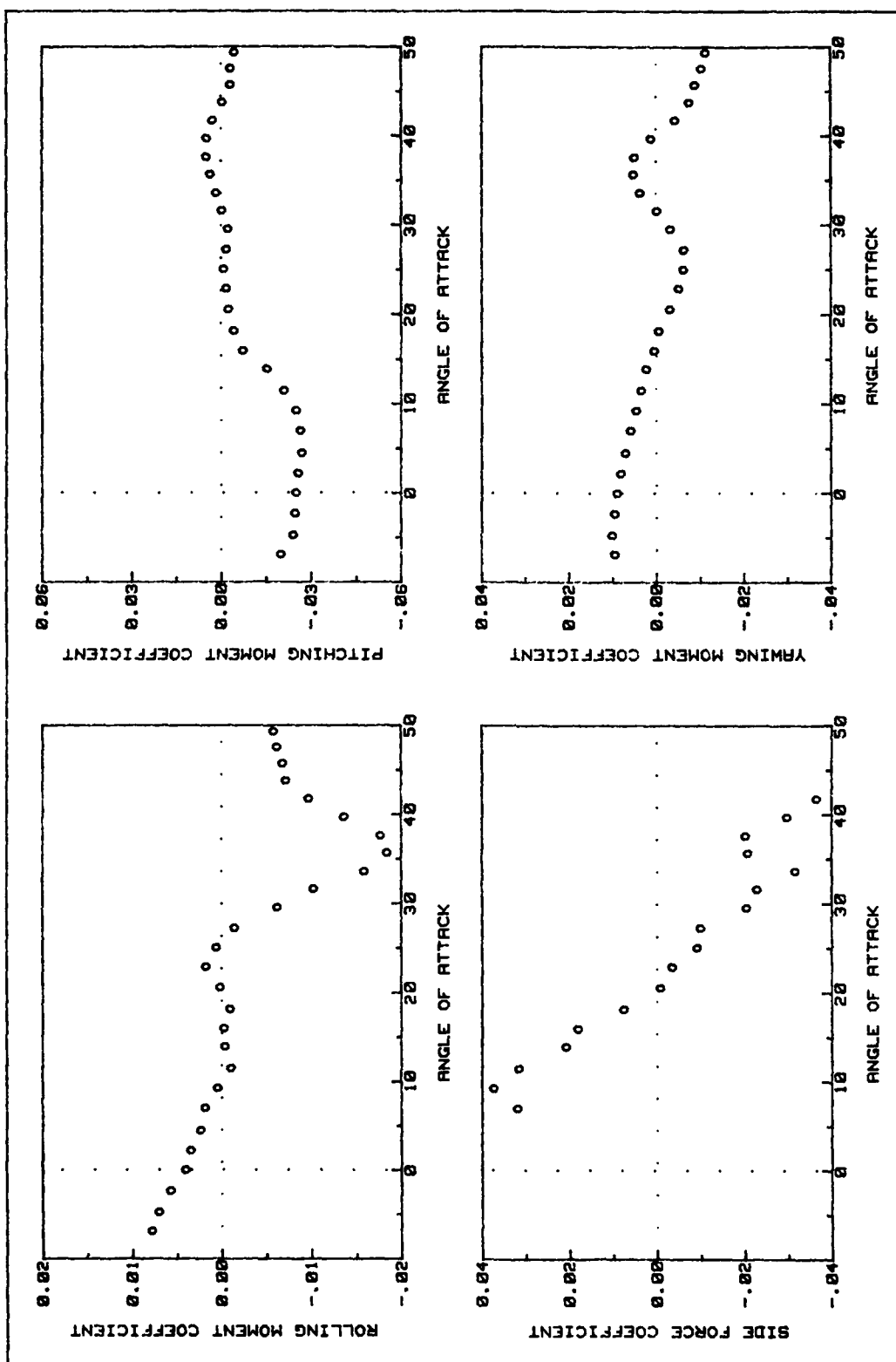


Fig A71. C4 Flap Side Force and Moments Data (deployed 90 deg asymmetric)

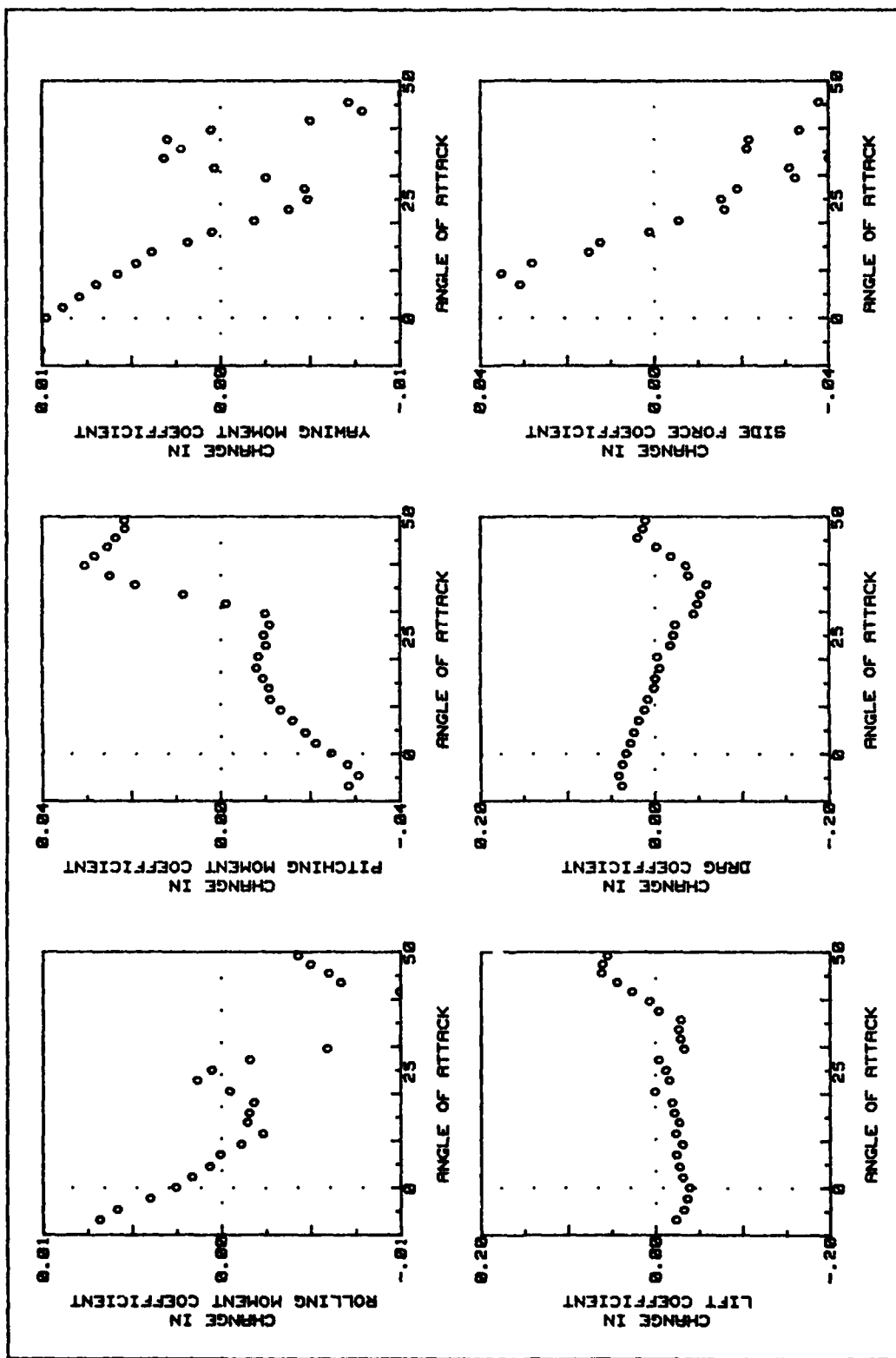


Fig A72. C4 Flap Force and Moment Changes (deployed 90 deg asymmetric)

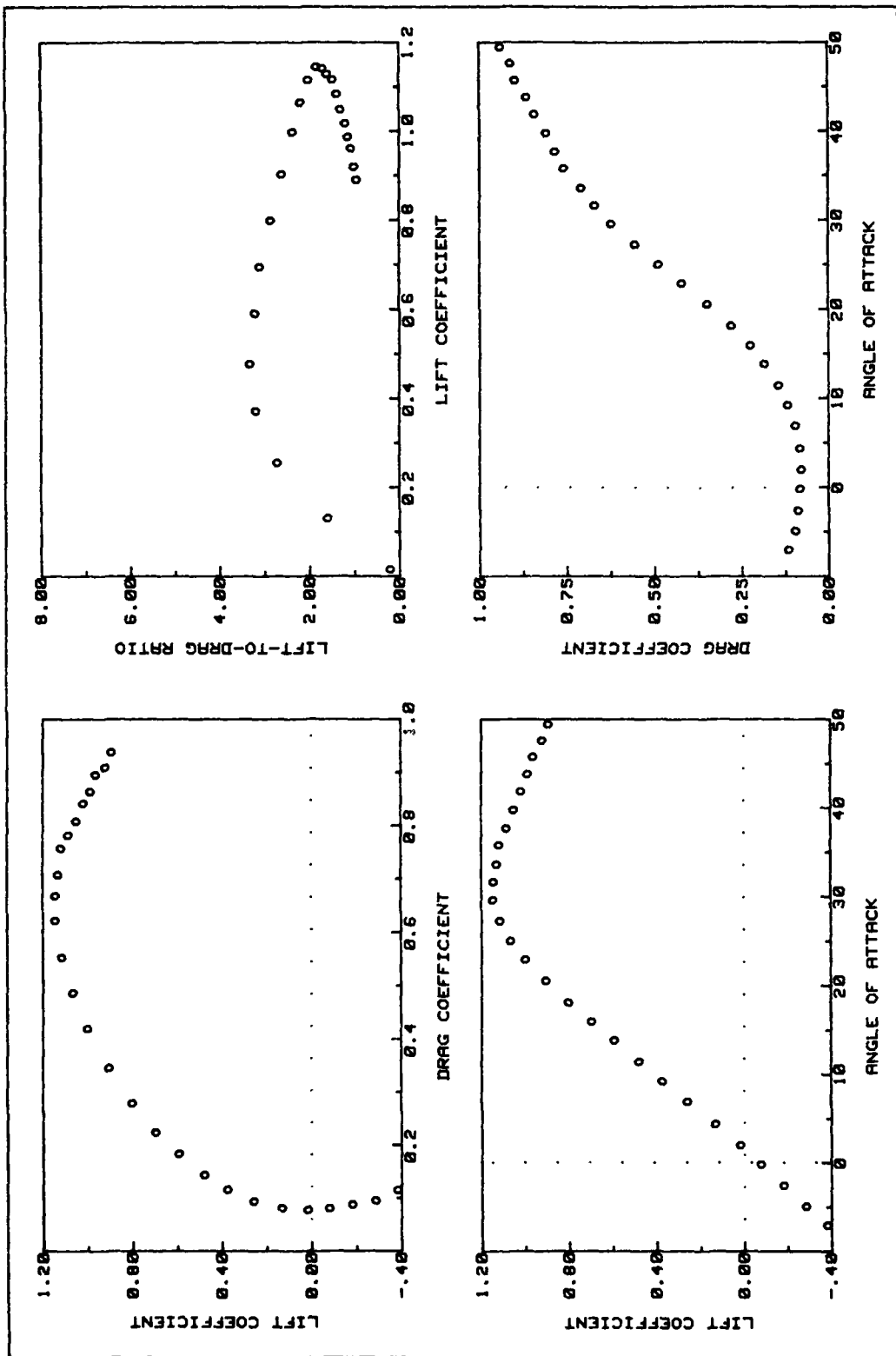


Fig A73. C4 Flap Lift and Drag Data (deployed 90 deg symmetric)

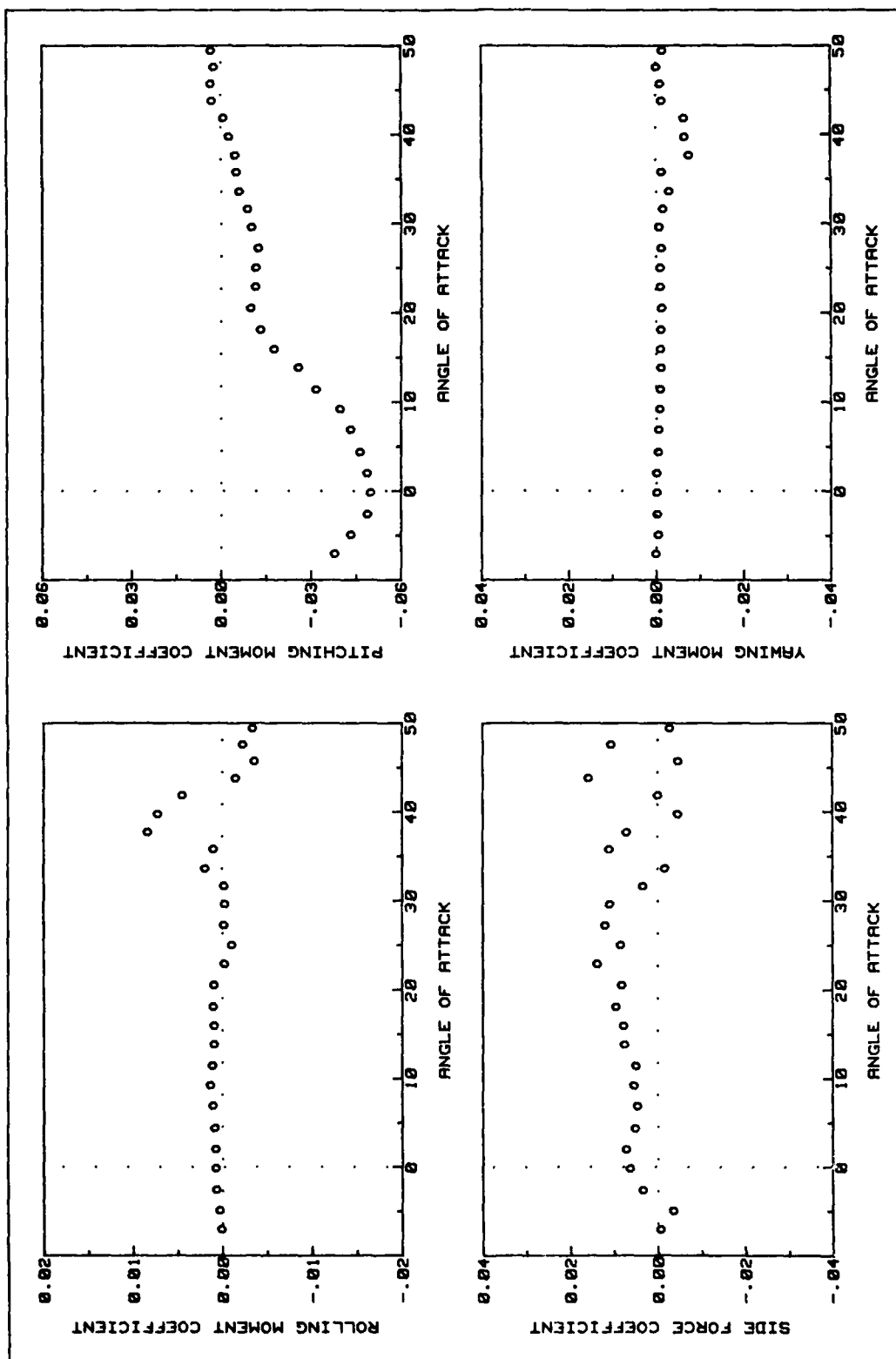


Fig A74. C4 Flap Side Force and Moments Data (deployed 90 deg symmetric)

AD-A164 104

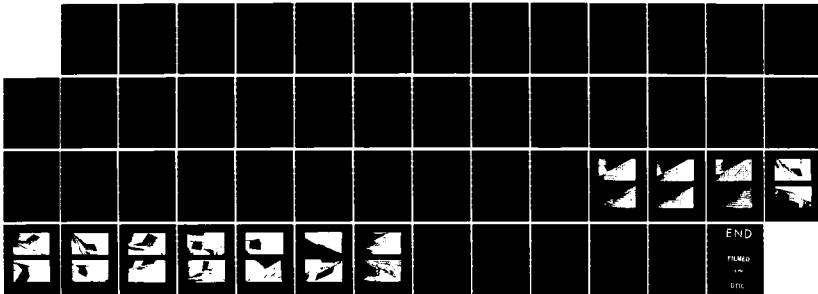
EXPERIMENTAL ASSESSMENT OF VORTEX RETAINING CAVITY
FLAPS FOR MANEUVERABILITY. (U) AIR FORCE INST OF TECH
WRIGHT-PATTERSON AFB OH SCHOOL OF ENGI.. H C SMITH
DEC 85 AFIT/GAE/RA/85D-13 F/G 1/3

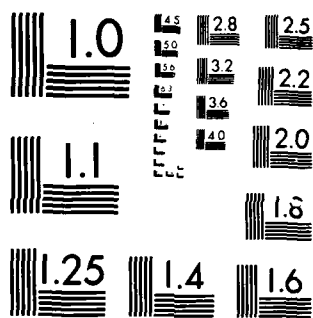
3/3

UNCLASSIFIED

F/G 1/3

NL





MICROCOPY RESOLUTION TEST CHART
NATIONAL BUREAU OF STANDARDS 1963-A

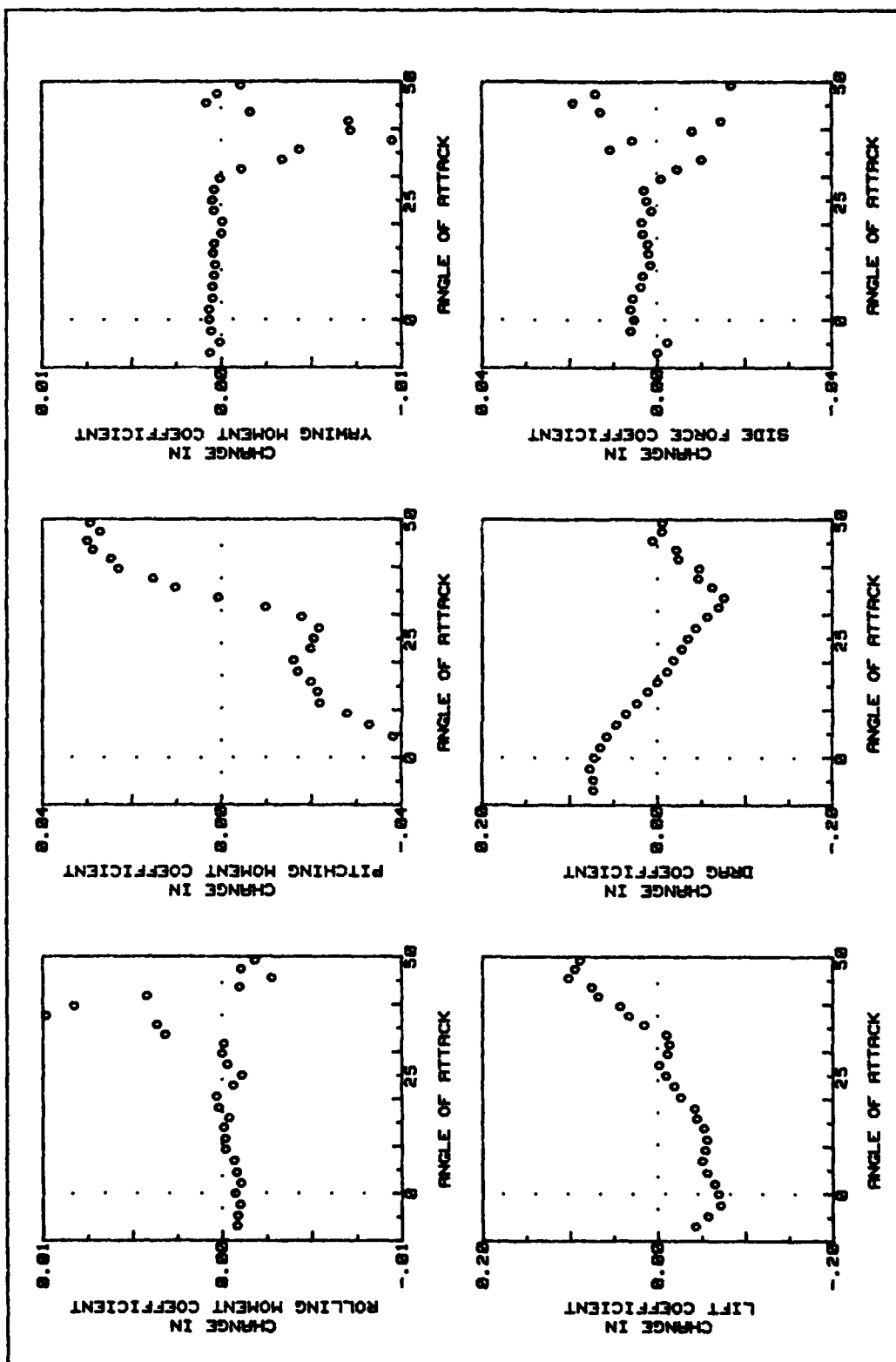


Fig A75. C4 Flap Force and Moment Changes (deployed 90 deg symmetric)

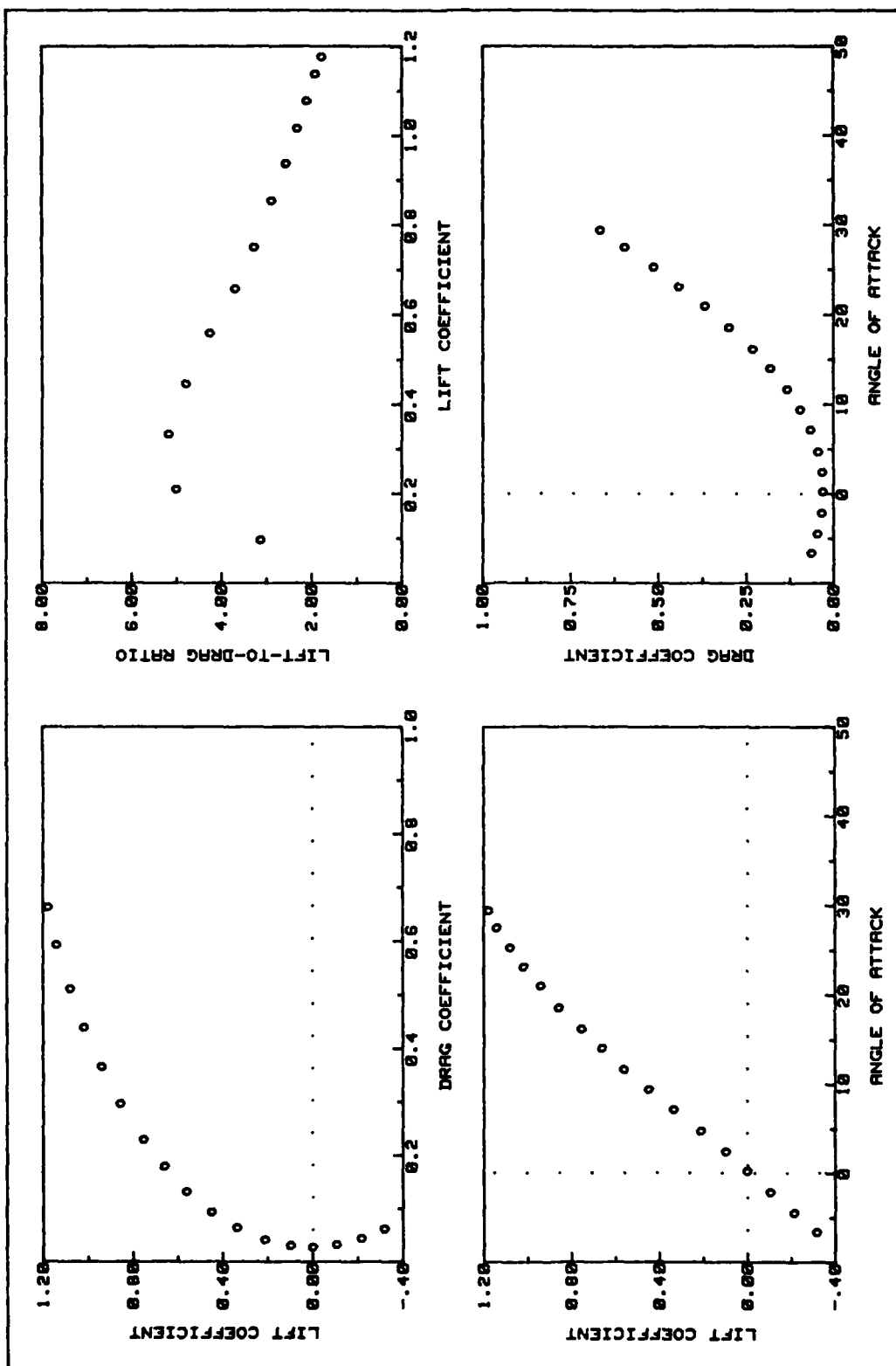


Fig A76. C5 Flap Lift and Drag Data (deployed 60 deg asymmetric)

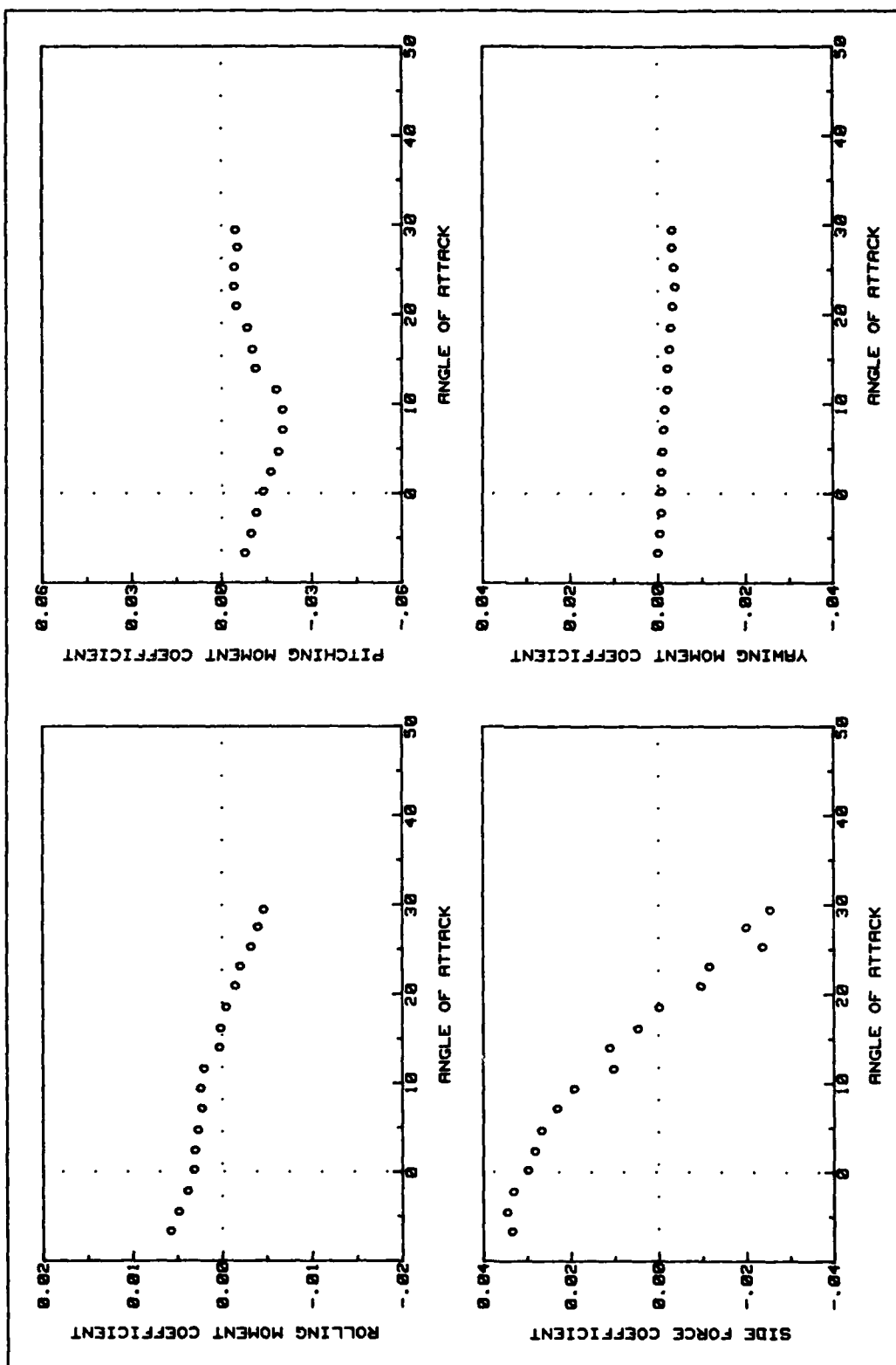


Fig A77. C5 Flap Side Force and Moments Data (deployed 60 deg asymmetric)

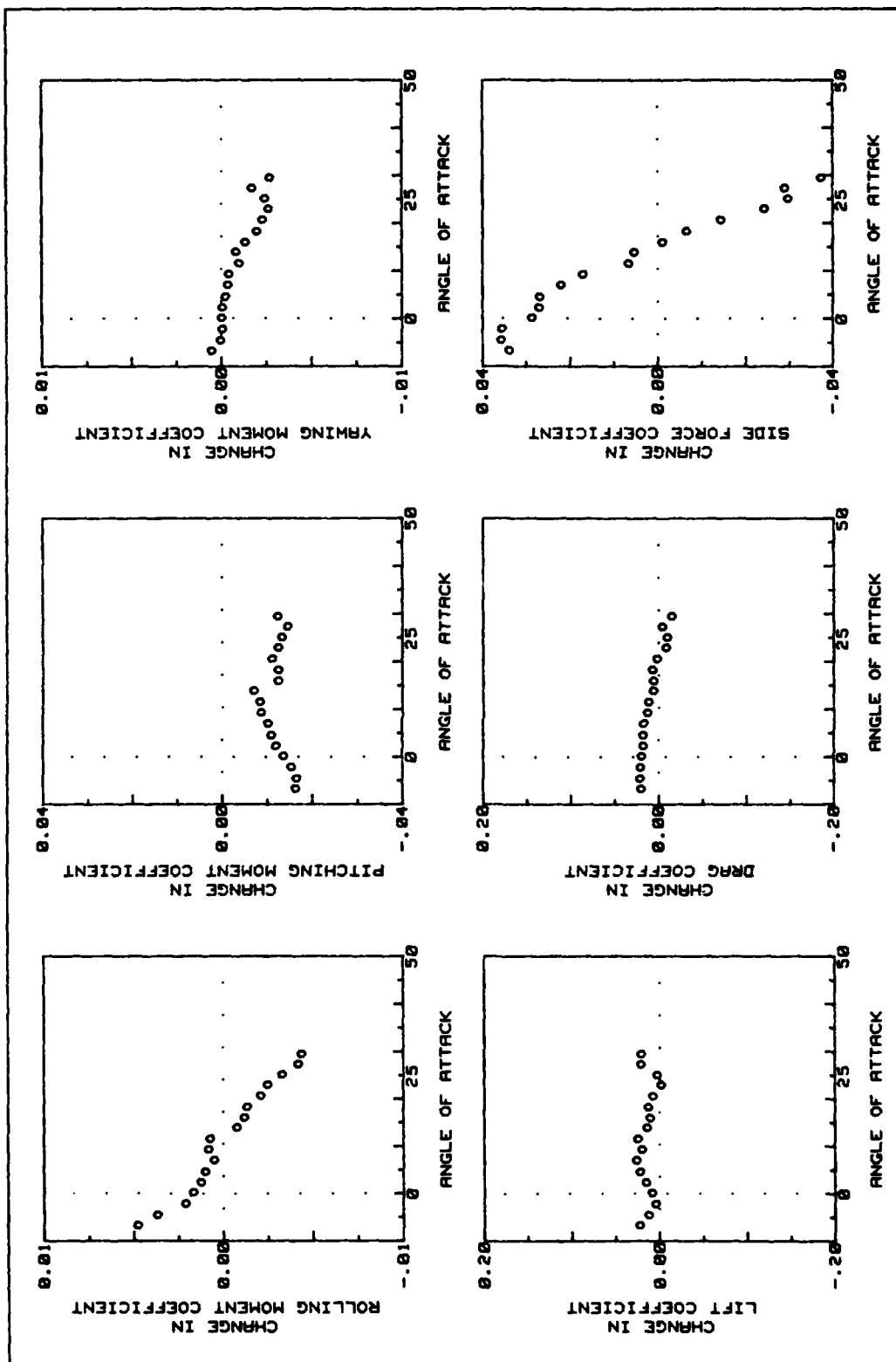


Fig A78. C5 Flap Force and Moment Changes (deployed 60 deg asymmetric)

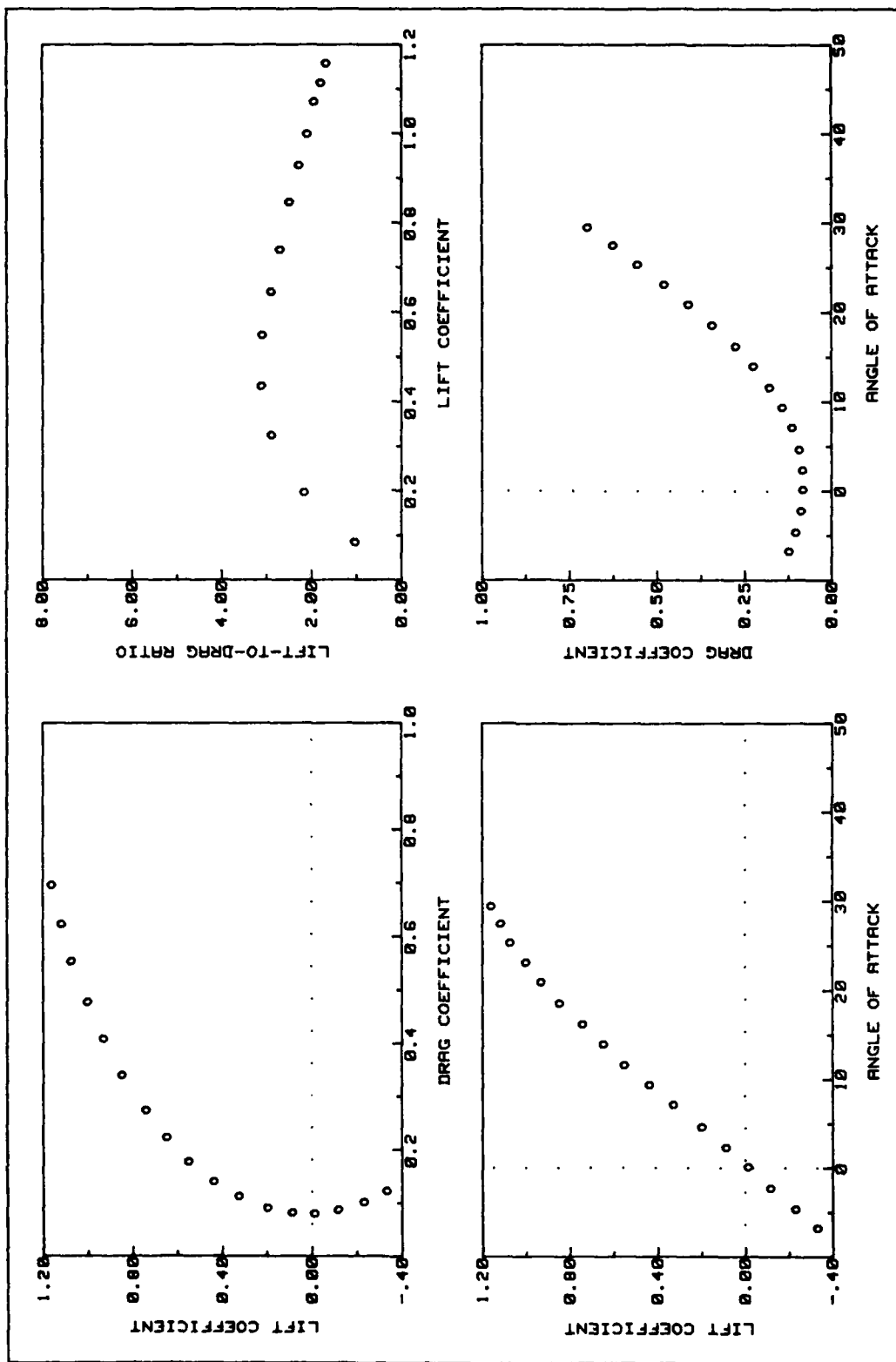


Fig A79. C5 Flap Lift and Drag Data (deployed 75 deg asymmetric)

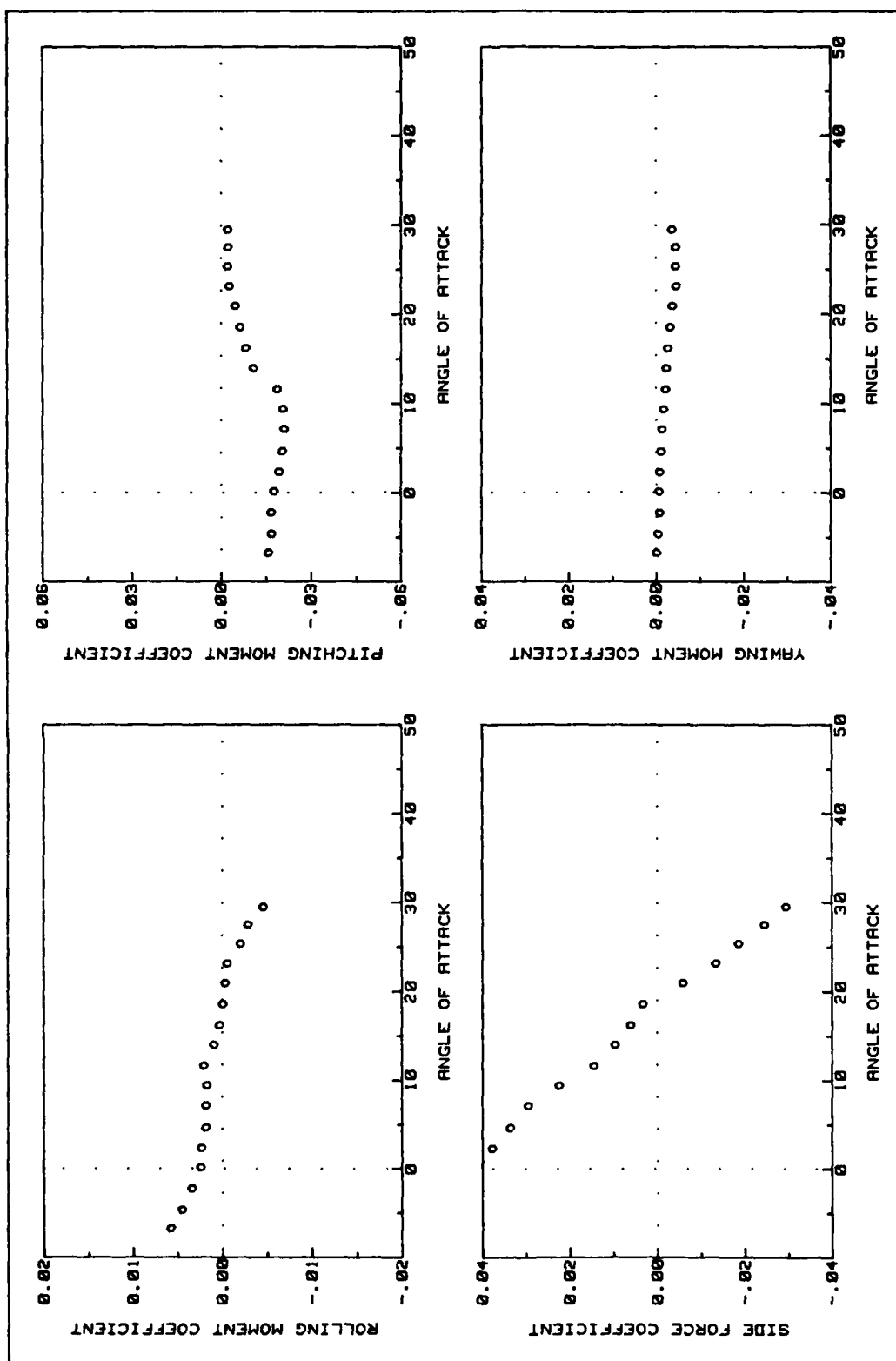


Fig A80. C5 Flap Side Force and Moments Data (deployed 75 deg asymmetric)

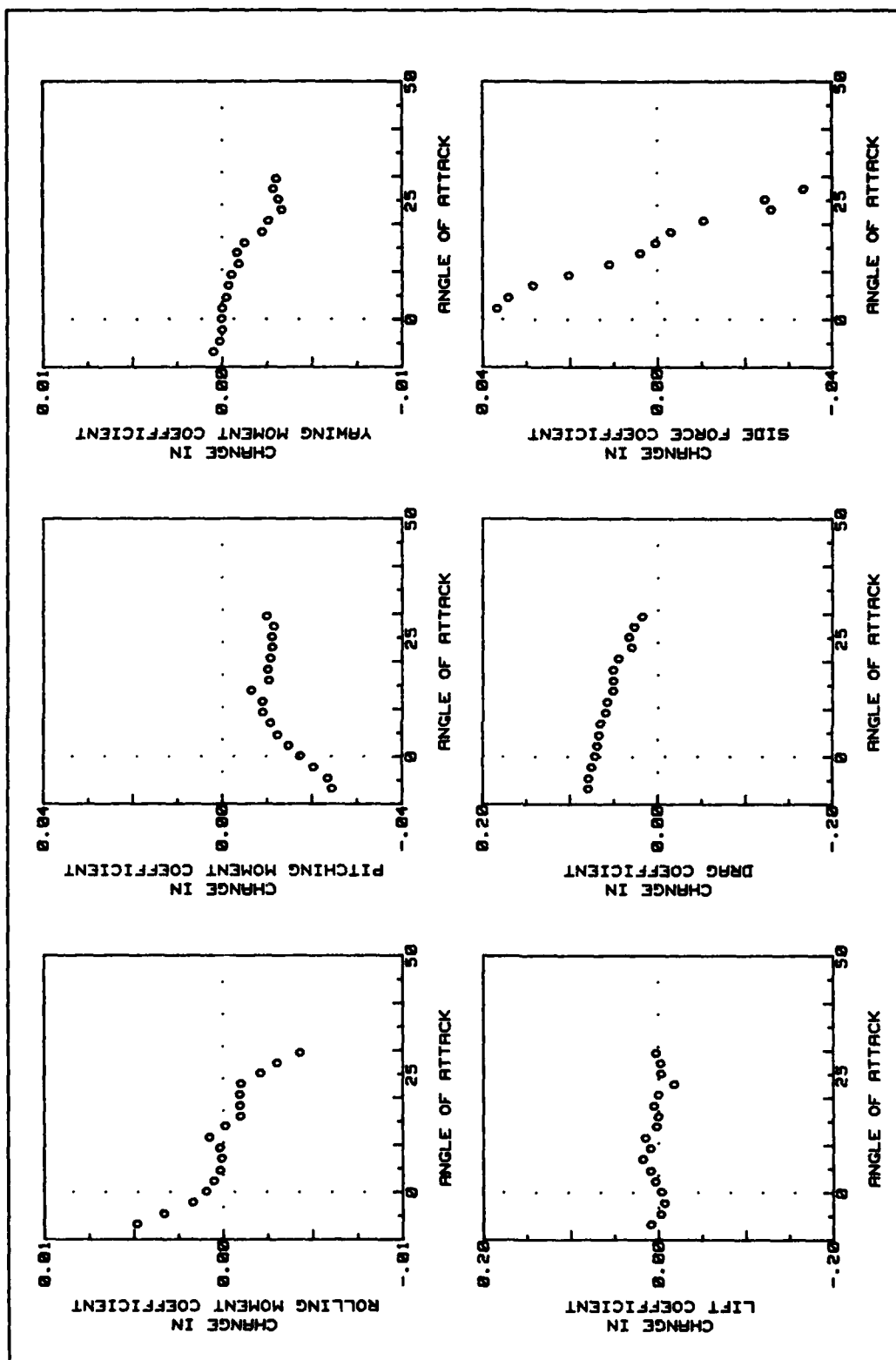


Fig A81. C5 Flap Force and Moment Changes (deployed 75 deg asymmetric)

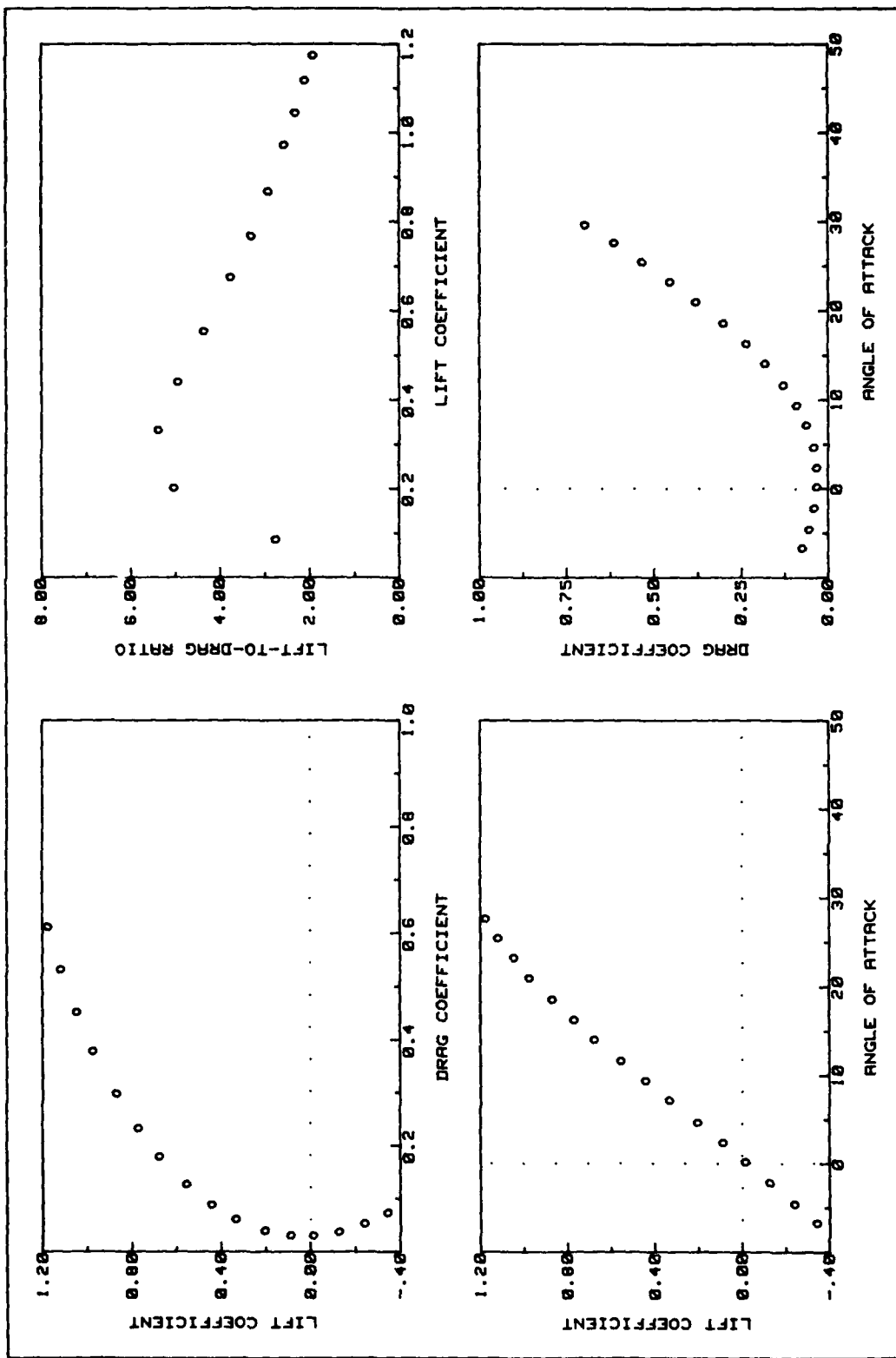


Fig A82. C6 Flap Lift and Drag Data (deployed 90 deg asymmetric)

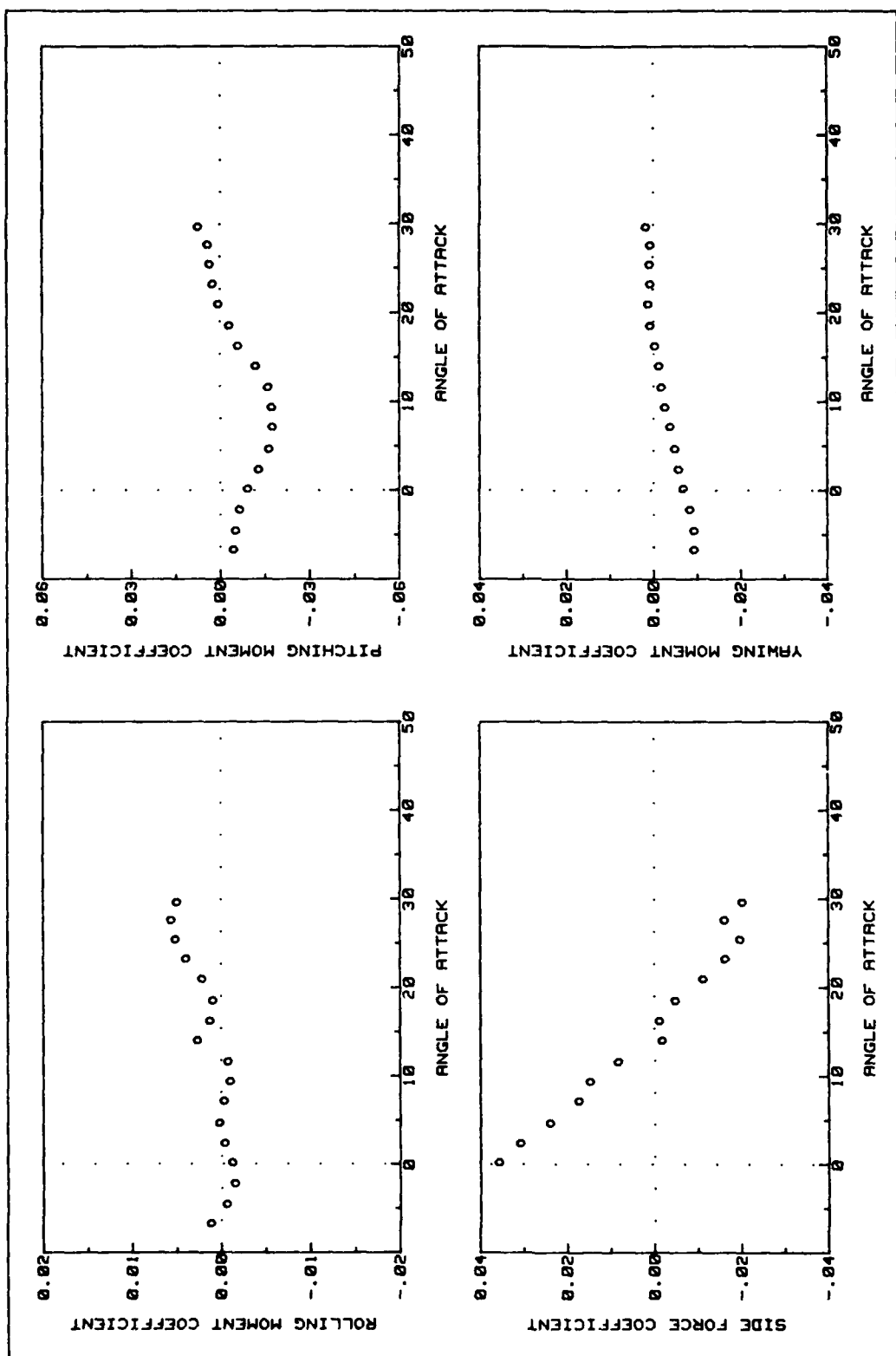


Fig A83. C6 Flap Side Force and Moments Data (deployed 90 deg asymmetric)

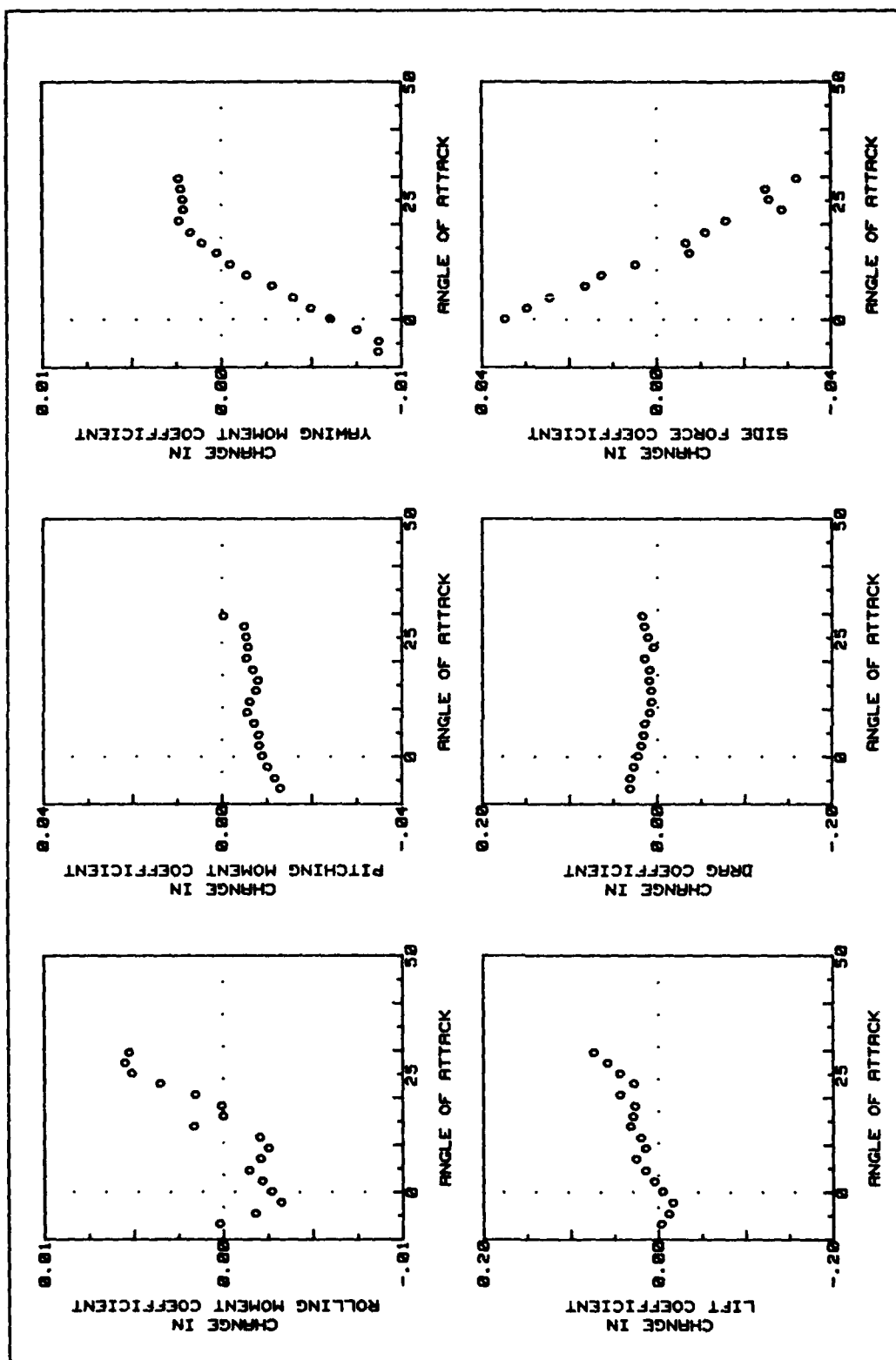


Fig A84. C6 Flap Force and Moment Changes (deployed 90 deg asymmetric)

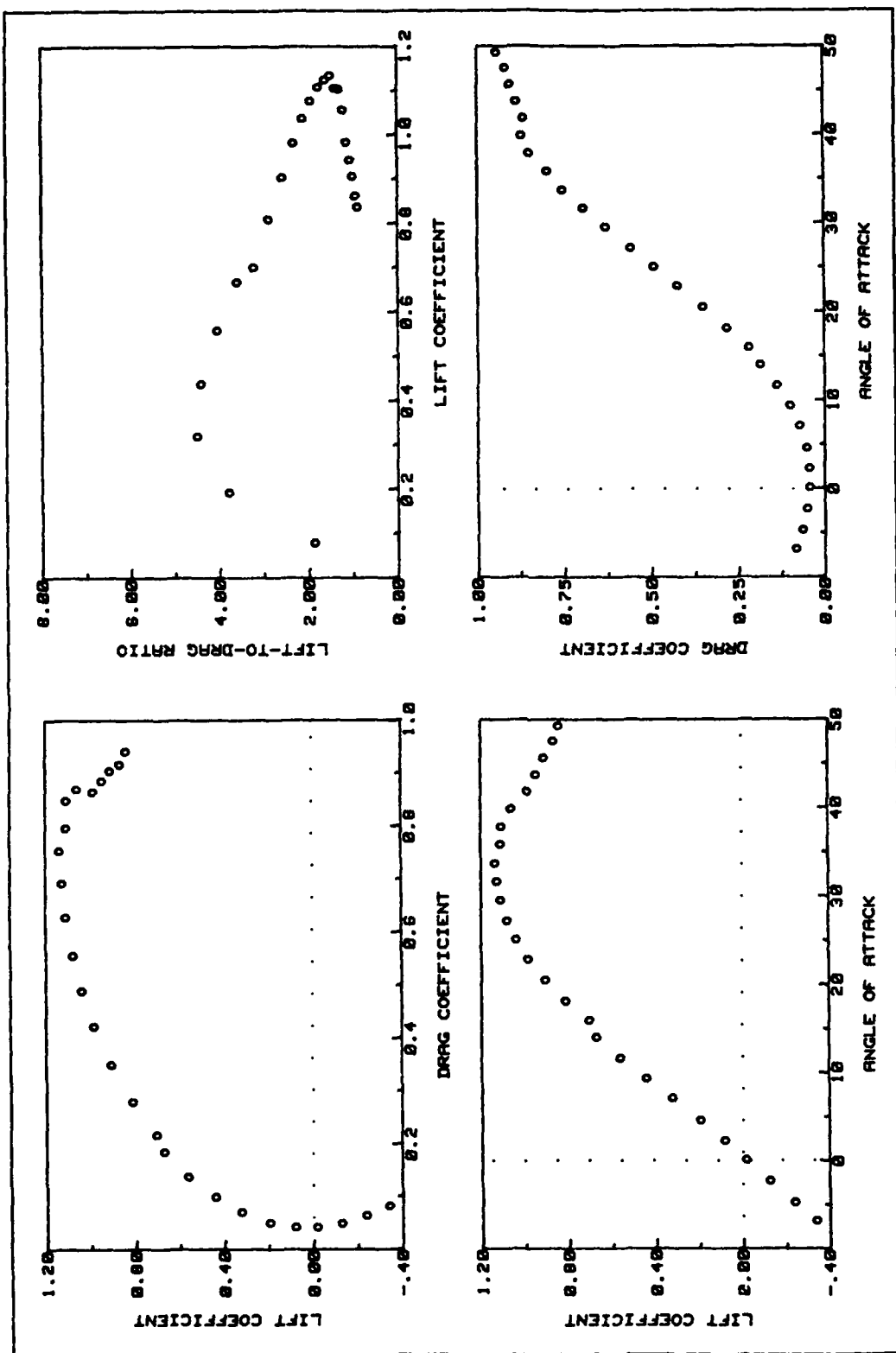


Fig A85. C7 Flap Lift and Drag Data (deployed 90 deg asymmetric)

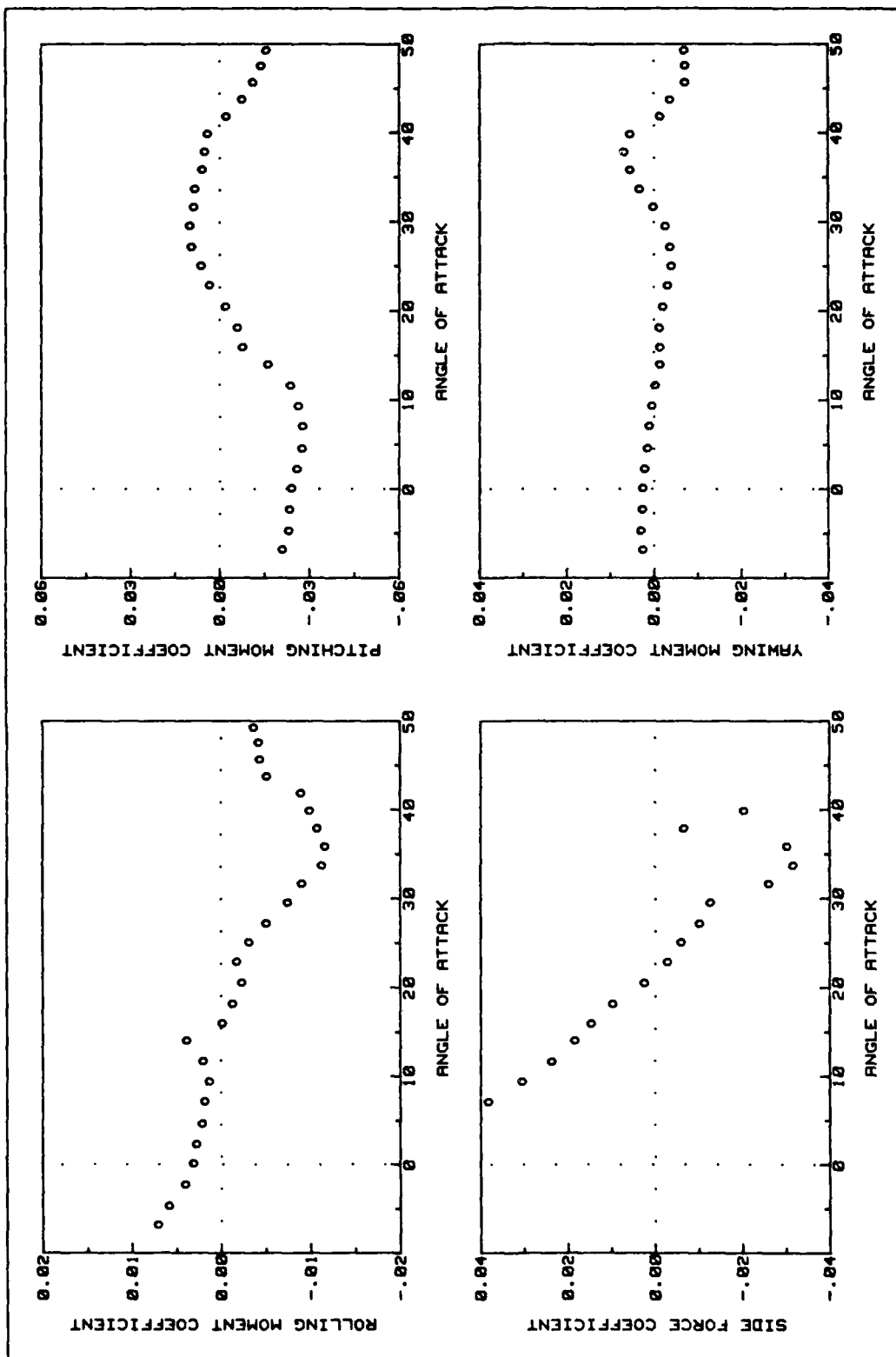


Fig A86. C7 Flap Side Force and Moments Data (deployed 90 deg asymmetric)

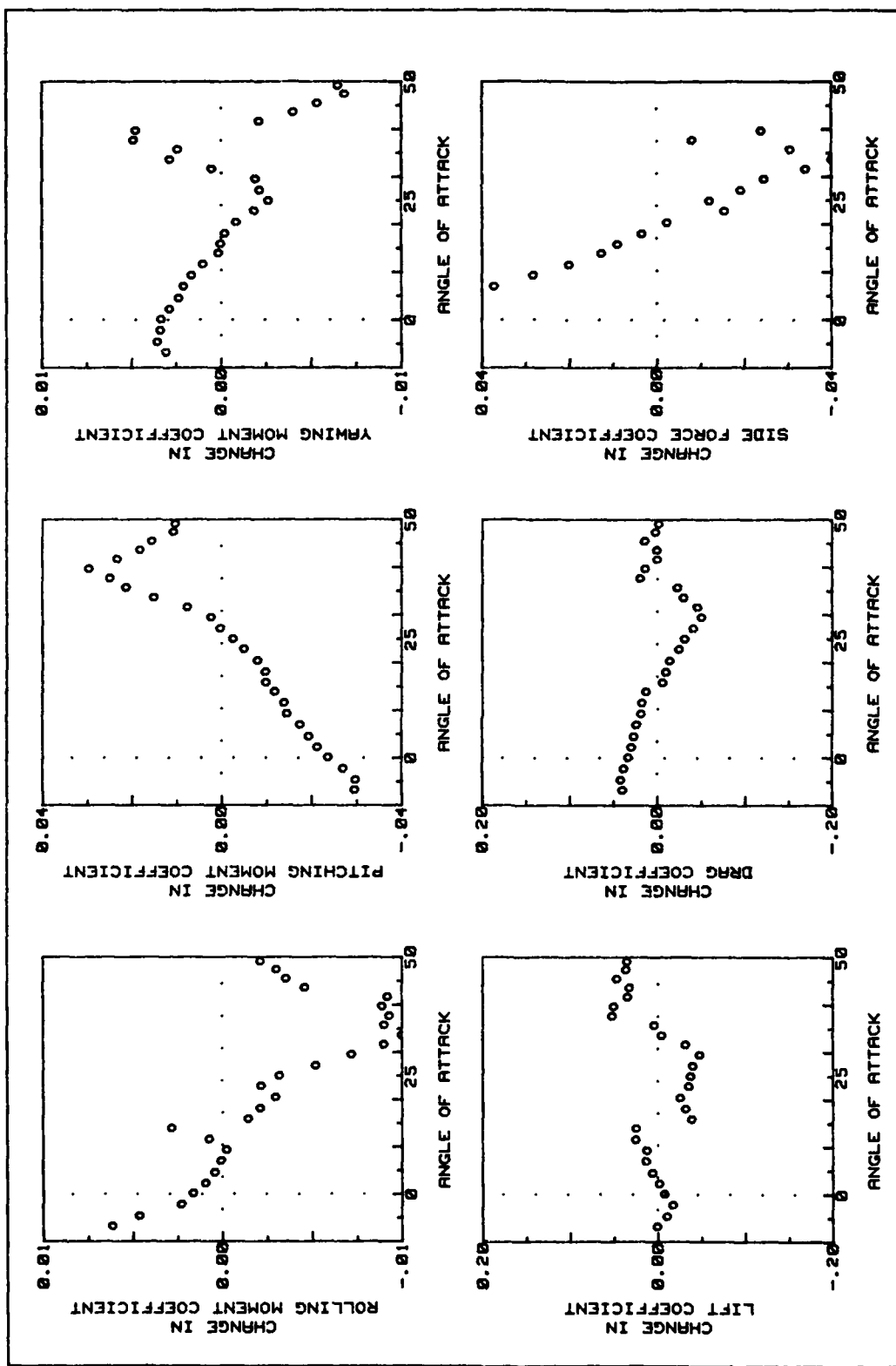


Fig A87. C7 Flap Force and Moment Changes (deployed 90 deg asymmetric)

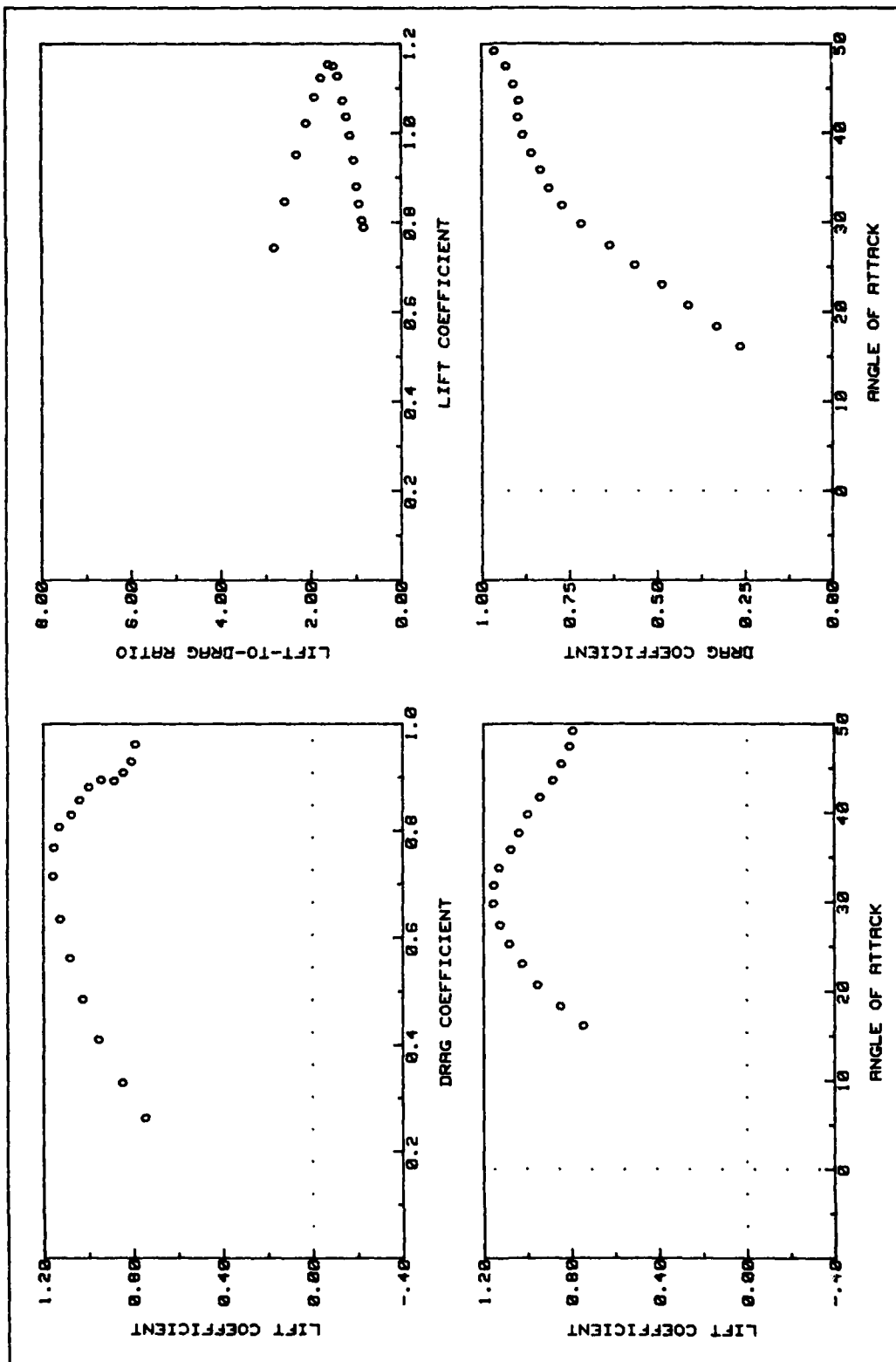


Fig A88. C8 Flap Lift and Drag Data (deployed 90 deg asymmetric)

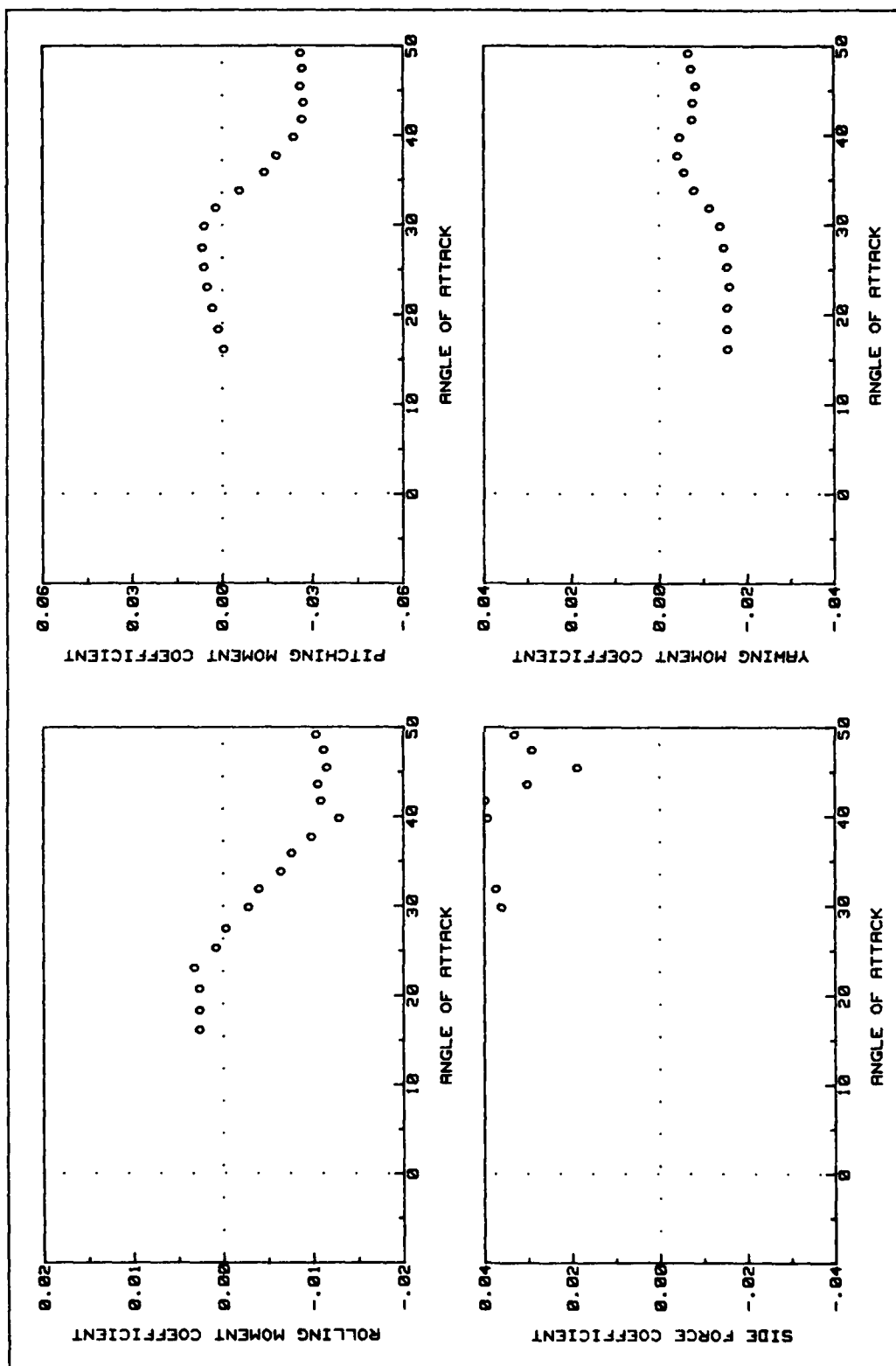


Fig A89. C8 Flap Side Force and Moments Data (deployed 90 deg asymmetric)

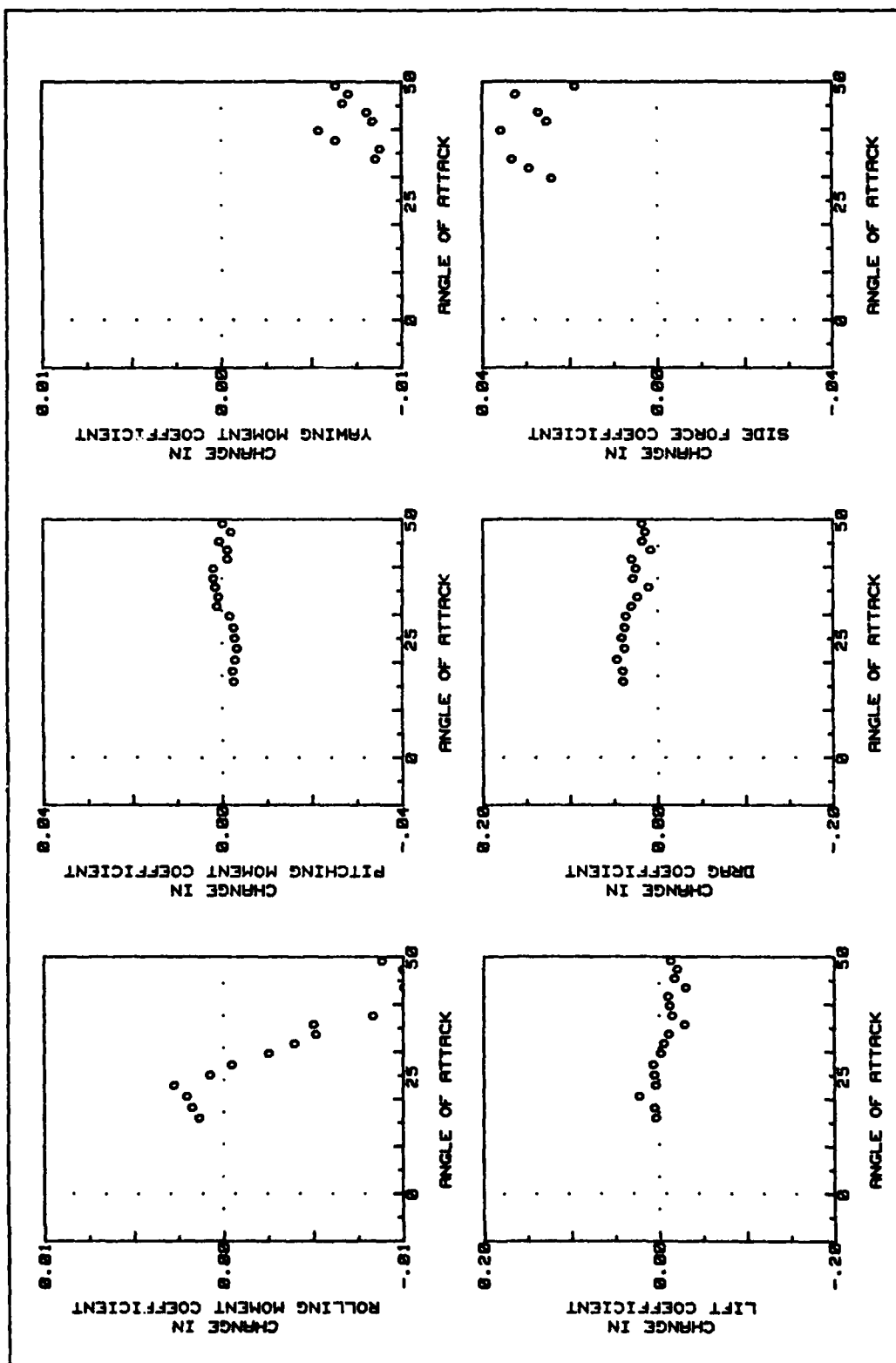


Fig A90. C8 Flap Force and Moment Changes (deployed 90 deg asymmetric)

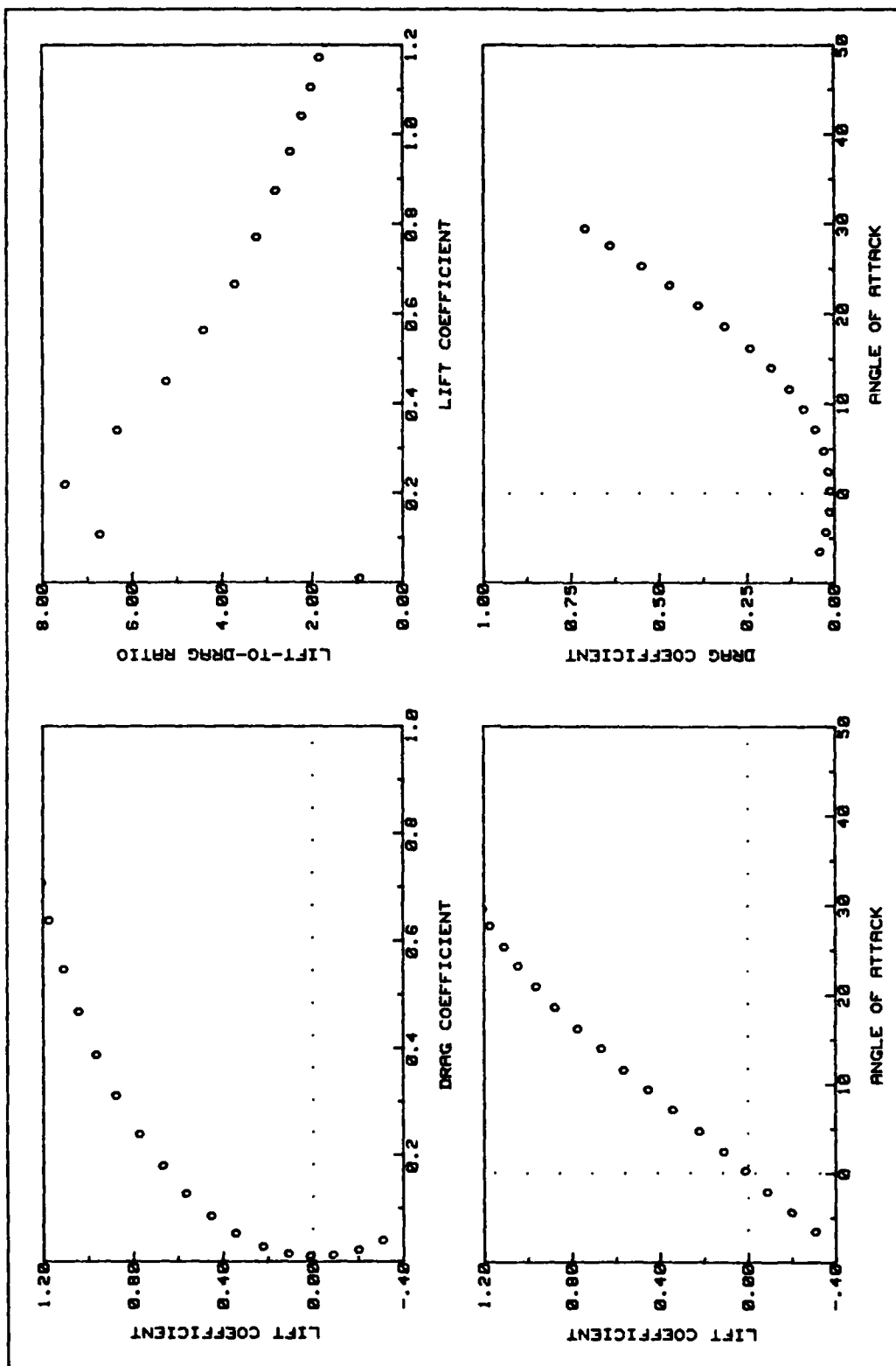


Fig A91. C9 Flap Lift and Drag Data (deployed 30 deg asymmetric)

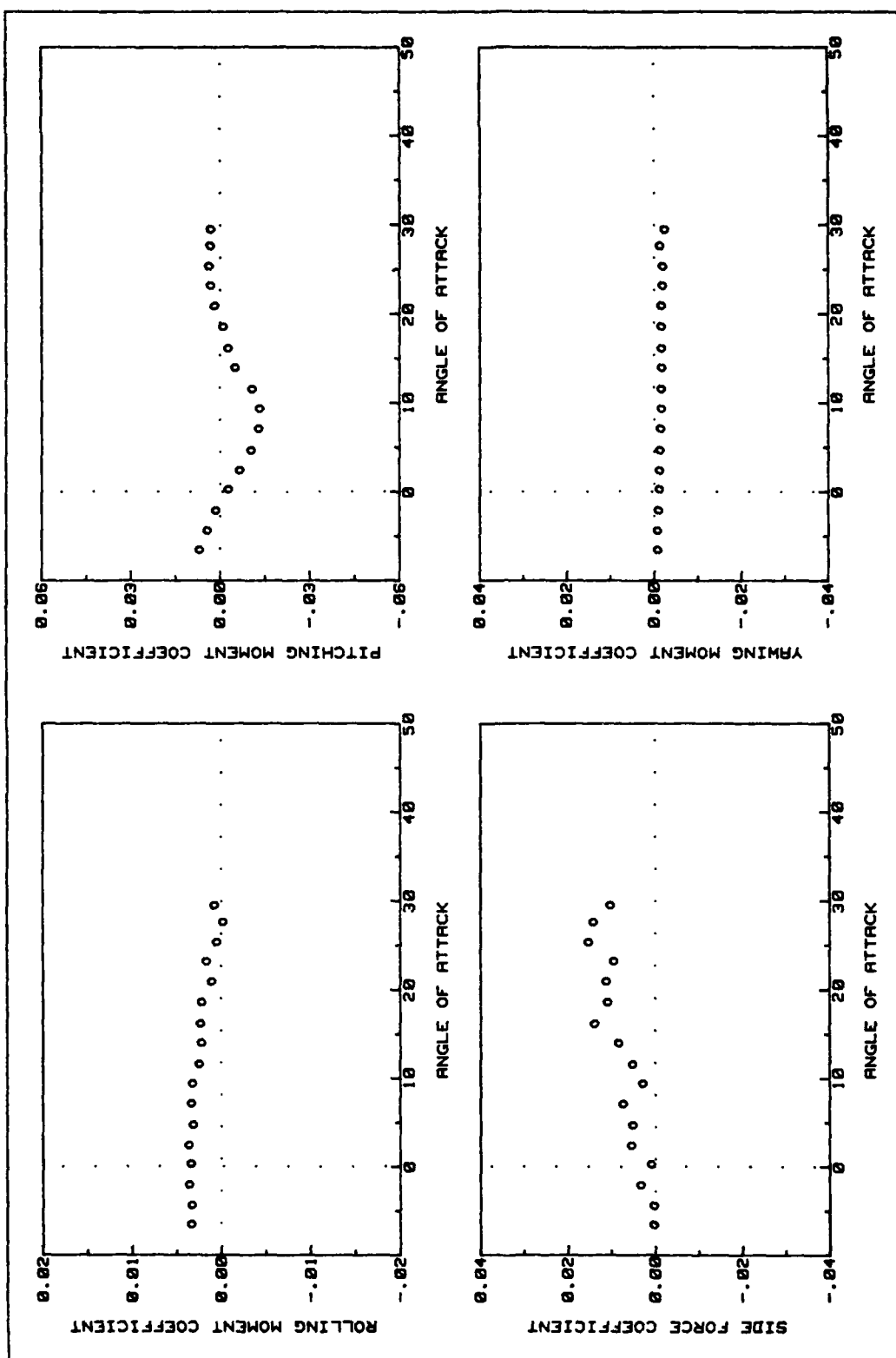


Fig A92. C9 Flap Side Force and Moments Data (deployed 30 deg asymmetric)

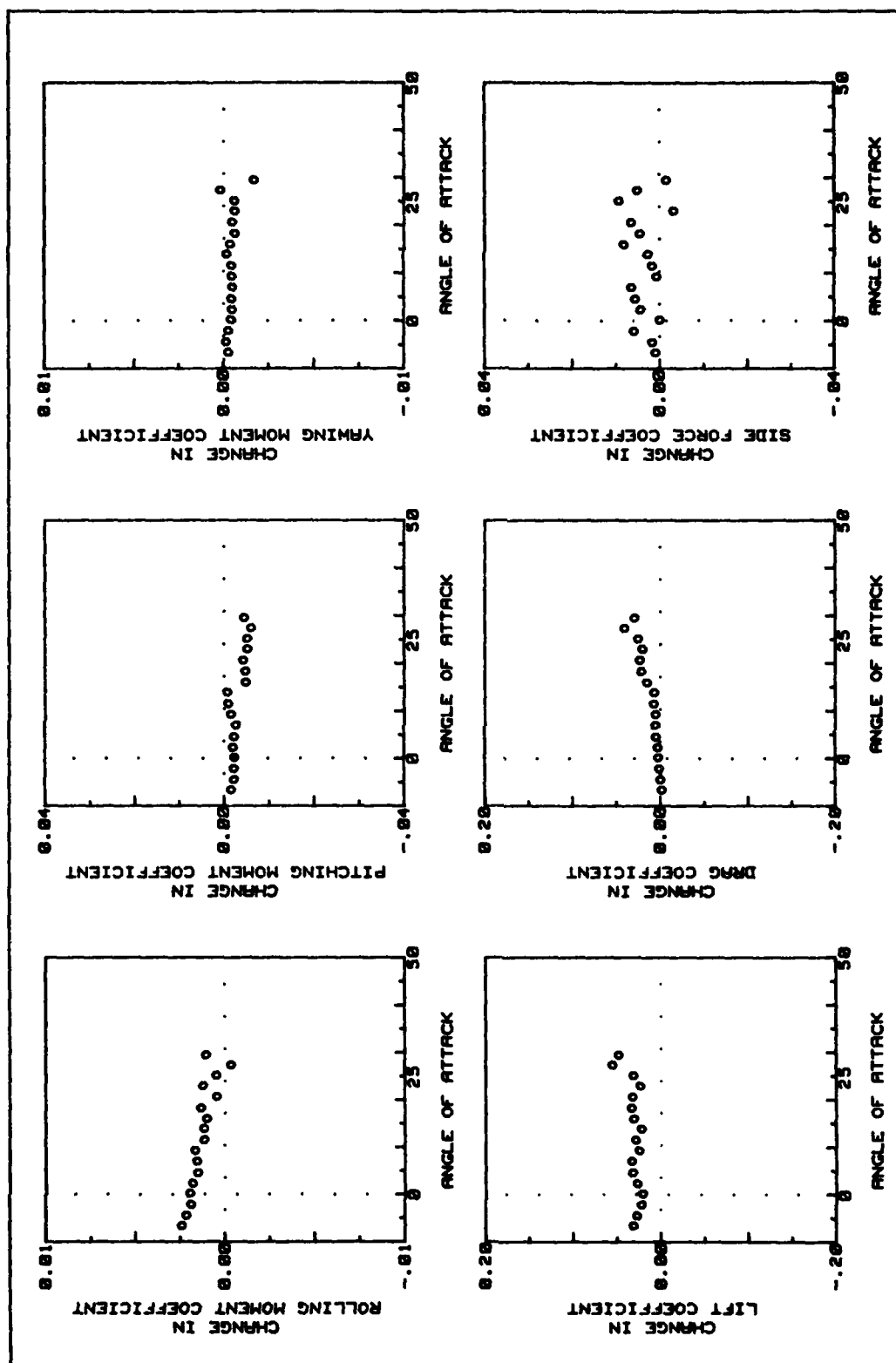


Fig A93. C9 Flap Force and Moment Changes (deployed 30 deg asymmetric)

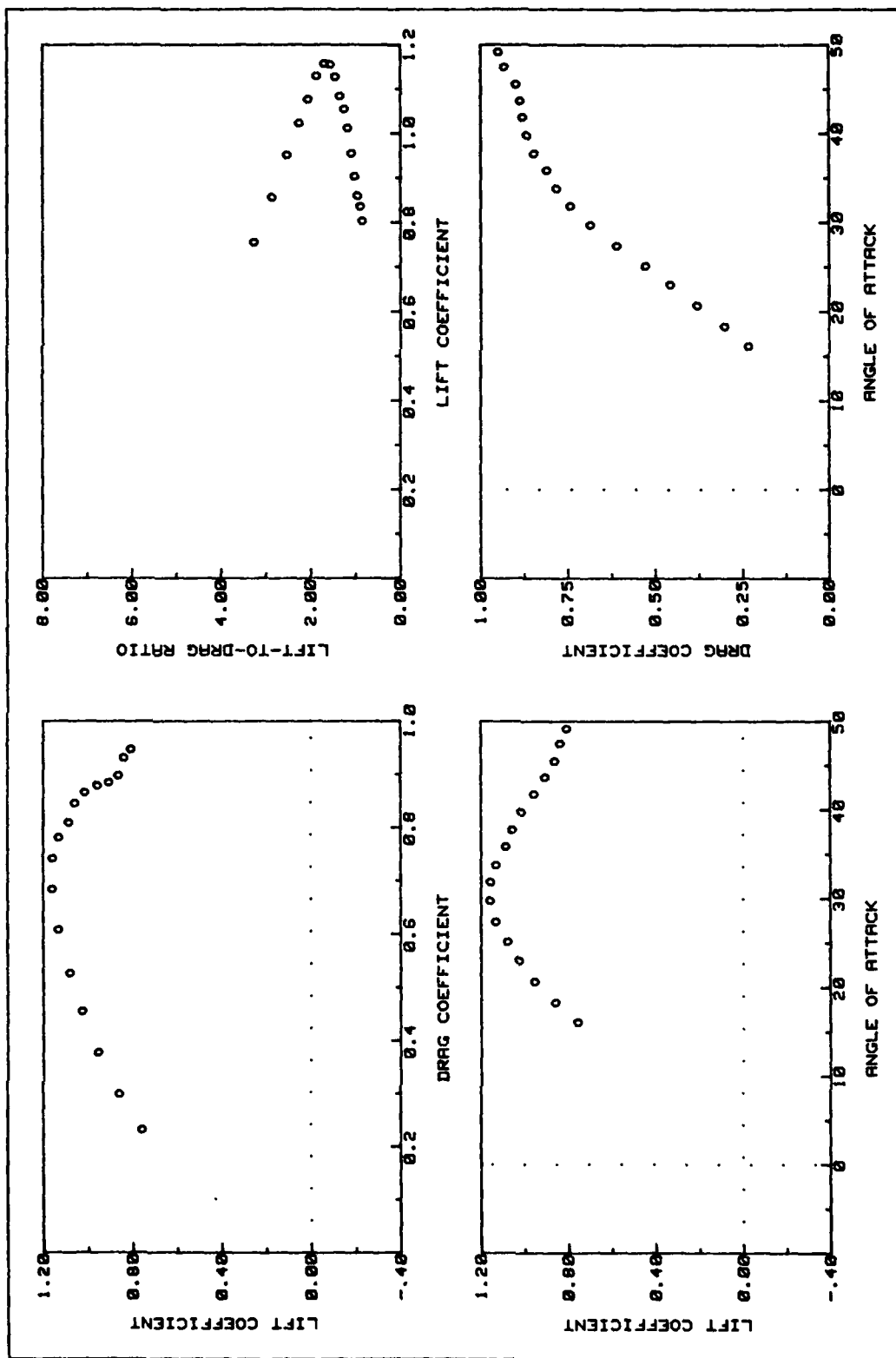


Fig A94. C10 Flap Lift and Drag Data (deployed 60 deg asymmetric)

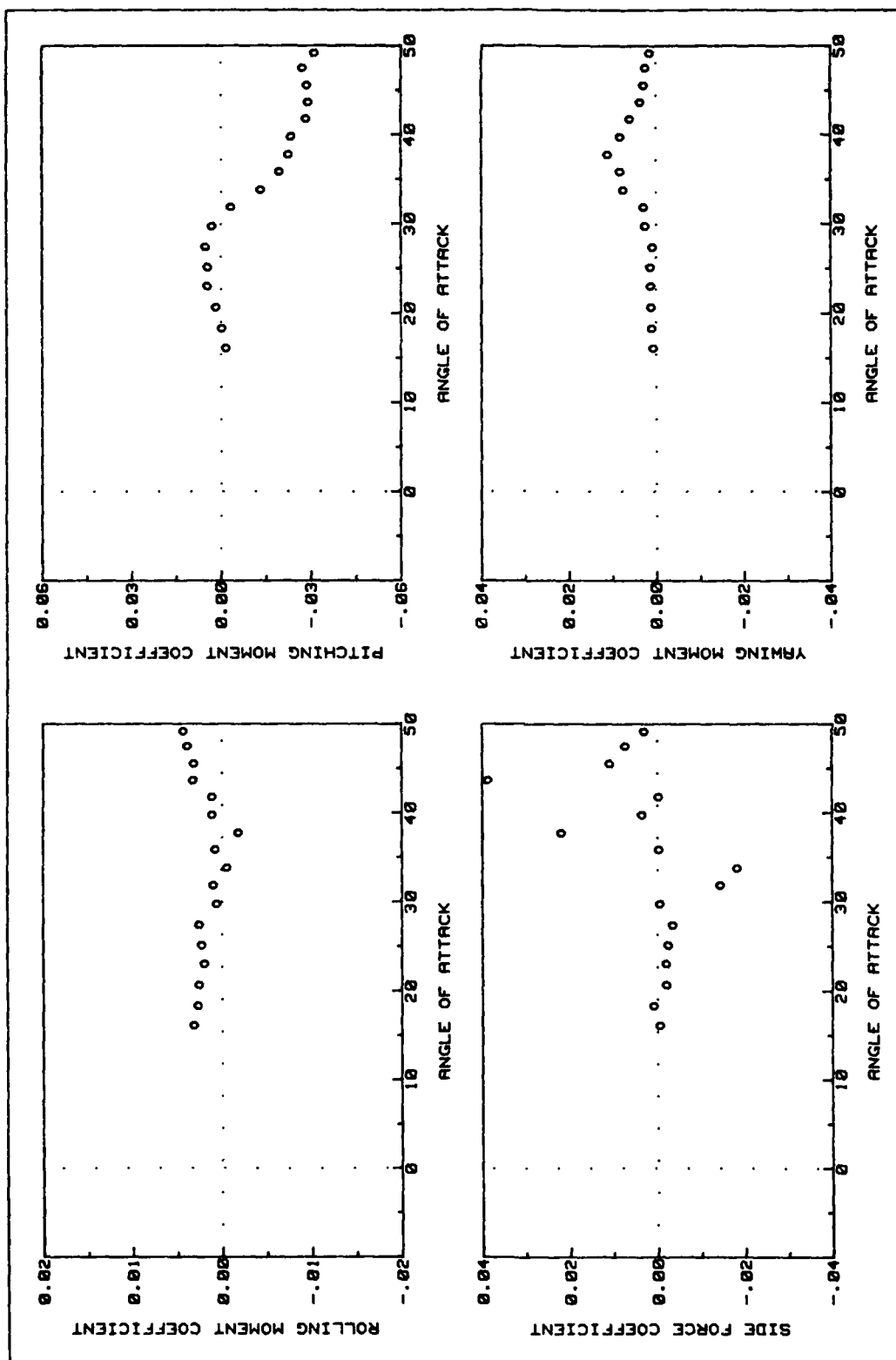


Fig A95. C10 Flap Side Force and Moments Data (deployed 60 deg asymmetric)

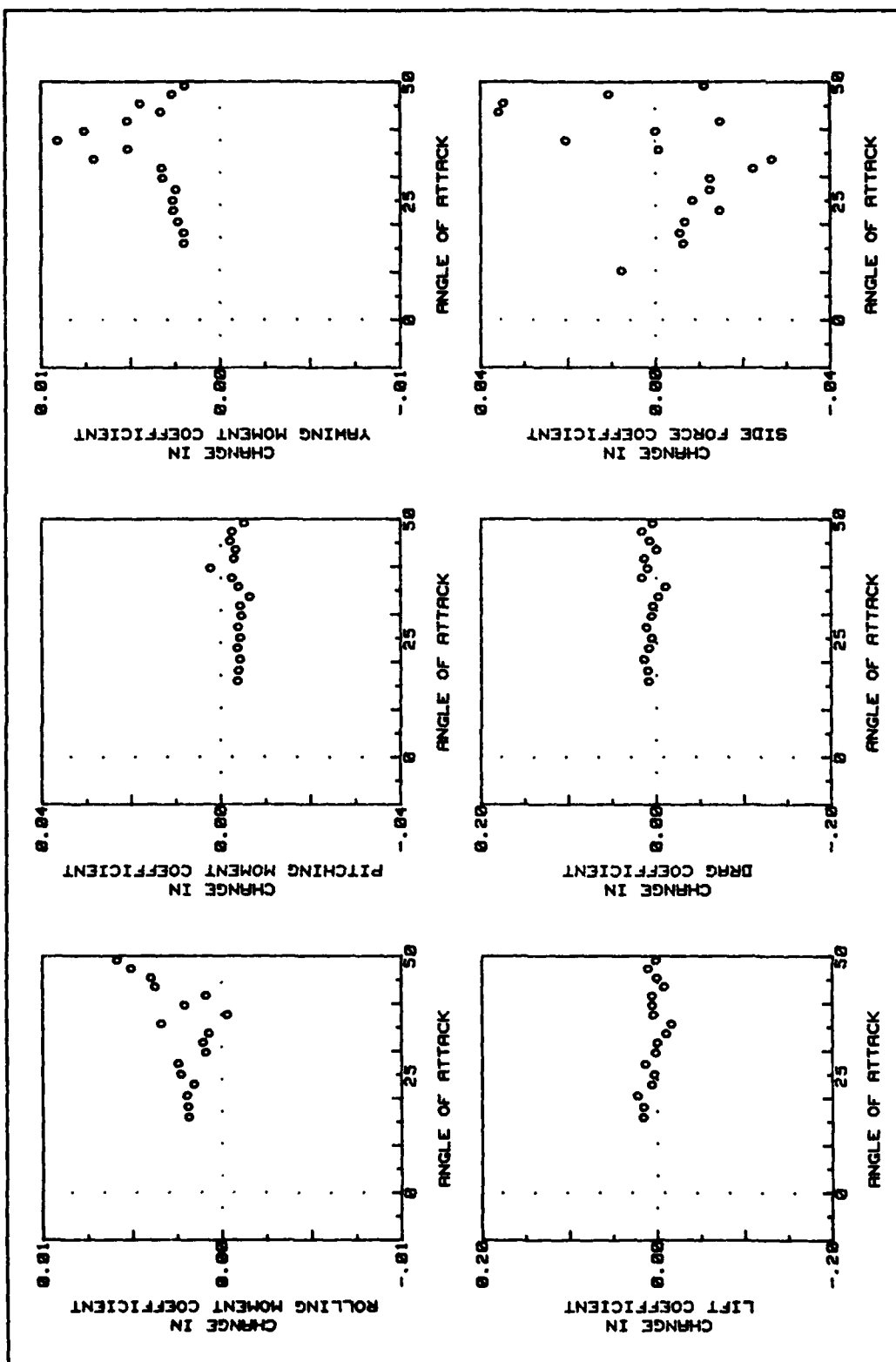


Fig A96. C10 Flap Force and Moment Changes (deployed 60 deg asymmetric)

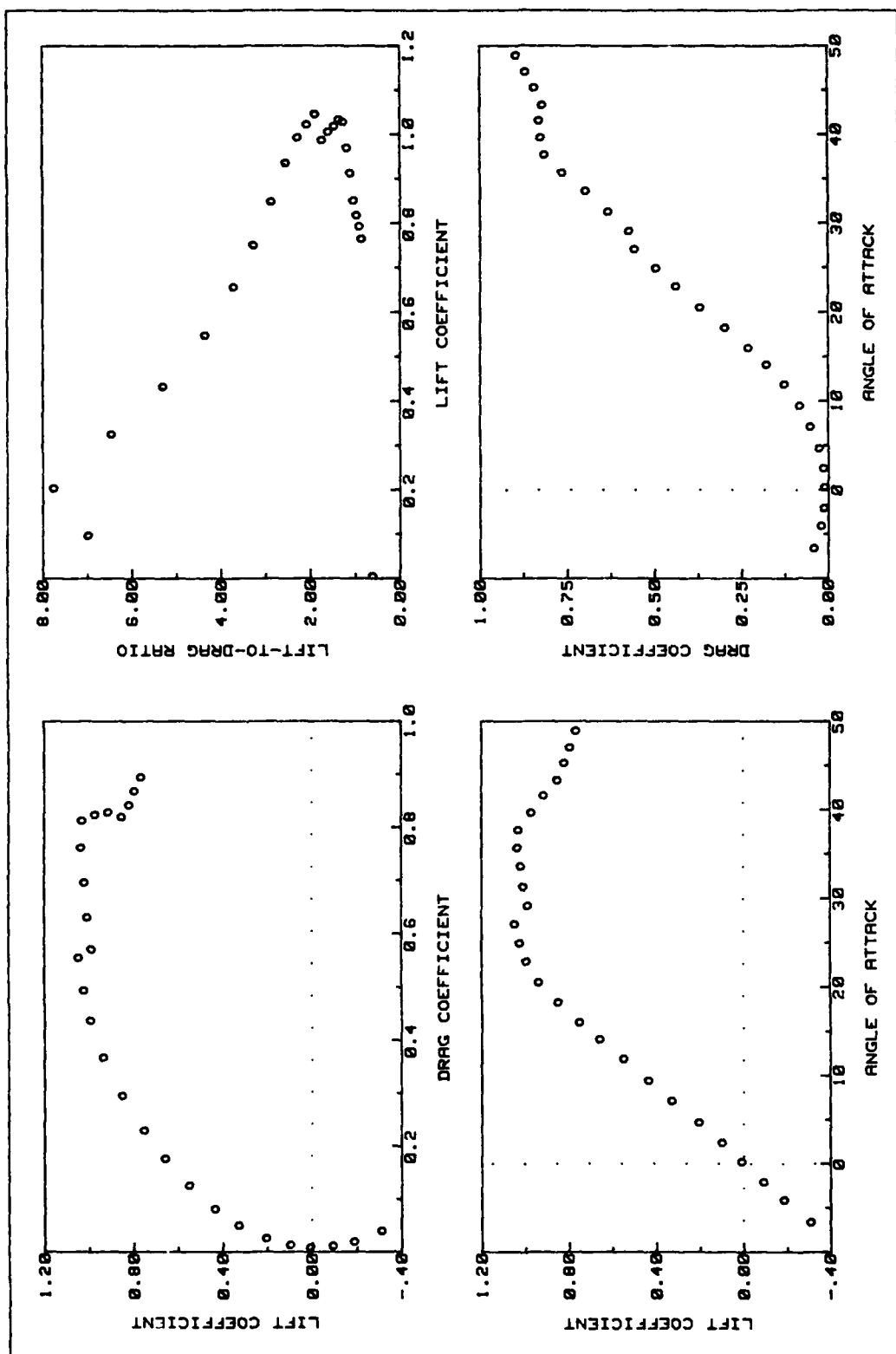


Fig A97. C1 Flap Lift and Drag Data (deployed 60 deg asymmetric)(+6 deg yaw)

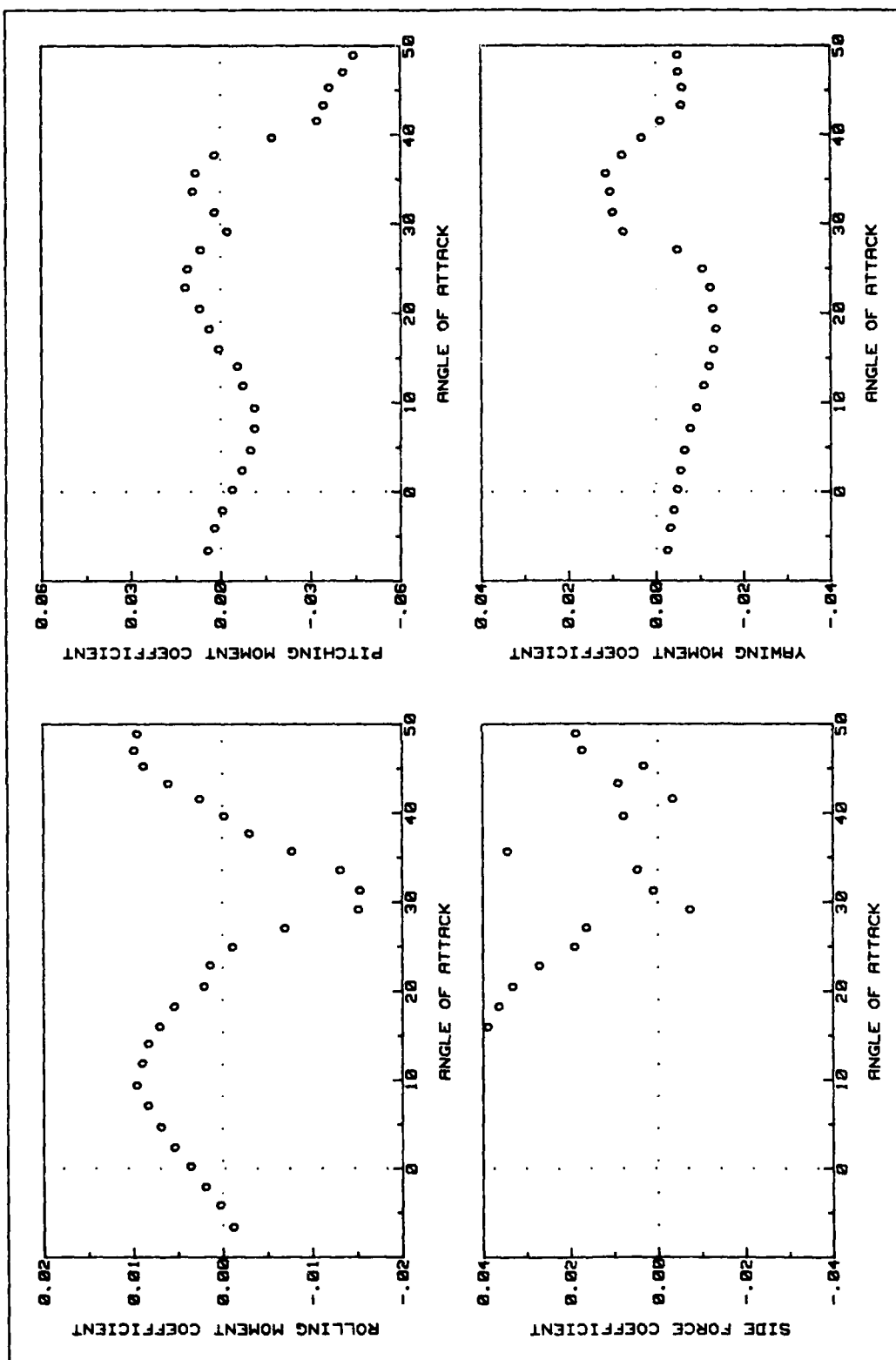


Fig A98. C1 Flap Side Force and Moments Data (deployed 60 deg asymmetric)(+6 deg yaw)

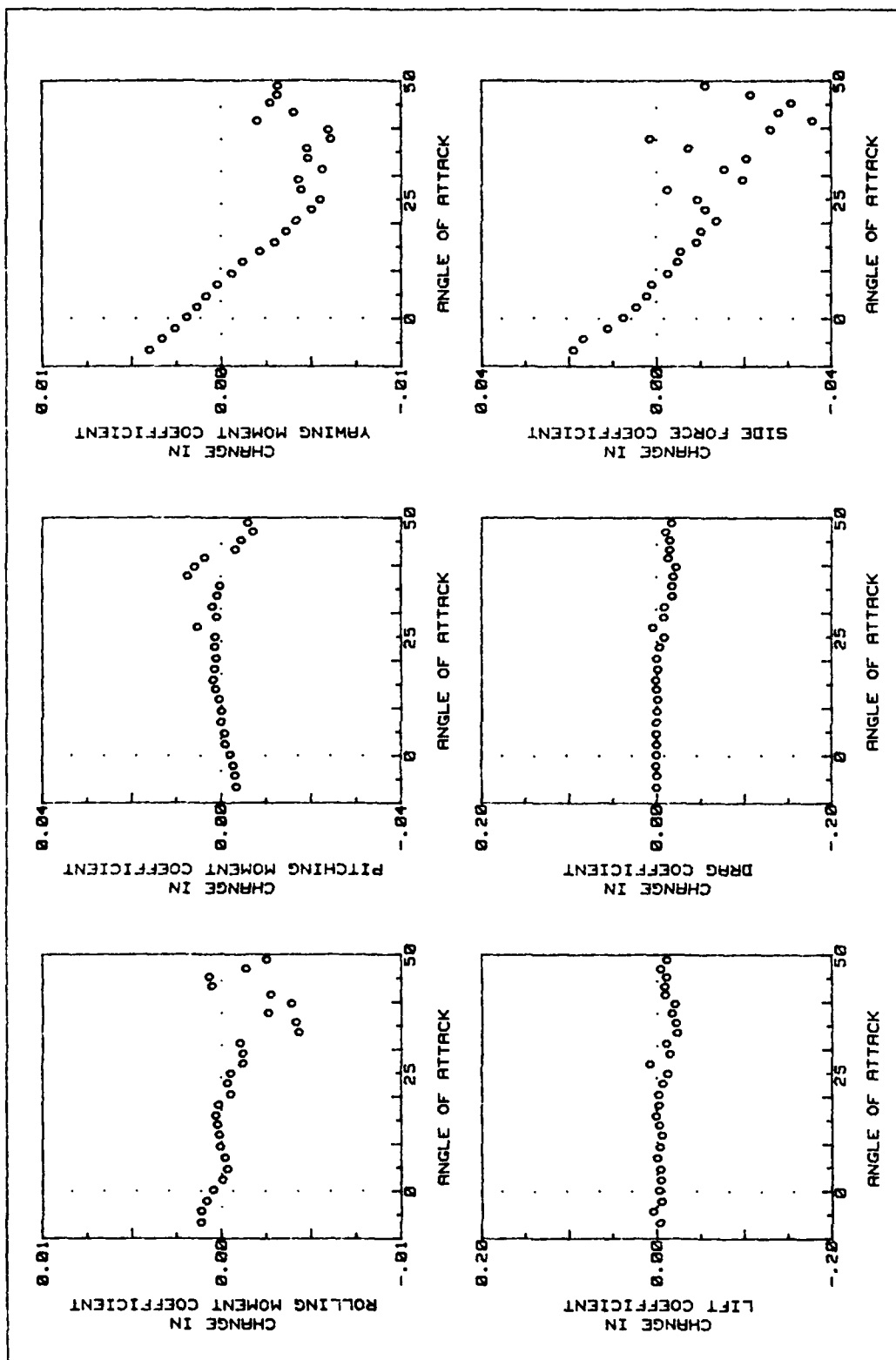


Fig A99. C1 Flap Force and Moment Changes (deployed 60 deg asymmetric)(+6 deg yaw)

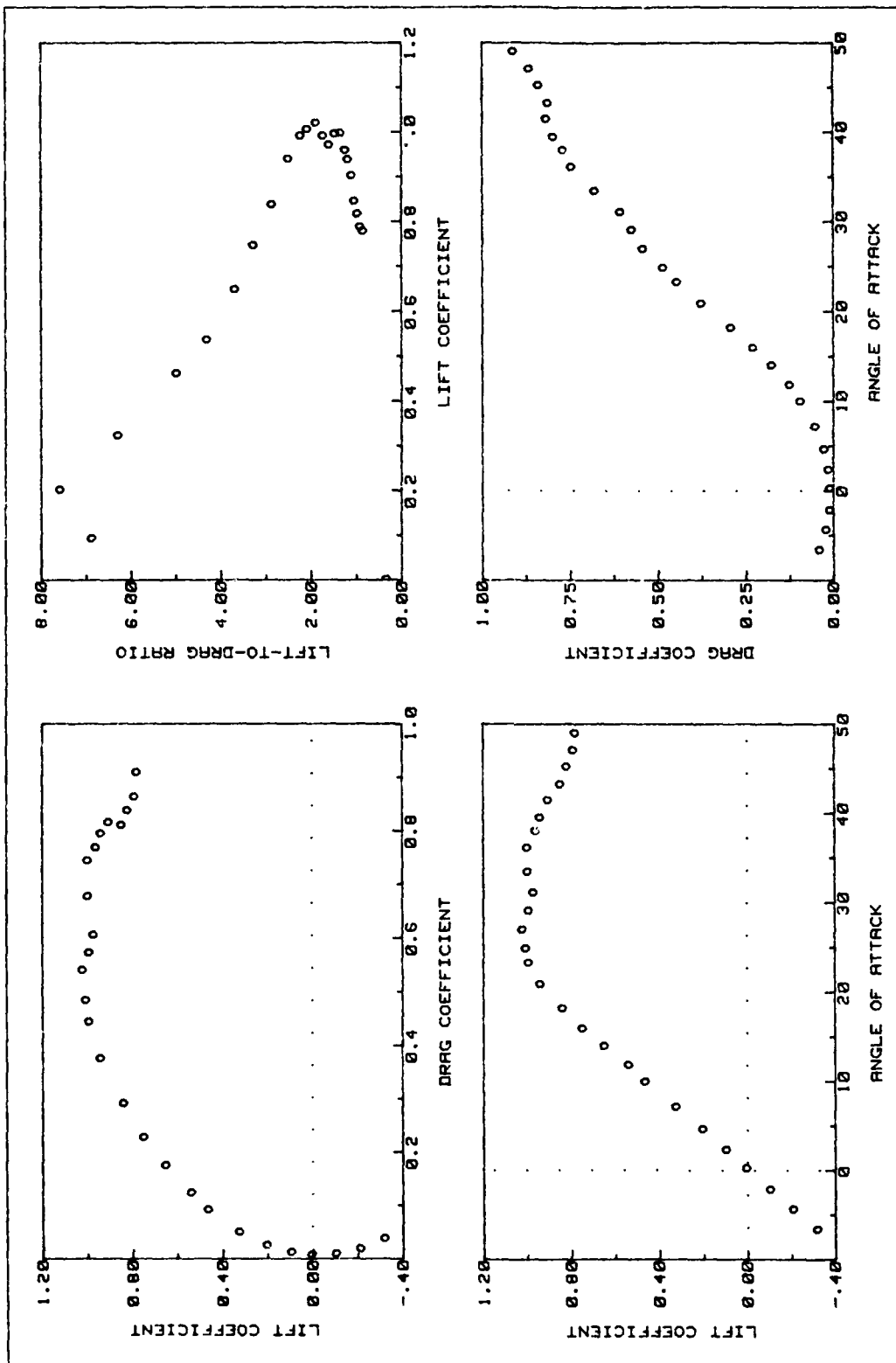


Fig A100. C1 Flap Lift and Drag Data (deployed 60 deg symmetric)(+6 deg yaw)

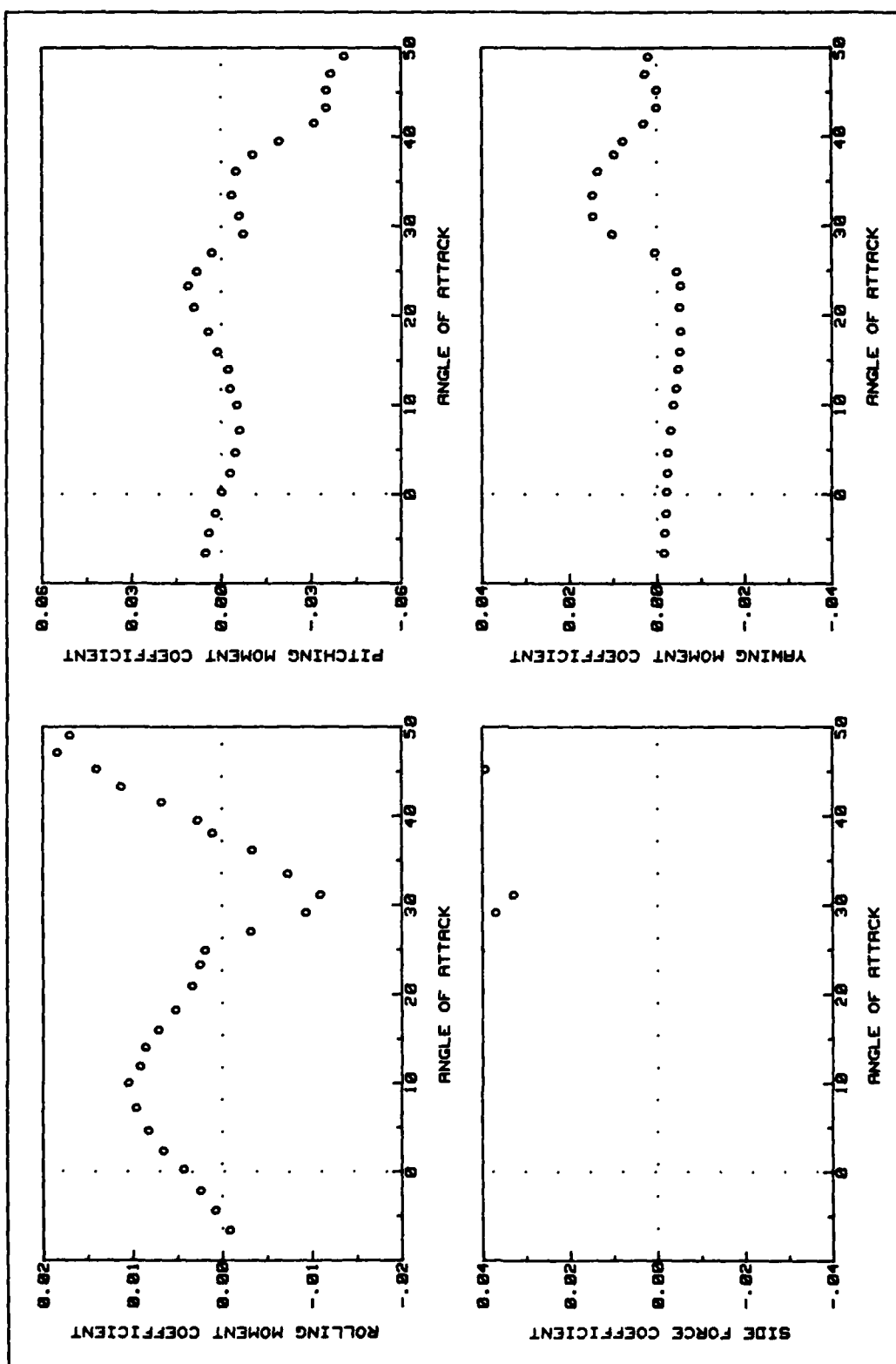


Fig A101. C1 Flap Side Force and Moments Data (deployed 60 deg symmetric)(+6 deg yaw)

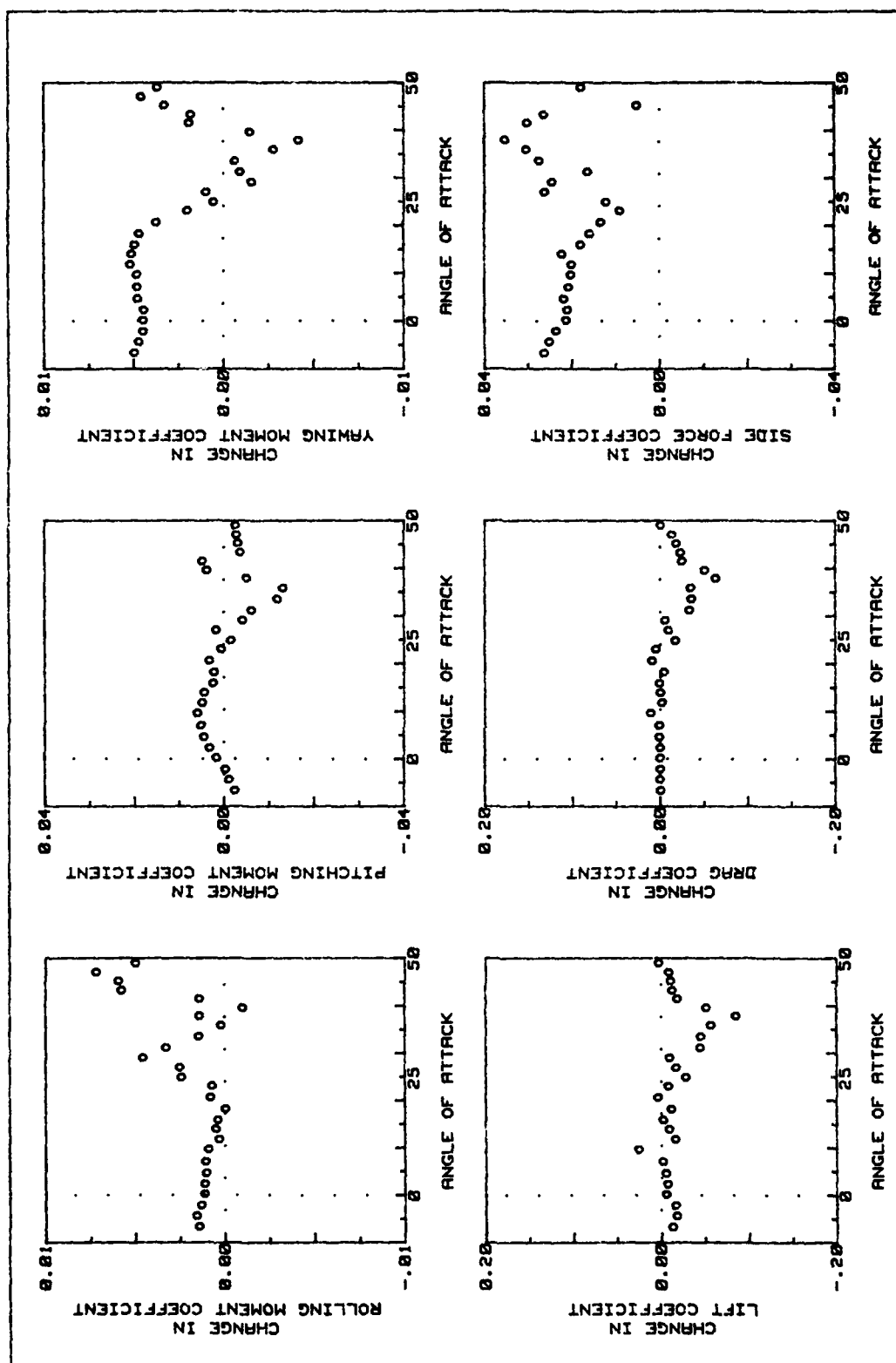


Fig A102. C1 Flap Force and Moment Changes (deployed 60 deg symmetric)(+6 deg yaw)

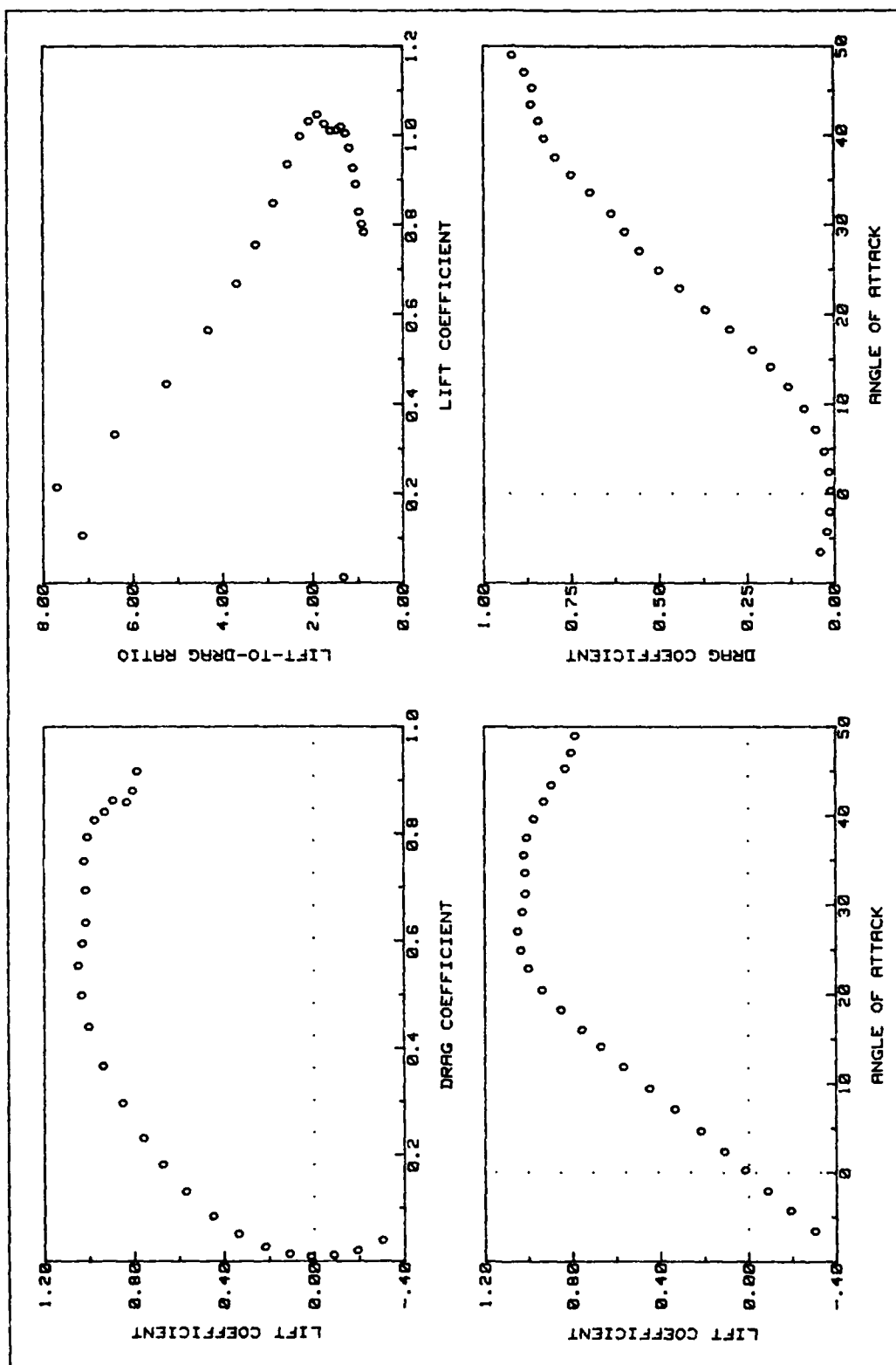


Fig A103. C1 Flap Lift and Drag Data (deployed 60 deg asymmetric)(-6 deg yaw)

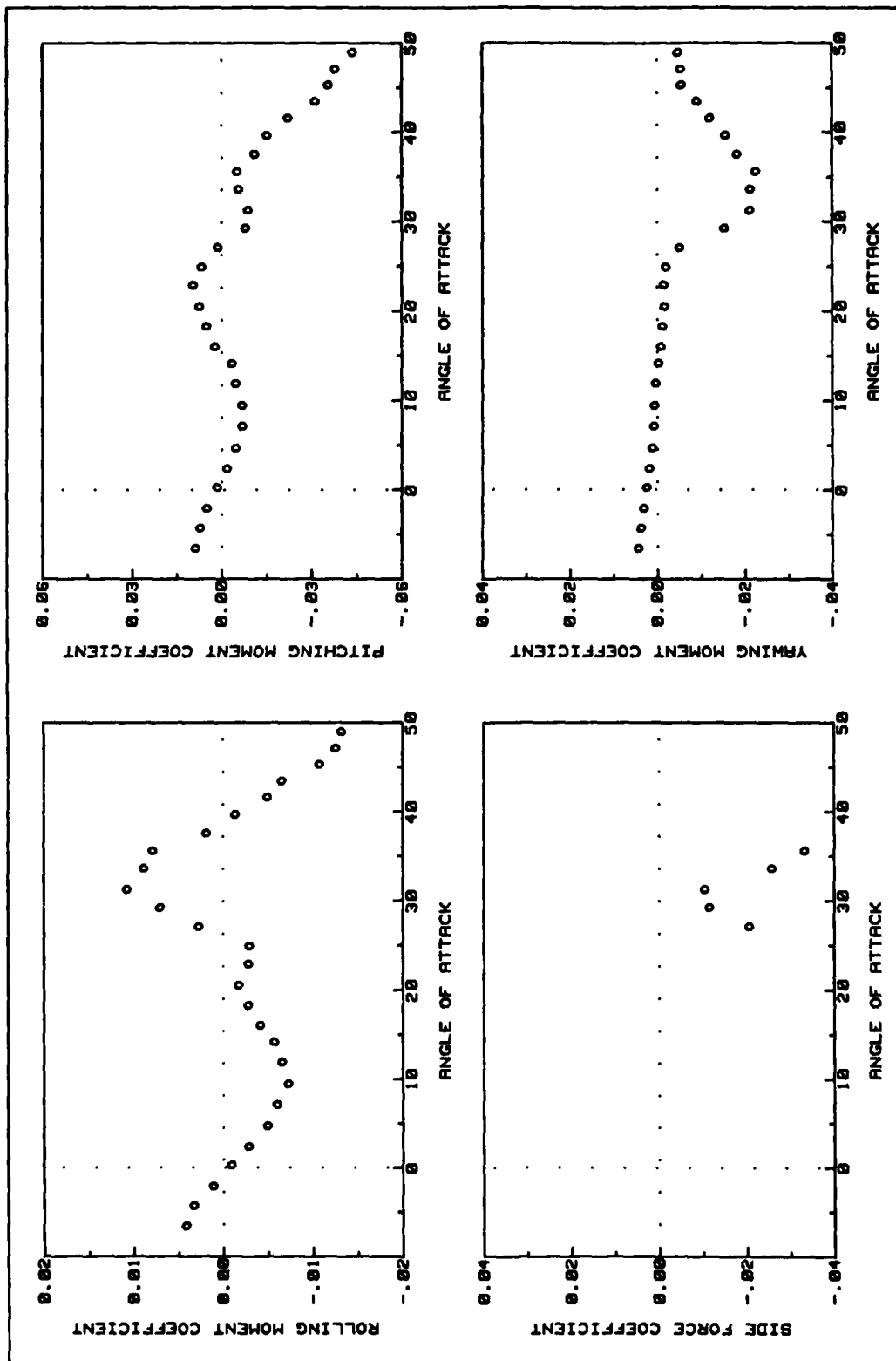


Fig A104. C1 Flap Side Force and Moment Data (deployed 60 deg asymmetric)(-6 deg yaw)

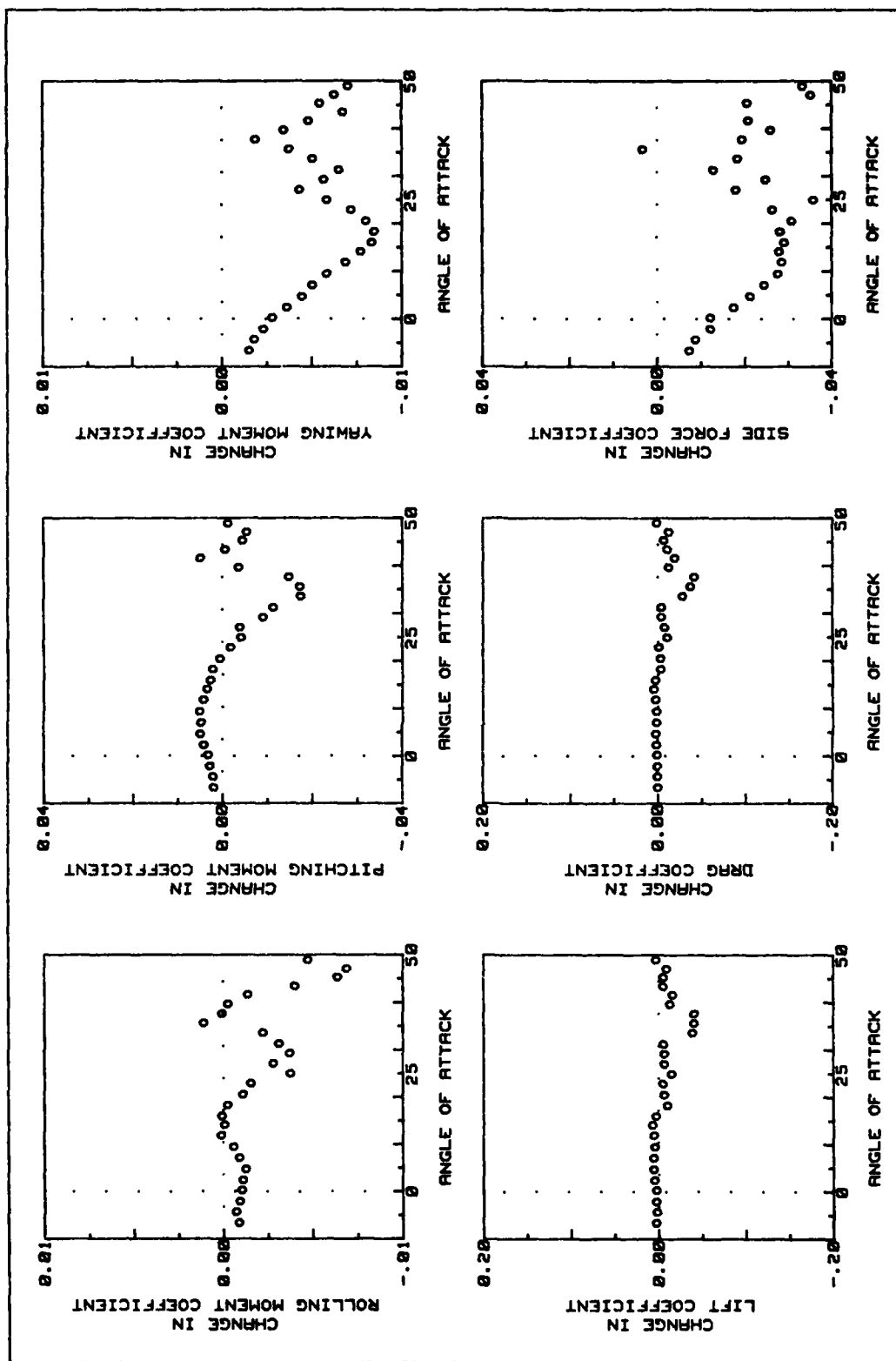


Fig A105. C1 Flap Force and Moment Changes (deployed 60 deg asymmetric)(-6 deg yaw)

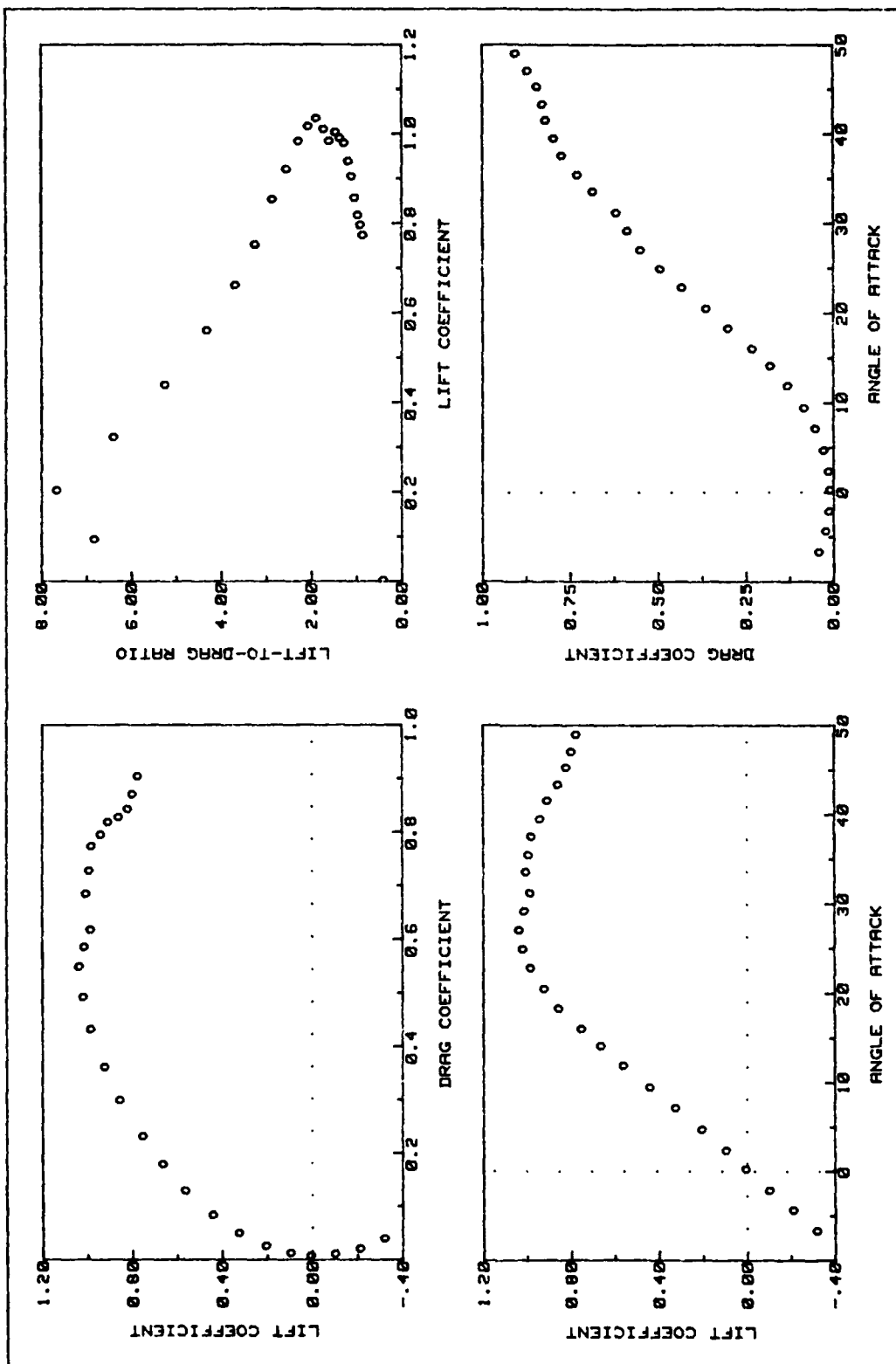


Fig A106. C1 Flap Lift and Drag Data (deployed 60 deg symmetric)(-6 deg yaw)

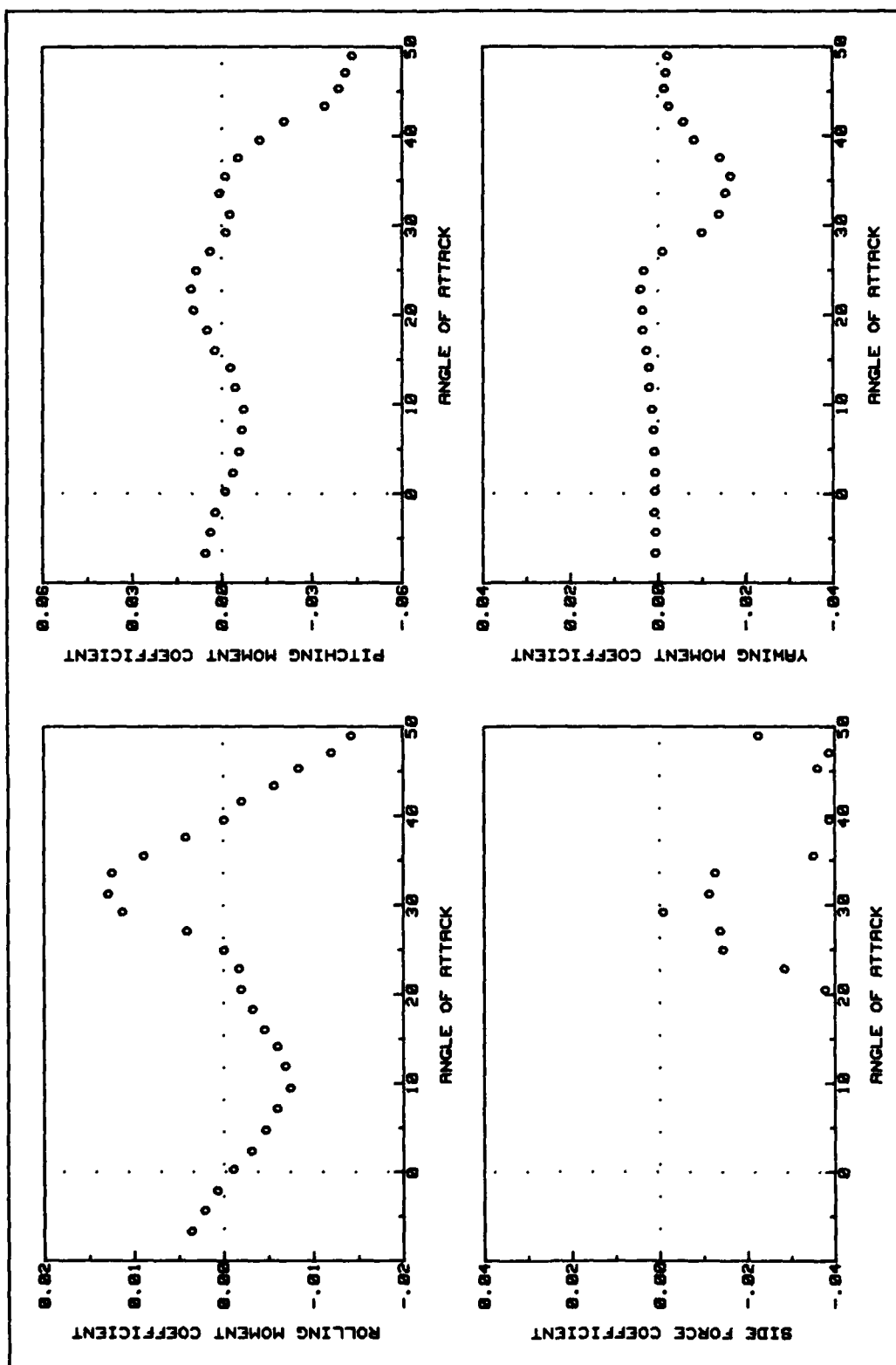


Fig A107. C1 Flap Side Force and Moments Data (deployed 60 deg symmetric)(-6 deg yaw)

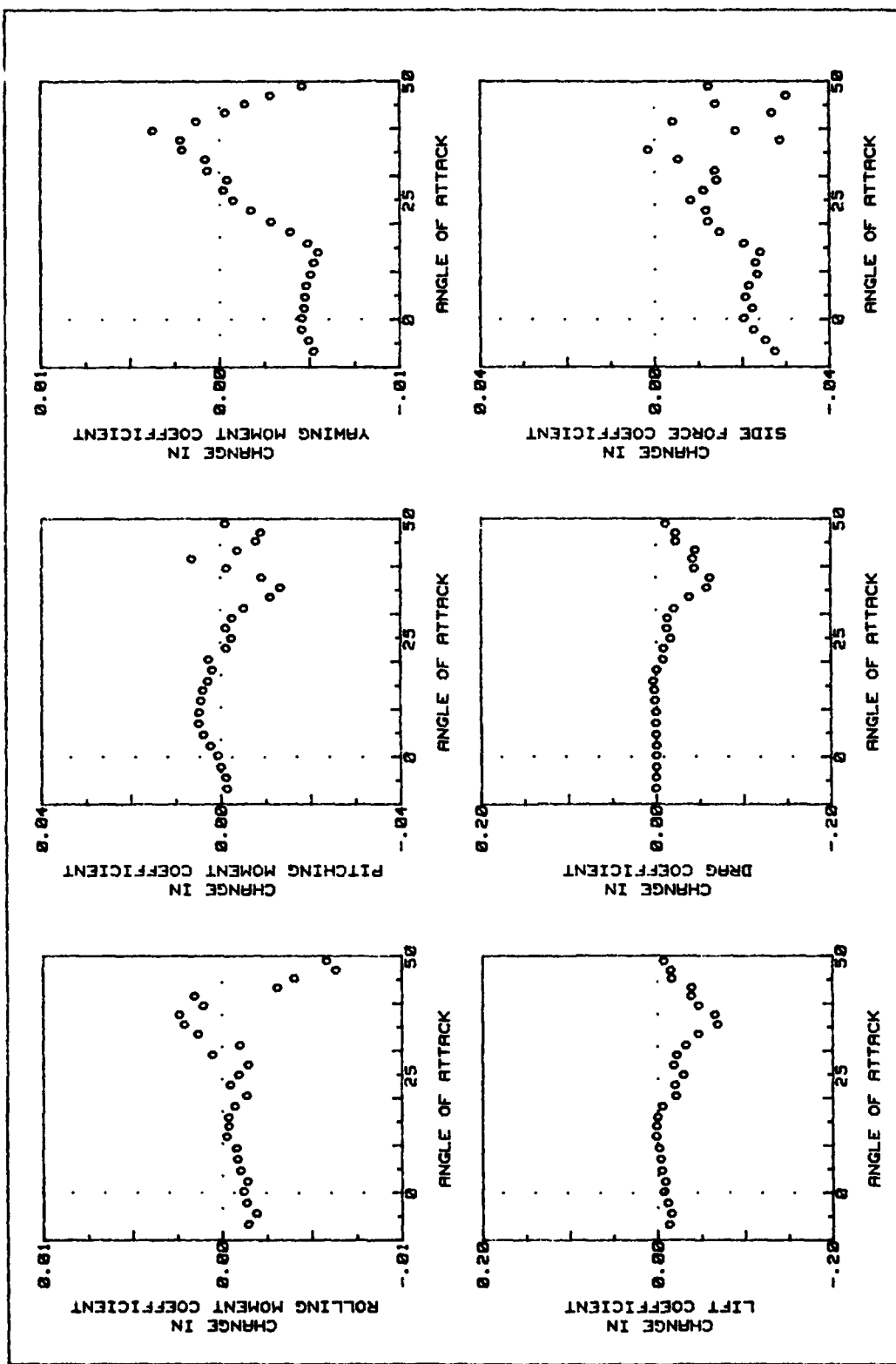


Fig A108. C1 Flap Force and Moment Changes (deployed 60 deg symmetric)(-6 deg yaw)

Appendix B

Oil Flow Visualizations

This appendix contains the photographs of an oil flow visualization study done during this thesis project. Due to the extensive time and effort involved, only a limited number of cavity flaps and α 's were studied. This should be considered a qualitative study only and not a quantitative one. It is hard, if not impossible, to back quantitative data out of oil flow visualizations since the oil flow is influenced by factors other than the air over it. The oil is immersed in a boundary layer, it has its own viscosity, and the wing and cavity flap have surface friction. However, the few cavity flaps tested gave a general understanding of what the air flow was doing over the wing surfaces and in the flap vicinity. The α 's selected for the study were 8° , 18° , and 26° . With the sting deflections, the resulting α 's were 9.5° , 20° , and 30° . thus providing a low, a middle, and a high α . These angles were obtained with no prebend in the sting.

The oil was applied to the upper and lower wing surfaces using a one inch square grid and a cotton swab. The oil was applied to both cavity flap surfaces in rows using a cotton swab. This method of application allowed com-

parisons of oil flows between the flaps themselves, and comparisons of the upper and lower wing surfaces with a cavity flap deployed against the model's baseline flow visualizations.

Figures B1 through B6 contain photographs for the model's baseline flow visualizations. They show the upper and lower wing surfaces at each of the α settings. The remaining figures are a grouping of upper and lower wing surfaces and the cavity flap surfaces for the cavity flap configuration specified. Photographs of some surfaces for each cavity flap and α studied are not present.

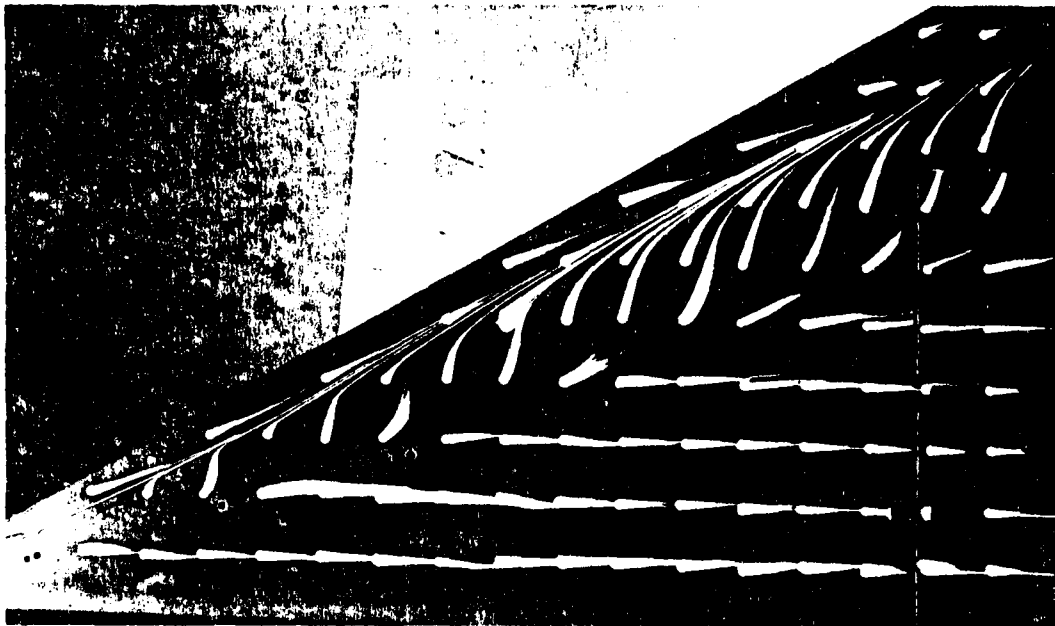


Figure B1. Upper Wing Surface of Model Baseline at $9.5^\circ \alpha$

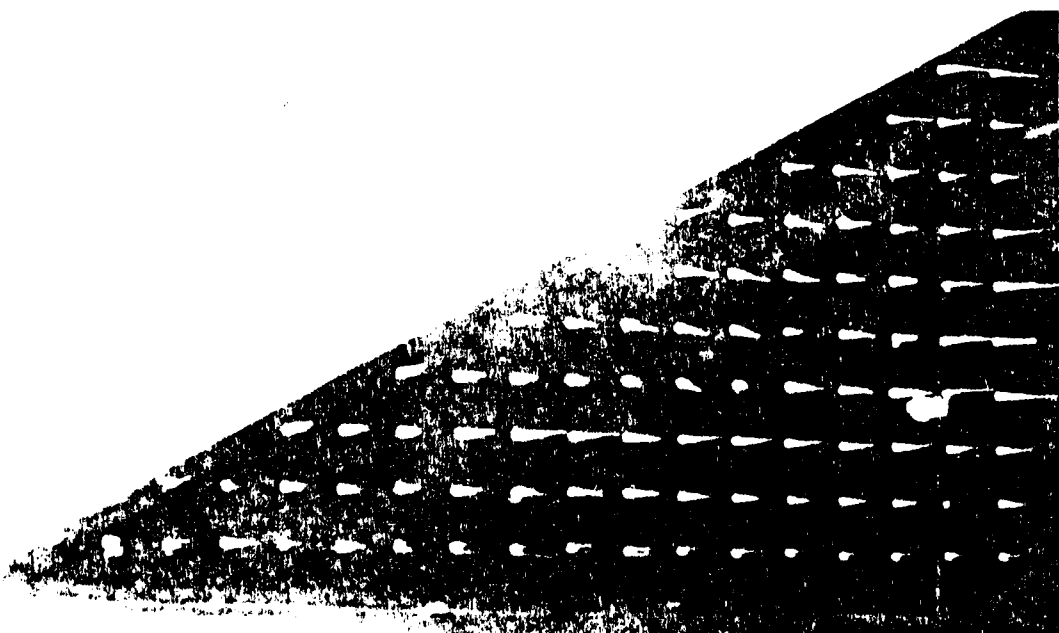


Figure B2. Lower Wing Surface of Model Baseline at $9.5^\circ \alpha$

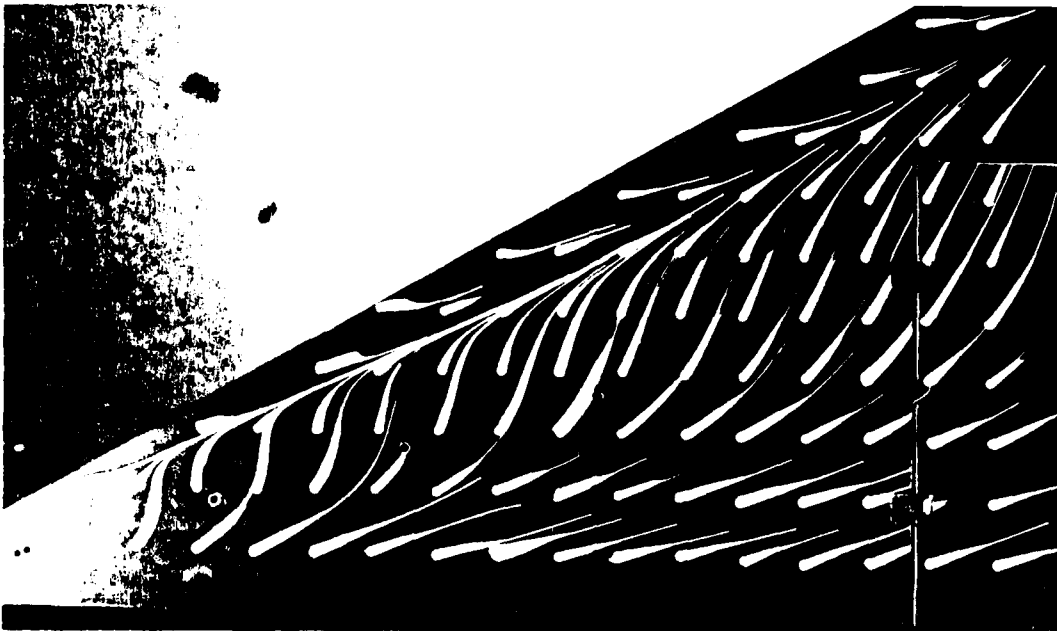


Figure B3. Upper Wing Surface of Model Baseline at $20^\circ \alpha$

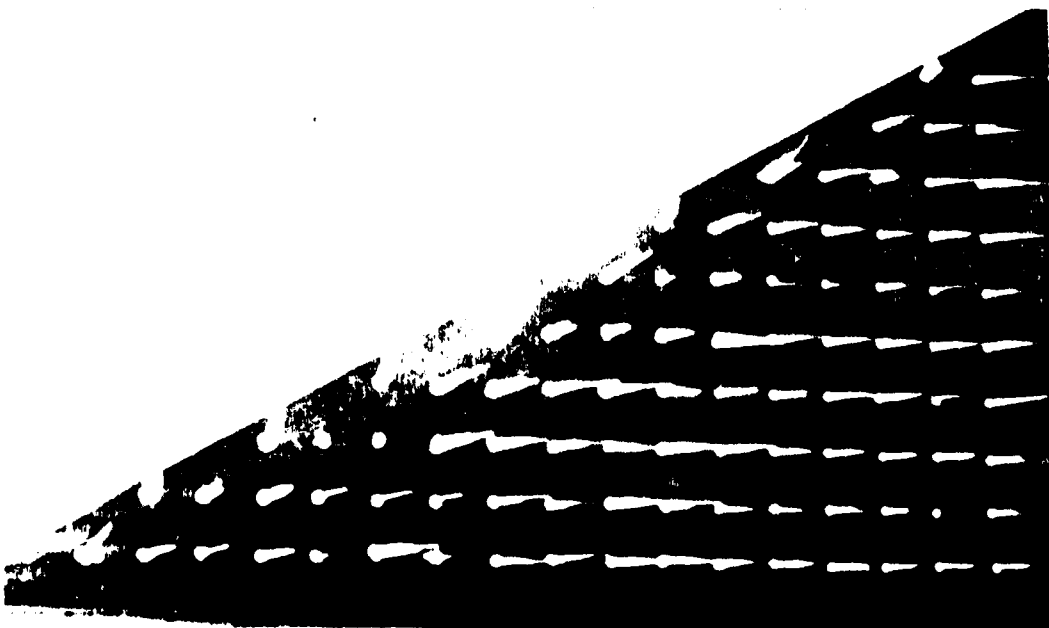


Figure B4. Lower Wing Surface of Model Baseline at $20^\circ \alpha$

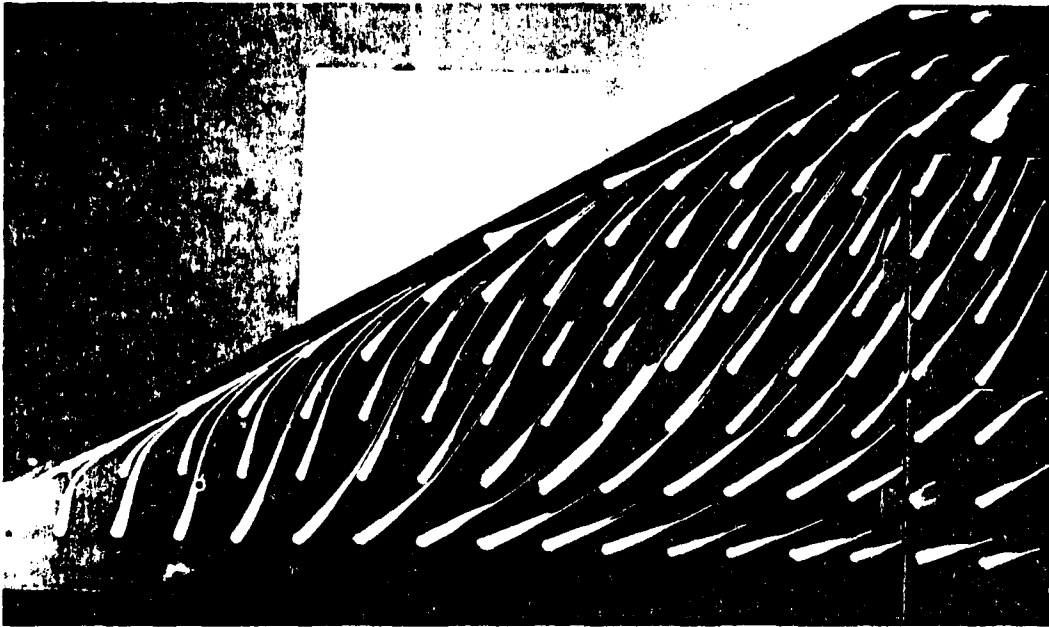


Figure B5. Upper Wing Surface of Model Baseline at $30^\circ \alpha$

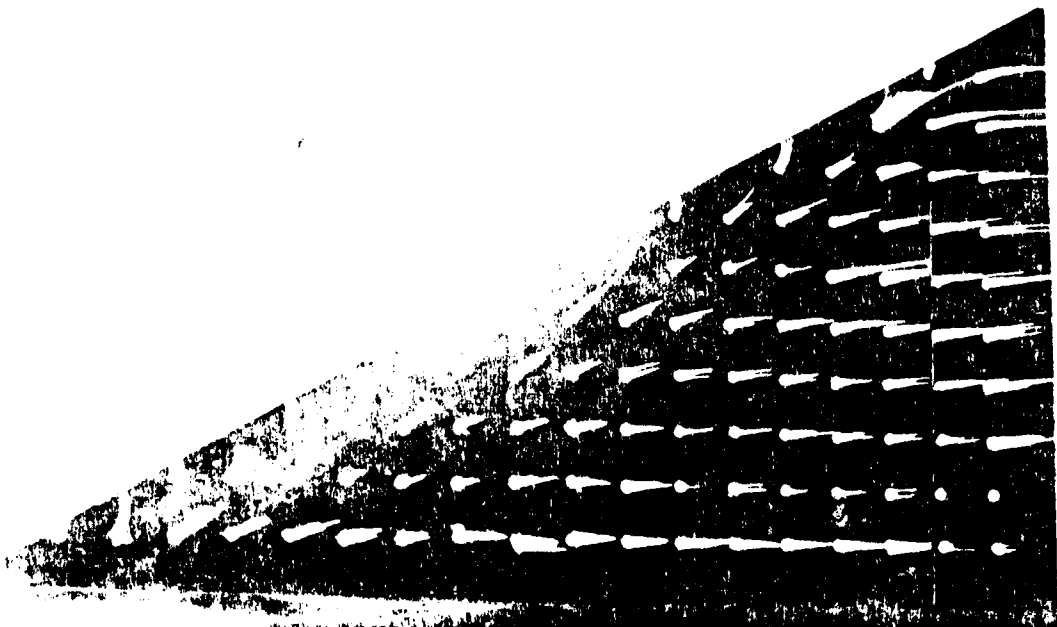


Figure B6. Lower Wing Surface of Model Baseline at $30^\circ \alpha$

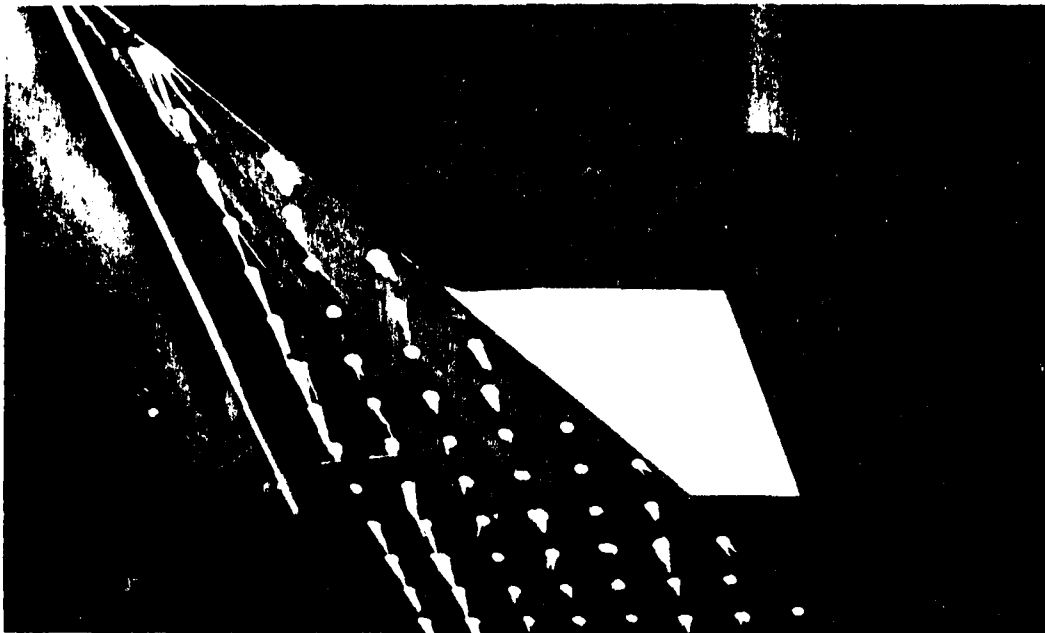


Figure B7. Lower Wing Surface with C1 Flap
Deployed 60° at $9.5^\circ \alpha$

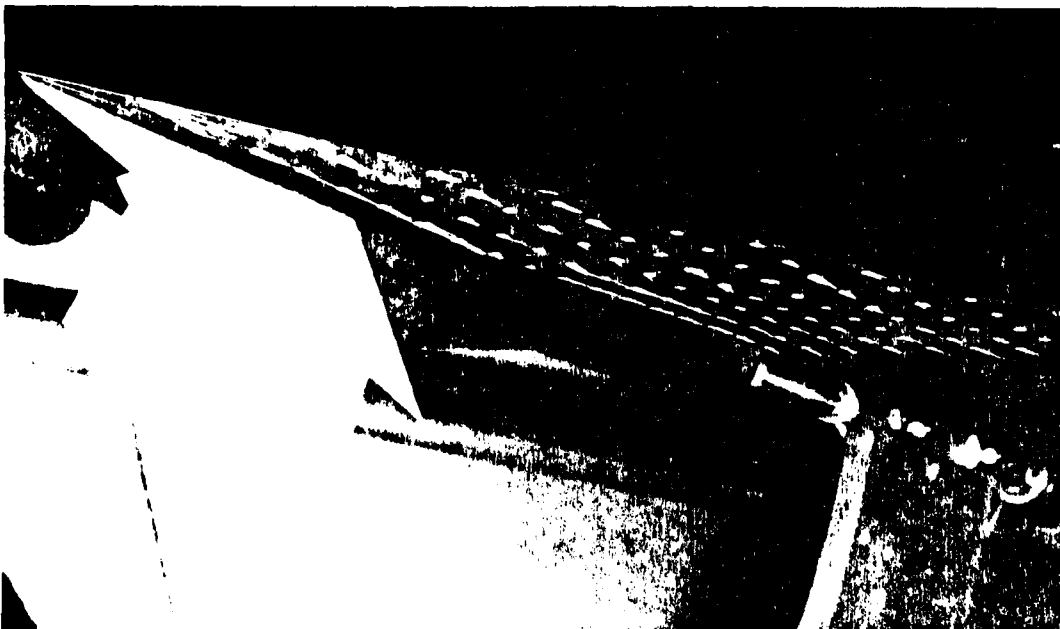


Figure B8. Inside Surface of C1 Cavity Flap
Deployed 60° at $9.5^\circ \alpha$

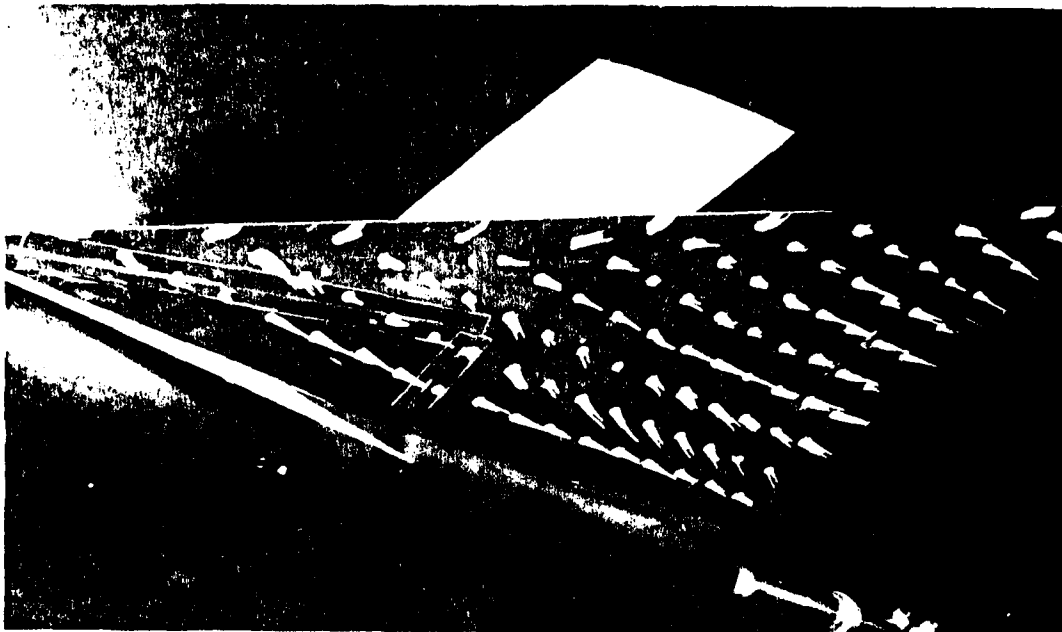


Figure B9. Lower Wing Surface with C1 Flap
Deployed 60° at 20° α

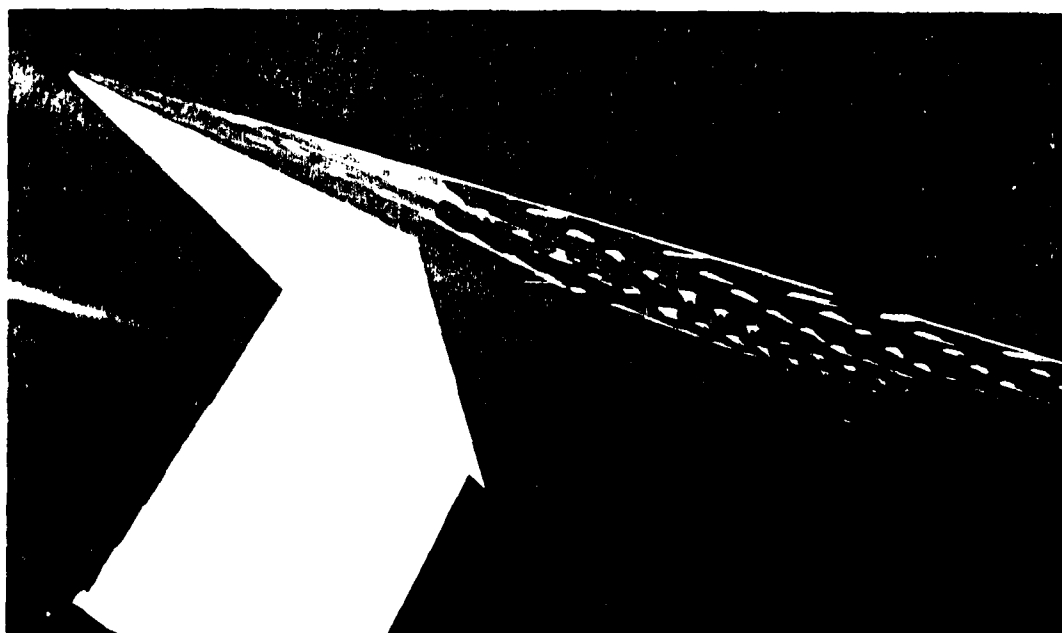


Figure B10. Inside Surface of C1 Cavity Flap
Deployed 60° at 20° α

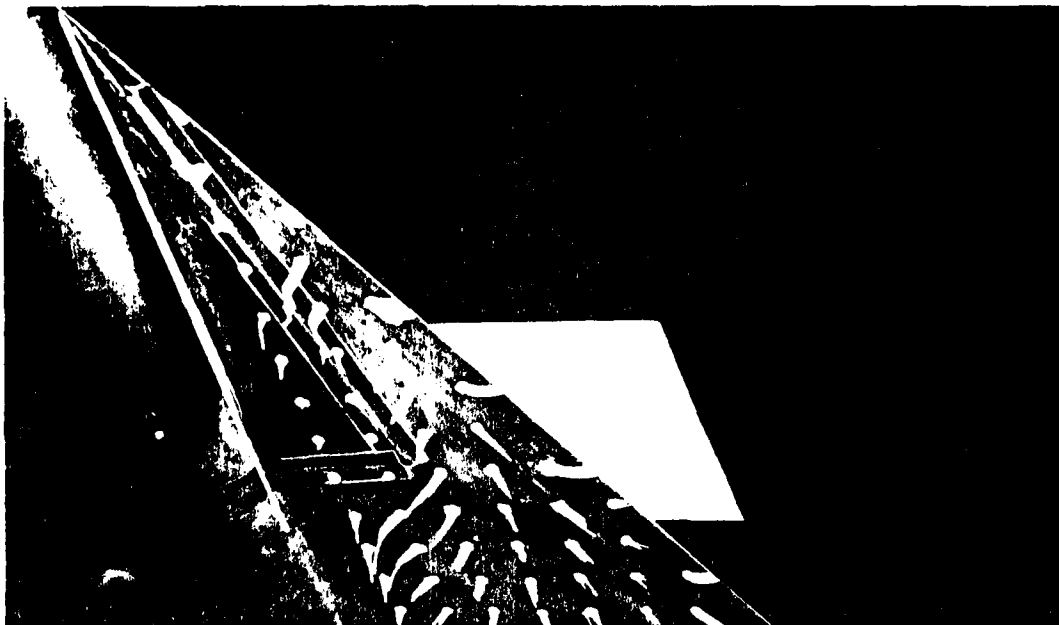


Figure B11. Lower Wing Surface with C1 Flap
Deployed 60° at $30^\circ \alpha$

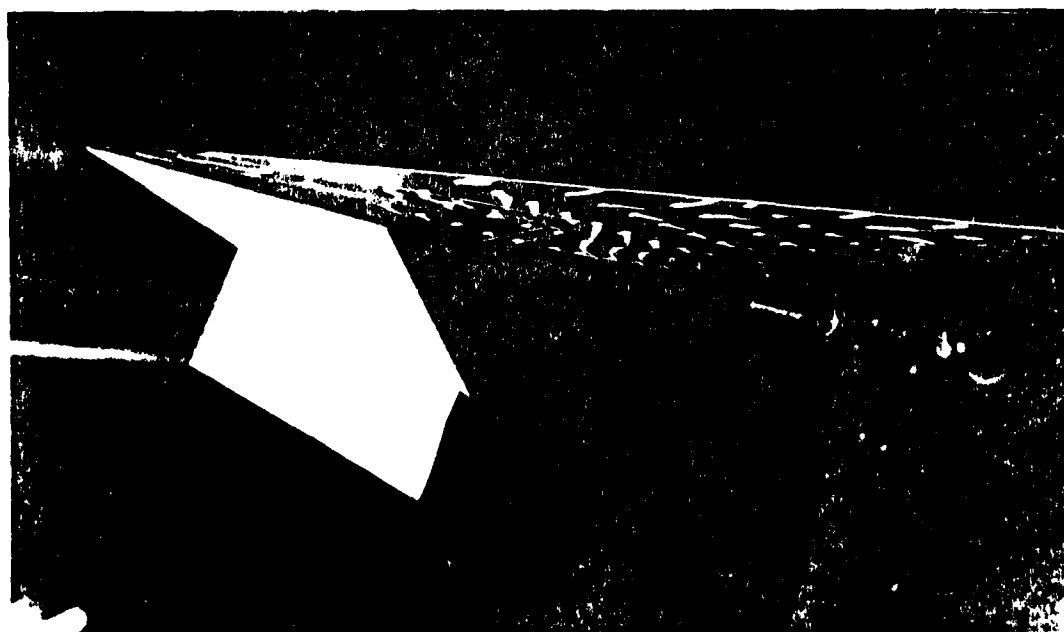


Figure B12. Inside Surface of C1 Cavity Flap
Deployed 60° at $30^\circ \alpha$

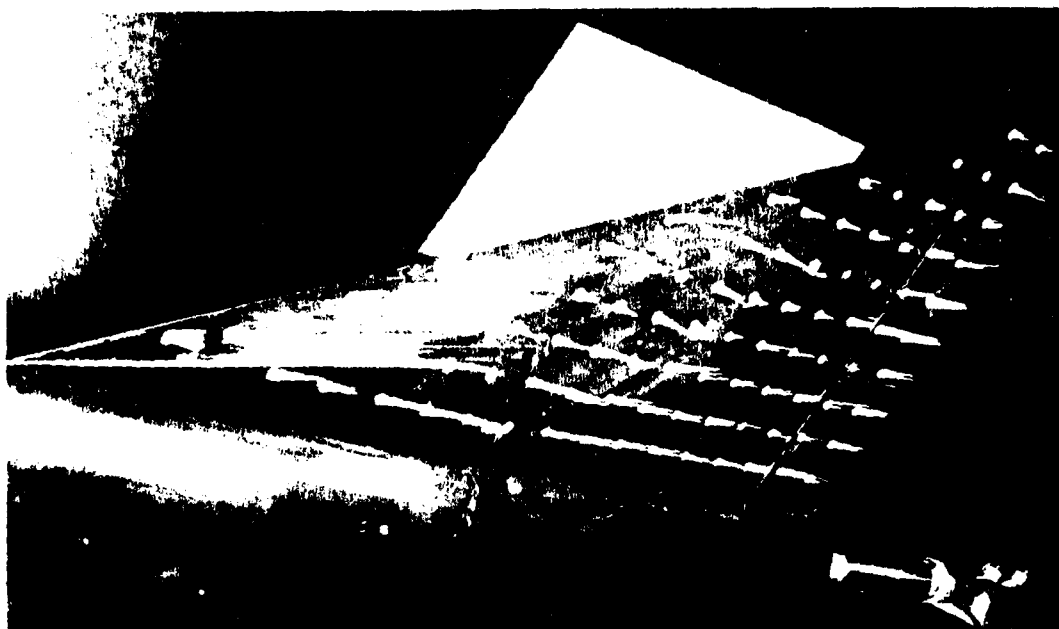


Figure B13. Lower Wing Surface With C2 Flap
Deployed 60° at 9.5° α

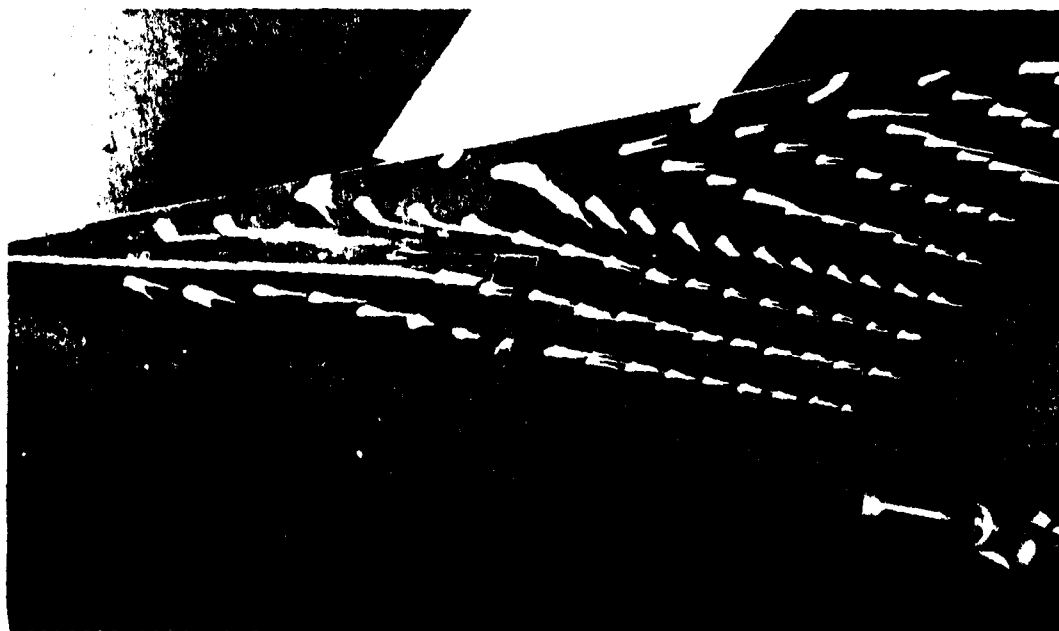


Figure B14. Lower Wing Surface with C2 Flap
Deployed 60° at 20° α

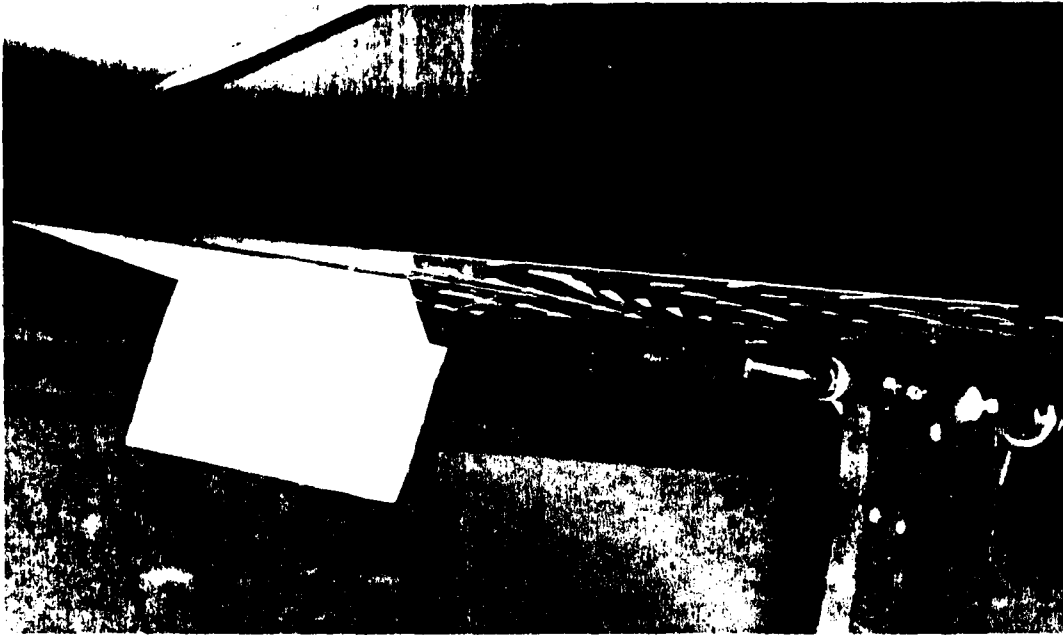


Figure B15. Inside Surface of C2 Cavity Flap
Deployed 60° at $20^\circ \alpha$

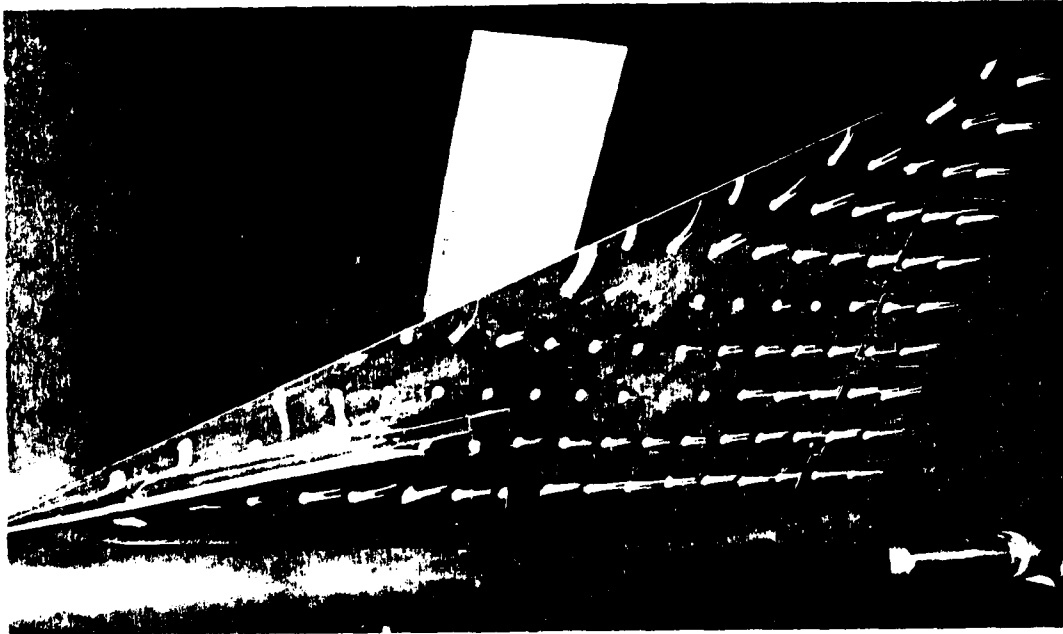


Figure B16. Lower Wing Surface with C2 Flap
Deployed 60° at $30^\circ \alpha$

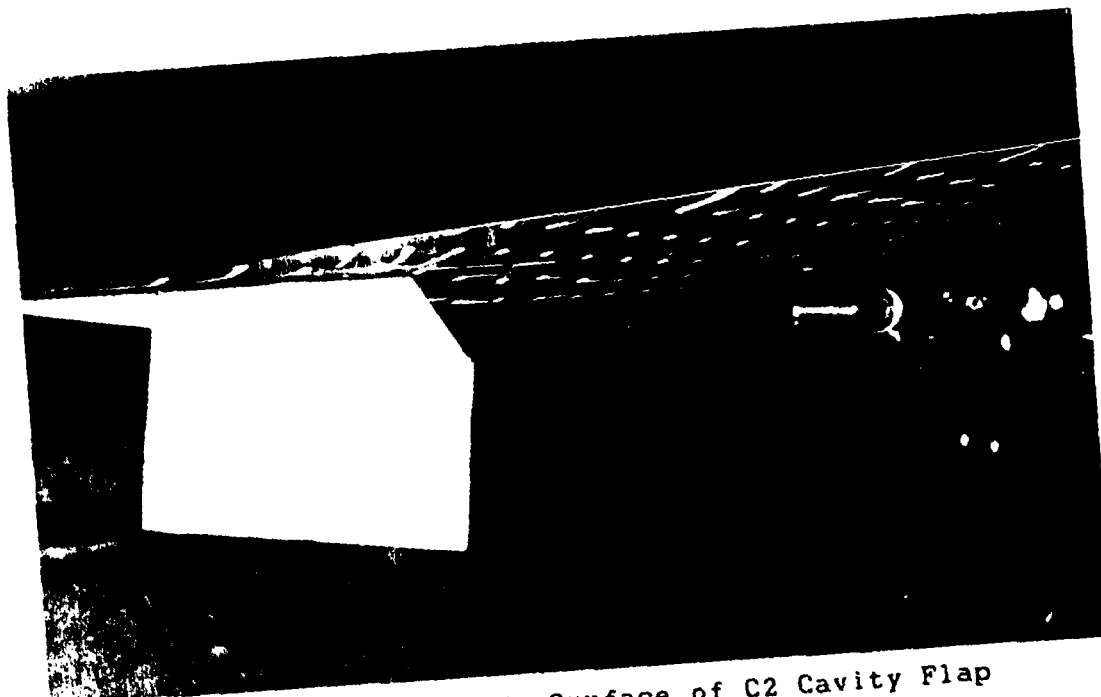


Figure B17. Inside Surface of C2 Cavity Flap
Deployed 60° at $30^\circ \alpha$

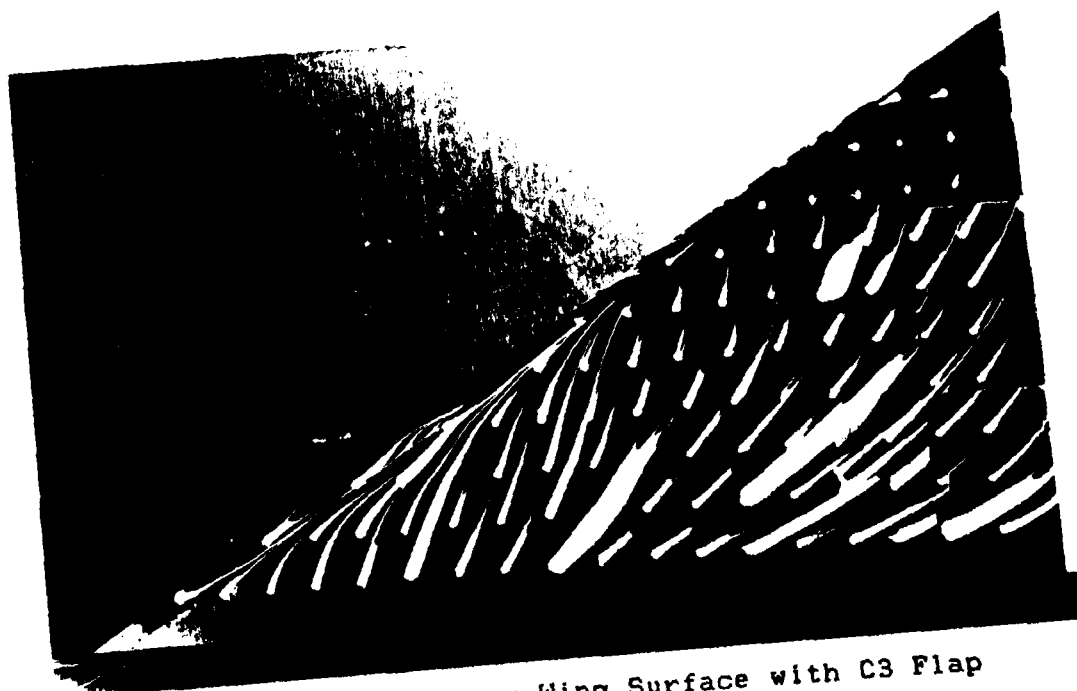


Figure B18. Upper Wing Surface with C3 Flap
Deployed 60° at $30^\circ \alpha$

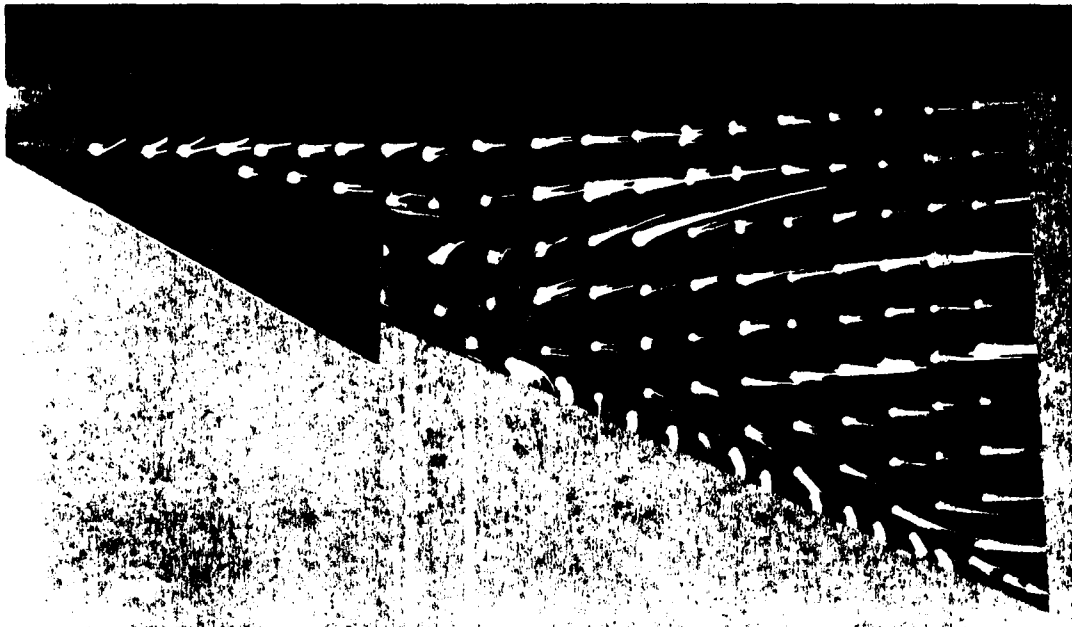


Figure B19. Lower Wing Surface with C3 Flap
Deployed 60° at $30^\circ \alpha$

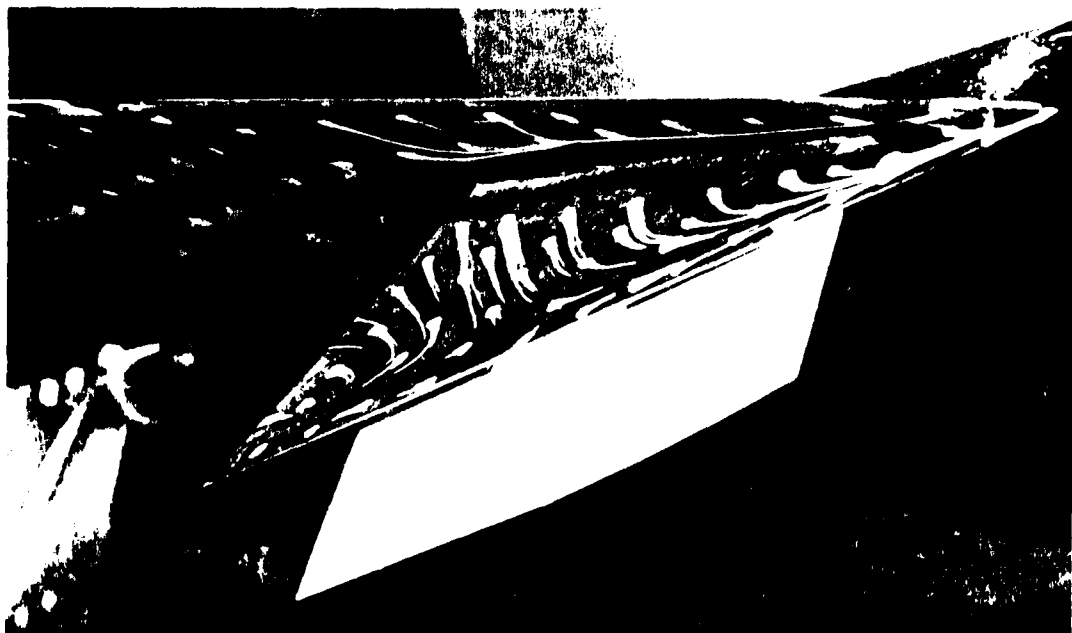


Figure B20. Inside Surface of C3 Cavity Flap
Deployed 60° at $30^\circ \alpha$

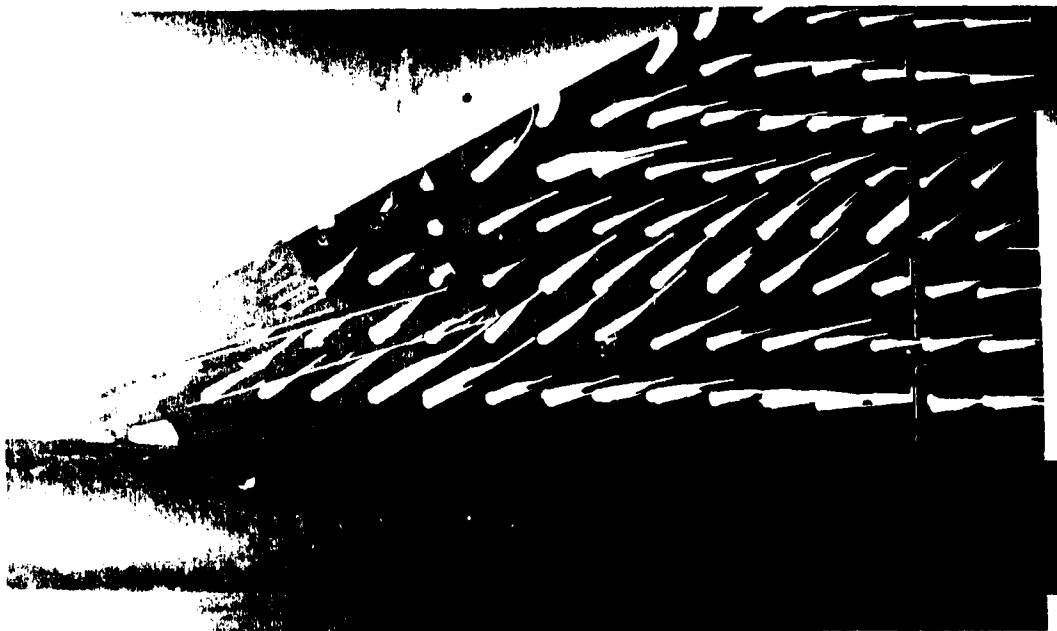


Figure B21. Lower Wing Surface with C4 Flap
Deployed 60° at $20^\circ \alpha$



Figure B22. Upper Wing Surface with C4 Flap
Deployed 60° at $20^\circ \alpha$

Bibliography

1. Duncan, Capt Terry A. A Wind Tunnel Investigation to Determine Dominant Forebody Strake Design Characteristics for an F-15 Equipped with Conformal Fuel Tanks. MS Thesis GAE/AA/83D-7. School of Engineering, Air Force Institute of Technology (AU), Wright-Patterson AFB OH, December 1983.
2. Etkin, Bernard. Dynamics of Atmospheric Flight. New York: John Wiley and Sons, Inc., 1972.
3. Hoffler, Keith D. Personal Interviews. Vigyan Research Associates, Inc., Hampton, Virginia, July and August 1985.
4. Kuethe, Arnold M. and Chuen-yen Chow. Foundations of Aerodynamics: Bases of Aerodynamic Design (Third Edition). New York: John Wiley and Sons, Inc., 1976.
5. Marchman, James F. III and Mark L. Hollins, "Fuselage Effects in Leading Edge Vortex Flow Aerodynamics," ICAS-82-6.7.5, August 1982.
6. McKernan, Capt Thomas J., Jr. A Wind Tunnel Investigation to Examine Stability and Control Characteristics of the T-46A at High Sideslip Angles. MS Thesis GAE/AA/85D-16. School of Engineering, Air Force Institute of Technology (AU), Wright-Patterson AFB OH, December 1984.
7. Payne, F. M. and R. C. Nelson, "An Experimental Investigation of Vortex Breakdown on a Delta Wing," Vortex Flow Aerodynamics Conference, 8-10 October 1985. NASA Langley Research Center, Langley Field, Virginia.
8. Rae, William H., Jr. and Alan Pope. Low-Speed Wind Tunnel Testing (Second Edition). New York: John Wiley and Sons, Inc., 1984.
9. Rao, Dhanvada M., Vice-President. Personal Interviews. Vigyan Research Associates, Inc., Hampton, Virginia, July 1985.
10. Rao, Dhanvada M., and Keith D. Hoffler Pressure and Flow Investigation of Apex Fences and Cavity Flaps on a 60 Degree Delta Wing. Contract Report for Air Force Flight Dynamics Laboratory, Wright-Patterson AFB OH, December 1985.

11. Rao, Dhanvada M. Investigation of a High-Alpha Yaw Control Concept on Highly Swept Wing Configuration. Control No. L-69183B. Contract Report for NASA Langley Research Center, Langley Field, Virginia, April 1985.

12. Rao, Dhanvada M. "Vortical Flow Management for Improved Configuration Aerodynamics - Recent Experiences", Paper No. 30. AGARD Symposium on Aerodynamics of Vortical Type Flows in Three Dimensions, 25-28 April 1983.

13. Spitler, Capt Charles R. A Wind Tunnel Investigation of Stability and Control Characteristics of the Fairchild T-46 at High Angles of Attack. MS Thesis GAE/AA/84D-27. School of Engineering, Air Force Institute of Technology (AU), Wright-Patterson AFB OH, December 1984.

14. Stuart, 2Lt Michael. Experimental Study of Apex Fences for Lift Enhancement on a Highly Swept Delta Wing Configuration. Ms Thesis GAE/AA/85D-14. School of Engineering, Air Force Institute of Technology (AU), Wright-Patterson AFB OH, December 1985.

Vita

Captain Huland Christopher Smith was born on 12 June 1958 in Poplarville, Mississippi. He attended Poplarville's public school system and graduated with honors in May 1976. He entered Mississippi State University and received a degree of Bachelor of Science in Aerospace Engineering, Cum Laude, in May 1981. Upon graduation, he was commissioned in the United States Air Force through the Reserve Officers' Training Corps program. He was assigned to the 6585th Test Group (Armament Division), Holloman Air Force Base, New Mexico. His primary responsibilities involved flight testing and analyzing inertial navigation systems for all Department of Defense agencies. He served in this position for three years. In May 1984, he entered the School of Engineering, Air Force Institute of Technology, to pursue a masters' degree.

Permanent Address:

Rural Route 4, Box 460
Poplarville, Mississippi
39470

UNCLASSIFIED

SECURITY CLASSIFICATION OF THIS PAGE

REPORT DOCUMENTATION PAGE

1a. REPORT SECURITY CLASSIFICATION Unclassified			1b. RESTRICTIVE MARKINGS			
2a. SECURITY CLASSIFICATION AUTHORITY			3. DISTRIBUTION/AVAILABILITY OF REPORT Approved for public release; distribution unlimited.			
2b. DECLASSIFICATION/DOWNGRADING SCHEDULE						
4. PERFORMING ORGANIZATION REPORT NUMBER(S) AFIT/GAE/AA/85D-13			5. MONITORING ORGANIZATION REPORT NUMBER(S)			
6a. NAME OF PERFORMING ORGANIZATION School of Engineering		6b. OFFICE SYMBOL (If applicable) AFIT/ENY		7a. NAME OF MONITORING ORGANIZATION		
6c. ADDRESS (City, State and ZIP Code) Air Force Institute of Technology Wright-Patterson AFB, Ohio 45433			7b. ADDRESS (City, State and ZIP Code)			
8a. NAME OF FUNDING/SPONSORING ORGANIZATION AFWAL		8b. OFFICE SYMBOL (If applicable) FIMM		9. PROCUREMENT INSTRUMENT IDENTIFICATION NUMBER		
8c. ADDRESS (City, State and ZIP Code) AFWAL/FIMM Wright-Patterson AFB, Ohio 45433			10. SOURCE OF FUNDING NOS.			
11. TITLE (Include Security Classification) see item 19.			PROGRAM ELEMENT NO.		PROJECT NO.	TASK NO.
						WORK UNIT NO.
12. PERSONAL AUTHOR(S) Huland Christopher Smith, B.S.E., Captain, USAF						
13a. TYPE OF REPORT MS Thesis		13b. TIME COVERED FROM _____ TO _____		14. DATE OF REPORT (Yr., Mo., Day) December 1985		15. PAGE COUNT 237
16. SUPPLEMENTARY NOTATION						
17. COSATI CODES			18. SUBJECT TERMS (Continue on reverse if necessary and identify by block number)			
FIELD	GROUP	SUB. GR.	Cavity Flaps, Leading Edge Vortex Flaps, Vortex Flaps, Delta Wing, Vortices, High Alpha, Yaw Control, Vortex Lift Effect, Maneuverability, Hinge Line Sweep			
01	03					
20	04					
19. ABSTRACT (Continue on reverse if necessary and identify by block number)						
Title: EXPERIMENTAL ASSESSMENT OF VORTEX RETAINING CAVITY FLAPS FOR MANEUVERABILITY IMPROVEMENT ON DELTA WING FIGHTER AIRCRAFT						
Thesis Advisor: Wesley R. Cox, Captain, USAF Assistant Professor of Aeronautical Engineering						
Abstract on reverse.						
<div style="text-align: right;"> Approved for public release: IAW AFR 190-1. LYNN E. WOLAVER 16 JAN 86 Dean for Research and Professional Development Air Force Institute of Technology (AFIT) Wright-Patterson AFB OH 45433 </div>						
20. DISTRIBUTION/AVAILABILITY OF ABSTRACT			21. ABSTRACT SECURITY CLASSIFICATION			
UNCLASSIFIED/UNLIMITED <input checked="" type="checkbox"/> SAME AS RPT. <input type="checkbox"/> DTIC USERS <input type="checkbox"/>			Unclassified			
22a. NAME OF RESPONSIBLE INDIVIDUAL Cox, Wesley R., Captain, USAF			22b. TELEPHONE NUMBER (Include Area Code) (513) 255-6998		22c. OFFICE SYMBOL AFIT/ENY	

DD FORM 1473, 83 APR

EDITION OF 1 JAN 73 IS OBSOLETE.

UNCLASSIFIED

SECURITY CLASSIFICATION OF THIS PAGE

19. Abstract

An experimental study was conducted to determine the effectiveness of cavity flaps on delta wing aircraft maneuverability. Cavity flaps are conformal control surfaces deployed in the apex region on the wing's lower surface. A 60° swept delta wing model was built and tested in the Air Force Institute of Technology five-foot diameter, subsonic wind tunnel. Ten different cavity flap configurations were tested at deflection angles ranging from 30° to 90° for both asymmetric and symmetric deployments. One configuration was tested at sideslip angles of -6° and 6° to determine the effect of yaw on the cavity flap. For all configurations the angle of attack was varied from -6° to 49°.

Coefficients of aerodynamic forces and moments versus angle of attack along with the lift to drag ratio versus lift coefficient and the drag polar were plotted for each flap configuration. The changes to the aerodynamic coefficients produced by adding the cavity flaps were also plotted. Oil flow visualization studies were performed on a limited number of cavity flap configurations at different angles of attack: 9.5, 20, and 30 degrees.

Results indicate that for longitudinal, lateral and directional maneuverability, the best cavity flap deflection angle will vary depending on the desired response. However, the smaller deflection angles, 30° and 45°, gave the greatest moment changes. These results confirmed an earlier yaw control investigation by Rao at high angles of attack using a cavity flap deflected 45° along the fuselage. Data results also indicated it is best not to have the cavity flap hinge line located along or parallel to the fuselage for rolling and pitching moment considerations. Of the two hinge line sweep angles tested, 75° and 90°, the former produced greater moment changes. The cavity flap surface area had a large influence on the aerodynamic moments. The larger areas tested, 6% and 12% of the total wing area, showed the greatest changes. These larger areas were also responsible for significant drag reductions, up to 15%, in some configurations. But minimum lift losses as a result of cavity flap deployments came from the smaller cavity flap areas tested, 3% and 6% of the total wing area.

END

FILMED

3-86

DTIC